University Library

A gateway to Melbourne's research publications

Minerva Access is the Institutional Repository of The University of Melbourne

Author/s:
Momeni, Arash

Title:
Energy-Efficient Liquid Sorbent for Carbon Dioxide Separation

Date:
2025

Persistent Link:
https://hdl.handle.net/11343/361223

Terms and Conditions:
Terms and Conditions: Copyright in works deposited in Minerva Access is retained by the copyright owner. The work may not be altered without permission from the copyright owner. Readers may only download, print and save electronic copies of whole works for their own personal non-commercial use. Any use that exceeds these limits requires permission from the copyright owner. Attribution is essential when quoting or paraphrasing from these works.

Energy-Efficient Liquid Sorbent for Carbon Dioxide Separation

Arash Momeni

Student number: 1156199

Doctor of Philosophy

July 2025

Department of Chemical Engineering

The University of Melbourne

A thesis submitted in total fulfilment of the requirements for the degree of Doctor of Philosophy at the University of Melbourne

Abstract

The rapid increase in global CO_2 emissions has become a major environmental concern, with atmospheric CO_2 concentrations now exceeding 420 ppm, nearly 50% higher than preindustrial levels. This rise has contributed to a global temperature increase of approximately 1 °C. The Paris Agreement seeks to keep global temperature rise below 2 °C, with the ambitious goal of limiting it to 1.5 °C. Achieving this goal requires not only reducing greenhouse gas emissions but also actively removing CO_2 through Negative Emissions Technologies (NETs). Direct Air Capture (DAC) is a crucial technology designed to achieve this goal, as it captures CO_2 directly from the atmosphere. Among the CO_2 capture methods, solvent-based technology is considered as one of the most mature and viable options due to its implementation in industrial sectors. These systems can also be adapted for DAC applications. However, they face several challenges, primarily due to the ultra-low concentration (~0.04%) of CO_2 in ambient air compared to industrial scenarios. This low concentration necessitates high operating temperatures (due to different CO_2-containg species in the solvent) and significantly increases the energy required for solvent regeneration per ton of CO_2 captured which is a major drawback. As a result, DAC remains an energy-intensive process with notable technical and economic challenges to address.

Given these challenges, various strategies have been explored in liquid-based CO_2 capture applications to lower energy consumption and improve cost-effectiveness, including low temperature membrane vacuum regeneration (MVR), hybrid solvents, phase change solvents, catalytic solvent regeneration, crystallization-based regeneration, etc. Due to the high energy intensity of DAC, combining suitable solvents with low-temperature, energy-efficient regeneration methods that are compatible with renewable energy sources offers a promising route to improve efficiency, sustainability, and viability of these systems. Such an approach

could ultimately support the large-scale implementation of DAC process. Therefore, the main goal of this thesis is to develop an integrated system of advanced, sustainable regeneration methods in a liquid-based DAC process, aiming to experimentally quantify and evaluate its operability, CO_2 separation efficiency, and overall energy demand which has been accomplished in three main Chapters (Chapter 4, 5, and 6).

In Chapter 4, two bench-scale solvent-based DAC systems, CO_2 absorption and desorption units, were designed and developed using hollow fiber membrane contactors (HFMCs). In the absorption unit, the kinetics and equilibrium performance of five amino acid salts were examined in long-term operations, revealing high absorption stability for all amino acid salts and identifying potassium glycinate (GlyK) as the suitable solvent among those evaluated in this Chapter. To optimize CO_2 absorption efficiency, a parametric analysis was performed using GlyK, evaluating the effects of air and solvent flow rates, as well as solvent temperature and concentration. In the desorption unit, low-temperature MVR experiments with GlyK were conducted to investigate the influence of solvent temperature and concentration, solvent CO_2 loading, vacuum pressure, and sweep gas on CO_2 stripping efficiency. A validated model was then employed to assess the impact of membrane characteristics on the overall absorption-desorption performance.

Building on the knowledge gained in Chapter 4 and acknowledging that desorption is the most energy-intensive step in the process, Chapter 5 focused on advancing the desorption unit by integrating catalytic solvent regeneration with low-temperature MVR. First, non-catalytic regeneration experiments were conducted using three different HFMCs and four green amino acid salts under varying conditions (e.g., temperatures and flowrates). Based on CO_2 transfer rates, ultra-thin dense composite membranes and aqueous potassium taurinate (TauK) were most promising for MVR in DAC application. For catalytic membrane vacuum regeneration (C-MVR) trials, commercial ion-exchange resins were used and improved CO_2 desorption

fluxes by up to 64.4% and reduced thermal energy requirements by up to 39.1%. TauK demonstrated the highest CO_2 flux and lowest thermal energy consumption. A parametric study was also conducted to examine the effects of temperature, catalyst loading, and solvent concentration on catalyst impact. The results highlight C-MVR as a promising and energy-efficient approach for sustainable DAC.

In the final Chapter, building on the demonstrated benefits of energy-efficient methods in previous Chapter, the effectiveness of several advanced technologies was further evaluated. Hybrid green amino acid solvents, catalytic solvent regeneration, and MVR were integrated to enhance the desorption step in the DAC process. First, iron-sulfated zirconia (Fe-SZ) was impregnated on two catalytic supports, Al_2O_3 and SiO_2, and their effects on MVR efficiency were evaluated, with SiO_2 selected as the preferred support. Various SZ/SiO_2 ratios were then synthesized to identify the optimal composition for enhancing CO_2 desorption. Using the optimum ratio of Fe-SZ/SiO_2(1/1), the impact of different catalyst concentrations was examined, leading to a reduction in relative heat duty to 59.7%. Subsequently, a series of hybrid solvents based on 3 M TauK blended with 0.5-1.5 M SarK were prepared and tested, with the 3 M TauK + 1 M SarK formulation showing the best CO_2 desorption performance, achieving a 69.1% improvement compared to 3 M TauK alone. Finally, the selected hybrid solvent and optimized composite catalyst were integrated and trialed in MVR at 90 °C, yielding a 66.8% decrease in energy consumption relative to the benchmark 3 M GlyK system, bringing the energy requirement down to 2.6 GJ/tCO_2 under liquid-based DAC conditions.

Overall, this thesis studies the absorption-desorption kinetics and equilibrium performance of green amino acid salts under DAC conditions and highlights the critical importance of integrating energy-efficient and sustainable technologies to enhance the viability and energy performance of liquid-based DAC systems.

Declaration

This is to certify that:

(i) This thesis comprises only my original work towards the Ph.D.,
(ii) Due to acknowledgment has been made in the text to all other material used, and
(iii) This thesis is less than 100,000 words in length, exclusive of tables, bibliographies, appendices, and footnotes.

Arash Momeni

July 2025
Department of Chemical Engineering
The University of Melbourne

Preface

This thesis consists of eight Chapters. The first Chapter provides an introduction, while Chapter 2 presents a literature review that outlines prior research in the field and highlights gaps and the objectives of this research. Chapter 3 details the experimental techniques employed throughout this study. Chapters 4, 5, and 6 contain material that has either already been published (Chapters 4 and 5) or is currently being reviewed for publication (Chapter 6) as show below. Chapter 7 provides a summary of the main conclusions and provides recommendations for future research. Appendix provides supplementary information for Chapter 4 to 6.

Chapter 4:

Momeni A, McQuillan RV, Alivand MS, Zavabeti A, Stevens GW, Mumford KA. Direct air capture of CO_2 using green amino acid salts. Chemical Engineering Journal.

Chapter 5:

Momeni A, McQuillan RV, Anisi H, Alivand MS, Zavabeti A, Stevens GW, et al. Catalytic Membrane Vacuum Regseneration: Enhancing Energy Efficiency and Renewable Compatibility in Direct Air Capture. Small.

Chapter 6:

Momeni A, Anisi H, McQuillan RV, Alivand MS, Zavabeti A, Askari S, Zhang R, Stevens GW, Mumford KA. Catalytic Hybrid Solvent Regeneration in Membrane Vacuum Processes for Direct Air Capture. ***Under Review***.

All Publications

The following publications have been produced during the PhD candidature:

- McQuillan RV, Niu Y, **Momeni A**, Zavabeti A, Jafari M, Alivand MS, et al. Employing SO_4^{2-}/ZrO_2 Super-Acid Catalysts for Energy-Efficient Direct Air Capture of CO_2. Separation and Purification Technology, 133895.
- **Momeni A**, Anisi H, Alivand MS, Mumford KA. Australian Provisional Patent Application No. 2025900700.
- **Momeni A**, McQuillan RV, Anisi H, Alivand MS, Zavabeti A, Stevens GW, et al. Catalytic Membrane Vacuum Regeneration: Enhancing Energy Efficiency and Renewable Compatibility in Direct Air Capture. Small, 2503023.
- Kim S, **Momeni A**, Alivand MS, Bolne PC, Mumford KA, Kentish SE. Catalytic Carbon Dioxide Absorption and Stripping Using Nanofibrous Membrane Contactors. Separation and Purification Technology, 133079.
- Anisi H, McQuillan RV, Alivand MS, Stevens GW, **Momeni A**, Mazaheri O, Mumford KA. Synergistic Effect of Amino Acid Salt Hybrid Systems for DAC of CO_2. ACS Sustainable Chemistry & Engineering, 4691-702.
- **Momeni A**, McQuillan R, Alivand M, Zavabeti A, Stevens G, Mumford K. Hollow Fiber Membrane Application in Direct Air Capture Using Amino Acid Salts. Available at SSRN 5048010.
- **Momeni A**, McQuillan RV, Alivand MS, Zavabeti A, Stevens GW, Mumford KA. Direct Air Capture of CO_2 Using Green Amino Acid Salts. Chemical Engineering Journal, 147934.
- McQuillan RV, **Momeni A**, Alivand MS, Stevens GW, Mumford KA. Evaluation Of Potassium Glycinate as a Green Solvent For Direct Air Capture and Modelling Its Performance in Hollow Fiber Membrane Contactors. Chemical Engineering Journal, 148764.
- Alivand MS, McQuillan RV, **Momeni A**, Zavabeti A, Stevens GW, Mumford KA. Facile Fabrication of Monodispersed Carbon Sphere: A Pathway Toward Energy-Efficient Direct Air Capture (DAC) Using Amino Acids. Small, 2300150.
- **Momeni A**, Anisi H, McQuillan RV, Alivand MS, Zavabeti A, Askari S, Zhang R, Stevens GW, Mumford KA. Catalytic Hybrid Solvent Regeneration in Membrane Vacuum Processes for Direct Air Capture. Under Review.

Acknowledgments

Completing this Ph.D. has been a challenging yet rewarding journey, and it wouldn't have been possible without the support, guidance, and encouragement of so many wonderful people. I am deeply grateful to everyone who has played a part in this experience.

First and foremost, I would like to express my sincere thanks to my supervisors, Prof. Kathryn Mumford, Dr. Ali Zavabeti, and Dr. Masood Sheikh Alivand. Your guidance, patience, support, sharing your expertise and feedback have made all the difference.

I would like to acknowledge my colleagues in the Department of Chemical Engineering for their support throughout this journey. A special thanks to Majid Soltani, Rebecca McQuillan, Omid Mazaheri, and Hossein Anisi for their help, support, friendship and for making this journey memorable.

I would like to thank my wife, Donya, for her endless love and support, and boundless understanding, which have been my greatest source of strength throughout this journey.

Finally, to my parents, words cannot express how grateful I am for your constant love, kindness, support, and understanding.

Thank you all for making this journey possible and for being part of my story.

Table of Contents

Abstract ii
Declaration v
Preface vi
All Publications vii
Acknowledgments viii
Nomenclature 19
1 Introduction 20
2 Literature Review 25
2.1 Perspective 26
2.2 Direct Air Capture 26
2.3 Gas-liquid Membrane Contactors 35
2.4 Catalytic Solvent Regeneration 41
2.4.1 Catalytic CO_2 Desorption Mechanism 42
2.4.2 Solid Acid Catalysts 48
2.5 Research Objectives 64
3 Experimental Methods 65
3.1 Perspective 66
3.2 DAC Absorption-Desorption Apparatus 66
3.2.1 Absorption Set-up 67
3.2.2 Desorption Set-up 69
3.2.2.1 Membrane Vacuum Regeneration for Chapter 4 69
3.2.2.2 Membrane Vacuum Regeneration for Chapter 5 70
3.2.2.3 Membrane Vacuum Regeneration for Chapter 6 73
3.3 OptiMaxTM workstation 1001 (Mettler-Toledo) 76
3.4 Chittick Apparatus 79
3.5 Characterization Methods 80
3.5.1 Fourier Transform Infrared (FTIR) 80
3.5.2 X-ray Photoelectron Spectroscopy (XPS) 80
3.5.3 Elemental Analysis 81
3.5.4 Scanning Electron Microscopy (SEM) 81
3.5.5 Transmission Election Microscopy (TEM) 81
3.5.6 Nuclear Magnetic Resonance (NMR) Spectroscopy 81

3.5.7 Ammonia and CO_2 Temperature Programmed Desorption (TPD) Technique..82
3.6 Materials....82
3.7 Hollow Fiber Membrane Contactors (HFMCs)....83
3.7.1 Used HFMC for Chapter 4....83
3.7.2 Used HFMCs for Chapter 5....83
3.7.3 Used HFMCs for Chapter 6....84
3.8 Materials Preparation....84
3.8.1 Amino Acid Salt Solution Preparation....84
3.8.2 Synthesis Procedure of Acidic Silica and Alumina....85
4 Direct Air Capture of CO_2 Using Green Amino Acids....86
4.1 Introduction....87
4.2 Results and Discussion....89
4.2.1 DAC-Absorption....89
4.2.1.1 Screening Amino Acid Salt Sorbents....90
4.2.1.2 Solvent Temperature....94
4.2.1.3 Solvent Concentration....96
4.2.2 Low-Temperature DAC Regeneration....97
4.2.2.1 Solvent Temperature....98
4.2.2.2 Vacuum Pressure....101
4.2.2.3 Solvent Concentration....101
4.2.2.4 Sweep Gas....102
4.2.3 Simulation....104
4.3 Conclusion....106
5 Catalytic Membrane Vacuum Regeneration: Enhancing Energy Efficiency and Renewable Compatibility in Direct Air Capture....110
5.1 Introduction....111
5.2 Results and Discussion....113
5.2.1 Membrane Module Performance....113
5.2.2 Amino Acid Performance....114
5.2.3 Solvent Temperature and Flow Rate....116
5.2.4 Catalytic Membrane Vacuum Regeneration (C-MVR)....118
5.2.5 Catalyst Impact by Solvent Condition....124
5.2.6 Catalyst Stability....126
5.3 Conclusion....127

6 Catalytic Hybrid Solvent Regeneration in Membrane Vacuum Processes for Direct Air Capture 130
6.1 Introduction 131
6.2 Results and Discussion 134
6.2.1 Membrane Module Performance 134
6.2.2 Composite Solid Acid Catalyst 136
6.2.2.1 Catalytic Support (SiO_2 vs. Al_2O_3) 136
6.2.2.2 SZ to SiO_2 ratio 140
6.2.2.3 Catalyst Concentration and Stability 142
6.2.3 Hybrid Amino Acid Solvents 145
6.2.4 Catalytic Hybrid Amino Acid Solvents in MVR 148
6.3 Conclusion 151
7 Conclusion and outlooks 153
7.1 Thesis Summary 154
7.2 Recommendations for Future Work 157
Appendix 160
A.1. Supplementary Information of Chapter 4 161
A.2. Supplementary Information of Chapter 5 165
A.3. Supplementary Information of Chapter 6 171
References 176

List of Figures

Figure 2.1. Illustration of the alkali-based DAC process Carbon Engineering contactor design; reused with permission (60).....27
Figure 2.2. Process flow diagram of the alkali-scrubbing DAC process; reused with permission (6, 54).....28
Figure 2.3. Used DAC-apparatus for screening different amine-based solvent in the study of Barzagli et al.; reused with permission (2020)(69).....31
Figure 2.4. Process flow diagram for direct air capture using MEA solvent; reused with permission (13).....32
Figure 2.5. Breakdown of capital costs for key equipment in liquid-based DAC system using MEA; reused with permission (13).....33
Figure 2.6. a) CO_2 loading profiles of 1M GlyK (indicated by red squares) and SarK (represented by blue dots) under DAC conditions, using an air humidifier (shown on the left) as air-solvent contactor. b) Consecutive absorbing/desorbing cycles with sarcosine/m-BBIG; reused with permission (11, 12).....35
Figure 2.7. Process flow diagram of the apparatus used in the work by Nieminen et al.; reused with permission (87).....36
Figure 2.8. Photograph of the setup used in the study by Nieminen et al.; reused with permission (87).....36
Figure 2.9. CO_2 mass transfer resistance in MVR process; reused with permission; reused with permission (89).....38
Figure 2.10. Process flow diagram of the experimental apparatus for regenerating CO_2-rich solvent using MVR in the study of Fang et al.; reused with permission (89).....38
Figure 2.11. Diagram illustrating a gas-filled porous membrane contactor alongside a thin film composite membrane contactor, highlighting both dry and wetted conditions of porous support; reused with permission (91).....39
Figure 2.12. Synthesis procedure for preparation of water-dispersible Fe_3O_4 nanospheres using amino acids; reused with permission (103).....49
Figure 2.13. Analysis of ζ potential values of diverse water-dispersible Fe_3O_4 nanomaterials produced with various amino acids (all nanoparticles were dispersed in 0.1 M 3-(n-morpholino) propane sulfonic acid (MOPS) buffer at pH 9.0). The abbreviations used for amino acids from left to right: Histidine (His), Alanine (Ala), Glycine (Gly), Sarcosine (Sarc), Arginine (Arg), Proline (Pro), Lysine (Lys), Valine (Val), Leucine (Leuc), Glutamine (Glu), Serine (Ser), Asparagine (Asp); reused with permission (103).....50
Figure 2.14. Tuning the acidic features of magnetic Fe_3O_4 nanospheres with different ratio of amino to sulfanilic acid in single-pot synthesis technique. Each ratio is designated with a distinct letter (e.g., C refers to Fe_3O_4-Ala-C with a ratio of 0.5:1); reused with permission (103).....50
Figure 2.15. Sulfur concentration detected by XPS at various ratios of amino to sulfanilic acid; reused with permission (103).....51
Figure 2.16. a) Enhancement of CO_2 desorption rate for water-dispersible nanocatalysts with various tailored chemical characteristics. b) CO_2 desorption profiles in the presence and absence of selected nancatalyst (Fe_3O_4−Ala-C); reused with permission (103).....52

Figure 2.17. Utilizing the selected water-dispersible nanocatalyst Fe_3O_4-Ala-C in various solutions for energy-saving regeneration. a) for different types of amino acids (1 M). b) for variety types of amines (primary type (MEA, 5 M), tertiary type (MDEA, 2 M), and primary-tertiary blend type (MEA−MDEA, 5 M-2 M)); reused with permission (103).....52
Figure 2.18. The production of nanoclusters by a one-pot synthesis technique; reused with permission (34) 54
Figure 2.19. The metal and ligands utilized to synthesize different MOF coatings with distinct physicochemical properties; reused with permission (34).....54
Figure 2.20. SEM images of (a) Fe_3O_4@ZIF-8, (b) Fe_3O_4@ZIF-67, (c) Fe_3O_4@MOF-Fe(II), (d) Fe_3O_4@MIL-100(Fe), (e) Fe_3O_4@HKUST-1, and (f) Fe_3O_4@UiO-66. All scale bars correspond to 200 nm. (g) Pore volume and mesoporosity of the different Fe_3O_4@MOFs; reused with permission (34).....55
Figure 2.21. The influence of different water-dispersible nanocatalysts on relative heat duty (RH) and cyclic CO_2 capacity of MEA aqueous solution; reused with permission (34).....56
Figure 2.22. Schematic illustration of the synthesis process for monodispersed carbon spheres (MCSs), accompanied by their b) SEM and c) TEM images; reused with permission (40). ..57
Figure 2.23. a) Chemical structures of the selected amino acids, and b) schematic of the custom-built rising-bubble setup for capturing CO_2 from ambient air. c) Equilibrium CO_2 loading of 1 M amino acid solutions across various temperatures. d) Cyclic CO_2 capacities of these solutions between 25 and 98 °C, representing absorption and desorption conditions. All equilibrium measurements were performed using air containing approximately 410 ppm CO_2 ; reused with permission (40).....58
Figure 2.24. a) MCS-SO_3H Catalytic CO_2 desorption improvement at 98 °C in different amino acid aqueous solutions (1 M). b) CO_2 desorption curves of catalytic and blank LysK; reused with permission (40) 59
Figure 2.25. Comparative plots showing a) mesopore surface area versus average pore diameter, b) total surface area versus average pore diameter, c) Lewis to Brønsted acid sites, and d) acid strength versus total acid sites for various catalysts utilized for CO_2 desorption in low temperature ranges; reused with permission (43). 60
Figure 2.26. Impact of various catalysts on relative heat duty of the MEA solution (43); reused with permission.....62
Figure 3.1. Desorption CO_2 profile of various amino acids, a) potassium glycinate (GlyK), b) potassium sarcosinate (SarK), c) potassium prolinate (ProK), d) potassium lysinate (LysK), and e) potassium argininate (ArgK) solutions. 78
Figure 4.1. a) Schematic diagram of DAC-absorption using HFMC, absorption mechanism, and amino acid salts structures b) Absorption efficiency (η_a) of 1 M GlyK in a long-term operation at different solvent loadings. c) The DAC-equilibrium CO_2 loading points for different amino acid salt solutions and the comparison with previously obtained DAC-equilibrium data (40). d) Absorption efficiency (η_a) of 1 M of different amino acid salt solutions at various solvent loadings. All data were obtained at 20 °C, air flow rate = 7.2 L/min, and solvent flow rate = 0.25 L/min.....94
Figure 4.2. a) The DAC-equilibrium point and average outlet RH% for 1 M GlyK at different temperatures. b) The DAC-equilibrium point for different GlyK concentrations at 20 °C. c) The CO_2 absorption flux (J_a) of 1 M GlyK at different temperatures in various solvent loading conditions. All data was obtained at air flow rate = 7.2 L/min, and solvent flow rate = 0.25 L/min.....97

Figure 4.3. a) Schematic diagram of low-temperature DAC regeneration using HFMC, desorption mechanism, and Gly structure b) 1 M GlyK cyclic capacity and overall desorption efficiency at different regeneration temperatures. c) 1 M GlyK DAC-desorption flux (J_d) at different temperatures and solvent CO_2 loadings. All data were obtained at 21 $kPa_{(a)}$, and solvent flow rate = 0.25 L/min.....100
Figure 4.4. a) 1M GlyK overall DAC-desorption efficiency at different vacuum pressures. b) 1M GlyK DAC desorption flux (J_d) at different vacuum pressure levels and solvent loadings. c) Total g of removed CO_2 using different GlyK concentration at 21 $kPa_{(a)}$. d) DAC desorption flux (J_d) of GlyK at different level of concentration at 21 $kPa_{(a)}$. The result of two modes of trials for Vacuum, and Vacuum/sweep gas mode e) Water make-up percentage. f) CO_2 solvent loading values through time. The data were obtained at 80°C, and solvent flow rate = 0.25 L/min.....104
Figure 4.5. a) Schematic of dense membrane layer thickness effect on the CO_2 separation efficiency. Dense membrane layer thickness effect on b) Absorption efficiency c) Desorption flux using developed model.....108
Figure 5.1. a) CO_2 flux, b) water flux, and c) ratio of water to CO_2 flux for three used HFMCs at 90 °C. d) CO_2 desorption profiles over time, and e) water flux and CO_2 flux of various 3M amino acids at 100 °C. All trials were accomplished at 2-4 kPa(a), 0.25 L/min.....116
Figure 5.2. a) A schematic illustrating the superior performance of TauK over GlyK across the entire regeneration temperature range of 80-100 °C. b) 3 M TauK CO_2 desorption profiles over time at various temperatures. c) 3 M TauK and GlyK CO_2 flux at various temperatures. d) 3 M GlyK CO_2 flux at 100 °C under different solvent flow rates. All trials were accomplished at 2-4 kPa(a). Solvent flow rates set to 0.25 L/min for (b, c). 118
Figure 5.3. a) Schematic diagram of acidic cation resins, SEM images and TEM-EDX mapping of Resin A. b) Sulfur content analyzed by XPS for two cation resins. c) High-resolution XPS spectra of Resin A, and d) Resin B. e) 3 M TauK CO_2 desorption profiles over time, and f) CO_2 flux values for various 3 M amino acids without/with catalyst for different concentrations. g) Catalyst enhancement values for different concentrations and various 3 M amino acids. h) Relative heat duty using 6wt% catalyst for 3 M amino acids. All trials were accomplished at 100 °C, 2-4 $kPa_{(a)}$, 0.25 L/min, using Resin A. No catalyst was used for blank solvent.....123
Figure 5.4. a) CO_2 desorption profiles for GlyK, and b) TauK with/without catalyst at 90 °C. c) CO_2 desorption profiles for 2 M TauK, d) 2.5 M TauK, and e) 3 M TauK+0.5 M K_2CO_3 with/without catalyst at 100 °C. f) CO_2 flux and catalyst enhancement values for (a-e). g) Catalyst stability in four cycles. h) Sulfur and O-H bond content for fresh, first and forth cycles. All trials were accomplished at 2-4 kPa(a), 0.25 L/min, using Resin A (6wt% concentration). 127
Figure 6.1. a) Schematic flow diagram of MVR unit with fixed bed catalyst. HFMCs performance detailing b) maximum CO_2 flux, c) Water flux, and d) Water flux to CO_2 flux ratio. 135
Figure 6.2. a) Schematic synthesis procedure (impregnation method) for two mesoporous substrate silica and alumina. b) SEM images and TEM-EDX mapping of Fe-SZ/SiO_2(1/1). High-resolution XPS spectra of the Fe-SZ/SiO_2(1/1) catalyst showing core-level signals of c) S 2p, d) Zr 3d, and e) Fe 2p. f) CO_2 flux profiles with and without Fe-SZ/SiO_2(1/1). g) Total desorbed CO_2 and catalyst enhancement of Fe-SZ/SiO_2(1/1) and Fe-SZ/Al_2O_3(1/1). All MVR

trials were accomplished using 3M GlyK at 90 °C. No catalyst is used for blank solvent. All catalysts were doped with 10% Fe. 139
Figure 6.3. a) CO_2 flux curves and total desorbed CO_2 with and without 6wt% Fe-SZ/SiO_2(1/2), and catalyst enhancement. b) NH_3-TPD spectra of catalysts. c) CO_2 flux curves with and without 9wt% Fe-SZ/SiO_2(1/1). d) CO_2-TPD spectra of catalysts. e) Total desorption CO_2 amount, maximum CO_2 flux, f) catalyst enhancements, enhancement factor, g) relative heat duty, and thermal energy consumption of Fe-SZ/SiO_2(1/1) with 10% Fe doped at different catalyst concentrations. All MVR trials were accomplished using 3M GlyK at 90 °C. No catalyst is used for blank solvent. 144
Figure 6.4. a) Measured CO_2 DAC equilibrium points for hybrid amino acid solvents alongside obtained values for single solvents in our previous studies (124, 128) (**A-**3M SarK, **B-**3M GlyK, **C-**3M TauK, **D-**3M TauK+0.5M SarK, **E-**3M TauK+1M SarK, **F-**3M TauK+1.5M SarK). b) CO_2 desorption flux profiles, c) maximum CO_2 flux, water flux, d) total desorbed CO_2, and thermal energy consumption for single and hybrid amino acid solvents. All MVR trials were conducted at 90 °C. 148
Figure 6.5. CO_2 flux profiles for a) 3M SarK, b) 3M TauK, and c) 3M TauK+1M SarK with and without catalyst. d) Total desorption CO_2 amount for single and hybrid solvent with and without catalyst, and e) corresponding relative and absolute enhancement of catalyst. f) Relative heat duties in comparison with 3M GlyK performance. g) Thermal energy consumption of catalytic single and hybrid solvents. All MVR trials were accomplished at 90 °C. Fe-SZ/SiO_2(1/1) with 10% Fe doped used as catalyst and the concentration was kept at 9wt% in all experiments. No catalyst is used for blank solvent. 151
Figure A.1. Effect of air flow rate on CO_2 absorption efficiency (η_a) for 1 M GlyK at 20°C, solvent flow rate=0.25 L/min 161
Figure A.2. Accuracy and repeatability of DAC-absorption unit over three long-term trials for 1 M GlyK **a)** Absorption efficiency (η_a) versus solvent loaded percentage. **b)** Absorption flux (J_a) versus solvent loadings. All the trials were completed at 20 °C, air flow rate = 7.2 L/min, and solvent flow rate = 0.25 L/min. 161
Figure A.3. Amino acid absorption efficiency (η_a) in long-term operation at different solvent loadings for 1 M **a)** LysK. **b)** SarK. **c)** ProK. **d)** HisK. All the trials were completed at 20 °C, air flow rate = 7.2 L/min, and solvent flow rate = 0.25 L/min. 162
Figure A.4. Insolubility of 3 M LysK in water for aqueous solution preparation 163
Figure A.5. The kinetic performance (absorption flux, J_a) of GlyK at different concentrations in various solvent loading conditions. All data were obtained at 20 °C, air flow rate = 7.2 L/min, and solvent flow rate = 0.25 L/min. 163
Figure A.6. Accuracy and repeatability of vacuum low-temperature DAC-desorption unit over three trials for 1 M GlyK. **a)** Temperature profile. **b)** CO_2 desorption flux (J_d) within the range of different solvent loadings. The data were obtained at 70°C, 21 $kPa_{(a)}$ and solvent flow rate = 0.25 L/min. 164
Figure A.7. GlyK DAC-desorption flux (Jd) at different solvent concentration and solvent CO_2 loading ranges. All data were obtained at 80°C, 21 kPa(a) and solvent flow rate = 0.25 L/min 164
Figure A.8. Three evaluated commercial HFMCs 165
Figure A.9. DAC equilibrium points for various used amino acid salts solutions 166
Figure A.10. a) Top-view SEM and EDX elemental analysis of multiple fibers, highlighting the PDMS coating layer elemental distribution. b) Cross-sectional SEM images at different

scales (100 µm to 3 µm), illustrating the thickness and uniformity of the PDMS coating layer. 166
Figure A.11. Repeatability and accuracy of MVR rig in three consecutive trials. All trials were conducted for 3M GlyK, at 90 °C, 2-4 $kPa_{(a)}$, 0.25 L/min. 167
Figure A.12. a) SEM images, b) TEM low-magnification, c) high resolution, d) SAED images, and e) TEM-EDX mapping for Resin B. The high resolution and SAED images show amorphous nature of catalyst. 167
Figure A.13. a) Low magnification, high-resolution TEM, and b) SAED images of Resin A showing amorphous catalyst materials. 168
Figure A.14. Resin A XPS spectrum for a) O-S and O-H scan,(181-183) b) carbon scan (184-186) of fresh catalyst, and c) sulfonate functional group for used catalyst (one cycle)(103, 148). 169
Figure A.15. FTIR spectra for catalysts Resin A and B (187, 188). 170
Figure A.16. Observed precipitations for a) 2M TauK, b) 2.5M TauK, c) 3M TauK, and d) 3M TauK+0.5M K_2CO_3. 170
Figure A.17. CO_2 desorption flux profiles of three used HFMC 171
Figure A.18. a) CO_2 desorption flux profiles, b) max. CO_2 flux, and c) water flux of three trials of 3M GlyK at 90 °C. 171
Figure A.19. a) TEM low-magnification, b) high resolution, and C) SAED image of Fe-SZ/SiO_2(1/1). 172
Figure A.20. The deconvoluted O 1s spectra of XPS for Fe-SZ/SiO_2(1/1) catalyst 172
Figure A.21. a) CO_2 flux curves and total desorbed CO_2 with and without 6wt% Fe-SZ/SiO_2(2/1), and catalyst enhancement. b) SEM-EDX images of Fe-SZ/SiO_2(2/1) highlight non-uniform dispersion of SZ on the SiO_2 support. 173
Figure A.22. a) CO_2 flux profile with and without 12wt% Fe-SZ/SiO_2(1/1). b) Catalyst stability in four cycles for 9wt% Fe-SZ/SiO_2(1/1). All MVR trials accomplished at 90°C using 3M GlyK. No catalyst is used for the blank trial. 174
Figure A.23. ^{13}C NMR spectra for CO_2 loaded single and hybrid solvents. 175

List of Schemes

Scheme 2.1. A schematic representation of the proposed regeneration pathways for CO_2-loaded potassium sarcosinate (KSar), highlighting the role of Lewis and Brønsted acid sites on the TiO_2 surface in Deka et al; reused with permission (115). 46
Scheme 2.2. Schematic representation of the proposed CO_2 desorption mechanisms with.... 48
Scheme 3.1. a) Schematic diagram of DAC-absorption-desorption unit b) Photograph of the developed DAC units. 67
Scheme 3.2. Scheme of the C-MVR apparatus for DAC. 71
Scheme 3.3. Photograph of the OptiMax^{TM} workstation 1001 (Mettler-Toledo) 76
Scheme 3.4. Schematic diagram of the CO_2 desorption apparatus operating at 88-98 °C; reused with permission (34) 77
Scheme 3.5. Schematic illustration of the Chittick apparatus used for measuring the CO_2 loading of aqueous solution. 80
Scheme A.1. Detailed schematic diagram of C-MVR unit 165

List of Tables

Table 3.1. Specification of the applied HFMC 83
Table 3.2. Specifications of three commercial HFMCs 84
Table 3.3. Specifications of three commercial HFMCs 84
Table 5.1. Thermal energy consumption for well-established DAC technologies 122
Table A.1. Weight percentage elements analysis of catalysts using CHNS method 170
Table A.2. Total acidity and basicity strengths of various synthesized samples, measured by NH_3-TPD and CO_2-TPD analyses. 174

Nomenclature

DAC	Direct Air Capture
HFMC	Hollow Fiber Membrane Contactor
MVR	Membrane Vacuum Regeneration
C-MVR	Catalytic Membrane Vacuum Regeneration
GlyK	Potassium Glycinate
TauK	Potassium Taurinate
ProK	Potassium Prolinate
SarK	Potassium Sarcosinate
ArgK	Potassium Argininate
HisK	Potassium Histidine
LysK	Potassium lysinate
SEM	Scanning Electron Microscopy
TEM	Transmission Election Microscopy
FTIR	Fourier Transform Infrared
XPS	X-ray Photoelectron Spectroscopy
NMR	Nuclear Magnetic Resonance Spectroscopy
NH_3-TPD	Ammonia temperature programmed desorption technique
CO_2-TPD	CO_2 temperature programmed desorption technique

CHAPTER 1

Introduction

The accelerating increase in global CO_2 emissions has become as a serious environmental concern (1). Atmospheric CO_2 levels have now surpassed 420 parts per million, representing a nearly 50% rise compared to preindustrial times (2). This significant elevation has contributed to an approximate 1 °C increase in global temperatures. In response, the Paris Agreement has established targets to limit global temperature rise to below 2 °C, with a more ambitious target of restricting it to 1.5 °C by century's end (3). Meeting these objectives requires not only significant reductions in greenhouse gas emissions but also the deployment of technologies capable of actively capturing CO_2 from the atmosphere. Negative Emissions Technologies (NETs) are essential in this context, with Direct Air Capture (DAC) standing out as one of the most effective methods (4). First introduced by Lackner in 1999 (5), DAC enables the capture of ultra-dilute atmospheric CO_2 through technologies that can be flexibly located and yield high-purity CO_2 streams.

Among various DAC methods, absorption and adsorption are the most prominent (6, 7). While most current research focuses on solid sorbents, such as those used by Global Thermostat and Climeworks (8), there is comparatively less development in liquid-phase chemical absorption using established solvents like amines. Amine-based absorption is a well-established and extensively used method for CO_2 capture at the industrial scale (9, 10). Applying the broad operational experience gained from these solvent-based systems can offer valuable advantages for DAC applications. In particular, amino acid salts are a promising class of solvents for DAC due to their favorable characteristics, including low volatility, high reaction rate, strong resistance to oxidative degradation, and minimal toxicity (11, 12).

Despite these advantages, applying liquid-based CO_2 capture in DAC poses several challenges. The low atmospheric CO_2 concentration requires large air volumes in the system, resulting in low solvent-to-air flow ratios for capturing CO_2 (13). Furthermore, conventional solvent regeneration processes require high operating temperatures (typically between 120 and

140 °C), which significantly increases energy consumption (14). These conditions not only raise operating costs but also accelerate thermal degradation of the solvent, including amino acid salts (15, 16). To overcome these issues, combining suitable contactors and solvents with low-temperature, energy-efficient regeneration methods are key approaches to improving the sustainability and scalability of liquid-based DAC systems.

HFMCs represent a hybrid approach that merges the benefits of solvent-based and membrane separation technologies (17, 18). Their compact and modular design, large surface area, and operational flexibility make them strong candidates for DAC systems (19, 20). Specifically, in the desorption step, membrane vacuum regeneration (MVR) using HFMCs offers a promising approach for low-temperature CO_2 stripping (21). Operating under vacuum conditions on one side of the membrane allows the process to run at a temperature below 100°C, reducing energy use and minimizing solvent degradation (22, 23). This temperature range also enables integration with renewable heat sources like solar thermal energy or low-grade waste heat (24). In this context, a key factor influencing CO_2 transfer through membranes is the optimization of membrane characteristics and structure, which is crucial for minimizing mass transfer resistance (21). While hydrophobic porous membranes are preferred due to their minimal resistance, their performance can deteriorate over time as a result of pore wetting (25, 26). This problem can be effectively managed by employing hydrophobic ultra-thin composite membranes featuring a thin dense layer that contacts the solvent and prevents it from entering the pores (27, 28). Therefore, an evaluation of HFMC's performance with different characteristics (especially ultra-thin composite membranes) is required to further optimize and enhance the CO_2 transfer rates in MVR in DAC, which has not yet been experimentally studied.

Considering the high energy intensity of DAC (29), integrating MVR with advanced low-temperature regeneration strategies offers a promising pathway to enhance overall process energy-efficiency and sustainability. In recent years, researchers have proposed several energy-

efficient CO_2 regeneration techniques, including phase-change solvents (30, 31), hybrid solvents (32), crystallization-based regeneration (11, 12), and catalytic solvent regeneration (33). Catalytic solvent regeneration using heterogeneous solid acid-base catalysts is an emerging approach with strong potential to enhance CO_2 desorption kinetics at low-temperatures (34). Various materials such as zeolites (35), metal oxides (36), mesoporous silica (37), and carbon-based compounds (38) have been explored as catalysts in combination with solvents like amines and amino acid salts (39). However, few have been tested under DAC conditions (40). Among these, sulfated zirconia (SZ) stands out for its strong acidity, environmentally friendly nature, ease of synthesis and remarkable enhancement especially when supported on mesoporous materials like silica or alumina (41, 42). Moreover, the catalytic performance of SZ can be improved through metal doping, which generates additional basic sites and amplifies the activity of both Lewis and Brønsted acid sites (43). Among the various metals investigated, iron has shown notable effectiveness, owing to its ability to simultaneously enhance acidic and basic active sites (44, 45). Hence, investigating the impact of Fe-doped SZ impregnated on catalytic support in MVR systems could provide valuable insights into low-temperature energy-efficient solvent regeneration for DAC.

In addition to solid acid catalysts, ion-exchange resins offer a versatile, low-cost alternative for catalytic regeneration. These water-insoluble polymers, characterized by strong acidic functional groups, macroporosity, and stability, are already used in fields ranging from water treatment to catalysis (46-49). Their properties make them well-suited for use in DAC-MVR. However, they remain largely unexplored in this application.

In addition to catalytic solvent regeneration, hybrid solvents have emerged as another viable method for reducing the energy demands in liquid-based CO_2 capture technologies (50). Blending solvents with different properties can improve CO_2 absorption capacity while lowering the energy input requirement for regeneration (51, 52). Although amine-based solvent

mixtures have been widely studied for flue gas applications, their potential in DAC, particularly with amino acid salts, has received limited attention. Investigating such blends could offer a practical and energy-efficient pathway for advancing liquid-based DAC systems, especially when combined with advanced regeneration methods.

Considering the above-mentioned, research gaps are highlighted in the form of questions, which are listed below:

- Q1-What is the behavior and performance of green amino acid salts in a system of absorption and desorption in a DAC application using hollow fiber membrane modules?
- Q2-What is the effect of membrane characteristics and catalysts in a DAC-MVR process using a suitable solvent?
- Q3-What is the impact of combining hybrid solvents with hybrid composite catalysts on the performance of DAC-MVR?

Based on the above questions, the research objectives are outlined as follows:

1. Designing and developing bench-scale absorption-desorption DAC units using HFMCs and screening various amino acid salts under different process conditions.
2. Evaluating different types of membrane characteristics and integrating catalytic solvent regeneration technology into a low-temperature DAC-MVR unit.
3. Integrating hybrid solvent with hybrid composite catalysts with a low-temperature DAC-MVR unit.

These objectives will be addressed and discussed in detail in Chapters 4, 5, and 6, respectively.

CHAPTER 2

Literature Review

2.1 Perspective

This chapter provides a comprehensive literature review focusing on direct air capture (DAC), membrane-based CO_2 separation technologies, vacuum membrane regeneration, and catalytic solvent regeneration. The review begins by examining various methods and designs employed in liquid-based DAC systems. A thorough analysis of membrane separation is then presented, highlighting CO_2 separation using polymeric composite membranes. Subsequently, the fundamentals of catalytic solvent regeneration are explored, with a focus on the contribution of solid acid catalysts in improving CO_2 stripping efficiency and minimizing energy consumption. Finally, based on the insights gained from the literature, and identifying the gaps, the research objectives of this thesis are outlined.

2.2 Direct Air Capture

Negative emission technologies (NETs) are playing an increasingly essential role on the route to net zero emissions by 2050 (53). Among the suggested NETs, DAC has the greatest potential to influence climate mitigation by removing CO_2 directly from ambient air (54). This was initially suggested in 1999 by Lackner et al. (55). The need for DAC is driven by the increasing levels of atmospheric CO_2, which have surpassed 420 ppm, contributing to global warming and climate instability. While decarbonization efforts through renewable energy and efficiency improvements are critical, they are not enough to fully address past and remaining emissions (56). DAC provides an approach by actively removing CO_2 from the air, making it essential for meeting climate targets outlined in the Paris Agreement. These systems operate by drawing in air and passing it through chemical or physical sorbents that selectively capture CO_2. These sorbents can be solid materials, such as amine-functionalized adsorbents, or liquid solvents, like alkaline solutions (57). Once CO_2 is captured, it is released through a regeneration process that typically involves heat, pressure changes, or temperature (58, 59). Among these systems,

liquid-based DAC has received notable attention, particularly the large-scale commercial plant developed by Carbon Engineering (54). Their system utilizes a crossflow air contactor, where ambient air moves perpendicularly to a downward flow of potassium hydroxide (KOH) solution, requiring the circulation of extremely large volumes of air to enhance CO_2 loading in the solvent (54, 60). This crossflow arrangement is particularly advantageous for maximizing the available surface area for mass transfer for the absorption section while maintaining a low pressure drop. **Figure 2.1** displays the Carbon Engineering air contactor design.

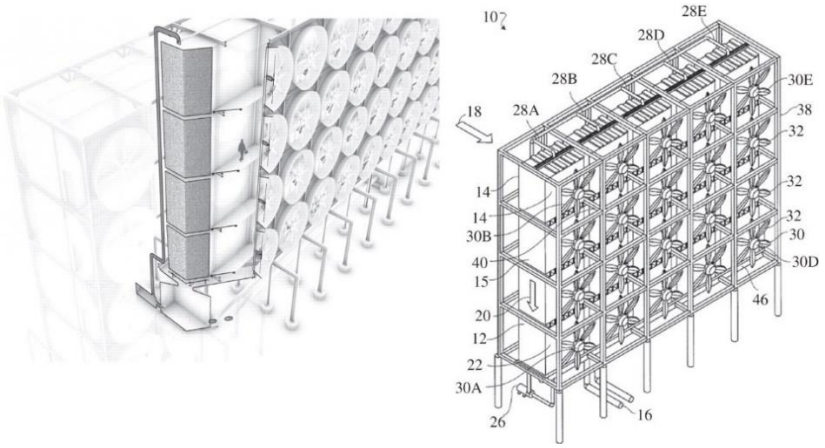

Figure 2.1. Illustration of the alkali-based DAC process Carbon Engineering contactor design; reused with permission (60)

The overall process of CO_2 capture via alkali scrubbing in Carbon engineering technology is depicted in **Figure 2.2**.

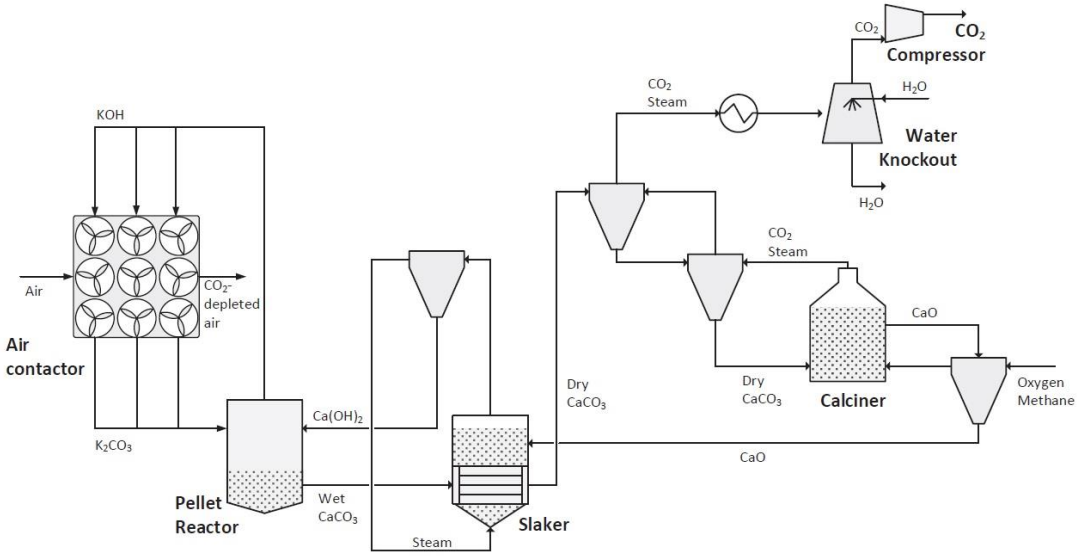

Figure 2.2. Process flow diagram of the alkali-scrubbing DAC process; reused with permission (6, 54)

In the initial stage of this process (**Figure 2.1**), CO_2 is captured in the air contactor unit through absorption into an aqueous KOH solution, leading to the formation of potassium carbonate (K_2CO_3). The captured CO_2 is then regenerated through a calcium-based thermochemical cycle, wherein the K_2CO_3 solution reacts with calcium hydroxide $Ca(OH)_2$, leading to the precipitation of calcium carbonate $CaCO_3$. This precipitate is subsequently processed in a calciner, where it breaks down into calcium oxide CaO and produce a purified stream of CO_2.

CO_2 uptake via chemical absorption in alkaline solutions follows a well-established reaction mechanism consisting of two sequential steps (61), with the overall absorption rate being controlled by the slowest, rate-determining step, as represented in Equation 1.1.

$$CO_{2(aq)} + OH^- \leftrightarrow HCO_3^- \quad (1.1)$$

$$HCO_3^- + OH^- \leftrightarrow CO_3^{2-} + H_2O \quad (1.2)$$

This absorption pathway is a common characteristic of all alkali hydroxide-based sorbents; however, studies indicate that potassium hydroxide exhibits superior kinetics compared to other hydroxides (62). Once CO_2 is absorbed and converted into a carbonate-rich solution, it must undergo regeneration to recover both the solvent and the captured CO_2. In this stage, the CO_2-laden solution exiting the air contactor is directed into a pellet reactor, where potassium carbonate undergoes causticization with calcium hydroxide, leading to the production of potassium hydroxide and calcium carbonate (6):

$$K_2CO_{3(aq)} + Ca(OH)_{2(aq)} \leftrightarrow 2KOH_{(aq)} + CaCO_3 \quad (1.3)$$

Since calcium carbonate exhibits extremely low solubility in aqueous solutions, it readily precipitates, making it relatively easy to separate from the liquid phase. The remaining liquid, which now consists primarily of regenerated potassium hydroxide, is subsequently returned to the air contactor to be reused in the absorption process. However, one of the key challenges associated with this reaction lies in the inherently low solubility of calcium hydroxide under highly alkaline conditions. Therefore, the availability of free Ca^{2+} ions in solution remains limited, which in turn affects the reaction kinetics (63). This issue becomes particularly significant given that the CO_2-rich solution exiting the air/solvent contactor unit still retains a non-negligible concentration of unreacted potassium hydroxide. To address this limitation, the process is designed to ensure that calcium hydroxide acts as the limiting reactant while also maintaining prolonged residence within the pellet reactor to promote complete conversion (54).

The solid calcium carbonate particles formed during this reaction accumulate at the bottom of the pellet reactor, from where they are collected and subjected to further processing. These particles are initially dried and heated before being introduced into the calciner which undergo thermal decomposition (around 900 °C) to release pure CO_2 (6):

$$CaCO_{3(s)} \rightarrow CaO_{(s)} + CO_{2(g)} \quad (1.4)$$

Following calcination, the final stage of the regeneration cycle consist of the hydration of calcium oxide to regenerate calcium hydroxide, which is subsequently recycled back into the system for reuse in the causticization step (6):

$$CaO_{(s)} + H_2O_{(g)} \rightarrow Ca(OH)_{2(s)} \quad (1.5)$$

However, one of the main limitations of the mentioned process is its high energy consumption, particularly in the calcination step, where calcium carbonate ($CaCO_3$) is broken down at temperatures exceeding 900°C to release CO_2. This step demands a considerable amount of energy. Additionally, the use of KOH as the absorbent presents a significant challenge due to its highly corrosive nature, which can lead to material degradation in equipment and pipelines, necessitating the use of specialized corrosion-resistant materials and increasing capital costs. Therefore, it is essential to design and develop new energy-efficient techniques that operate at lower temperatures, along with the exploration of alternative, environmentally friendly solvents that can enhance process sustainability and durability.

Amine-based solvents with thermal regeneration have been known as the most developed and mature technology and are likely to be the first pathway applied on a large-scale for CO_2 capture among many different types of solvents used for liquid absorption (64, 65). A wide variety of alkanolamines ranging from monoethanolamine (MEA) as primary amines, to diethanolamine (DEA) as secondary amines, and methyldiethanolamine (MDEA) as tertiary amines exists (66) MEA is treated as a benchmark solvent because of its high absorption activity, reliability, high loading capacity, accessibility, and low cost (9, 67, 68). A study accomplished by Barzagli et al.(69) focuses on the screening of different amine-based sorbents for DAC of CO_2 as a different approach compare to conventional alkali hydroxide sorbents, such as KOH and NaOH, which require comparatively high regeneration temperatures and energy inputs. The study aimed to identify amine-based solvents capable of efficiently

capturing CO_2 from ultra-dilute air while lowering the required energy for regeneration, thereby improving the overall feasibility of DAC. To achieve this, 18 different alkanolamines were screened, including sterically hindered amines and also primary, secondary, and tertiary amines, under identical operating conditions. A bench-scale packed absorption column was used (**Figure *2.3***), where compressed air containing 0.044% CO_2 was continuously introduced, and the liquid solvent circulated in a countercurrent flow arrangement. The CO_2 content in the inlet and outlet air streams was measured and monitored using gas chromatography, while ^{13}CNMR spectroscopy was applied to determine the CO_2-containg species in solution.

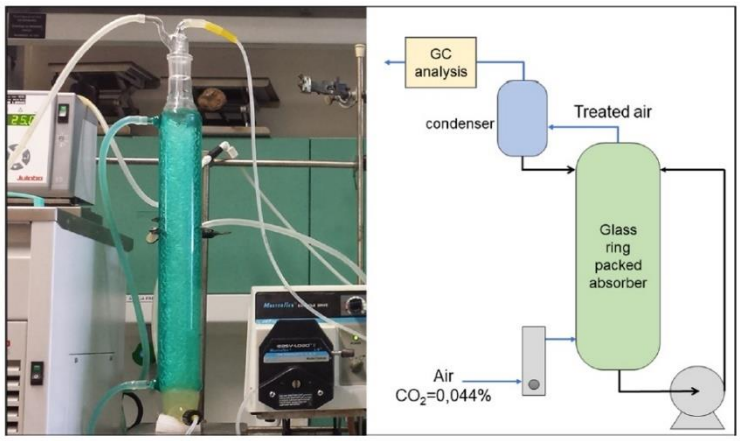

Figure 2.3. Used DAC-apparatus for screening different amine-based solvent in the study of Barzagli et al.; reused with permission (2020)(69)

It was observed that unhindered primary amines, including MEA, DGA (diglycolamine), and 2A1B (2-amino-1-butanol), exhibited the highest CO_2 absorption efficiency in DAC condition. Their performance was comparable to KOH and potassium glycinate solutions, but with the advantage of requiring lower regeneration temperatures. A strong conversion to amine carbamate was identified as the dominant mechanism responsible for efficient CO_2 capture. The study underscores the importance of selecting appropriate solvents that balance CO_2 capture efficiency, chemical stability, and regeneration energy demand, highlighting the need for further optimization in DAC solvent development.

Despite the well-established efficiency and widespread application of MEA, its role as a solvent in CO_2 capture processes entails multiple limitations. One of the primary concerns is its high volatility, which leads to solvent losses during operation, requiring frequent replenishment and increasing operational costs (70). Additionally, MEA exhibits low thermal stability, meaning that it undergoes thermal and oxidative degradation over extended use, forming undesirable degradation byproducts such as heat-stable salts (HSSs) and amides, which not only reduces absorption efficiency but also necessitates periodic solvent reclamation or replacement (71, 72). In 2020, Kiani et al.(13) carried out a techno-economic analysis on DAC using a traditional packed bed absorption system, evaluating its feasibility and performance. The study focused on a MEA-based absorption process and simulated its operation under realistic conditions using Aspen Plus. As mentioned, a major challenge in DAC is the CO_2 low concentration in ambient air, which requires processing of a large volume of air and circulating a low amount of solvent (high G/L ratios). To compensate for this, the study conducted a continuous recirculation solvent system in the simulation that cycled part of the rich solvent back through the absorber to improve efficiency and hydraulic performance of the absorber (**Figure *2.4***).

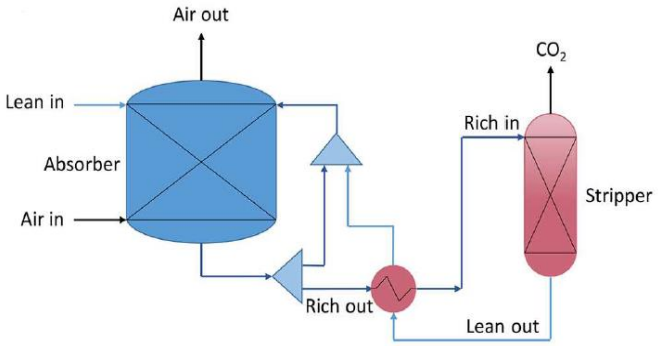

Figure 2.4. Process flow diagram for direct air capture using MEA solvent; reused with permission (13)

The study explored different operating conditions and found that, among capture rates ranging from 20% to 90%, a moderate rate of 50% offered the best balance between energy consumption and absorber size, and was therefore selected as the optimum scenario. The

process required a reboiler heat duty of 10.7 GJ/tCO_2 and an electricity consumption of 1.4 MWh/tCO_2. A key issue identified was the evaporative loss of the MEA solvent, which was addressed by introducing a wash water section at the top of the absorption column. While this modification successfully minimized solvent losses, it also increased capital costs by approximately 60%. Hence using alternative non-volatile solvent can help reduce the CO_2 capture cost considerably in DAC. **Figure *2.5*** shows the distribution of capital costs for major equipment.

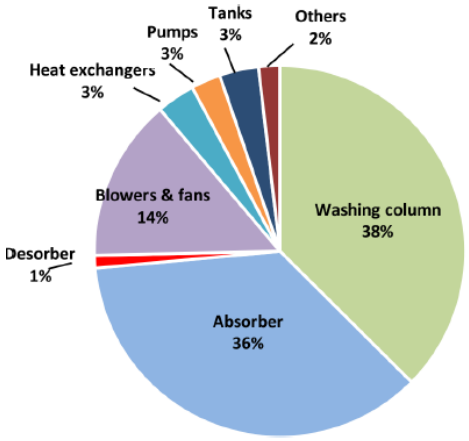

Figure 2.5. Breakdown of capital costs for key equipment in liquid-based DAC system using MEA; reused with permission (13)

Amino acid-based solvents have gained attention as a compelling alternative to traditional amine-based solvents for CO_2 capture because of their unique physicochemical properties and environmental advantages. One of the key advantages that make amino acid solvents well-suited for DAC is their low volatility, which significantly minimizes solvent losses and reduces operational costs associated with solvent replenishment (13). Additionally, their strong oxidative stability enhances resistance to oxygen-induced degradation, while their negligible toxicity and biodegradability mitigate environmental concerns and health risks, making them a more suitable option for large-scale DAC implementation (73, 74).

Amino acid aqueous solutions, such as glycine, sarcosine, proline, lysine, etc. have been extensively studied for CO_2 absorption-desorption cycles in system of flue gas as a feed (75, 76). However, their application in DAC has recently started to be explored (40, 74, 77, 78). Despite these advantages, a major drawback of amino acid-based solvents (also in solvent-based processes) is their high energy regeneration demand, which remains one of the most significant challenges limiting their commercial usage (79, 80). Addressing this issue requires the development of more energy-efficient regeneration strategies such as employing low-temperature desorption methods, catalytic solvent regeneration, hybrid solvents, phase-change solvents systems (30, 43, 81, 82). Brethomé et al. (11) developed a direct air capture system using aqueous amino acid solutions (glycine and sarcosine) as CO_2 sorbents, employing a crystalline-phase release process for solvent regeneration. They used a household humidifier as an air-solvent contactor for capturing CO_2 from ambient air, which was then precipitated as a guanidinium carbonate salt. The CO_2 was afterward released through heating (80-120°C) using concentrated solar power (CSP), offering a low-energy regeneration approach. Building on this concept, Custelcean et al.(12) introduced a bis-iminoguanidine (BIG)-based system for amino acid regeneration, aiming to further lower energy consumption and enhance process efficiency. Their approach achieved a CO_2 cyclic capacity of 0.12-0.20 mol/mol with a regeneration heat energy of 360 kJ/mol (8.2 GJ/ton CO_2) at temperatures of 60-120°C, which was lower than conventional $CaCO_3$-based DAC. However, despite this improvement, the formation of sticky sludges posed challenges to solid-liquid separation, limiting the feasibility of continuous operation. **Figure 2.6** displays the equipment used, the CO_2 loading curves obtained, and the sequential loading/regeneration DAC cycles with sarcosine/m-BBIG.

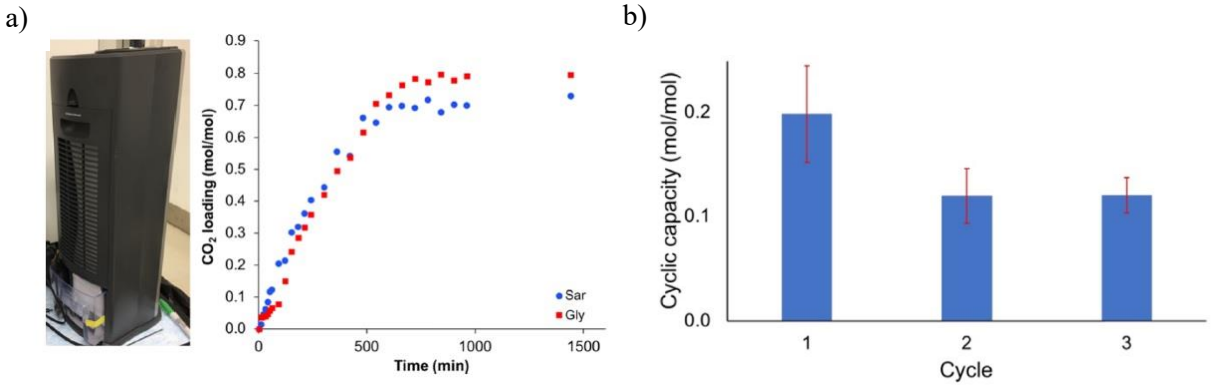

Figure 2.6. a) CO_2 loading profiles of 1M GlyK (indicated by red squares) and SarK (represented by blue dots) under DAC conditions, using an air humidifier (shown on the left) as air-solvent contactor. b) Consecutive absorbing/desorbing cycles with sarcosine/m-BBIG; reused with permission (11, 12)

Therefore, while crystallization-based DAC approaches contribute to reducing solvent regeneration energy, they still face practical and scalability challenges. Alternative strategies, such as membrane vacuum regeneration, catalytic solvent regeneration, and hybrid solvents present viable options worth exploring. Membrane vacuum regeneration eliminates the need for solid-liquid separations and enables low-temperature, robust and continuous CO_2 desorption, while catalytic solvent regeneration enhances desorption kinetics and reduces thermal input by accelerating solvent regeneration reactions. These emerging techniques can address key drawbacks of solvent-based DAC process and present more scalable and energy-efficient and sustainable pathways for large-scale deployment.

2.3 Gas-liquid Membrane Contactors

Gas-liquid membrane contactors are an advanced separation technology that enables efficient mass transfer between a gaseous and liquid phase without direct dispersion of one phase into the other (83). In liquid-based CO_2 capture applications, membrane contactor modules combine the benefits of both membrane separation and solvent, offering a compact and highly efficient approach (17, 84). These modules significantly increase the effective contact area, leading to improved mass transfer rates and also enhanced CO_2 stripping performance for solvent regeneration (17, 22, 85, 86). A study conducted by Nieminen et al.(87) designed and developed a continuously operated membrane contactor-based CO_2 capture unit, integrating a

hollow fiber membrane contactor (HFMC) for CO_2 uptake and a vacuum-assisted desorption system in flue gas specification. The process flow diagram and a photograph of their experimental apparatus are illustrated in **Figure 2.7** and **Figure 2.8**, respectively.

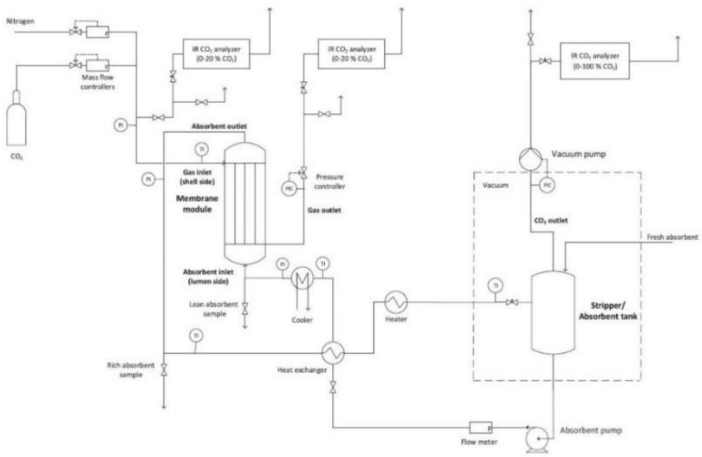

Figure 2.7. Process flow diagram of the apparatus used in the work by Nieminen et al.; reused with permission (87)

Figure 2.8. Photograph of the setup used in the study by Nieminen et al.; reused with permission (87)

In their experimental setup, the researchers employed potassium glycinate (GlyK), an amino acid salt solution, as the absorbent due to compatibility with polypropylene (PP) membranes. The desorption process was conducted under vacuum conditions to enhance CO_2 removal efficiency while reducing the thermal energy input. Based on the performance of their unit, a

high specific energy consumption was recorded for the developed rig (104.5 GJ/tCO_2 heat and 18.2 GJ/ton CO_2 electricity). To overcome the energy-intensive nature of the process, the study highlighted the potential benefits of replacing the vacuum desorption vessel with a membrane vacuum regeneration (MVR) process.

MVR is a promising approach that enhances CO_2 desorption efficiency while lowering the energy intensity of regeneration process. Unlike conventional thermal regeneration, which relies on high temperatures to strip CO_2 from the solvent (above>120 °C), MVR utilizes a vacuum-driven process to facilitate desorption at lower temperatures (70-100 °C) (21). This method operates through vacuum applied on one side of a membrane gas-solvent contactor, creating a pressure gradient that drives CO_2 liberation from the solvent (88). A comprehensive study by Fang et al. (89) highlighted the potential of MVR as an energy-efficient option in place of conventional thermal regeneration for CO_2 desorption from amine solvents. In their experimental setup, a PP hollow fiber membrane module was employed, and CO_2-rich MEA solution (with flue gas specification) was regenerated under vacuum at low temperatures, with regeneration performed at 75 °C and 20 kPa. **Figure 2.9** depicts the CO_2 mass transfer resistance in MVR process. Two flow configurations (tube-side and shell-side) were evaluated, with the tube-side flow showing superior performance due to reduced mass transfer resistance. **Figure 2.10** shows the process flow diagrams of two configurations used in their experimental setup.

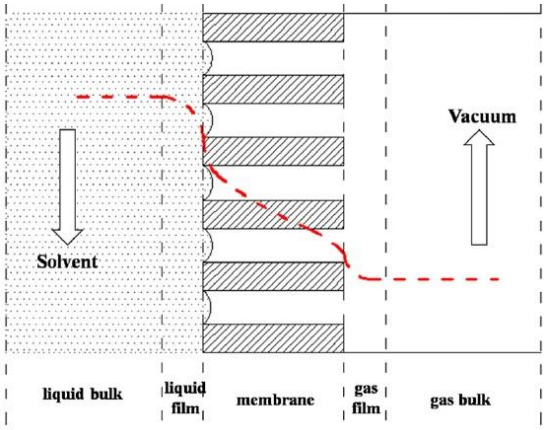

Figure 2.9. CO_2 mass transfer resistance in MVR process; reused with permission; reused with permission (89).

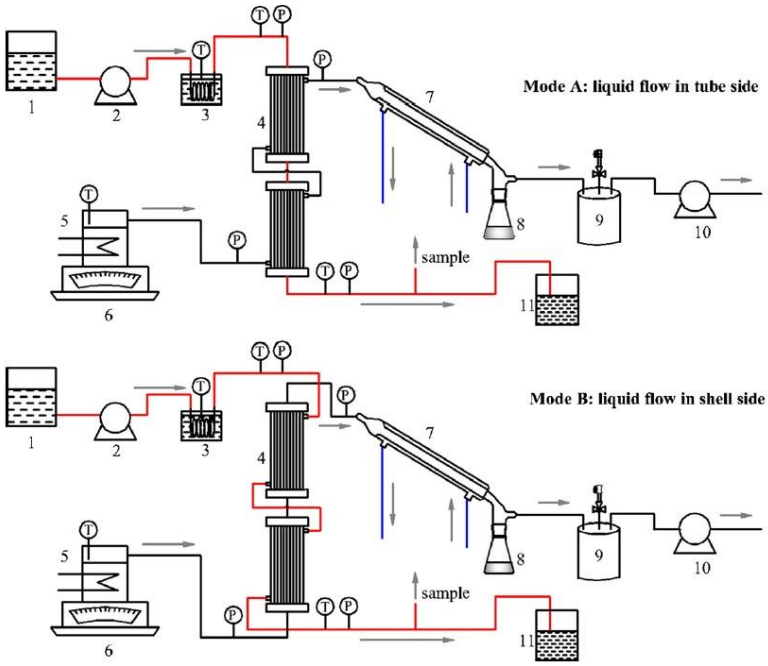

Figure 2.10. Process flow diagram of the experimental apparatus for regenerating CO_2-rich solvent using MVR in the study of Fang et al.; reused with permission (89).

Notably, their MVR set-up achieved a CO_2 desorption flux of 2.2×10^{-4} mol/m²·s, while the total equivalent work was significantly lower than that of traditional thermal regeneration methods. The authors highlighted that the lower operating temperature reduces the risk of thermal degradation and amine loss, with MEA loss measured at just 0.5 g MEA/kg CO_2, much lower than typical values in high-temperature regeneration (2.05 g MEA/kg CO_2). These

findings support the viability of MVR applications, particularly for integrating into low-carbon CO_2 capture systems where energy-efficiency, operational stability, and solvent longevity are critical design considerations. It also worth noting that the reduced operating temperature of MVR processes makes them well suited for coupling low grade heat or solar energy, thereby improving their sustainability (24).

To fully take advantage of the benefits mentioned, it is also important to consider how the membrane characteristics affect the process. Achieving optimal MVR performance also depends heavily on the choice of membrane material and its structural properties, which directly affect mass transfer efficiency and long-term operational stability (21, 85, 90). As illustrated in **Figure 2.11**, the mass transfer mechanism in membrane gas-liquid contactors are dependent on the pore structure and whether the pores remain gas-filled or become wetted by the solvent (91).

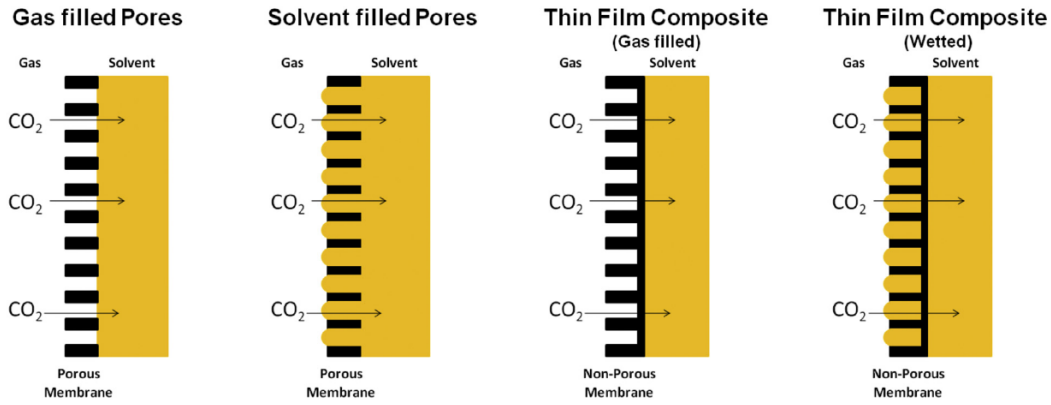

Figure 2.11. Diagram illustrating a gas-filled porous membrane contactor alongside a thin film composite membrane contactor, highlighting both dry and wetted conditions of porous support; reused with permission (91).

When the pores are filled with gas, CO_2 transfer occurs primarily through gaseous diffusion, leading to a significantly higher mass transfer rate, attributed to the high CO_2 diffusivity in the gas phase (21, 91). This configuration ensures efficient separation and minimizes the required membrane area, making it an ideal scenario for optimizing CO_2 capture performance. However, a major challenge in membrane contactors is the risk of pore wetting, where solvent infiltration

into the membrane pores blocks the gas-liquid interface. This transition reduces CO_2 transfer efficiency because the diffusivity of CO_2 in liquid is nearly hundredfold lower than in the gas phase (91).

To prevent this issue when using aqueous solvents, hydrophobic microporous membranes such as polyethylene (PE), polypropylene (PP), and polytetrafluoroethylene (PTFE) and etc. are commonly used, as they provide resistance against wetting under normal operating conditions (92-94). Nevertheless, over extended operational periods or under high transmembrane pressure differences, even these materials can suffer from partial wetting, leading to performance reduction (17).

Therefore, to better prevent wetting under harsh conditions, thin-film composite (TFC) membranes have been developed, incorporating a non-porous, selective dense layer on top a porous support structure (27). As shown in **Figure 2.11**, TFC membranes prevent direct contact between the solvent and the porous support, ensuring stable long-term operation by eliminating pore wetting (95). In this case, CO_2 transport occurs via a solution-diffusion mechanism, where CO_2 dissolves into the dense layer and diffuses across it before desorbing into the gas phase (21). While this approach effectively blocks solvent entrance into the pores, the added dense layer introduces additional mass transfer resistance, which can reduce overall CO_2 flux (21, 27). This trade-off between preventing membrane wetting and maintaining sufficient mass transfer was investigated in the work by Scholes et al. (85). The authors investigated the use of non-porous PDMS hollow fiber membranes and porous PP and PTFE membranes for solvent-based CO_2 capture from flue gas, conducting experiments at both lab and pilot scales. Owing to the dense, nonporous nature of the PDMS membrane, the pore wetting issue was effectively eliminated, resulting in stable operation across both scales. In contrast, porous membranes PP and PTFE exhibited significant wetting under pilot-scale conditions, particularly due to transmembrane pressure fluctuations. Moreover, the improved wetting resistance of the PDMS

membrane was accompanied by a reduction in CO_2 flux. The overall mass transfer coefficients were approximately hundredfold lower compared to the PP membrane, primarily due to the higher diffusion resistance imposed by the relatively thick PDMS selective layer. Since CO_2 transport in this configuration follows a solution–diffusion mechanism, the dense layer acts as a rate-limiting barrier to mass transfer. The authors noted that this limitation could be addressed by reducing selective layer thickness, as thinner coatings were shown in other studies (96, 97) to significantly improve gas permeability while maintaining wetting resistance.

Considering the above-mentioned observing, the integration of membrane contactors into liquid-based DAC systems offers clear advantages, particularly in the solvent regeneration stage, which accounts for the highest energy demand in the process. By enabling low-temperature operation, membrane contactors enhance the overall sustainability and durability of the DAC unit. Notably, the low CO_2 partial pressure in ambient air demands highly efficient capture and regeneration strategies to overcome the associated thermodynamic limitations. In this context, tailoring the morphological structure and surface properties of membrane contactors under DAC conditions is crucial for enhancing mass transfer performance. Furthermore, coupling membrane contactors with additional energy-efficient regeneration methods, such as catalytic solvent regeneration, can reduce thermal energy requirements. Catalytic regeneration accelerates the breaking down of CO_2-containing species at lower ranges of temperatures, thereby addressing the challenges of low solvent equilibrium loading and overall slow CO_2 desorption kinetics in DAC.

2.4 Catalytic Solvent Regeneration

As mentioned, one of the key difficulties in the solvent-based CO_2 DAC capture method is the slow kinetics of CO_2 desorption (98). Consequently, various studies have been conducted recent decades to overcome the issue of energy-intensive solvent regeneration (99-101).

Utilizing acid-base catalysts during CO_2 desorption is a novel and effective technique for lowering the required heat duty (43, 102, 103). In catalyst-assisted solvent regeneration, catalysts can accelerate the CO_2 stripping rate and reduce the regeneration time and overall energy consumption. In Sections 2.4.1 and 2.4.2, the catalytic promotion mechanism in solvents and a variety of acid catalysts that have been used in the field are described.

2.4.1 Catalytic CO_2 Desorption Mechanism

It has been established that the Zwitterion mechanism governs the chemical absorption-desorption for primary amine solutions such as MEA (104, 105). CO_2 absorption results in the formation of protonated amine ($MEAH^+$) and carbamate ($MEACOO^-$) through Equation 1.6. Furthermore, based on Equation 1.7, a portion of the formed $MEACOO^-$ may undergo reaction with water to produce bicarbonate (HCO_3^-) (106, 107).

$$2MEA + CO_2 \leftrightarrow Zwitterion \leftrightarrow MEACOO^- + MEAH^+ \quad (1.6)$$

$$MEACOO^- + H_2O \leftrightarrow MEA + HCO_3^- \quad (1.7)$$

For regeneration, two major steps are recognized, $MEAH^+$ deprotonation and carbamate breakdown, which are Equation 1.8 and 1.9, respectively.

$$MEAH^+ + H_2O \leftrightarrow MEA + H_3O^+ \quad (1.8)$$

$$MEACOO^- + H_3O^+ \leftrightarrow MEA + CO_2 + H_2O \quad (1.9)$$

Notably, both Equation 1.8 and 1.9 are highly endothermic (73.4 kJ/mol for Equation 1.8 and 15.5 kJ/mol for Equation 1.9) (39). Comparing these two reactions, amine deprotonation requires a great deal of energy and is considered the main barrier in the CO_2 desorption procedure since it releases a proton (H^+) which is a main requirement for carbamate decomposition and CO_2 release (108, 109).

The HCO_3^- molecules, which are produced by Equation 1.7, can play a similar crucial role to H_2O in Equation 1.8 (amine deprotonation) in transferring a proton from $MEAH^+$ to $MEACOO^-$ (Equation 1.10); This proton transfer is more readily achieved with HCO_3^- than with H_2O (109, 110). Thus, an abundant number of HCO_3^- in solution may function as a catalyst and minimize the amount of energy needed for amine deprotonation (39). Furthermore, carbonic acid can also decompose to liberate CO_2 (Equation 11).

$$MEAH^+ + HCO_3^- \leftrightarrow MEA + H_2CO_3 \quad (1.10)$$

$$H_2CO_3 \leftrightarrow CO_2 + H_2O \quad (1.11)$$

Unlike primary and secondary amines, which produce carbamate and bicarbonate through Equation 1.6 and 1.7, the reaction of CO_2 with tertiary amines forms bicarbonate (rather than carbamate). Equation 1.12 shows that the main product of reaction between MDEA (a common tertiary amine) and CO_2 is HCO_3^-. The presence of bicarbonate rather than carbamate in solution leads to a lower energy requirement for amine deprotonation (due to a superior proton acceptor compared to H_2O) (111).

$$MDEA + CO_2 \leftrightarrow MDEAH^+ + HCO_3^- \quad (1.12)$$

Since the presence of HCO_3^- facilitates the desorption process, tertiary amines are less energy-intensive compared to primary amines (110).

As stated, the energy-intensive behavior of solvent regeneration is attributed to the low quantity of protons in solution to facilitate the reaction of carbamate decomposition. In this regard, the imperative roles of physical and chemical properties in catalysts (Lewis and Brønsted acid sites) are described in the following text.

Lewis acidity (L) is one of the principal acid types on the surface of catalysts. Unsaturated metal atoms in a structure of a catalyst are considered Lewis acid sites, allowing them to receive

a lone electron pair (112). The Lewis acidity contribution in the amine deprotonation pathway is described in Equation 1.13 and 1.14 (42, 45).

$$MEAH^+ + L \leftrightarrow MEA + LH \quad (1.13)$$

$$LH + H_2O \leftrightarrow L^- + H_3O^+ \quad (1.14)$$

The second type of acidity for catalysts is Brønsted acidity (B), which can transfer a proton (H^+) to a base (113). Equation 1.15 and 1.16 highlight the catalytic contribution of Brønsted acid sites in the process of carbamate decomposition (41, 114).

$$MEACOO^- + BH^+ \leftrightarrow MEACOOH + B \quad (1.15)$$

$$MEAH^+ + B \leftrightarrow MEA + BH^+ \quad (1.16)$$

For the tertiary amines, the effects of Lewis and Brønsted acid sites' presence are described in Equation 1.17, 1.18, and Equation 1.19, 1.20, respectively.

$$MDEAH^+ + L \leftrightarrow MDEA + LH \quad (1.17)$$

$$LH + HCO_3^- \leftrightarrow L^- + CO_2 + H_2O \quad (1.18)$$

$$BH^+ + HCO_3^- \leftrightarrow B + CO_2 + H_2O \quad (1.19)$$

$$MDEAH^+ + B \leftrightarrow MDEA + BH^+ \quad (1.20)$$

Based on Equation 1.13, 1.14 and Equation 1.17, 1.18, Lewis acids must execute two sequential stages to fulfil its part in the reaction process. The first step is to take protons from the protonated amine, and the second step is to transfer the protons to speed up the rate of CO_2 desorption. Moreover, according to Equation 1.15, 1.16 and Equation 1.19, 1.20, Brønsted acids participate in the solvent regeneration process by directly donating protons.

In amino acid solvents, the same fundamental reactions occur, governed by the nature of the amine group. Although detailed information on the catalytic regeneration mechanism in amino

acid salt systems is limited, one study has examined the imapct of TiO_2 catalysts on potassium sarcosinate (KSar) (115). In this system, the absorption of CO_2 results in the formation of carbamate and protonated species, as shown in Equation 1.21.

$$2KSar + CO_2 \leftrightarrow KSarCOO^- + KSarH^+ \quad (1.21)$$

Under non-catalytic conditions, regeneration proceeds through two main reactions. First, protonated KSar ($KSarH^+$) undergoes deprotonation by water, releasing a hydronium ion (Equation 1.22):

$$KSarH^+ + H_2O \leftrightarrow KSar + H_3O^+ \quad (1.22)$$

The carbamate anion reacts with H_3O^+ to liberate CO_2 and restores the amino acid base (Carbamate Breakdown-Equation 1.23):

$$KSarCOO^- + H_3O^+ \leftrightarrow KSar + CO_2 + H_2O \quad (1.23)$$

Additionally, bicarbonate can also be formed in the solution. It acts as a proton acceptor, transferring protons from $KSarH^+$ and subsequently decomposing to release CO_2 (Equation 1.24 and 1.25):

$$KSarH^+ + HCO_3^- \leftrightarrow KSar + H_2CO_3 \quad (1.24)$$

$$H_2CO_3 \leftrightarrow CO_2 + H_2O \quad (1.25)$$

To enhance the efficiency of this process, TiO_2 catalysts have been examined for their dual acid functionality. The Lewis acid sites (L) are capable of accepting a proton from $KSarH^+$ and subsequently transferring it to water to generate H_3O^+ (Equation 1.26 and 1.27).

$$KSarH^+ + L \leftrightarrow KSar + LH \quad (1.26)$$

$$LH + H_2O \leftrightarrow L^- + H_3O^+ \quad (1.27)$$

Similarly, LH can donate a proton to HCO_3^-, promoting CO_2 release (Equation 1.28):

$$LH + HCO_3^- \leftrightarrow L^- + CO_2 + H_2O \quad (1.28)$$

Furthermore, Brønsted acid sites (B), on the other hand, can directly donate protons to carbamate and bicarbonate species, accelerating their decomposition (Equation 1.29 and 1.30):

$$BH^+ + KSarCOO^- \leftrightarrow KSarCOOH + B \quad (1.29)$$

$$BH^+ + HCO_3^- \leftrightarrow B + CO_2 + H_2O \quad (1.30)$$

Finally, the spent base site B can be regenerated by accepting a proton from $KSarH^+$ (Equation 1.31):

$$KSarH^+ + B \leftrightarrow KSar + BH^+ \quad (1.31)$$

The overall mechanism is illustrated schematically in **Scheme 2.1**, highlighting the proposed catalytic pathways enabled by Lewis and Brønsted acid sites on TiO_2 (115). This can facilitate the liberation of CO_2 which reduces the energy demand.

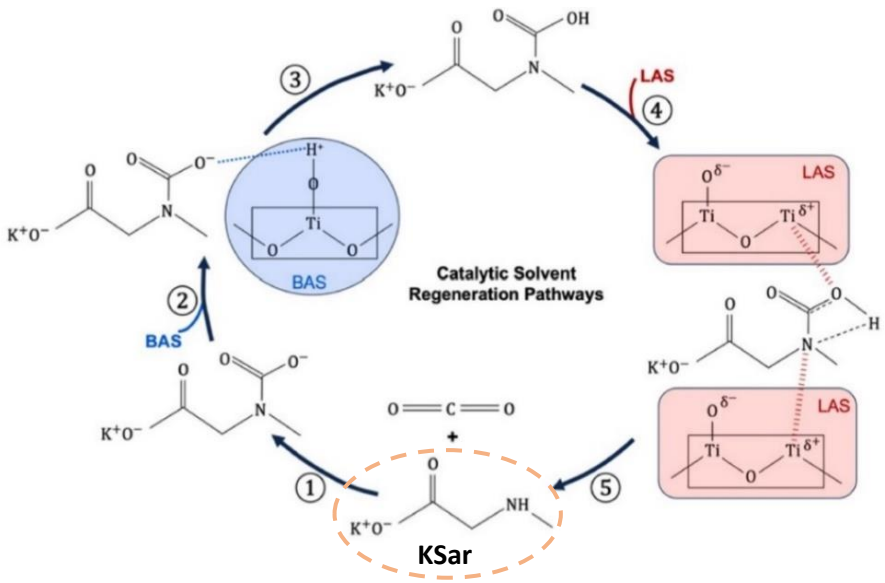

Scheme 2.1. A schematic representation of the proposed regeneration pathways for CO_2-loaded potassium sarcosinate (KSar), highlighting the role of Lewis and Brønsted acid sites on the TiO_2 surface in Deka et al; reused with permission (115).

As shown in step 1 of **Scheme 2.1**, the reaction between KSar and CO_2 results in the formation of a carbamate intermediate. Step 2 initiates the breakdown of this species, where the oxygen anion (O^-) in the carboxylate group accepts a proton from a Brønsted acid site (BAS), forming a carboxylic acid in Step 3. In Step 4, both the nitrogen atom from the amine and the oxygen atom from the -COOH group coordinate with Lewis acid sites (LAS). This coordination results in the nitrogen atom losing its lone electron pair, shifting from sp^2 to sp^3 hybridization. This change weakens and extends the N-C bond and disrupts the conjugation within the $N\text{-}COO^-$ group. In step 5 the N-C bond will break, and CO_2 will be liberated. Altogether, these transformations reduce the energy required to break the carbamate structure, thereby enhancing the rate of CO_2 release (115).

Notably, in several other studies for catalytic solvent regeneration, the proposed CO_2 desorption mechanisms follow the same main steps with minor variations. Some of these pathways, illustrating the role of catalysis in facilitating CO_2 release, are presented in **Scheme 2.2** (33, 43).

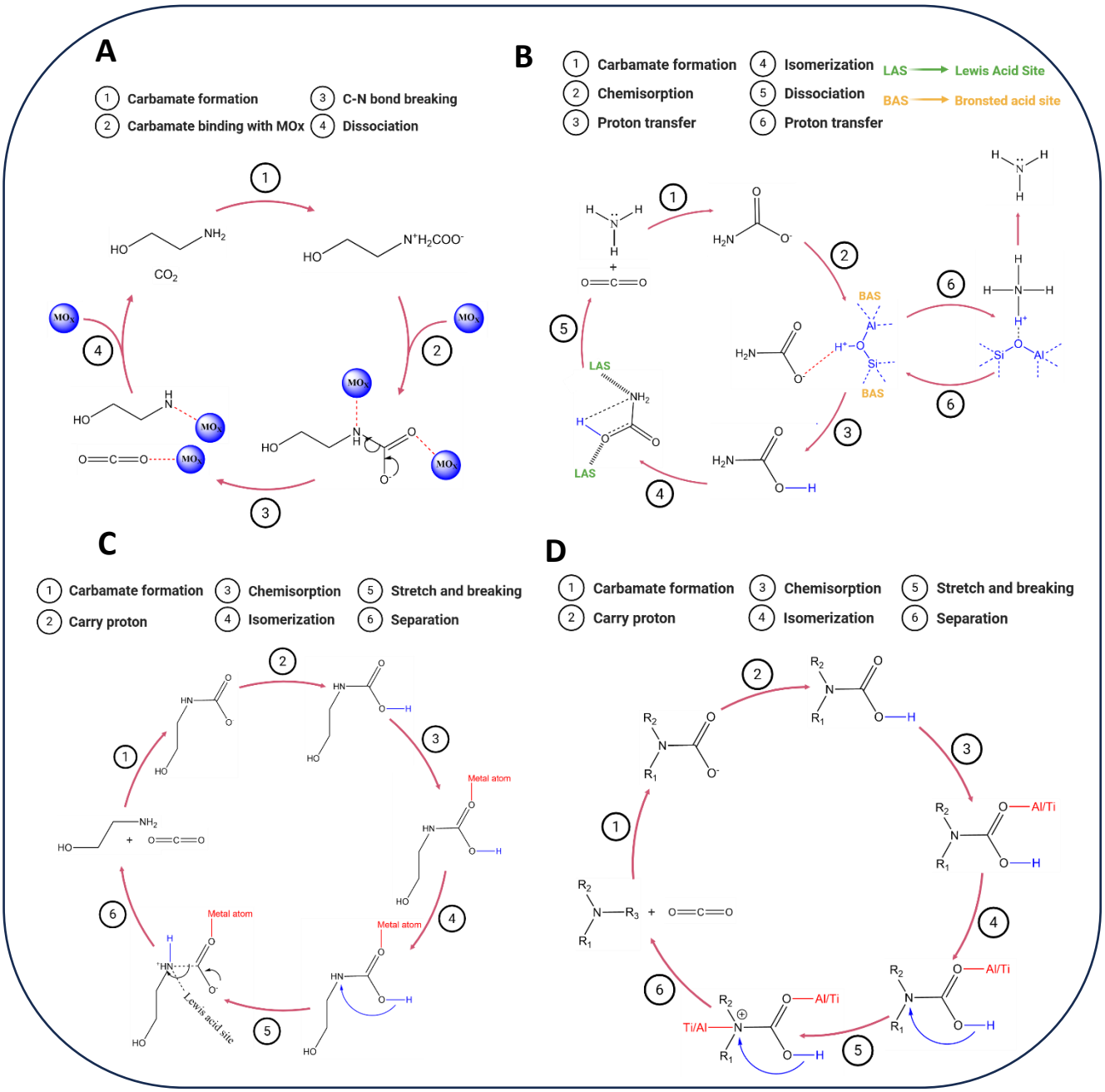

Scheme 2.2. Schematic representation of the proposed CO_2 desorption mechanisms with various solid acid catalysts. (A) MEA regeneration facilitated by metal oxide catalysts, (B) CO_2 release from ammonia solution using HZSM-5, TiO_2, and γ-Al_2O_3, (C) MEA regeneration promoted by $SO_4^{2-}/ZrO_2/\gamma$-Al_2O_3, and (D) desorption from a 3M MEA–2.5M AMP–0.5M MPZ mixed solution using γ-Al_2O_3, SAPO-34, H-ZSM-5 and SO_4^{2-}/TiO_2 catalysts. This scheme is adapted from Alivand et al; reused with permission (43).

2.4.2 Solid Acid Catalysts

Numerous acidic catalysts with diverse physical and chemical characteristics for energy-efficient CO_2 desorption have been explored. (e.g., metal-oxides, sulfated metal-oxides, zeolites, mesoporous silica, and nanocomposites) (33, 43).

It is well acknowledged that the physical and chemical features (i.e., physicochemical) of nanocatalysts make a major contribution in desorption efficiency. Hence, a broad range of studies have focused on the fine-tuning of these parameters to maximize catalytic efficiency.

In 2021, water-dispersible nanospheres with a high density of acidic sites on the exterior surface for high dispersibility and efficiency were produced and their performance evaluated in different aqueous amine and amino acid solutions under flue gas condition (**Figure 2.12**)(103). One of the key advantages of these magnetic nanoparticles is a one-pot synthesis method in the solution without the need for post functionalization.

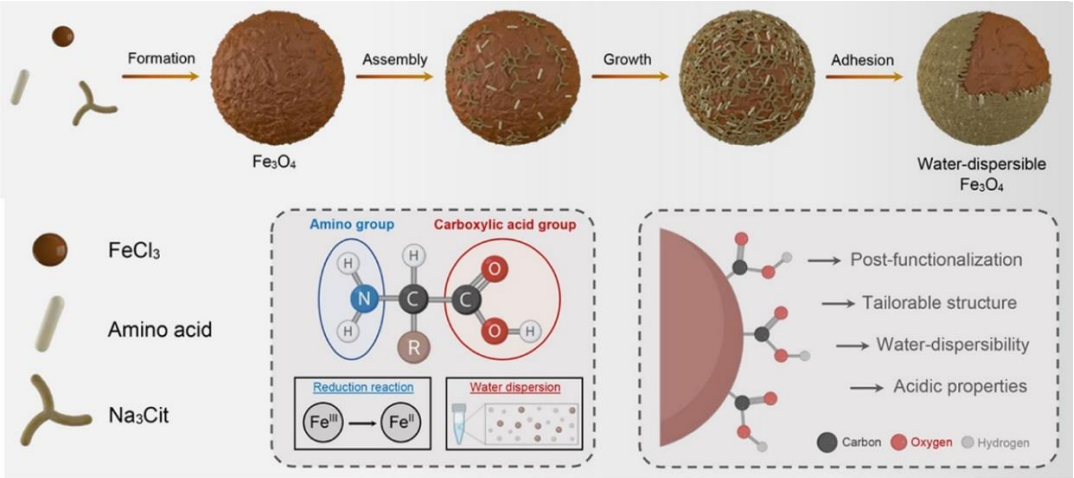

Figure 2.12. Synthesis procedure for preparation of water-dispersible Fe_3O_4 nanospheres using amino acids; reused with permission (103)

As it is illustrated in **Figure 2.12**, the amino groups' existence is crucial for the ultimate Fe_3O_4 formation (Fe^{III} to Fe^{II} conversion) in a one-pot synthesis technique. In addition, the carboxyl acid group has a direct and considerable influence on dispersibility (due to hydrogen bonding with water molecules), and acidity (Brønsted acid sites).

To evaluate the applicability of the synthesis approach, a broad variety of amino acids (12 distinct molecules, i.e., cyclic, long-chain, short-chain) were utilized during the hydrothermal synthesis of Fe_3O_4 nanospheres. As depicted in **Figure 2.13**, all 12 synthesized Fe_3O_4 nanoparticles with different amino acids exhibited a negative surface (ζ) potential, which

represents the level of deprotonation of carboxylic acid groups on the external surface of nanospheres.

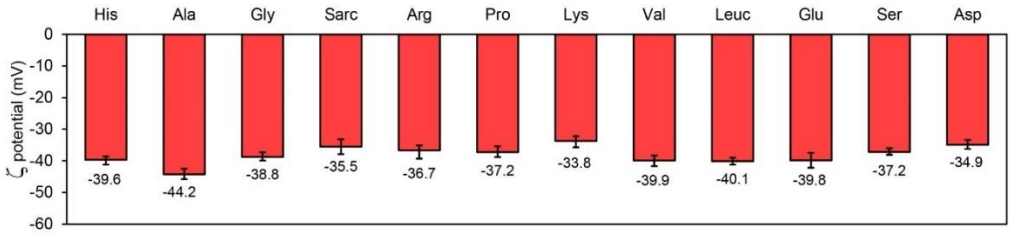

Figure 2.13. Analysis of ζ potential values of diverse water-dispersible Fe_3O_4 nanomaterials produced with various amino acids (all nanoparticles were dispersed in 0.1 M 3-(n-morpholino) propane sulfonic acid (MOPS) buffer at pH 9.0). The abbreviations used for amino acids from left to right: Histidine (His), Alanine (Ala), Glycine (Gly), Sarcosine (Sarc), Arginine (Arg), Proline (Pro), Lysine (Lys), Valine (Val), Leucine (Leuc), Glutamine (Glu), Serine (Ser), Asparagine (Asp); reused with permission (103).

According to **Figure 2.13**, Fe_3O_4-Ala is picked for further investigation due to the lowest negative surface (ζ) potential -44.2 mV (highest -COOH density on the surface).

To boost the acidic features (stronger Brønsted acid) on the surface of magnetic nanospheres, sulfanilic acid is used in a one-pot synthesis method with the selected amino acid (Fe_3O_4-Ala). To evaluate the function of sulfanilic acid in the production of Fe_3O_4-Ala, a range of nanomaterials with varying ratios of amino to sulfanilic acid were synthesized (**Figure 2.14**).

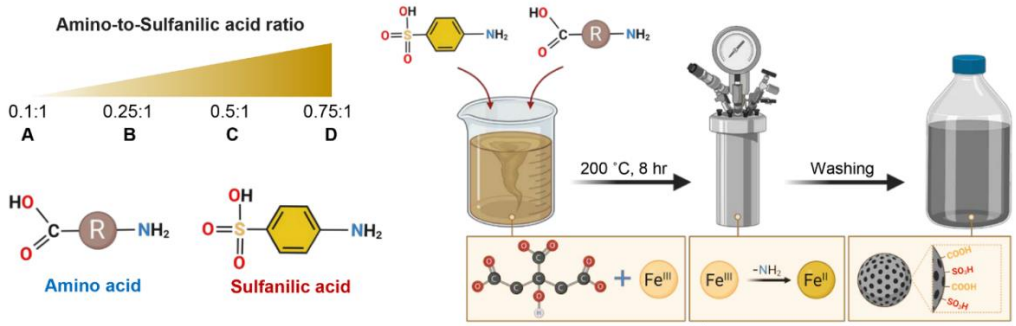

Figure 2.14. Tuning the acidic features of magnetic Fe_3O_4 nanospheres with different ratio of amino to sulfanilic acid in single-pot synthesis technique. Each ratio is designated with a distinct letter (e.g., C refers to Fe_3O_4-Ala-C with a ratio of 0.5:1); reused with permission (103)

X-ray photoelectron spectroscopy (XPS) was conducted to investigate the sulfur coverage on the external surface of nanospheres in different ratios (A to D). As indicated in **Figure 2.15**,

sample C with the greatest sulfur level of 3.83% is considered with the highest acidity of water-dispersible nanocatalyst (Fe_3O_4-Ala-C) among the others.

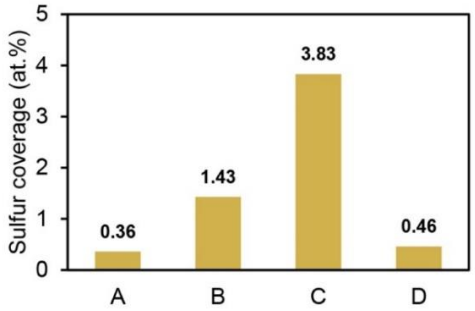

Figure 2.15. Sulfur concentration detected by XPS at various ratios of amino to sulfanilic acid; reused with permission (103)

In the next step, the authors investigated the CO_2 stripping rate of the rich solution of 5 M MEA with different tailored Fe_3O_4. It is notable that the desorption performance of Fe_3O_4-Ala (without sulfation) was analyzed and considered as a benchmark. Throughout all catalytic regeneration studies, the regeneration temperature was set to 88 °C. As demonstrated in **Figure 2.16a**, all designed nanocatalysts with distinct acidic properties exhibited a favorable impact on the CO_2 desorption kinetics. Notably, from **Figure 2.16a, b**, the Fe_3O_4−Ala-C magnetic nanospheres achieved the greatest performance with a 63.3% increase in total CO_2 desorption, which is a four-fold improvement in comparison with benchmark Fe_3O_4−Ala (only carboxylic group). This underlines the significant contribution of the chemical characteristics of synthesized nanomaterials to catalytic solvent regeneration efficiency. Having a desired platform that is compatible with assembling strong Brønsted acidic groups on the surface with high efficiency is a critical factor in CO_2 desorption kinetics and regeneration energy required.

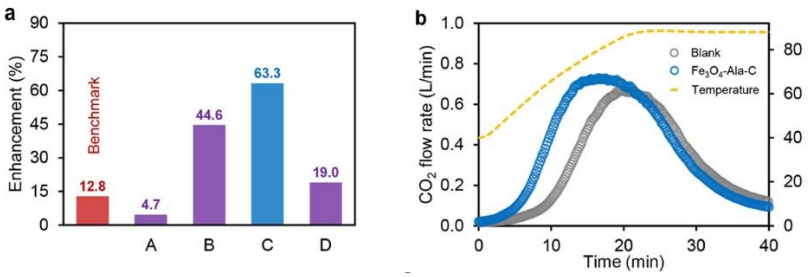

Figure 2.16. a) Enhancement of CO_2 desorption rate for water-dispersible nanocatalysts with various tailored chemical characteristics. b) CO_2 desorption profiles in the presence and absence of selected nancatalyst (Fe_3O_4−Ala-C); reused with permission (103).

With the observed catalytic nanospheres performance in MEA solution, the effect of Fe_3O_4-Ala-C in various solutions, including amino acids and amines was further studied by authors (103).

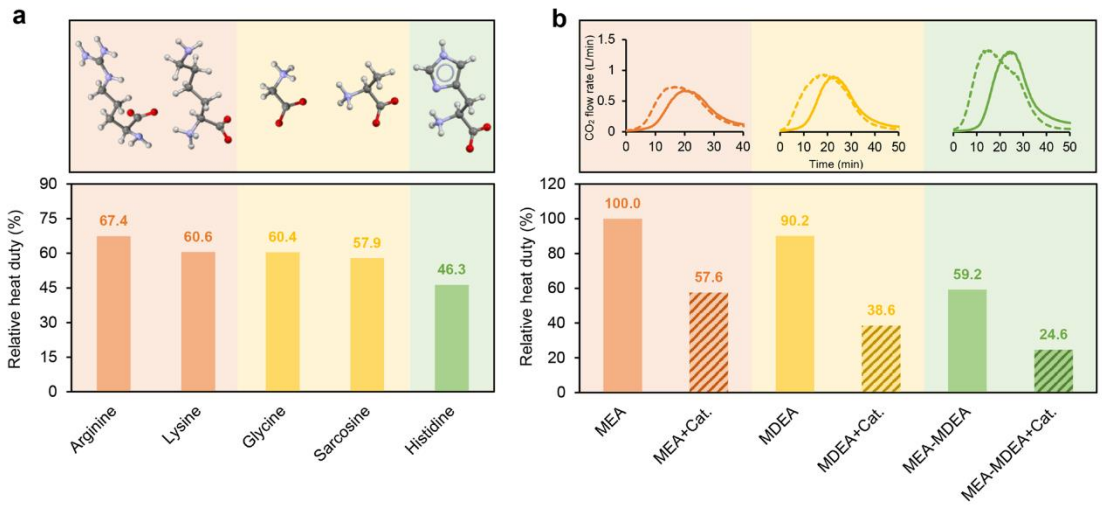

Figure 2.17. Utilizing the selected water-dispersible nanocatalyst Fe_3O_4-Ala-C in various solutions for energy-saving regeneration. a) for different types of amino acids (1 M). b) for variety types of amines (primary type (MEA, 5 M), tertiary type (MDEA, 2 M), and primary-tertiary blend type (MEA−MDEA, 5 M-2 M)); reused with permission (103)

According to **Figure 2.17**, the Fe_3O_4-Ala-C nanocatalyst improved CO_2 desorption rate and lowered the heat demand for regeneration in all types of amino acids and amine solutions. For amino acid solutions, several factors influenced catalyst efficiency. Solubility in water, quantity of amine functional group in the structure, pKa values, and molecular weight are examples of the physical and chemical characteristics of amino acid solutions which contribute to catalyst impact. In **Figure 2.17a**, the relative heat duties of regeneration process for various

amino acid aqueous solutions are evaluated and compared to their respective heat duties without the use of nanocatalysts. According to this figure, long-chain amino acids with a higher number of amine functional groups (Arginine) are less impacted by the presence of nanocatalysts than short-chain amino acids (Glycine and Sarcosine). Furthermore, Histidine showed the lowest relative heat duty of 46.3%, which can be attributed to the phase change behavior and solid formation of this solution during CO_2 absorption.

The amine solutions heat duties are shown in **Figure 2.17b** and calculated relative to blank 5 M MEA solution as a benchmark. As it is depicted without the use of nanocatalysts, MEA-MDEA blend achieved a desirable heat duty of 59.2% compared to MEA alone which highlights the effective role of hybrid solvents in lowering the required energy. As is mentioned, in the CO_2 absorption process, the presence of tertiary amine molecules leads to the bicarbonate formation (without any carbamate production), which promotes proton transfer for carbamate breakdown reaction. Furthermore, in the presence of nanaocataslyst in MEA-MDEA mixtures, the relative heat duty value remarkably decreased to 24.6% which is much lower than the catalytic trial of MEA alone (57.6%). This demonstrates the importance and effectiveness of integrating catalytic solvent regeneration with hybrid solvents.

In another study accomplished in 2022, water-dispersible super acidic nanaocatalyst with a core-shell structure was developed (34). For the core part, Fe_3O_4 nanoclusters were used which can serve as ideal substrates for the development of highly efficient nanocatalysts. Ferric ammonium citrate, which consists of citric acid and iron (Fe^{3+}), was utilized as an inexpensive and eco-friendly precursor for the synthesis of Fe_3O_4 nanoclusters with carboxylate functional group on the exterior surface (**Figure 2.18**). The COOH functional group can be considered as the metal coordination point, which plays a crucial role in coating the shell on the acidic core.

Figure 2.18. The production of nanoclusters by a one-pot synthesis technique; reused with permission (34)

For the shell part, self-assembled metal-organic frameworks (MOFs) were coated and grown on the acidic substrate (Fe_3O_4@MOFs). Various MOFs, including UiO-66, UiO-66-NH_2, ZIF-8, HKUST-1, MOF-Fe(II), MIL-100(Fe), and ZIF-67were used to investigate the structural variety of a developed porous shell. Each type of MOFs contains a combination of specific metals and ligands which can lead to diverse structural and physicochemical characteristics (**Figure 2.19**).

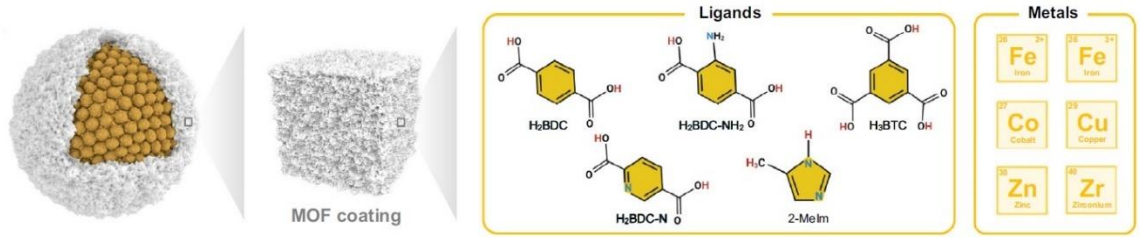

Figure 2.19. The metal and ligands utilized to synthesize different MOF coatings with distinct physicochemical properties; reused with permission (34)

Using scanning electron microscopy (SEM) pictures, the exterior of Fe_3O_4@MOFs nanoparticles was further examined. As illustrated in **Figure 2.20a-f** the structure of core-shell nanomaterials with various MOFs varies from uniform spherical forms (i.e., Fe_3O_4@UiO-66) to semi-spherical conjunct core-shell architecture (i.e., Fe_3O_4@MIL-100(Fe)). This is due to the varied coated framework associated with the coordination of diverse metals and ligands, which produces distinct physicochemical characteristics.

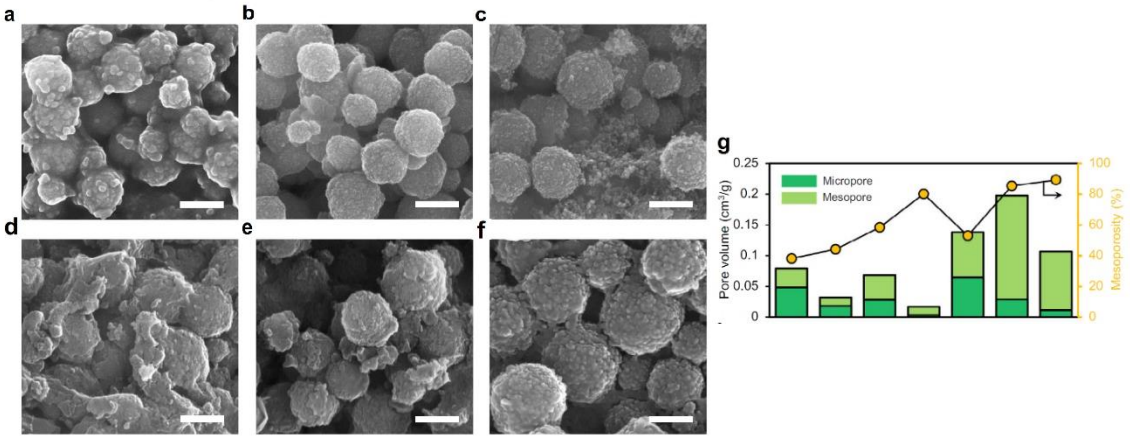

Figure 2.20. SEM images of (a) Fe_3O_4@ZIF-8, (b) Fe_3O_4@ZIF-67, (c) Fe_3O_4@MOF-Fe(II), (d) Fe_3O_4@MIL-100(Fe), (e) Fe_3O_4@HKUST-1, and (f) Fe_3O_4@UiO-66. All scale bars correspond to 200 nm. (g) Pore volume and mesoporosity of the different Fe_3O_4@MOFs; reused with permission (34).

The physical properties of the synthesized core-shell nanomaterial were further evaluated. **Figure 2.20g** depicts the total pore volume and mesoporosity for different prepared Fe_3O_4@MOFs. Based on the various pore networks of coated MOFs, different physical characteristics are obtained. Fe_3O_4@UiO-66 possesses the largest pore volume (approximately 0.2 cm^3/g) compared with other synthesized core-shell materials, which underlines the coordination effect of different metals and ligands on the framework. Interestingly, it was discovered that the coated MOFs on the shell side possess a hierarchical structured micro and mesoporous network, whereas pristine MOFs are typically microporous. This can be related to the linker defects created during the MOFs self-assembly on the substrate which caused the framework to acquire mesoporosity. Notably, defect-tailored MOFs are viable substrates for post-treatment synthesis because they can offer active metal sites with a high affinity for a wide range of functional groups. Hence, by introducing sulfate functional groups into the defective structures of tailored Fe_3O_4@MOFs, the chemical characteristics (Brønsted acid site) of these materials was further improved.

The synthesized core-shell nanomaterials were utilized in MEA 5 M solution to investigate the CO_2 desorption efficiency at 88 °C under flue gas conditions. According to **Figure 2.21**,

Fe_3O_4@UiO-66 and Fe_3O_4@UiO-66-NH_2 demonstrated the lowest relative heat values and highest cyclic capacity among the other synthesized core-shell nanocatalysts, which can be attributed to the large pore volumes and mesoporosity structure (**Figure 2.20g**). This demonstrates the influence of the catalyst's specifically designed physical and chemical features on improving CO_2 desorption.

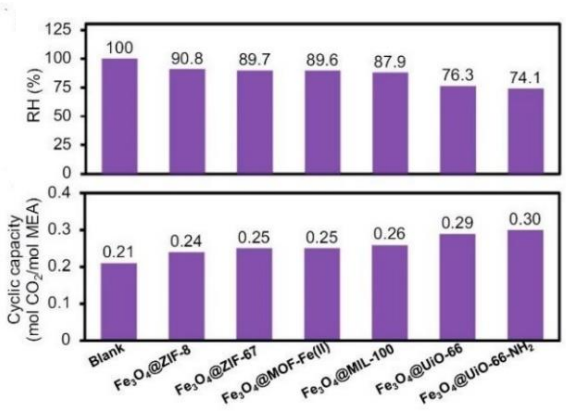

Figure 2.21. The influence of different water-dispersible nanocatalysts on relative heat duty (RH) and cyclic CO_2 capacity of MEA aqueous solution; reused with permission (34).

As most catalytic solvent regeneration studies have been conducted under flue gas conditions, only a few have employed regeneration under DAC scenarios. A 2023 study presented a novel approach that evaluated the performance of synthesized monodispersed carbon spheres (MCS) and their sulfonated derivative MCS-SO_3H as catalysts for enhancing CO_2 desorption in DAC using suitable amino acid solvents (40). These catalysts were synthesized through a single-step hydrothermal method using glucose and trisodium citrate (Na_3Cit), which acted as a structure-directing agent. The use of Na_3Cit helped form highly uniform, water-dispersible carbon nanospheres. This uniform morphology, confirmed through SEM imaging (**Figure 2.22**), minimized aggregation and provided an ideal platform for acid functionalization.

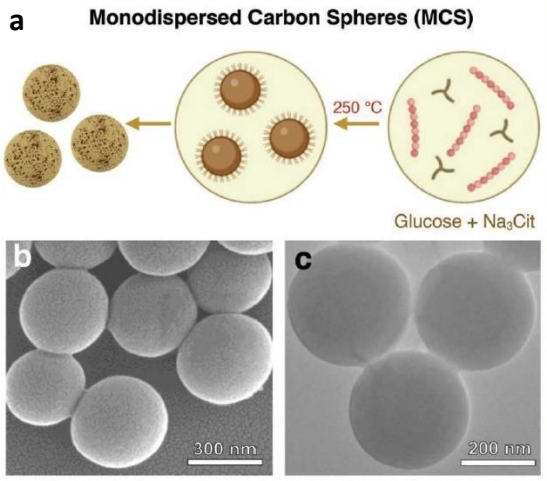

Figure 2.22. Schematic illustration of the synthesis process for monodispersed carbon spheres (MCSs), accompanied by their b) SEM and c) TEM images; reused with permission (40).

The sulfonation of these spheres using concentrated sulfuric acid yielded MCS-SO_3H nanocatalysts containing strong Brønsted acid sites. Characterizations via XPS, FTIR, and EDX confirmed the successful incorporation of sulfonic acid groups on the carbon sphere surfaces.

To evaluate the catalytic effectiveness of the MCS-SO_3H materials, five potassium-based amino acid aqueous solutions, sarcosine (SarK), glycine (GlyK), arginine (ArgK), proline (ProK), and lysine (LysK) were selected. These solvents were saturated with atmospheric CO_2 (~410 ppm) using a custom-built rising-bubble DAC apparatus. Notably, their equilibrium CO_2 capacities and corresponding cyclic capacities were measured across a temperature range of 25 to 98 °C (**Figure 2.23**).

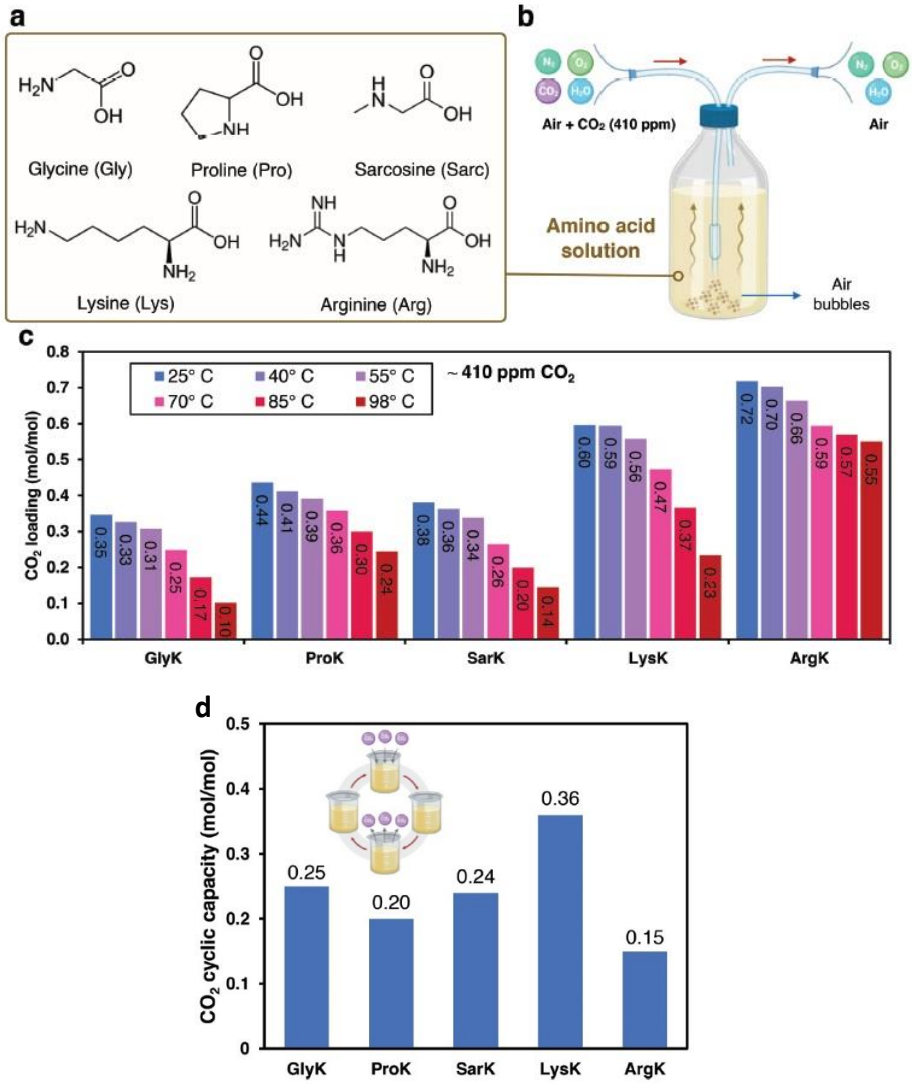

Figure 2.23. a) Chemical structures of the selected amino acids, and b) schematic of the custom-built rising-bubble setup for capturing CO_2 from ambient air. c) Equilibrium CO_2 loading of 1 M amino acid solutions across various temperatures. d) Cyclic CO_2 capacities of these solutions between 25 and 98 °C, representing absorption and desorption conditions. All equilibrium measurements were performed using air containing approximately 410 ppm CO_2 ; reused with permission (40).

According to **Figure 2.23d**, the result revealed that among long-chain amino acids, LysK achieved the highest cyclic capacity of approximately 0.36 mol/mol, while among short-chain variants, GlyK demonstrated the best performance with 0.25 mol/mol. These findings indicated that longer-chain amino acids with multiple amine groups tend to have higher CO_2 absorption capacities in DAC operation. However, their regeneration efficiency varied significantly depending on the chemical binding strength of CO_2 to the amino group.

Following the solvent screening, the catalytic regeneration performance of MCS-SO_3H was further assessed. According to **Figure 2.24**, When 0.2 wt% of MCS-SO_3H was added to the amino acid solutions, a significant reduction in energy demand for CO_2 desorption was observed. Specifically, LysK showed a 41.1% increase in CO_2 desorption efficiency with the catalyst, while GlyK exhibited a 25.6% improvement. The desorption profile of catalytic and blank trials of LysK are depicted in **Figure 2.24b**.

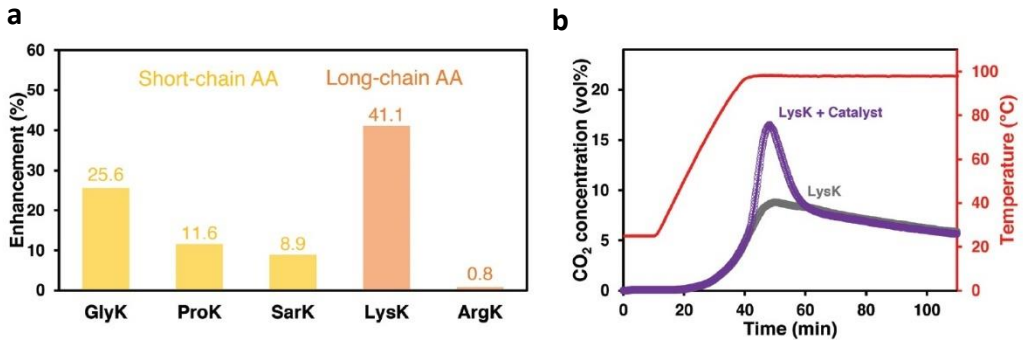

Figure 2.24. a) MCS-SO_3H Catalytic CO_2 desorption improvement at 98 °C in different amino acid aqueous solutions (1 M). b) CO_2 desorption curves of catalytic and blank LysK; reused with permission (40)

These results confirmed the role of MCS-SO_3H in lowering the regeneration energy requirement and accelerating desorption kinetics under DAC conditions. Interestingly, although ArgK had the highest initial CO_2 loading, it demonstrated negligible catalytic enhancement, highlighting that high absorption capacity does not always correlate with effective catalytic regeneration. In general, the study underscores the viability of catalytic solvent regeneration in DAC, particularly with amino acid solvents.

Based on the reviewed literature and discussions presented here, three key physical characteristics of nanocatalysts emerge as the most influential in achieving high catalytic efficiency: total surface area, average pore diameter and mesoporous surface area (43). Mesoporous surface area (pore width of 2-50 nm) compared to microporous surface area (less than 2 nm pore width), enables easier access to large amine carbamate molecules. This results in higher catalytic impact (39, 43, 44, 116). Additionally, average pore diameter is another key

characteristic that needs to be considered. Increased pore size for acid catalysts results in increased molecular accessibility, availability of acidic sites, and molecular diffusion within the porous structure of the catalyst by lowering the resistance of mass transfer (117-120). The quantity and types (Lewis and Brønsted acid sites) of active acidic sites and acid strength are regarded as chemical features of the catalysts which affect considerably on low-temperature regeneration heat duty. Notably, it has been experimentally shown that this effectiveness can surpass the mesoporous surface area (35, 118, 121). The Brønsted and Lewis acid sites of the catalysts, supply sufficient protons which facilitate carbamate breakdown reactions and, consequently, reduce the required desorption energy (122, 123). Acid strength is another important chemical characteristic, which is described as the ratio of strong acid sites to the overall acidity of the surface (i.e., the summation of weak, medium, and strong acid sites)(41). **Figure 2.25a-d** illustrate the mentioned physical and chemical characteristics of different used catalyst (43).

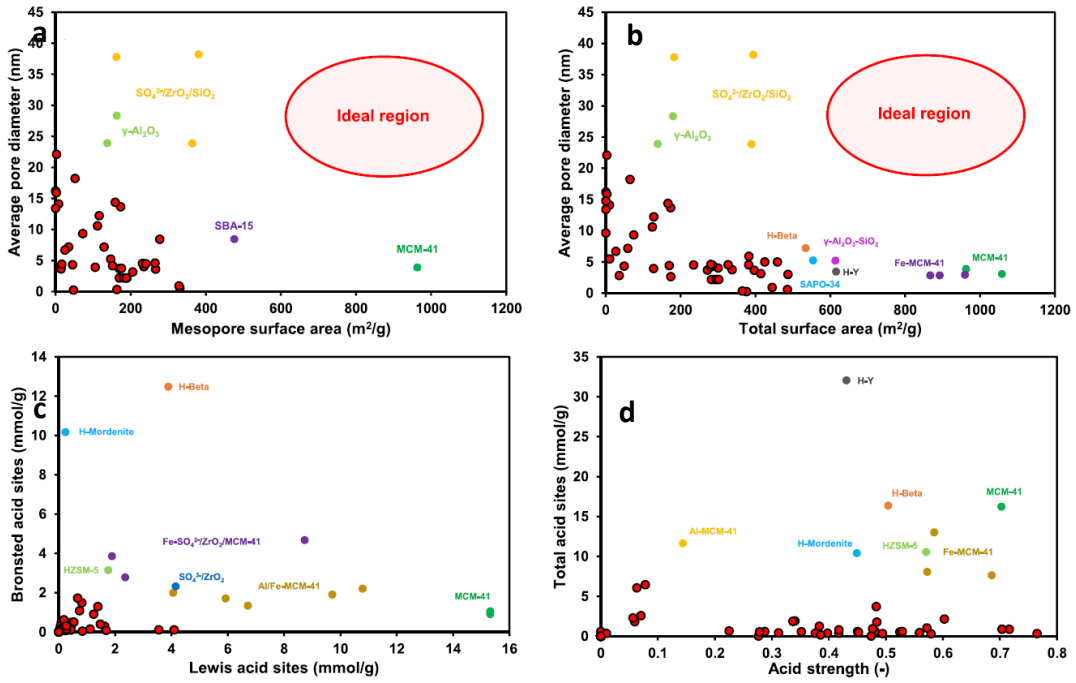

Figure 2.25. Comparative plots showing a) mesopore surface area versus average pore diameter, b) total surface area versus average pore diameter, c) Lewis to Brønsted acid sites, and d) acid strength versus total acid sites for various catalysts utilized for CO_2 desorption in low temperature ranges; reused with permission (43).

As shown in **Figure 2.25a, b**, mesoporous silica, MCM-41, possesses the highest total surface area and mesopore surface area. However, the narrow pore size diameter of MCM-41, might be regarded as a constraint on catalyst performance. In contrast, a high average pore diameter was observed for nanocomposite $SO_4^{2-}/ZrO_2/SiO_2$ catalysts. As indicated on **Figure 2.25a, b**, a catalyst with a high mesoporous and total surface area along with a large average pore size diameter, is an ideal catalyst for solvent regeneration (suitable for large carbamate molecules). In **Figure 2.25c**, H-beta with the predominant quantity of Brønsted acid sites, has the greatest acidic characteristics. On a subsequent level, Fe-promoted SO_4^{2-}/ZrO_2/MCM-41 stands out with high number of Brønsted and Lewis acid sites. In fact, the nanocomposite Fe-SO_4^{2-}/ZrO_2/MCM-41 is a blend of materials with distinct characteristics, each contributing unique advantages. The Fe.MCM-41 component possesses high acid strength (**Figure 2.25d**) and a substantial concentration of Brønsted acid sites, significantly enhancing the overall acidity of the nanocomposite. Moreover, the combination of Fe.MCM-41 with SO_4^{2-}/ZrO_2 (known for its abundance of Brønsted acid sites) can drastically influence the chemical properties of the material (43, 45).

These structural and acidic properties are key factors in defining the catalytic efficiency of each material. As a result, catalysts with distinct physical and chemical characteristics exhibit varying impact on lowering the heat duty during regeneration of solvent. **Figure 2.26** presents the comparative impact of each synthesized acidic catalysts on the relative heat duty in MEA solution under flue gas condition (43).

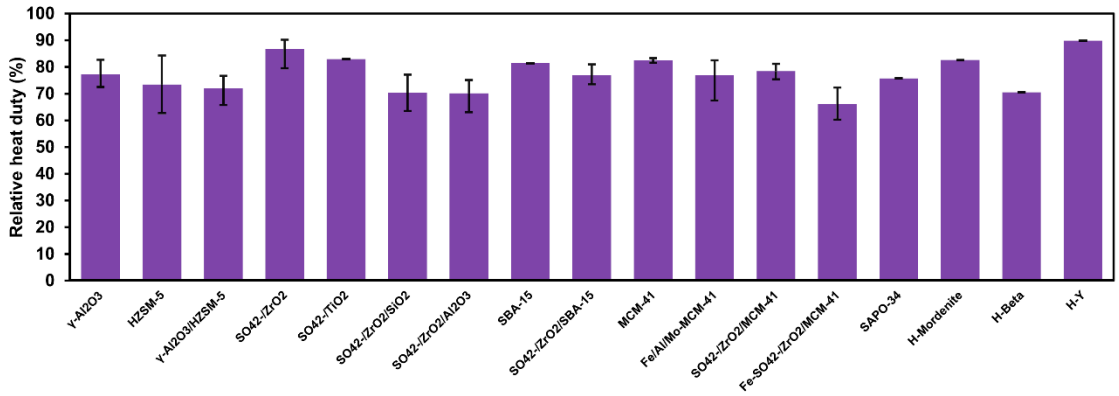

Figure 2.26. Impact of various catalysts on relative heat duty of the MEA solution (43); reused with permission

According to **Figure 2.26**, among the various synthesized and applied catalysts, Fe-SO_4^{2-}/ZrO_2/MCM-41 has the lowest relative heat duty with a value of 60.6 % for a 5 M MEA solution at 98°C. This can be attributed to the strong chemical properties (Brønsted and Lewis acid sites) and suitable physical characteristics (average pore size diameter) of this nanocomposite, which are described in the previous paragraphs.

To summarize, based on all the discussions and analyses presented in this section, it becomes evident that due to the inherently high energy intensity of DAC (attributed to ultra-low CO_2 partial pressure and corresponding low CO_2 equilibrium concentration in absorbed solvent) there is a critical requirement to employ low-temperature and energy-efficient regeneration approaches. Among these, membrane modules stand out as a particularly promising contactor, especially for the desorption step. Their unique capability to facilitate regeneration at low temperatures aligns well with sustainability goals and enables the utilization of low-grade heat sources to drive the process, while reducing solvent degradation, especially for amino acid-based solvents.

To further enhance CO_2 desorption performance during low-temperature regeneration under DAC conditions, integrating MVR with catalytic solvent regeneration offers a promising pathway to lower energy consumption and enhance operational efficiency. In terms of

operability, since the fibers in membrane modules have porous structures, adding solid catalysts directly into the system could block the pores and limit mass transfer. To avoid such issues, employing a fixed-bed system filled with bead-sized catalysts (1-2 mm) would be beneficial, which can prevent blockage of the membrane fibers while ensuring adequate catalytic activity. As discussed, a broad range of acidic catalysts have been synthesized and their impact evaluated in the context of catalytic solvent regeneration in CO_2 capture applications. Although ion-exchange resins can offer excellent properties for enhancing CO_2 stripping kinetics, they have received limited attention under both flue gas and DAC conditions. Ion-exchange resins are cross-linked, water-insoluble polymers that contain ion-active groups and are extensively employed in water treatment, purification, and catalysis (46-49). Their availability, high acidity, low cost, macroporosity, ease of handling, and thermal stability make them suitable for catalytic solvent regeneration under low-temperature conditions. This integration can further enhance the sustainability and energy-efficiency of liquid-based DAC processes.

Furthermore, based on experimental observations, among the evaluated catalysts, hybrid composites have consistently delivered superior performance compared to their individual components. This is largely due to their ability to combine multiple advantageous features as described, resulting in enhanced overall catalytic efficiency. These multifunctional characteristics make them suitable candidates for DAC applications. Moreover, as previously discussed, the use of hybrid solvents plays a significant role in improving CO_2 desorption under low-temperature conditions as well. These mixtures can enhance desorption efficiency through synergistic interactions, making them a valuable technique for improving DAC performance. Hence, integrating the hybrid solvent system with tailored hybrid composite catalyst in a low-temperature MVR unit, can offer a strong pathway toward a viable, sustainable, and low-energy liquid-based DAC process.

2.5 Research Objectives

Based on the literature review, research gaps are highlighted in the form of questions, which are listed below:

- Q1-What is the behavior and performance of green amino acid salts in a system of absorption and desorption in a DAC application using hollow fiber membrane modules?
- Q2-What is the effect of membrane characteristics and catalysts in a DAC-MVR process using a suitable solvent?
- Q3-What is the impact of combining hybrid solvents with hybrid composite catalysts on the performance of DAC-MVR?

Based on the above questions, the research objectives are outlined as follows:

1. Designing and developing bench-scale absorption-desorption DAC units using HFMCs and screening various amino acid salts under different process conditions.
2. Evaluating different types of membrane characteristics and integrating catalytic solvent regeneration technology into a low-temperature DAC-MVR unit.
3. Integrating hybrid solvent with hybrid composite catalysts with a low-temperature DAC-MVR unit.

These objectives will be addressed and discussed in detail in Chapters 4, 5, and 6, respectively.

CHAPTER 3

Experimental Methods

3.1 Perspective

This chapter outlines the materials and methodologies employed in experiments to obtain the results presented in this thesis. It includes detailed descriptions of the experimental rigs, CO_2 measurement techniques, and the synthesis of superacid catalysts. Additionally, this chapter presents an overview of the characterization methods employed to examine the physical and chemical features of the used catalysts.

3.2 DAC Absorption-Desorption Apparatus

Hollow fiber membrane modules were selected as contactors for DAC absorption and desorption units. Considering the required heating, cooling and pumping devices, a detailed sketch of the designed and developed system is depicted in **Scheme 3.1**.

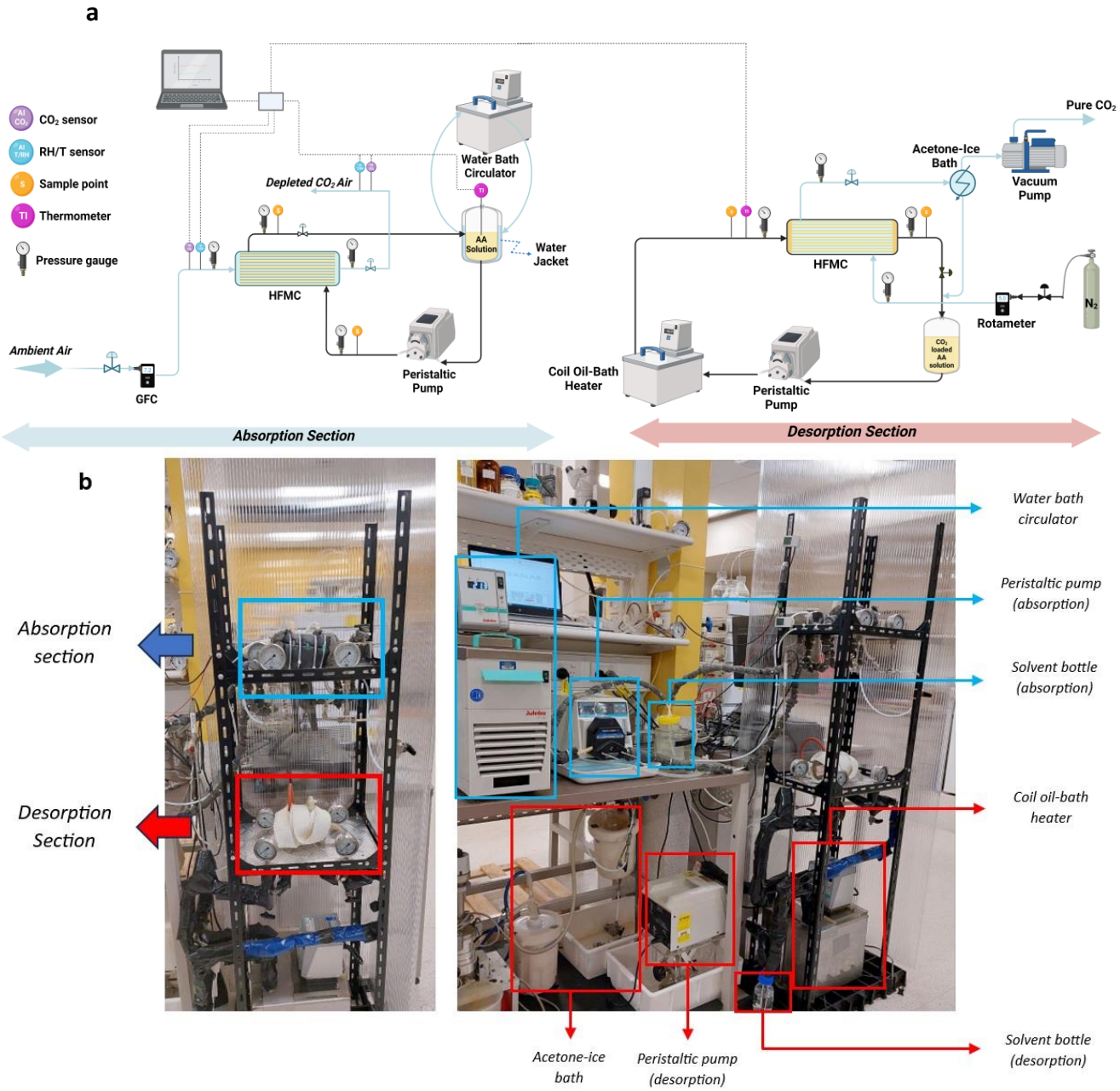

Scheme 3.1. a) Schematic diagram of DAC-absorption-desorption unit b) Photograph of the developed DAC units.

3.2.1 Absorption Set-up

The detailed schematic of the experimental DAC-absorption setup using HFMC is illustrated in **Scheme 3.1a**. A photo of the developed set-up is shown in **Scheme 3.1b**. An in-house compressed dry air line in the laboratory was used to supply the required amount of air into the lumen side of the HFMC with an average specification of ~415 ppm and a relative humidity of ~3% (at ambient temperature). To adjust the air pressure, a regulator (Swagelok) was installed

on the air line. A gas flow controller (GFC) from Aalborg (0–100 L/min) was utilized to regulate the air volume flow rate. Once the desired value was set on the GFC, air was introduced into the module. Two inline CO_2 analyzers (CO_2Meter, 0-1%) and two inline temperature/relative humidity sensors (HOBO, 1–100%) were installed at the inlet and outlet air streams to monitor and log the CO_2 content and temperature/relative humidity during operation, respectively. In order to monitor the air pressure drop along the membrane module, two pressure gauges (Braeco, 0-100 kPa) were located at the inlet and outlet of the module. After achieving a stable airflow and measurement values, 500 ml of the prepared amino acid solution was transferred into a bottle and circulated in a closed loop on the shell side of the HFMC via a peristaltic pump (Master Flex, Easy Load II). Sample points were installed at the inlet and outlet of the membrane module to measure the solvent loading using Chitick Apparatus (**Scheme 3.5**). During operation, the solvent and the air were routed to the module in a counter-current mode, and the transfer of CO_2 and subsequent increase in solvent loading occurred over time. The experiment ended when the concentration of CO_2 in the outlet reached within ±10 ppm of the inlet CO_2 concentration. This criterion signifies that the solvent had reached equilibrium and no longer possesses further considerable absorption capacity. The temperature of the solvent was maintained at the desired value using a water bath circulator (JULABO) while a thermocouple data logger was inserted into the solvent bottle to accurately track temperature during experiments. It is noted that to keep the temperature of the solvent constant, and minimize heat transfer to/from the surroundings, the membrane module and associated lines and valves were insulated.

To analyze the CO_2 separation efficiency, Equation 3.1 and 3.2 were employed.

$$\eta_a = \frac{Q_{in}C_{in} - Q_{out}C_{out}}{Q_{in}C_{in}} \times 100 \quad (3.1)$$

$$J_a = \frac{Q_{in}C_{in} - Q_{out}C_{out}}{A} \quad (3.2)$$

where η_a is the CO_2 absorption efficiency (%), J_a is the CO_2 absorption flux (mol/m^2·s), C_{in} and C_{out} are the CO_2 concentrations for the inlet an outlet air (mol/m^3), Q_{in} and Q_{out} are the inlet and outlet air flow rates (m^3/s), and A is the membrane contact area (m^2).

3.2.2 Desorption Set-up

3.2.2.1 Membrane Vacuum Regeneration for Chapter 4

As depicted in **Scheme 3.1a**, the membrane vacuum regeneration technology entails two distinct sides: the solvent side and the vacuum/sweep gas side. 500 ml of DAC CO_2-loaded amino acid solution (from the DAC-absorption unit) was placed into a bottle and circulated on the lumen side via a pump (Master Flex, Easy Load II). Prior to entering the module, the solvent passed through a coil immersed in an oil bath (JULABO) to be heated to the desired temperature. Due to the elevated operating temperature (70-90 °C), the apparatus was insulated using glass wool. The solvent temperature and pressure were monitored by a thermometer (OMEGA) at the inlet and two pressure gauges (Braeco, 0-100 kPa) at the inlet and outlet of the membrane module, respectively. Additionally, sample points were provided to measure the CO_2 content using Chittick apparatus (**Scheme 3.5**). When the solvent temperature reached the predetermined set value, it was regarded as the start point of the experiment. At this stage, the first solvent sample was extracted from the system, and a vacuum pressure/sweep gas was applied (Laboratory vacuum pump) on the shell side. To investigate the desorption efficiency at different solvent loadings, operation was conducted for 90 minutes, during which, a sample was extracted to measure the CO_2 content at every 15 minutes for the first 60 minutes. The CO_2 removal efficiency and flux were then calculated based on the obtained loading values and solvent CO_2 content according to Equation 3.3 and 3.4. After the final sample was collected at the 90-minute mark, operation was considered complete. Two vacuum pressure gauges (Braeco, -100 kPa to 0) were placed at each end of the module to monitor the pressure level

throughout the operation. To condense the transferred water across the fibers and recycle it back to the solvent container, an acetone-ice bath trap (-15±5 °C) was installed in-line at the outlet.

For sweep gas experiments, N_2 was used as a sweep gas and introduced to the shell side under vacuum condition. To monitor the volume flow rate of N_2, a rotameter was utilized.

$$\eta_d = \frac{\alpha_i - \alpha_j}{\alpha_i} \times 100 \tag{3.3}$$

$$J_{CO2} = \frac{C_i - C_j}{A\Delta t} \tag{3.4}$$

η_d is the CO_2 desorption efficiency (%), J_{CO2} is the CO_2 desorption flux (mol/m^2·s), C_i and C_j are the CO_2 mole content at time i and j, α_i and α_j are the solvent loading values at time i and j (mol/mol), and A is the membrane contact area (m^2) and Δt is the time difference between i and j (s).

3.2.2.2 Membrane Vacuum Regeneration for Chapter 5

Our previously designed and developed MVR DAC rig in previous chapter (124) was used with further development. **Scheme 3.2** shows the schematic view of the C-MVR apparatus (more details provided in **Scheme A.1**). The loaded solvents under DAC condition using the procedure outlined in our previous work (40) (equilibrium values are reported in **Figure A.9**) was placed in the solvent reservoir. Using a peristaltic pump and an oil bath, the solvent was circulated (0.25 L/min) and heated up to the desired set regeneration temperature, between 80-100 °C. At the solvent inlet and outlet of the HFMC, pressure gauges were installed to monitor the pressure drop during operation. One thermometer was used to record the temperature profile of the circulating solvent. Sample points were placed in the solvent loop to measure the CO_2 content of the solvent using the Chittick apparatus(124). A vacuum pump was used to apply vacuum pressure on one side of the membrane (2-4 $kPa_{(a)}$), and a pressure gauge was

used to monitor the vacuum pressure level. Two acetone-ice-baths were placed before the vacuum pump to condense and remove moisture from the high-purity CO_2 desorbed stream. The water collected at the end of each experiment was recycled back into the solvent container to ensure that the change in water content in the solvent remained minimal. To further analyze and accurately measure the high-purity CO_2 stream, a CO_2 analyzer and a flow meter were installed at the outlet of the vacuum pump. For C-MVR trials that include catalysts, a fixed bed was installed between the HFMC and oil batch heater so the solvent contacted the catalyst after heating and before entering the HFMC.

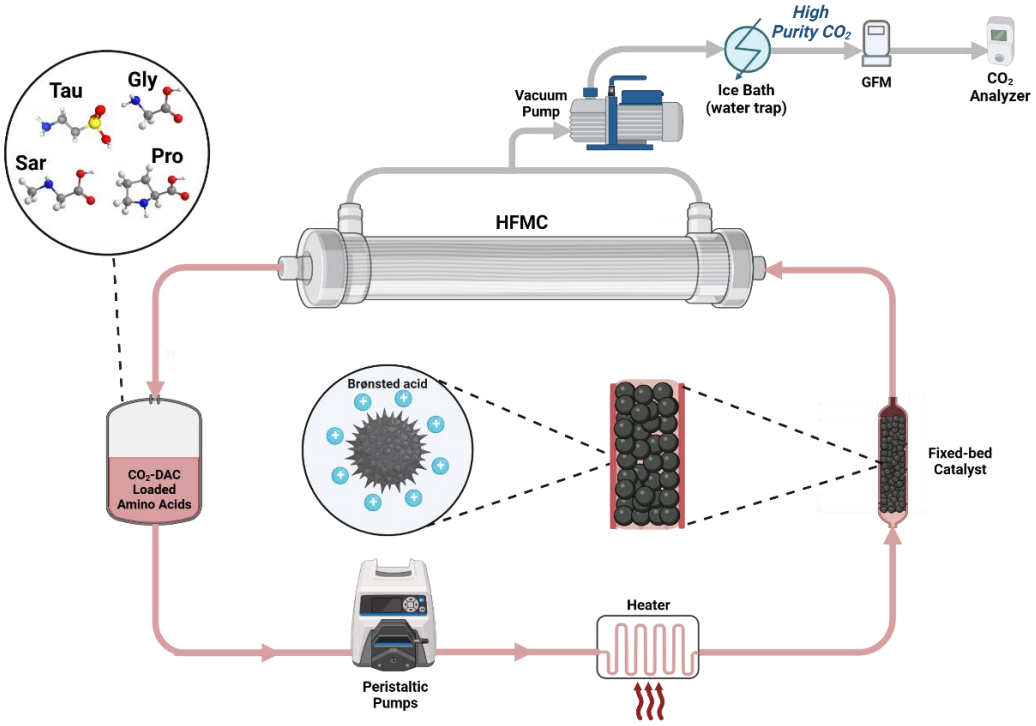

Scheme 3.2. Scheme of the C-MVR apparatus for DAC.

To evaluate the performance of CO_2 desorption in MVR trials, Equation 3.5 was used:

$$J_{CO_2}=\frac{N^{\circ}\times X_{CO_2}}{A} \tag{3.5}$$

where J_{CO2} (mol/m^2.s) is the CO_2 desorption flux, N° (mol/s) and X_{CO2} are the molar flow and CO_2 concentration of the outlet vacuum pump stream, respectively. A (m^2) is the effective surface area of the membrane.

To evaluate the water flux through the membrane, the liquid level in the solvent container was monitored during operation and compared to the water collected in acetone-ice-bath traps at the end of the experiment, which were in good agreement. Therefore, to calculate the water flux, Equation 3.6 was employed:

$$J_{water}=\frac{V}{A\Delta t} \quad (3.6)$$

where J_{water} (mol/m^2.s) is the water desorption flux, V (mol) is the collected water in the ice-bath trap, A (m^2) is the effective surface area of the membrane, and Δt (s) is the operational time frame.

For C-MVR tests, the CO_2 flux was calculated using Equation 3.5. To assess the enhancement of the acidic cation resins, Equation 3.7 was used:

$$CE=(J_{CO2_cat}- J_{CO2})/ J_{CO2}\times 100 \quad (3.7)$$

where CE (%) is the catalyst enhancement of the system, $J_{CO2\text{-}cat}$ and J_{CO2} (mol/m^2.s) are the CO_2 desorption flux with and without solid acid catalysts.

The thermal energy consumption (GJ/tCO_2) of the solvent in HFMC was evaluated using Equation 3.8:

$$Q=\eta(mc_p\Delta T)/(J_{CO2}M_wA\Delta t) \quad (3.8)$$

where m (kg) is the total mass of solvent in the system, c_p (kJ.kg^{-1}.°C^{-1}), and ΔT (°C) are the mass heat capacity and solvent temperature change, respectively, J_{CO2} (mol/m^2.s) is the recorded CO_2 flux, M_w (g.mol^{-1}) is the CO_2 molecular weight, A (m^2) and Δt (s) are membrane surface area and operation time. It is important to note 90% heat recovery (125-127), considering an efficient rich/lean heat exchanger and heat pump was assumed (η to be equal to 0.1). Additionally, for the calculated thermal energy consumption, an average operation time of 90 min was considered.

The relative heat duty (%) was calculated according to Equation 3.9:

$$RH = \frac{Q_{Cat}}{Q_{Blank}} \times 100 \quad (3.9)$$

where Q_{Cat} and Q_{Blank} are the thermal energy consumption (GJ/tCO_2) with and without catalyst, respectively.

3.2.2.3 Membrane Vacuum Regeneration for Chapter 6

An upscaled version of a previously developed MVR DAC system was employed in this study (124, 128). Design improvements were made to make the system compatible with larger commercial membrane modules and to enhance overall system performance, particularly in terms of CO_2 stripping, heating, water condensation, and hydraulics. A schematic of the system configurations is shown in **Figure 6.1a**. The DAC CO_2 saturated solvents (40, 128) were loaded into a 1 L stainless steel vessel and circulated through the system at 1.4 L/min using a chemically resistant magnetic drive pump (Micropump). The solvent was heated to a fixed regeneration temperature of 90 °C using an upgraded external oil bath. To monitor the pressure on the solvent side, a pressure gauge was installed at the inlet of the membrane module. A thermometer was also placed at the same location to monitor the solvent temperature at the membrane inlet. On the permeate side, a vacuum pump applied a low pressure (~ 2 $kPa_{(a)}$), and a gauge was installed to monitor vacuum pressure levels during operation. As the solvent heated and CO_2 and water vapor started transferring to the permeate side, the pressure gradually increased, reaching ~ 20 $kPa_{(a)}$. Two acetone-ice baths were used to condense water vapor on the permeate side, enabling accurate measurement of the high-purity CO_2 stream. A CO_2 analyzer and a flow meter were installed at the outlet of the vacuum pump for detailed analysis. Notably, in all tests, the CO_2 stream purity was >99%.

For catalytic trials, a fixed bed was placed upstream of the HFMC. After heating the solvent, it passed through the catalyst bed before entering the membrane module. All experimental runs were conducted for a duration of 30 minutes.

To calculate the CO_2 flux passing through the fibers in the membrane modules, Equation 3.10 was used:

$$J_{CO_2}=\frac{M^{\circ}\times x_{CO_2}}{A} \tag{3.10}$$

where J_{CO2} (mol/m^2.s) is the CO_2 desorption flux, M° (mol/s) is the molar flow rate of the high-purity CO_2 stream at the outlet of the vacuum pump, and x_{CO2} is CO_2 mole fraction. A (m^2) is the membrane surface area.

The total amount of CO_2 desorbed during operation, M_{total_CO2} (mol), was determined by integrating the flux profile over the duration of the process (Equation 3.11), where t is the operation time.

$$M_{total_CO_2}=\int J_{CO_2}dt \tag{3.11}$$

To determine the water flux over the 30 minutes of operation, the collected water was accurately measured before being returned to the solvent container. Based on this measurement, Equation 3.12 was used to calculate the water flux.

$$J_{H_2O}=\frac{N}{A\Delta t} \tag{3.12}$$

where J_{H2O} (mol/m^2.s) is the water desorption flux, N (mol) is the amount of water collected, A (m^2) is the surface area of the membrane, and Δt (s) is the duration of experiment.

To evaluate the enhancement of the synthesized catalysts and enhancement factor, Equations 3.13 and 3.14 were employed, respectively.

$$CE= (M_{total_CO2_cat} - M_{total_CO2})/ M_{total_CO2} \tag{3.13}$$

$$\text{Enhancement Factor} = \frac{CE}{W_{cat}} \tag{3.14}$$

where CE (%) is the catalyst enhancement, $M_{total_CO2_cat}$ and M_{total_CO2} (mol) are the total CO_2 desorbed in 30 minutes with and without the presence of synthesized catalysts, respectively. W_{cat} is the catalyst concentration (wt.%).

To estimate the thermal energy consumption (GJ/tCO_2) of the system Equation 3.15 was used:

$$Q = \frac{mc_p\Delta T}{M_{total_CO_2}M_w A} \tag{3.15}$$

Q (GJ/tCO_2) is the thermal energy consumption, m (kg) represents the total mass of the solvent in the system, while c_p (kJ/kg.°C), and ΔT (°C) refer to specific heat capacity and the temperature change of the solvent, respectively. M_w (g/mol) is the molecular weight of CO_2, and A (m^2) is membrane surface area. It is also important to note that a thermal approach temperature of 20 K was considered due to the integration of energy in a rich/lean heat exchanger (129, 130).

The relative heat duty, RH (%), was calculated using Equation 3.16 (43):

$$RH = \frac{Q_{Cat}}{Q_{Blank}} \times 100 \tag{3.16}$$

Q_{Cat} and Q_{Blank} are thermal energy consumption (GJ/tCO_2) with and without catalyst, respectively.

3.3 OptiMaxTM workstation 1001 (Mettler-Toledo)

The set up consists of different sections as shown below:

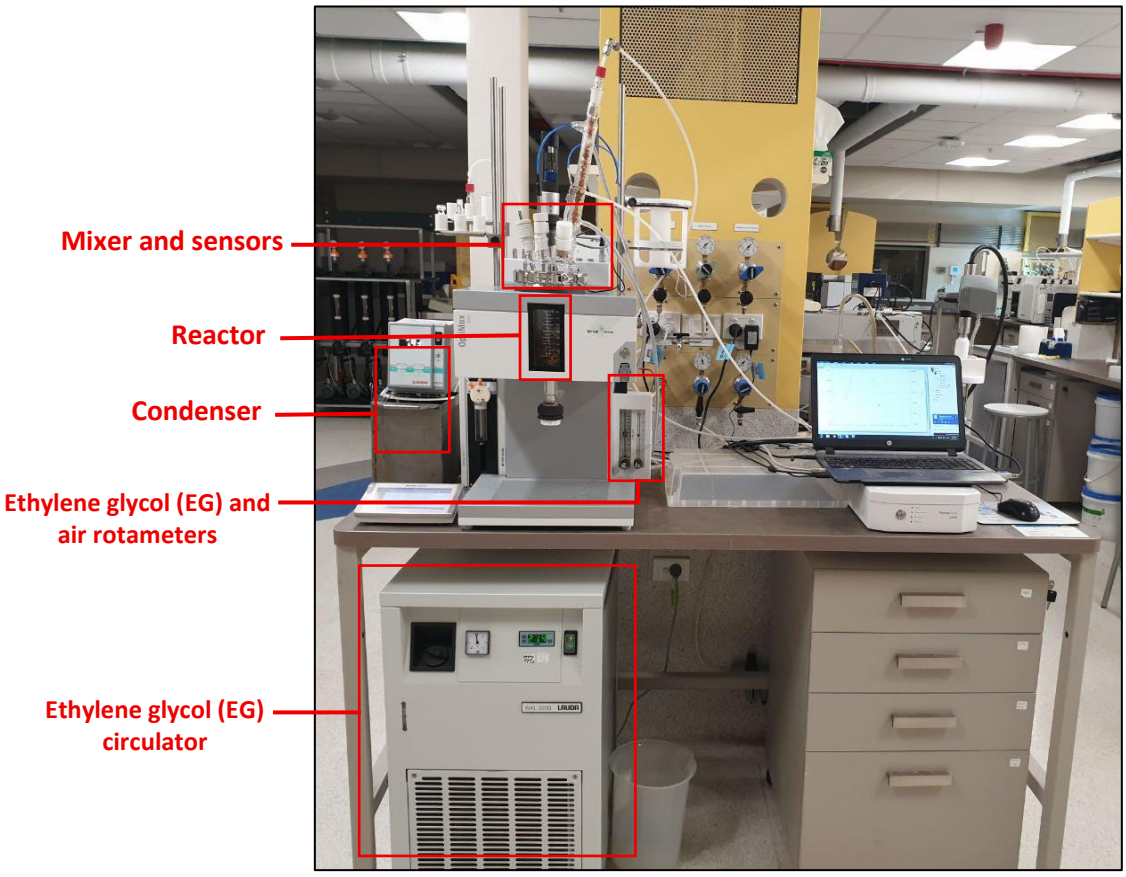

Scheme 3.3. Photograph of the OptiMax^{TM} workstation 1001 (Mettler-Toledo)

The schematic diagram of the apparatus is shown in **Scheme 3.4**.

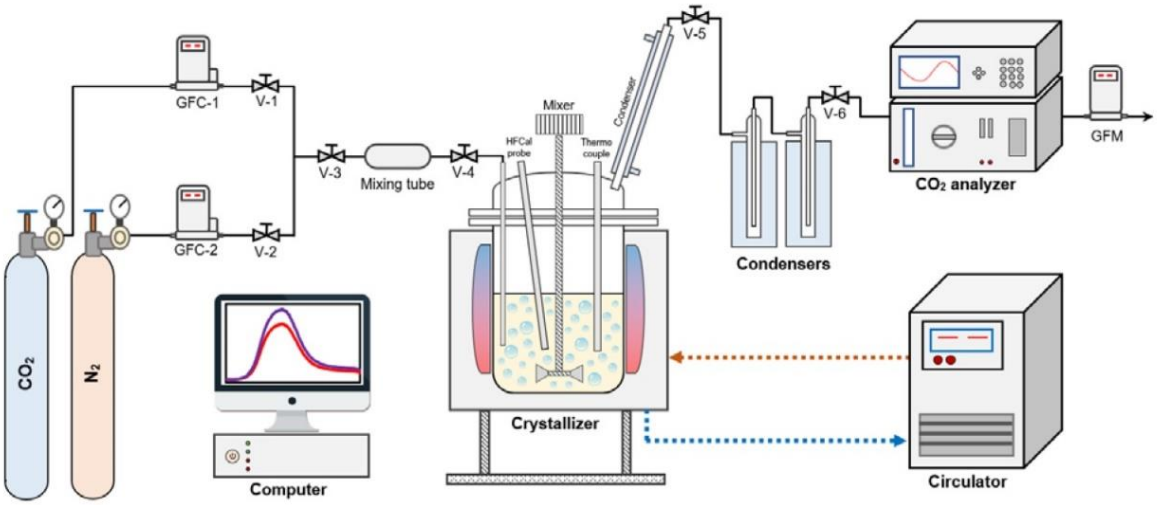

Scheme 3.4. Schematic diagram of the CO_2 desorption apparatus operating at 88-98 °C; reused with permission (34)

The setup featured a 1000 mL reactor, an adjustable mixer to maintain solution homogeneity, and a temperature control system comprising a thermocouple and a heating jacket, enabling precise regulation of the reactor's operating temperature and accurate measurement of heat transfer parameters. For solvent regeneration trials, 500 mL CO_2-saturated amino acid solutions were placed in the reactor. The regeneration process sequence was as follows:

- Keep the solution temperature at 25 °C
- Start to increase the temperature to 98 °C
- Keep the temperature at 98 °C for 90 min
- Return the temperature to 25 °C

N_2 flowing at 0.3 L/min, served as the carrier gas to dilute and direct the desorbed CO_2 to an online CO_2 analyzer (BlueSens, BCP-CO_2). To remove any residual moisture from the CO_2 stream, two acetone-ice bath condensers were used.

The desorption performance of each amino acid was evaluated and monitored in this apparatus, and an example of results are shown in **Figure 3.1**.

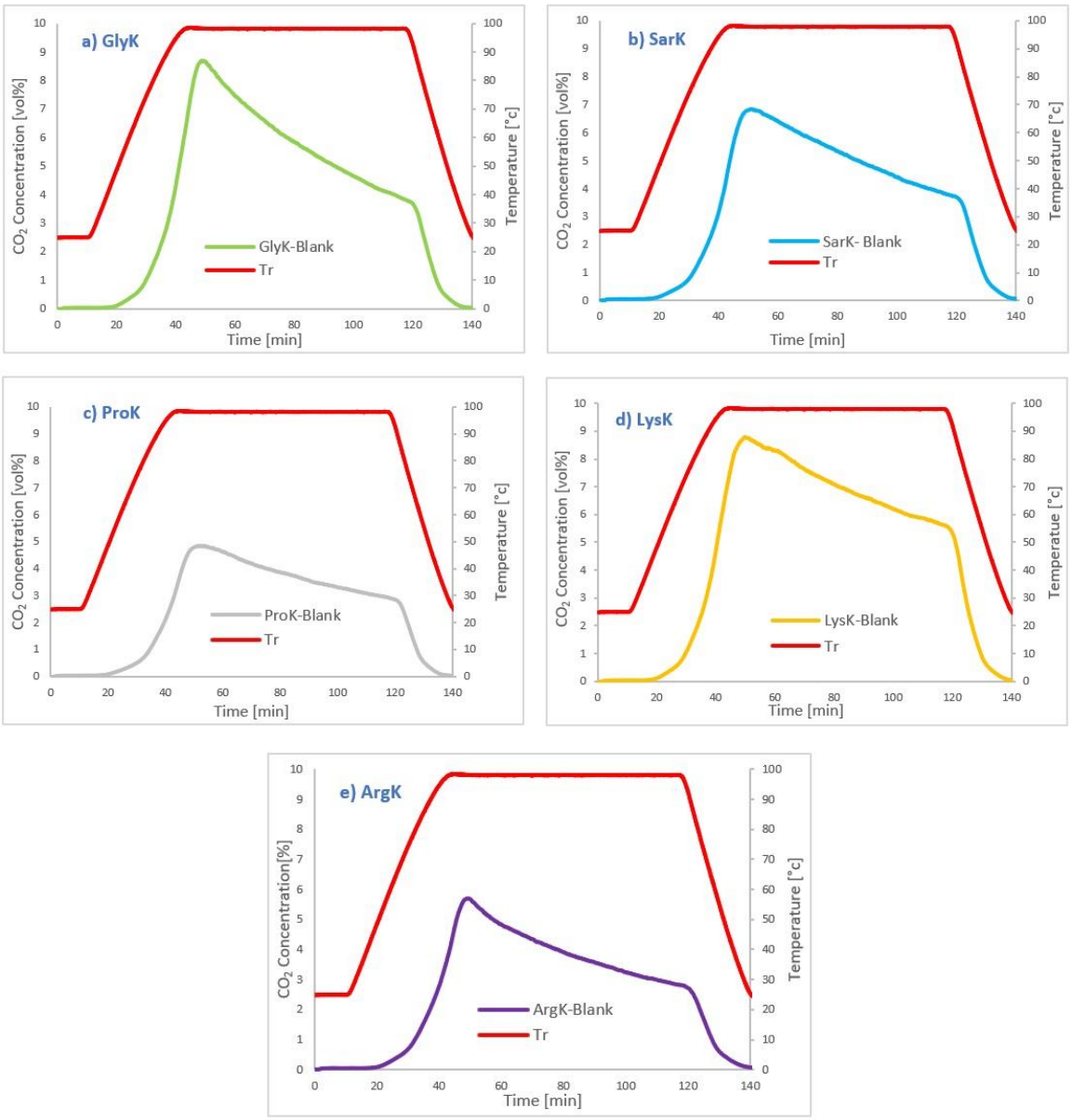

Figure 3.1. Desorption CO_2 profile of various amino acids, a) potassium glycinate (GlyK), b) potassium sarcosinate (SarK), c) potassium prolinate (ProK), d) potassium lysinate (LysK), and e) potassium argininate (ArgK) solutions.

To quantitatively evaluate the desorption performance of each amino acid, the area beneath the curves of **Figure 3.1** (represented as the number of CO_2 moles that were released from the solution throughout the regeneration process) was calculated. In this regard, using Equation 3.17 and 3.18, the amount of CO_2 released at specified time intervals was calculated (34, 103):

$$n_{CO_2} = \frac{X_{CO_2}}{1\text{-}X_{CO_2}} n_{N_2} \quad (3.17)$$

$$N_{CO_2} = \int_0^t n_{CO_2}\, dt \quad (3.18)$$

where X_{CO2} is the volume fraction of CO_2 in dilute mixture flow of CO_2/N_2 analyzed by the CO_2 sensor (data on vertical axis of **Figure 3.1**), n_{CO2} (mol/min) is the outlet flow rate of CO_2, n_{N2} (mol/min) is the inlet pure N_2 flow rate, t (min) is the time length of the solvent desorption process, and N_{CO2} is the total number of CO_2 moles desorbed during the solvent regeneration procedure.

3.4 Chittick Apparatus

A Schematic of the Chittick apparatus is illustrated in **Scheme 3.5**. A sample of known volume (2ml) with an indicator, methyl orange, was mixed in a flask (B). The flask was put on the magnetic stirrer and connected and sealed to one side of a long U-Tube manometer while the other side (fluid reservoir) was left open to atmosphere (D). 0.4 M of sulfuric acid (A) was then added dropwise from a 50 ml titration burette (A) to the sample until a color change was observed. The released CO_2 from the sample can be determined through the displacement of the fluid in the tube (C). To calculate the CO_2 loading of amino acid solutions (mol/mol), Equation 3.19 was used:

$$CO_2 \text{ Loading } (^{mol}/_{mol}) = \frac{\frac{P[(G_f - G_i) - (A_f - A_i)]}{RT}}{V_{sample} C_{sample}} \quad (3.19)$$

where T and P, are the experimental temperature (K) and pressure (kPa), R is the universal gas constant (L kPa/mol K), G_i and G_f are the levels of the displacement solution before and after adding acid (L), A_i and A_f are the levels of acid before and after titration (L), V_{sample} is the sample volume (L), and C_{sample} is the amino acid concentration (mol/L).

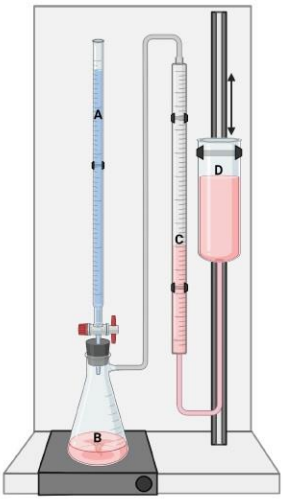

Scheme 3.5. Schematic illustration of the Chittick apparatus used for measuring the CO_2 loading of aqueous solution.

3.5 Characterization Methods

3.5.1 Fourier Transform Infrared (FTIR)

Fourier Transform Infrared Spectroscopy (FTIR) ATR was collected using Bruker TESNOR II. Each spectrum was obtained by averaging 64 scans across the wavenumber range of 400-4000 cm^{-1}, with a resolution of 4 cm^{-1}.

3.5.2 X-ray Photoelectron Spectroscopy (XPS)

X-ray Photoelectron Spectroscopy (XPS) analysis was performed using a Thermo Scientific K-alpha instrument equipped with a monochromated aluminum Kα source (1486.7 eV). The X-ray anode was operated at 220 W (22 mA, 10 kV) with a detection angle of 45°, while the chamber pressure was maintained below 8.0×10^{-9} mbar. A low-energy flood gun was utilized to mitigate surface charging effects. Broad survey scans and high-resolution scans were recorded with energy resolutions of 1.0 eV and 0.05 eV, respectively. Data analysis was conducted using CasaXPS software, with energy calibration performed by referencing the C 1s peak at 285.0 eV.

3.5.3 Elemental Analysis

CHNS was performed using Perkin Elmer 2400 Series II.

3.5.4 Scanning Electron Microscopy (SEM)

Scanning Electron Microscopy (SEM) was conducted using a FEI Nova NanoSEM 200, an ultra-high-resolution (UHR) SEM equipped with a Field Emission Gun (FEG). The system's combination of low vacuum mode and an ultra-stable source ensured high-quality imaging. UHR imaging was performed using a Through Lens Detector (TLD), with a spot size of 3.5 and an accelerating voltage below 10 kV. The instrument operated in immersion mode, utilizing the entire chamber as an objective lens to immerse the sample in a magnetic field for enhanced resolution. To prevent charging effects, samples were coated with a 1 nm iridium layer using the Leica EM ACE600 Sputter Coater prior to imaging.

3.5.5 Transmission Election Microscopy (TEM)

High-resolution transmission electron microscopy (TEM) and energy-dispersive X-ray spectroscopy (EDX) mapping were conducted with a JEOL JEM-F200 equipped with oxford EDX detector. To prepare TEM samples, the materials were first dispersed in ethanol to create a 0.01 wt.% solution. A single droplet of this dispersion was then deposited onto a formvar carbon-coated copper TEM grid and used for imaging.

3.5.6 Nuclear Magnetic Resonance (NMR) Spectroscopy

The species formed in the liquid after CO_2 absorption were identified using ^{13}C-NMR spectroscopy. The ^{13}C-NMR spectra were collected on a Bruker Advance NEO 500 MHz NMR Spectrometer with SampleJet. For sample preparation, D_2O was mixed with liquid samples, with each NMR tube containing 600 µL of sample and 100 µL of the D_2O. The ^{13}C-NMR analysis was conducted with a delay time of 20 seconds and 256 scans. Peak analysis was

performed using Bruker TopSpin software. The concentration of the chemical species formed was determined by calculating the area under the corresponding ^{13}C-NMR peaks.

3.5.7 Ammonia and CO_2 Temperature Programmed Desorption (TPD) Technique

NH_3-TPD and CO_2-TPD analyses were conducted using a Micromeritics AutoChem II 2920 chemisorption analyzer.

3.6 Materials

Amino acid salts with unique acidic and basic properties, namely glycine (Gly), L-lysine hydrochloride (Lys), sarcosine (Sar), and L-proline (Pro), histidine (His), L-arginine (Arg), purities over 98% were purchased from Sigma Aldrich. Taurine (Tau) was supplied by Consolidated Chemical Co., Australia (99.5% purity). Zirconium sulfate tetrahydrate ($Zr(SO_4)_2.4H_2O$) was obtained from Shanghai Minstar Chemical Co., Ltd, China. Potassium hydroxide (KOH, >85.0% purity) was purchased from Chem-Supply, Australia. A nitrogen gas cylinder (N_2, 99.9%) was purchased from BOC Gases Company, Australia. Sulfuric acid (H_2SO_4, 98.5%) was purchased from Chem-Supply, Australia. Iron (III) nitrate nonahydrate ($Fe(NO_3)_3.9H_2O$, >98%) was purchased from Sigma Aldrich. Ultra-pure water (Elix Millipore, resistivity >18.2 MΩ·cm) was utilized for all experiments.

3.7 Hollow Fiber Membrane Contactors (HFMCs)

3.7.1 Used HFMC for Chapter 4

A commercial non-porous PDMS HFMC (Permselect-MedArray, Ann Arbor, Michigan, USA) was selected and utilized. The non-porous (dense) hydrophobic PDMS has a high level of resistance to pore wetting, a critical factor when applying HFMCs, especially under high temperature operation. This guarantees a flexible and stable operation in the long-term, as well as minimizes solvent loss (84). Moreover, the PDMS exhibits suitable thermal and chemical stability which is important when considering long-term operation (131). The module consists of 30,000 number of fibers that offer a contact area of 2.1 m^2 and is operated in a counter-current parallel flow configuration. **Table 3.1** lists the details of the membrane modules used.

Table 3.1. Specification of the applied HFMC

Supplier	PermSelect
Membrane Material	PDMS (Silicone)
Module Diameter	8.9 cm
Module Length	14.2 cm
Fiber ID	190 µm
Fiber OD	300 µm
Fiber Wall Thickness	55 µm
Effective Fiber Length	7.4 cm
Number of Fibers	30,000
Membrane Area (based on fiber OD)	2.1 m^2

3.7.2 Used HFMCs for Chapter 5

For this chapter, three commercial membrane modules (**Figure A.8.**) fabricated with different materials and structures were assessed and compared for their CO_2 transfer mechanisms (i.e., membrane distillation and pervaporation) and rates in DAC operation. **Table 3.2** shows the detailed specifications of the used HFMCs. Notably, for $HFMC_2$ and $HFMC_3$ the solvent was operated on the shell side whilst for $HFMC_1$ it was on the lumen side due to the large volume of the shell side.

Table 3.2. Specifications of three commercial HFMCs

HFMCs	$HFMC_1$	$HFMC_2$	$HFMC_3$
Membrane type and material	porous PTFE	Dense PDMS	Ultra-thin PDMS composite
Module diameter	5.0 cm	6.0 cm	1.27 cm
Module length	80 cm	14 cm	30 cm
Effective fiber length	57.5 cm	8.4 cm	20 cm
Number of fibers	240	12,600	160
Fiber ID	0.8 mm	0.19 mm	0.1 mm
Fiber OD	1.57 mm	0.3 mm	0.374 mm
PDMS wall thickness	-	55 μm	0.9-1.2 μm
Membrane area (based on fiber OD)	0.68 m^2	1.0 m^2	0.0376 m^2

3.7.3 Used HFMCs for Chapter 6

Three commercial polypropylene (PP) HFMCs were obtained, and their CO_2 stripping performance were evaluated in the MVR DAC unit. The modules differ in pore size distribution, structural configuration, and surface modifications, all of which can influence mass transfer and wetting resistance. Detailed specifications are provided in **Table 3.3**.

Table 3.3. Specifications of three commercial HFMCs

HFMCs	$HFMC_1$	$HFMC_2$	$HFMC_3$
Membrane type and material	Porous PP	Porous PP+PDMS layer	Porous PP
Module length/dimeter (cm)		53.4/10 (all three modules)	
Effective fiber length (cm)	28	28	28
Number of fibers	1735	1800	4540
Fiber ID/OD (μm)	515/705	515/705	240/360
Pore size max (μm)	0.17	0.17	0.10
PDMS layer thickness (μm)	-	3-5	-
Membrane area (based on fiber OD)	1.1 m^2	1.1 m^2	1.4 m^2

3.8 Materials Preparation

3.8.1 Amino Acid Salt Solution Preparation

Solutions of potassium taurinate (TauK), potassium glycinate (GlyK), potassium sarcosinate (SarK), potassium prolinate (ProK), Potassium lysinate (LysK), Potassium argininate (ArgK), and potassium histidine (HisK) were prepared by dissolving the respective amino acids in Milli-Q water with an equimolar quantity of KOH. Only for potassium lysinate (LysK) solution, Lys was dissolved in Milli-Q water with two molar equivalents of KOH (one molar excess to neutralize HCl in lysine hydrochloride).

3.8.2 Synthesis Procedure of Acidic Silica and Alumina

A wet impregnation method, adapted from a previously reported procedure (45), with minor modifications, was used to synthesize the composite solid acid catalysts (Fe-SZ/SiO_2 and Fe-SZ/Al_2O_3); a schematic synthesis procedure is shown in **Figure 6.2a**. An aqueous solution of metal salts with a total concentration of 2.0 mol/L was first prepared by dissolving the desired amounts of $Fe(NO_3)_3 \cdot 9H_2O$ and $Zr(SO_4)_2 \cdot 4H_2O$ in deionized water. The solution was vigorously stirred and maintained at 60 °C for 2 hours. Afterward, the solution was cooled to room temperature (~25 °C). Mesoporous supports (either SiO_2 or Al_2O_3) were then added to Schott bottles containing the metal salt solution and mixed for 14 hours. Subsequently, the mixture was treated with ultrasonication for 30 minutes. The solid phase was separated by filtration, dried at 120 °C overnight, and then calcined in air at 500 °C for 5 hours. The final catalysts were labeled as Fe-SZ/SiO_2 or Fe-SZ/Al_2O_3. Depending on the SZ/support weight ratio (1/2, 1/1, or 2/1), these ratios were used as postfixes in the labeling, resulting in labels such as Fe-SZ/SiO_2(1/2), Fe-SZ/SiO_2(1/1), and Fe-SZ/SiO_2(2/1).

CHAPTER 4

Direct Air Capture of CO_2 Using Green Amino Acids

The chapter has resulted in the following publication:

Momeni A, McQuillan RV, Alivand MS, Zavabeti A, Stevens GW, Mumford KA. Direct air capture of CO_2 using green amino acid salts. Chemical Engineering Journal. 2024;480:147934.

4.1 Introduction

The adverse implications arising from the escalating global emissions of carbon dioxide (CO_2) have evolved into a major point of concern (1). For the first time in recorded human history, the atmospheric CO_2 concentration has exceeded 420 parts per million, marking a momentous rise of nearly 50% since the onset of the Industrial Revolution (280 ppm)(2). As a consequence of this significant rise, the average atmospheric temperature has experienced an approximate 1 °C increase. The primary objective of the Paris Agreement is to set a target of limiting global warming to 2 °C, with a more ambitious goal of possibly reaching 1.5 °C by the end of the 21st century (3). To accomplish this objective, in addition to significantly reducing human-caused greenhouse gas (GHG) emissions, it is imperative to take sustainable measures for actively removing carbon dioxide (CO_2) through the implementation of Negative Emissions Technologies (NETs) (4). Among the NETs, CO_2 direct air capture (DAC) has gained growing attention as a viable approach for mitigating climate change popularized by Lackner in 1999 (5). The viability of DAC operation can be attributed to high capacity, adaptable placement options, and the production of high-purity CO_2 streams. In this approach, ultra diluted CO_2 concentration (~415 ppm) in the atmosphere can be directly captured. Two approaches are considered most promising, adsorption, or absorption (6, 7). Currently, most studies are focused on solid sorbents (Global Thermostat and Climeworks (8)) while limited research and development is occurring in the domain of chemical absorption using well-known liquid sorbents in this field e.g., amine-based solvents. Furthermore, amine-based solvent absorption is undoubtedly one of the most reliable operations of CO_2 mitigation processes and has been used in a large fraction of industrial applications (9, 10). Hence, by prioritizing research and development efforts in this area, valuable knowledge acquired from these successfully implemented large-scale plants can be effectively utilized in the specification of DAC technologies, facilitating its smooth transfer and application. Among the different types of

amine-based solvents, amino acid salts are known to be a promising selection for DAC operation, owing to their unique physical and chemical features such as fast reaction rate, low volatility, low toxicity, and strong resistance to oxygen degradation (11, 12). Nevertheless, since the adoption of liquid sorbents in DAC is an emerging technology, there are number of challenges that need to be addressed to achieve widespread utilization at large scale. One of the main obstacles is the requirement of introducing a large amounts of air into the system due to the low concentration of CO_2 in the ambient air, which leads to low ratios of solvent to air flow rates (13). Additionally, typical regeneration processes require high operating temperatures near, 120-140 °C, which leads to high energy consumption (sensible heat plus latent heat). Consequently, these circumstances result in elevated operating costs and, more importantly, thermal degradation of the solvent (e.g., including amino acid salts which are suitable for DAC) (15, 16). Thus, prioritizing further research and development efforts in applying new technologies to address these challenges in DAC operation is of utmost importance.

Hollow fiber membrane contactors (HFMC) are a hybrid technology that benefits from the advantages of both solvent technology and membrane separation (17, 18). Their modular and compact design, flexibility in operation (different L/G ratios) due to a distinct and stable phase interface, large contact area and convenient scalability has made it a viable choice for DAC processes (19, 20). Additionally, by applying vacuum stripping, the operating temperature can be lowered below the solvent boiling point (<100 °C) which will considerably reduce the thermal degradation of aqueous solvents and facilitate use of solar energy for solvent regeneration (22, 23). Also, it will eliminate the necessity for steam in the process and the heating media can be altered to sustainable solar energy. There are vast quantities of work that analyze the absorption-desorption performance of aqueous solvents in different types of HFMCs (21, 84, 87). However, to the best of the author's knowledge, few studies have focused

on the application of this system in DAC-absorption processes, and none have investigated it for DAC-desorption.

Here, for the first time, the experimental and theoretical analysis of green amino acid salt sorbents in low temperature regeneration DAC operation are evaluated. Two DAC apparatuses, absorption and desorption, are designed and developed using commercial HFMCs, made of non-porous hydrophobic polydimethylsiloxane (PDMS). In the DAC-absorption section, the kinetics and equilibrium performance of five amino acid salts, potassium glycinate (GlyK), potassium lysinate (LysK), potassium sarcosinate (SarK), potassium prolinate (ProK), and potassium histidine (HisK) were examined in long-term operation (zero CO_2 solvent loading to completely saturated at DAC condition of 100%). As GlyK was found to be the most viable option for DAC operation, further long-term trials on important process parameters e.g., solvent temperature and concentration for the GlyK were conducted. For the low temperature DAC-desorption section, the kinetic performance analysis for the GlyK was accomplished at different solvent loadings for various operational conditions (solvent temperature and concentration, vacuum pressure, sweep gas effect). Finally, a validated DAC model with acquired absorption and desorption bench-scale data in Aspen Custom Modeler (ACM) was used to study the impact of membrane module characteristics on CO_2 separation efficiency. The findings of this study give deep insight into the operability and CO_2 absorption-desorption performance of green amino acid salt sorbent in a DAC operation, which is the start of a new path towards sustainable, cost-effective DAC.

4.2 Results and Discussion

4.2.1 DAC-Absorption

To better understand and optimize the performance of the developed system, an initial parametric analysis was completed to assess the appropriate air and liquid flow rates. To do

this, fresh GlyK was used due to its desirable properties and similar CO_2 absorption performance to monoethanolamine (MEA), a benchmark sorbent for chemical absorption in CO_2 capture (76). According to **Figure A.1**, increasing the air flow from 7.2 L/min to 17.3 L/min, decreases the absorption efficiency by a considerable amount, ~58.5%. This can be attributed to several factors. As the air flow rate increases, two phenomena occur simultaneously with counteracting effects. The first is the enhancement of the mass transfer coefficient on the air side due to increased turbulence. The second is the decrease in retention time, which limits the mass transfer between the air and solvent phases, resulting in lower overall efficiency. The significant drop in overall efficiency indicates the dominance of the latter factor which can be related to the type of membrane and the distribution of resistances within the module. Hence, the 7.2 L/min air flow rate, which exhibits maximum efficiency and introduces an acceptable number of CO_2 moles to the system, was selected for use in all additional experiments.

In the next step, the variation of the solvent flow rate was also assessed. Flow rates were operated between 0.1 to 0.5 L/min and did not display a noticeable impact on the system behavior (data not shown). Within the investigated temperature range (10–30 °C), there was minimal change in the observed CO_2 flux and overall efficiency, further confirming that the membrane is mainly contributing to the mass transfer resistance (132).

4.2.1.1 Screening Amino Acid Salt Sorbents

As shown in **Figure 4.1a**, five amino acid salts with different structures (short chain and long chain) were selected and prepared to a concentration of 1 M to be tested in the DAC-absorption unit. In order to examine the DAC equilibrium points and the CO_2 absorption kinetics at different solvent loadings, the DAC-absorption apparatus was continuously operated for several days until solvent saturation point was reached. **Figure 4.1c** shows the resulting DAC

equilibrium points of the varying amino acid salts acquired at 20 °C. The collected data was compared with the data obtained at 25 °C from the rising-bubble setup in our recent study (40). The strong agreement between these datasets provides compelling evidence for the reliability and precision of the data obtained through membrane technology, which holds the potential for large-scale utilization. According to **Figure 4.1c**, LysK has the highest DAC CO_2 loading capacity of 0.64 mol/mol (mol CO_2/mol solvent), attributed to its long-chain structure containing two amino groups that enable enhanced CO_2 absorption capacity. Among the short-chain solvents, ProK, SarK, GlyK, and HisK exhibit smaller values of 0.44, 0.39, 0.36, and 0.29 mol/mol, respectively. HisK demonstrated the lowest value of 0.29 despite having more amine functional groups in its structure compared to other short-chain amino acid salts. This could be attributed to the observed precipitation during operation, and the behavior and reaction of the specific amine groups to extremely low concentrations of CO_2 in the atmosphere.

By comparing the difference between the amount of CO_2 in the inlet and outlet air, as well as measuring the solvent CO_2 loading at regular intervals, a consistent evaluation of the CO_2 DAC-absorption performance at various solvent loadings was accomplished. **Figure 4.1b** shows the GlyK absorption performance at different solvent loadings at 20 °C. At experiment commencement, when the solvent was fresh, the absorption efficiency was 41%. A minimal loss (~6%) in CO_2 uptake was observed throughout a substantial portion of the operating period up to a solvent loading of 0.29 mol/mol (80% CO_2 loaded solution). This is related to the non-porous characteristics of the membrane, which prevent pore-wetting and solvent entrainment, two major issues that hinder stable operation. This is also related to the shape of the vapor liquid equilibria (VLE) curves of 1 M GlyK (133). A decline in absorption performance occurred when the solvent loading reached 0.29 mol/mol, caused by the solvent approaching its equilibrium point. This trial with GlyK was repeated three times to assess the repeatability of the DAC-absorption rig (**Figure A.2**), a factor which was found to be compelling.

Long-term analyses were also conducted for LysK, ProK, SarK, and HisK at 20 °C (**Figure A.3**). **Figure 4.1d** illustrates the CO_2 absorption efficiency data for all five amino acid salts at various levels of loading, extracted from **Figure A.3**. Among the fresh solvents, ProK showed the highest CO_2 uptake rate with 43%, and in contrast, LysK was the lowest with 37%. GlyK, SarK, and HisK exhibited the same efficiency value of 41%. This similarity can be related to ultra-low CO_2 concentration in air and also the resistance of the thick (55 μm) non-porous PDMS layer of membrane, which governs the CO_2 mass transfer. Until reaching 80% solvent loading, all amino acid salts except HisK demonstrated stable CO_2 uptake with minimal losses ranging from 6 to 9 percent, which can be explained by the VLE curves of the amino acid salts (133) and hydrophobic characteristics of the dense membrane layer. HisK, on the other hand, exhibited a dramatic loss in performance in CO_2 capture, likely due to the observed precipitation during operation. Importantly, it is observed that ProK, LysK, and GlyK maintained an efficiency of around 30% in absorbing CO_2 even up to a 90% CO_2 loading level. This highlights the capability of the hybrid technology of amino acid salts and HFMCs to utilize the maximum capacity of the solvent in DAC-absorption. Hence, ProK, LysK, and GlyK were chosen as the desired amino acid salt solutions for DAC-absorption due to their favorable kinetic performance under different solvent loading conditions.

Another important factor to consider when selecting an appropriate solvent is the cyclic capacity, which determines the sorbent's ability to effectively capture and release CO_2 during absorption-desorption cycles in a continuous process. Based on our recent study (40), the cyclic capacity of ProK, LysK, and GlyK in DAC operation was recorded at various temperature ranges (25-70 °C, 25-85 °C, and 25-98 °C); LysK and GlyK stood out as the top sorbent in terms of cyclic capacity across all temperature ranges. Hence, the selection was narrowed down to these solvents. Upon comparing these two, GlyK was chosen for further analysis due to its superior desorption kinetics (40), easier preparation as aqueous solvent, and its acceptable

cyclic capacity range. It is worth mentioning that LysK exhibited challenges in dissolving within water for aqueous solvent preparation for higher molarities, notably at a concentration of 3M (**Figure A.4**). This issue can be related to the long-chain structure and high molecular weight of L-lysine, which lowers its solubility and poses challenges in achieving dissolution at higher concentrations.

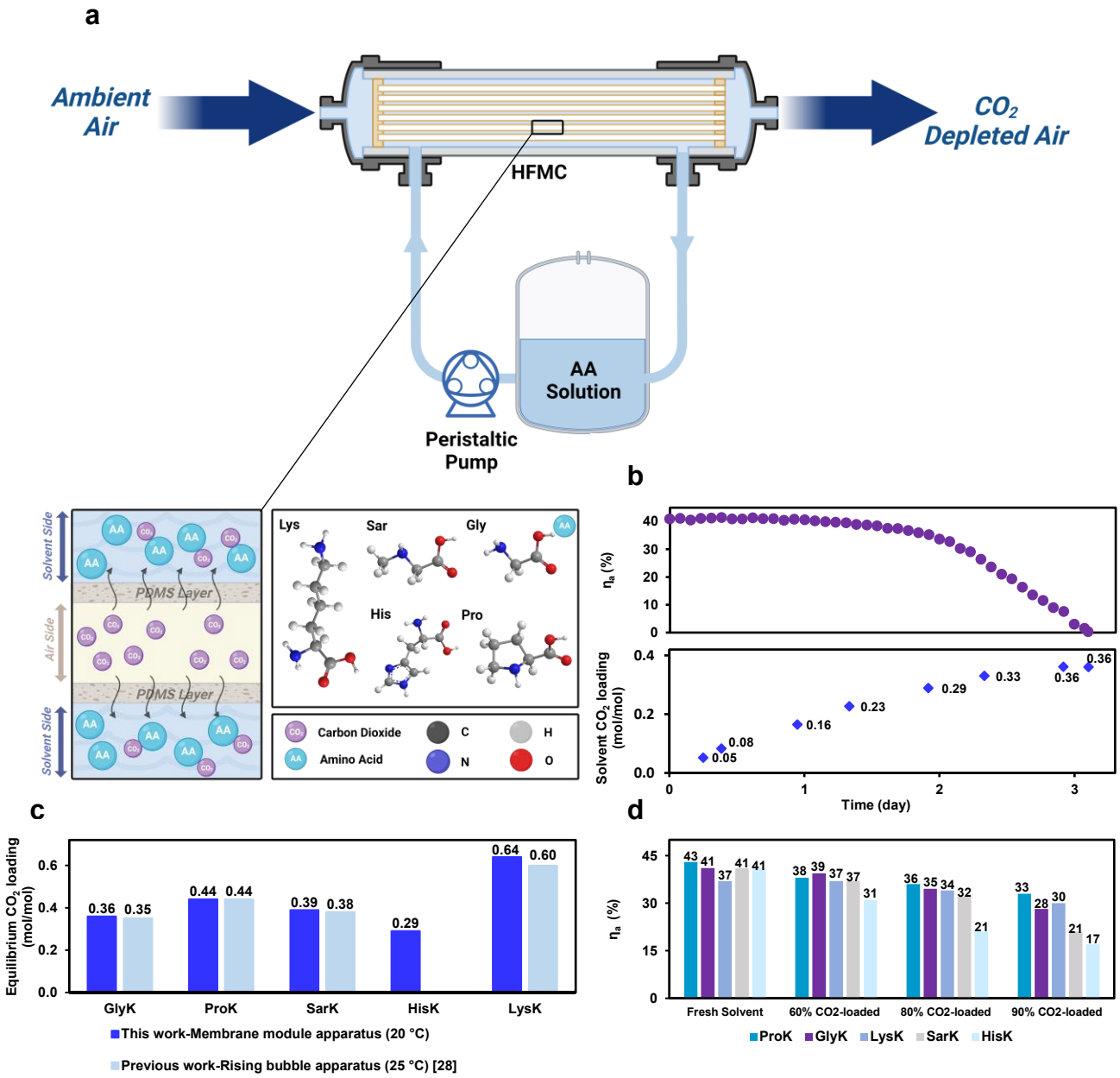

Figure 4.1. a) Schematic diagram of DAC-absorption using HFMC, absorption mechanism, and amino acid salts structures b) Absorption efficiency (η_a) of 1 M GlyK in a long-term operation at different solvent loadings. c) The DAC-equilibrium CO_2 loading points for different amino acid salt solutions and the comparison with previously obtained DAC-equilibrium data (40). d) Absorption efficiency (η_a) of 1 M of different amino acid salt solutions at various solvent loadings. All data were obtained at 20 °C, air flow rate = 7.2 L/min, and solvent flow rate = 0.25 L/min.

4.2.1.2 Solvent Temperature

To gain insight into how temperature affects equilibrium and the kinetics of CO_2 absorption at different loading levels, the DAC-absorption rig was run continuously with GlyK over several

days at three distinct temperatures (10, 20, 30 °C). **Figure 4.2a** depicts the equilibrium points obtained at three different temperature levels. As the temperature rises, the solubility of CO_2 in the solvent decreases, resulting in lower equilibrium solvent capacity. Another important factor is the water transfer through the membrane at different temperatures. Since the system has a relatively low RH feed air, the transfer of water from the liquid side to the air side was expected. In **Figure 4.2a**, average values of the RH in the air outlet during operation at the three different temperatures are presented. As the temperature increased, the water partial pressure on the liquid side increased, reinforcing the transfer of water across the membrane and leading to higher recorded values of RH outlet. The rise in temperature from 10 °C to 30 °C resulted in an increase in the average RH at the outlet from 40% to a nearly saturated state (150% increase), thereby emphasizing the impact of the solvent temperature.

Figure 4.2c displays the CO_2 absorption flux at three different temperatures under various solvent loading conditions. Upon Comparing the data for 10 °C and 20 °C, no major change was observed, which can be attributed to the dominance of the dense layer of the membrane, which acts as the primary resistance for CO_2 transfer. At higher loading levels, the flux at 10 °C outperformed the flux at 20 °C, related to the higher saturation point of GlyK at 10 °C (**Figure 4.2c**). Interestingly, when operating at 30 °C, a major reduction in performance was recorded across all solvent loading values. Typically, one would expect an increase in the mass transfer coefficient and flux with an increase in temperature due to the accelerated reaction rate in the solvent boundary layer and a decrease in solution viscosity. However, in this case, since the membrane phase dominates the mass transfer, and also there is a decrease in absorptive capacity, the enhanced effects resulting from increased temperature were not observed. Therefore, based on the results, 20 °C is deemed optimal for DAC-absorption using a non-porous membrane module, as it provides acceptable solvent capacity, kinetic performance, and energy demand input.

4.2.1.3 Solvent Concentration

To examine the impact of solvent concentration on CO_2 uptake capacity, kinetics, and any potential precipitation and operational issues across various solvent loadings, two sets of long-term trials were conducted using 2 M and 3 M GlyK. **Figure A.5** depicts the CO_2 absorption flux for GlyK 1 M, 2 M, and 3 M versus solvent CO_2-loading. As it is shown, no major change was achieved by increasing the solvent concentration at different levels of solvent loading. This behavior can be related to several factors, including the simultaneous two-fold effect, one being decreased CO_2 diffusivity in solvent (due to increased solvent viscosity) and the other being an increased mass transfer coefficient. Also, the presence of a dense PDMS layer, and the ultra-low concentration of CO_2 in the air can reduce the impact of solvent concentration. On the other hand, according to **Figure 4.2b**, the CO_2 uptake capacity (CO_2 mol/solvent liter) for 2 M and 3 M substantially increased (doubled and tripled) as a result of the increased molarity. Since no operational problems or precipitation were observed throughout the operations and with similar kinetic performance, selecting a higher level of solvent concentration in DAC-absorption is advantageous due to a higher absorption capacity. This implies reduced use of solvent (at least halved) in the absorption-desorption cycles is possible, leading to lowering the size of the heating equipment and the associated energy requirements.

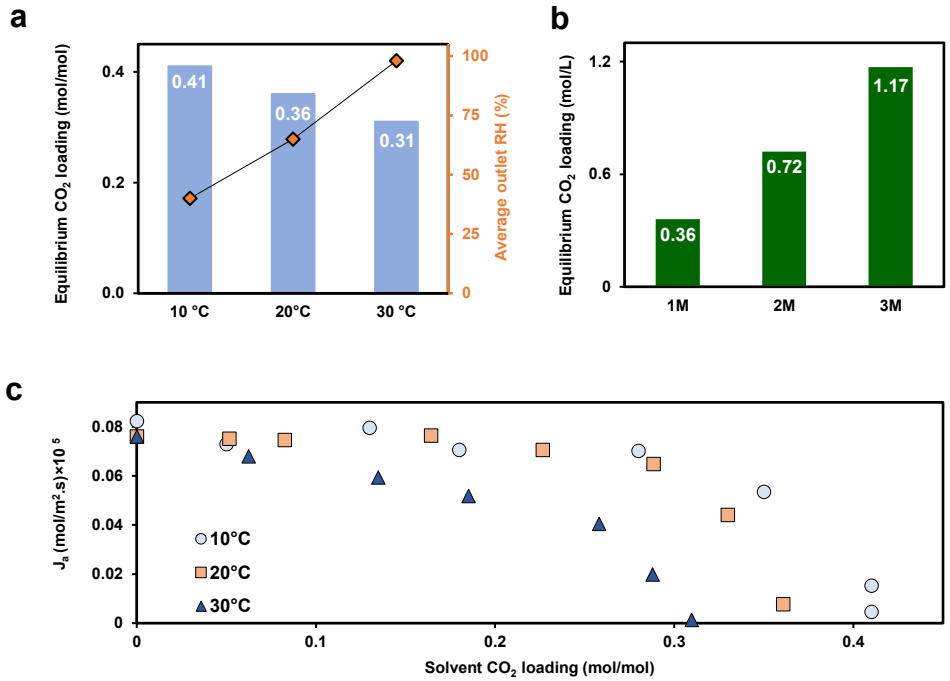

Figure 4.2. a) The DAC-equilibrium point and average outlet RH% for 1 M GlyK at different temperatures. b) The DAC-equilibrium point for different GlyK concentrations at 20 °C. c) The CO_2 absorption flux (J_a) of 1 M GlyK at different temperatures in various solvent loading conditions. All data was obtained at air flow rate = 7.2 L/min, and solvent flow rate = 0.25 L/min.

4.2.2 Low-Temperature DAC Regeneration

Due to the imperative role of low-temperature regeneration in DAC processes, regarding the capacity of the unit, thermal degradation of the solvent, and a major part of operating cost, a comprehensive study with various effective factors was completed to optimize the efficiency of the CO_2 stripping process.

As discussed in the absorption section, among the screened amino acid salt aqueous solutions, GlyK was chosen as it possesses favorable properties such as absorption kinetics, cyclic capacity, being less challenging in terms of operational problems and solution preparation for high molarities, and having a high desorption kinetics (40). Thus, the low temperature regeneration trials were conducted with an aqueous solution of the GlyK. All the stripping tests were accomplished under vacuum conditions (21-81 $kPa_{(a)}$) without sweep gas, with the exception of one trial used to investigate the effect of the sweep gas on performance. The

solvent flow rate was maintained at 0.25 L/min, equal to the absorption section. Each operation continued for 90 minutes to be able to observe the effect of solvent loading on CO_2 removal efficiency.

4.2.2.1 Solvent Temperature

Membrane contactor tests were performed within a temperature range of 70 to 90 °C under a vacuum pressure of 21 $kPa_{(a)}$, with the results presented in **Figure 4.3**. The schematic of the experimental DAC-desorption setup using HFMC is shown in **Figure 4.3a**. At the beginning of each trial, before applying vacuum pressure and as the solvent was preheated to the desired temperature, a sample was taken out of the system to measure the preheating effect on CO_2 removal (**Figure A.6a**). All the DAC CO_2-loaded GlyK solutions started with a similar level of CO_2 content, approximately 0.34-0.35 mol/mol. To assess the repeatability and accuracy of the DAC-desorption apparatus, three consecutive trials were carried out at 70 °C, and the results are plotted in **Figure A.6**, along with the temperature profile which showed good consistency. **Figure 4.3b** highlights the cyclic capacity of GlyK at various temperatures. Notably, as the temperature increased from 70 °C to 90 °C, there was an increase of over 75% in cyclic capacity and overall desorption efficiency. This indicates that each 10 °C can add 0.04 mol CO_2 per mol of solvent to the capacity of the system. Thus, increasing the temperature directly and positively impacts the stripping performance.

In **Figure 4.3c**, the desorption kinetics at different temperatures and solvent loadings are depicted. Comparing the CO_2 DAC-desorption flux with the acquired ones for DAC-absorption, the values are significantly higher because of the higher operating temperature, increased CO_2 driving force across the membrane and faster CO_2 diffusivity. Between 0.35 and 0.29 mol/mol (~80% CO_2-loaded), the highest kinetic rates were observed for all the temperature levels. This can be related to the higher CO_2 content in the solvent at the beginning

of the test, which increased the CO_2 driving force across the membrane. For loadings lower than 0.29 mol/mol, dramatic kinetic losses occurred at 70 °C. In this range, since the CO_2 desorption flux for 90 °C remained constant with the highest value, it suggests that the drop in the desorption performance for 70 °C and 80 °C is attributed to the thermodynamics of the solution and not a membrane-related issue (swelling or pore-wetting). In fact, working at higher temperatures led to higher equilibrium partial pressures of CO_2, chemical reaction equilibrium constants, diffusion coefficients, and reaction kinetics (133). For 80 °C and 90 °C, as the solvent loading fell below 0.25 and 0.23 mol/mol (65-70% CO_2-loaded), the average CO_2 flux declined and remained close to the kinetic values obtained for 70 °C, which highlights the effect of CO_2-laoding on stripping efficiency. Therefore, to be able to maintain the kinetic performance within a suitable range for a major part of the stripping operation, working above 0.23 mol/mol for 1 M GlyK is advantageous (~65% CO_2-loaded). In addition, this level of CO_2-loaded solvent allows for maximum and stable absorption performance in the DAC-absorption section (**Figure 4.1b, d**). It is worth mentioning that raising the temperature to a higher value of 90 °C allows for further reduction of the lean loading value and enhances stripping performance. However, due to the limitations of the apparatus, temperatures higher than 90 °C were not investigated. Considering the acceptable cyclic capacity, desorption efficiency, and the avoidance of potential operational issues, further experiments were conducted at 80 °C.

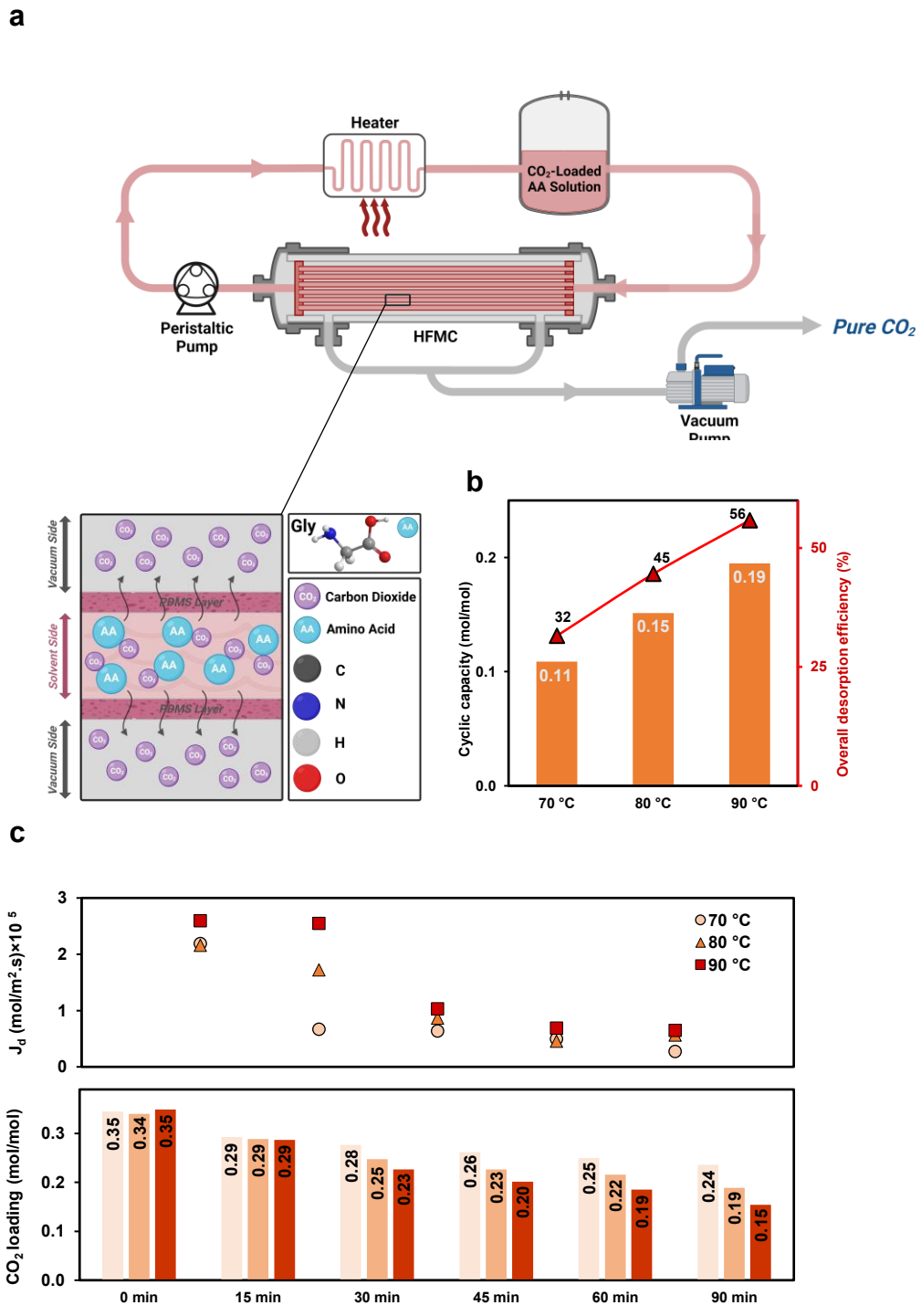

Figure 4.3. a) Schematic diagram of low-temperature DAC regeneration using HFMC, desorption mechanism, and Gly structure b) 1 M GlyK cyclic capacity and overall desorption efficiency at different regeneration temperatures. c) 1 M GlyK DAC-desorption flux (J_d) at different temperatures and solvent CO_2 loadings. All data were obtained at 21 $kPa_{(a)}$, and solvent flow rate = 0.25 L/min.

4.2.2.2 Vacuum Pressure

Experiments were conducted at 80°C under various vacuum pressures, 21-81 $kPa_{(a)}$, applied to the shell side of HFMC, and the impact on desorption efficiency was assessed. Interestingly, according to **Figure 4.4a**, a pronounced improvement was observed with a 60 kPa change in vacuum pressure, resulting in a 221% enhancement in overall desorption efficiency. The favorable effect of the vacuum is explained by the decreased CO_2 partial pressure on the shell side, which increased the mass transfer driving force for CO_2 desorption. Additionally, the reduced pressure on the permeate side of the membrane endured at higher vacuum levels, enhanced the driving force for CO_2 desorption.

Figure 4.4b, presents the desorption kinetics at three levels of vacuum pressure, 21, 51, and 81 $kPa_{(a)}$. In the initial stages of the process, where the solvent's CO_2 content is at its maximum, the CO_2 flux for 21 $kPa_{(a)}$ was over 1.4 times higher than for 51 and 81 $kPa_{(a)}$. However, as the operation continued and the solvent became leaner (~0.23 mol/mol), the CO_2 removal performance of the low vacuum pressure reduced and became similar to the other vacuum levels. This is attributed to a reduction in the CO_2 partial pressure, which appears insufficient to activate enhanced CO_2 diffusion for achieving a higher flux. Hence, to effectively maximize and harness the strength of high vacuum pressure during low temperature DAC regeneration, operating above 0.23 mol/mol (~65% CO_2-loaded) for 1 M GlyK at 80 °C is deemed suitable. Also, it is evident that the vacuum pressure for effective CO_2 removal should be as low as practically possible for non-wetting membranes, taking into account the energy requirements within the limitations of the final application.

4.2.2.3 Solvent Concentration

Here, the influence of GlyK concentration (1, 2, and 3 M) on the CO_2 desorption flux and the capacity of the system were studied. According to **Figure 4.4d**, higher molarities provided

higher CO_2 removal flux throughout a major part of operating period (Complete data set is provided in **Figure A.7**). This behavior is linked to the increased quantity of formed carbamate molecules present during DAC-absorption at increased solvent concentrations. As a result, a larger amount of accessible CO_2 will be available for stripping from the solution, leading to an increase in the CO_2 concentration and the corresponding driving force. From a capacity point of view, based on the discussion in Section 4.3.1.3 (**Figure 4.2b**), by increasing the GlyK concentration, the number of CO_2 moles required to reach equilibrium is increased. In **Figure 4.4c**, the total amount (g) of CO_2 removed for different GlyK concentrations through low-temperature vacuum regeneration is indicated. Comparing 1 M to 2 M and 3 M, a 47% and 65% enhancement was recorded. It is notable that the improvement rate between 1 M to 2 M is higher than 2 M to 3 M because of increased solvent viscosity, which leads to slower CO_2 diffusion (86, 89). Therefore, due to the enhanced kinetics and capacity in the DAC-desorption section, and since no precipitation or operational challenges were identified during the trials, utilizing higher molarities for GlyK is recommended.

4.2.2.4 Sweep Gas

To demonstrate and analyze the effect of sweep gas on CO_2 removal efficiency, a combined sweep gas/vacuum mode trial was conducted. 5 L/min of N_2 was introduced to the shell side while applying vacuum pressure (21 kPa(a)); the flow rate was monitored continuously using a flow meter during operation. Interestingly, no enhancement in CO_2 stripping performance was recorded in comparison to vacuum alone (**Figure 4.4f**). This is likely related to the membrane dense layer, which controls the CO_2 mass transfer in the membrane module. Generally, introducing a sweep gas to the system reduces the resistance on the vacuum side for CO_2 transfer due to enhanced evaporation and the elimination of a condensed water film layer (133). However, since the membrane's dense layer is the dominant resistance in CO_2 removal,

no improvement in stripping efficiency was observed. On the other hand, a dramatic change in water transfer across the membrane occurred. According to **Figure 4.4e**, in sweep gas/vacuum mode, over three times the amount of water was added for compensation during operation. This is attributed to the elimination of the mentioned condensed water film layer, leading to an increased water flux across the membrane. In addition, applying sweep gas caused less condensation and collection of water in the acetone-ice bath trap (due to the shorter residence time of vacuum side stream in the trap). This implies there will be greater energy demand in the condenser during sweep gas operation.

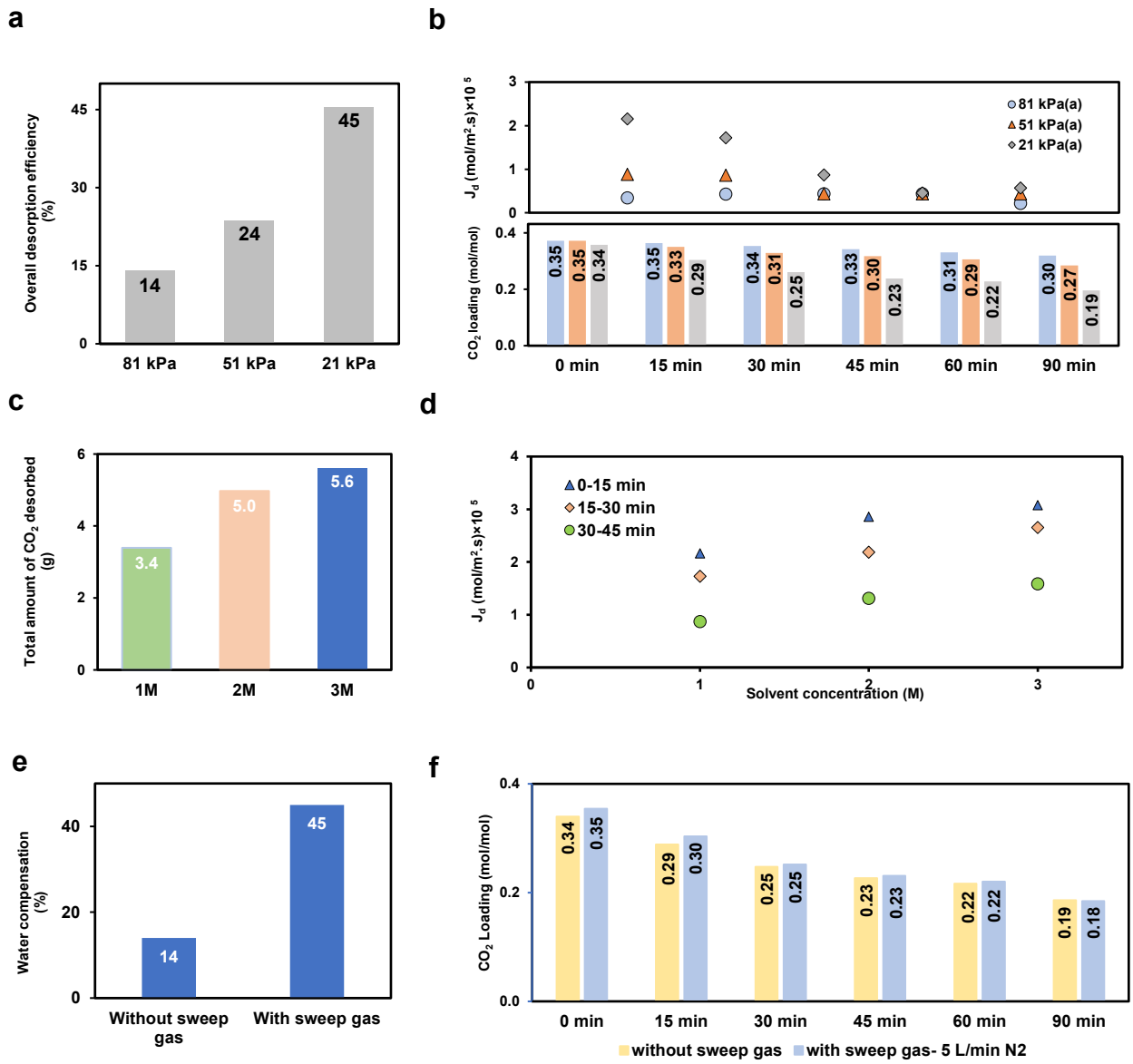

Figure 4.4. a) 1M GlyK overall DAC-desorption efficiency at different vacuum pressures. b) 1M GlyK DAC desorption flux (J_d) at different vacuum pressure levels and solvent loadings. c) Total g of removed CO_2 using different GlyK concentration at 21 $kPa_{(a)}$. d) DAC desorption flux (J_d) of GlyK at different level of concentration at 21 $kPa_{(a)}$. The result of two modes of trials for Vacuum, and Vacuum/sweep gas mode e) Water make-up percentage. f) CO_2 solvent loading values through time. The data were obtained at 80°C, and solvent flow rate = 0.25 L/min.

4.2.3 Simulation

Apart from the experimental approach detailed in the previous sections, a more detailed analysis of the overall mass transfer coefficient, K, was also required to evaluate the possibilities and limitations of membrane contactors used in the DAC-absorption and desorption processes. Hence, a mathematical model developed in Aspen Custom Modeler

(ACM) by McQuillan et al. (133) and validated using the data reported in this work, was used to help characterize and understand the performance of the described HFMC system.

Even though the thick, dense PDMS layer in the membrane (55 μm) provides stable operation without pore-wetting and favorable mechanical stability, it introduces considerable mass transfer resistance. In such cases, one of the most effective mechanisms to enhance the overall mass transfer efficiency is to reduce the membrane thickness. Therefore, the validated model was used to precisely determine the mass transfer resistance contribution of each phase in the gas-liquid membrane module at different thickness levels of the dense PDMS layer and its effect on DAC-absorption performance. According to **Figure 4.5a, b**, for the 55 μm thickness membrane, over 80 percent of the total resistance is included in the membrane phase, making the system less responsive to operating conditions. Decreasing the thickness from 55 μm to 25 μm and 10 μm, increased the gas phase contribution to the overall mass transfer, and a steep increase in overall absorption efficiency from 41% to 73% was observed. Further reducing the thickness of the dense layer to a minimum value of 1μm, the gas phase became the governing phase, and the absorption performance rose to more than 80%. These results highlight the significant influence of the dense layer thickness on the overall membrane module performance. Also, it shows HFMCs can be a high-efficient and viable technology for large-scale utilization of DAC (133). Meanwhile, it is noted that more experimental studies are necessary to examine the effect of thin dense layer membranes on the mechanical and thermal stability and pore-wetting phenomena (in porous support) in DAC operation.

To study the effect of membrane module characterization during low-temperature, vacuum regeneration in DAC operation, a series of simulations were conducted at 80 °C for 1 M GlyK to analyze the mass transfer resistance of each phase at different membrane thicknesses, and its impact on stripping performance. As shown in **Figure 4.5c**, the membrane phase accounts for a majority of the CO_2 mass transfer resistance during the regeneration process. As the

membrane thickness decreased from 55 to 1 μm, a >200% enhancement in CO_2 flux was achieved. In this condition, liquid is indicated as the dominant phase. Nevertheless, it is important to note that DAC stripping operations deal with lower CO_2 content in solvents and CO_2 partial pressures compared to conventional CO_2 stripping units designed with flue gas specifications. This will lead to a lower ratio of CO_2 to water vapor during the high-temperature process, which highlights the importance of the hydrophobic characteristics of the membrane during DAC regeneration. Since vacuum low-temperature regeneration with membrane modules has a high potential for utilization in the DAC processes, further experimental long-term trials are needed to be accomplished on GlyK with a lower membrane thickness to accurately analyze CO_2 and water transfer.

4.3 Conclusion

This work presents a successful demonstration of CO_2 separation efficiency in a DAC system through lab-scale experiments and simulations. Trials under various operating conditions, utilizing non-porous HFMCs and different types of environmentally friendly amino acid salt aqueous solutions for absorption and vacuum low-temperature desorption were conducted. Parametric studies were carried out to optimize the CO_2 flux and separation efficiency. Regarding absorption, five amino acid salts were screened in long-term operation at 20 °C. Stable CO_2 absorption performance over a major part of the experiment highlighted the beneficial use of hydrophobic membranes and green amino acid salts. GlyK was selected as the most suitable solvent for DAC in terms of kinetic performance, cyclic capacity, non-precipitating behavior at different levels of concentration and loading, and ease of preparation. Furthermore, it was shown that, DAC-absorption CO_2 flux and capacity is optimized by operating at 20 °C, a suitable solvent temperature when considering kinetic performance, solvent capacity, and energy demand. Working with higher solvent concentrations (2 M and 3

M) was found to be beneficial for both absorption and desorption in a DAC system due to their higher capacity (doubled to tripled), higher desorption rates and non-precipitating behavior. For the vacuum stripping process, operating at higher temperatures (70-90 °C) and vacuum pressures (21–81 kPa(a)) enhanced the CO_2 removal flux. Notably, to harness the maximum enhanced effect of temperature and vacuum pressure, 0.23 mol/mol (~65% loaded solvent) was considered the optimum resulting lean loading specification for 1 M GlyK. Interestingly, introducing a sweep gas stream to the vacuum system did not affect the CO_2 removal flux, which is attributed to the membrane PDMS dense layer. However, it remarkably escalated the water loss from the membrane module by up to three times. Hence, the vacuum mode without sweep gas was found to be more favorable. For the simulation a validated model was used to analyze the membrane thickness effect on DAC absorption-desorption performance. The model results highlighted the considerable improvement in CO_2 separation (over 100%) when the dense layer thickness decreased from 55 μm to 1 μm which shows the effectiveness of hybrid technology of HFMCs in DAC operation. Hence, more long-term experimental trials of DAC using thinner membrane thicknesses needs to be completed. In general, the findings in this work can start a new pathway for using HFMCs and green amino acid salt solutions in a sustainable DAC technology.

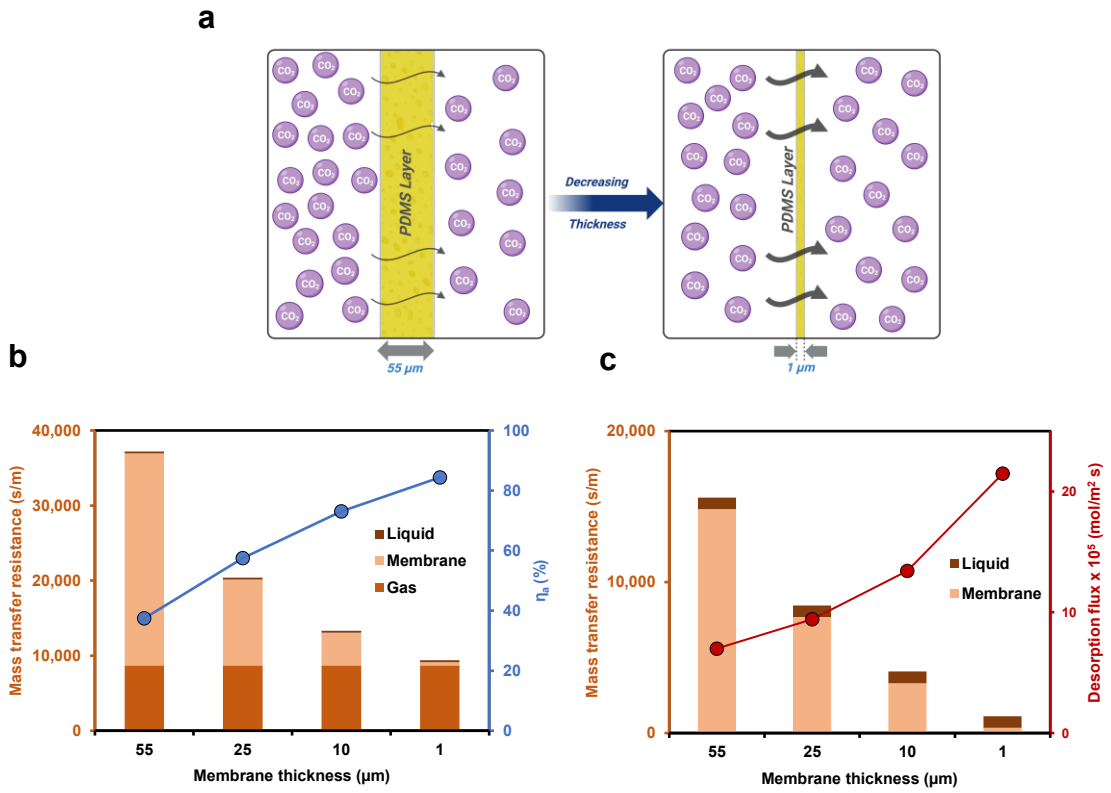

Figure 4.5. a) Schematic of dense membrane layer thickness effect on the CO_2 separation efficiency. Dense membrane layer thickness effect on b) Absorption efficiency c) Desorption flux using developed model.

This chapter provided a comprehensive evaluation of the CO_2 separation efficiency of various green amino acid solvents in HFMC-based absorption systems and low-temperature MVR units. The experimental results demonstrated that amino acid solvents can effectively capture ~420 ppm CO_2 with stable efficiency up to near their saturation point. The parametric study on the MVR process further highlighted its capability to regenerate amino acid salt solutions under low-temperature conditions. This is particularly important, as the operating temperature range of MVR makes it compatible with renewable energy sources, contributing to the sustainability of the DAC process. Moreover, the simulation results demonstrated the critical role of membrane characteristics in enhancing CO_2 separation efficiency. Building on these findings and the insights gained into the CO_2 separation performance of solvents with different acidic and basic structures, as well as identifying the challenges regarding the high energy intensity of the desorption step in solvent regeneration process, the next chapter focuses on improving

the energy efficiency of this part of process by integrating the MVR system with catalytic solvent regeneration technology. This approach aims to lower thermal energy demand and enhance the sustainability and overall efficiency of the process, which is the main objective of this study. Furthermore, based on the observed critical role of membrane characteristics in CO_2 separation performance, the following chapter experimentally explores a range of HFMCs with varying properties.

CHAPTER 5

Catalytic Membrane Vacuum Regeneration: Enhancing Energy Efficiency and Renewable Compatibility in Direct Air Capture

The chapter has resulted in the following publication:

Momeni A, McQuillan RV, Anisi H, Alivand MS, Zavabeti A, Stevens GW, Kim S, Mumford KA. Catalytic Membrane Vacuum Regeneration: Enhancing Energy Efficiency and Renewable Compatibility in Direct Air Capture. Small. 2025:2503023.

5.1 Introduction

Direct Air Capture (DAC) has emerged as a key climate solution by removing carbon dioxide directly from the atmosphere, offering a scalable way to reduce global emissions and support meeting the targets set by the Paris Agreement(134-136). One of the major challenges in this field is the energy-intensive nature of the applied technologies (e.g., absorption and adsorption) (57). So far, considerable advancements have been made in adsorption systems using solid sorbents, enhancing energy efficiency and enabling the integration of sustainable heat sources (8, 137). This is while, for solvent-based approaches (despite their strong history of industrial application (138, 139)) research and development have remained limited for DAC implementation. On of the key obstacle in this technology is the high energy demand of the solvent regeneration process, which typically requires boiling the solvent above 120 °C (6, 59). This not only hinders the use of sustainable energy sources but also poses a risk of thermal degradation of solvents (140). The latter is particularly critical for amino acid salts which are one of the most suitable solvents for DAC due to their favorable physicochemical properties such as low volatility and toxicity and high oxidative stability (11, 141). In this regard, selecting and properly designing a contactor capable of low-temperature CO_2 desorption, along with implementing advanced, energy-efficient regeneration methods, is essential to making the liquid-based DAC process viable, cost-effective, and sustainable.

Membrane vacuum regeneration (MVR) using hollow fiber module contactors (HFMCs) is a reliable and well-stablished method for low-temperature CO_2 stripping (142, 143). The applied vacuum enables regeneration at 80-100 °C, reducing thermal energy demand and limiting solvent degradation over time (75, 76). Additionally, lower operating temperatures can be further coupled with renewable energy sources such as solar energy or low-grade heat, making DAC processes sustainable (24). In this context, one of the most important factors in CO_2 transfer through membranes is the optimization of membrane characteristics and structure,

which is crucial for minimizing mass transfer resistance (21). Hydrophobic porous membranes are commonly used for this purpose, however they are prone to pore wetting, which reduce performance (25, 26). This issue can be effectively addressed by using hydrophobic ultra-thin composite membranes, which a dense selective layer prevents liquid entering the pores (27, 28). Therefore, evaluating the performance of HFMCs with varying characteristics (especially ultra-thin composite membranes) is essential to further optimize and enhance the CO_2 transfer rates in low-temperature MVR under DAC conditions, which has not been experimentally studied yet.

Since DAC process is highly energy-intensive (ultra-low CO_2 partial pressure), integrating MVR with an additional low-temperature, energy-efficient technology would be highly beneficial (144). Among different technologies,(30, 99, 103) catalytic solvent regeneration using heterogeneous solid acid-base catalysts is an emerging method that has shown promise in accelerating CO_2 stripping rates (34). So far, a broad range of heterogeneous solid acid catalysts (e.g., zeolites, sulfated metal oxides, etc.) with various physicochemical properties have been developed and tested for this purpose under flue gas conditions,(33, 43, 45) with a few under DAC conditions (40). However, to the best of the authors' knowledge, ion-exchange resins have not yet been investigated in liquid-based low-temperature CO_2 regeneration, either in flue gas specification or DAC, despite their promising characteristics and widespread use in various fields (46-49). Availability, low cost, strong acidic functional groups, stability, macroporosity, and ease of operation are some of the important specifications of strong cation resins, making them a great candidate for evaluating its performance in catalytic solvent regeneration in MVR DAC.

Herein, we have developed and evaluated green energy-efficient catalytic membrane vacuum regeneration (C-MVR) for liquid-based DAC, which is an integrated system of catalytic solvent regeneration with vacuum membrane distillation operating in low temperature ranges (80-100

°C). Following from our previous studies in DAC systems,(40, 124, 133) we have developed a DAC desorption unit suitable for C-MVR tests. This work examines the performance of three HFMCs with various characteristics, including a polytetrafluoroethylene (PTFE) porous membrane, an ultra-thin polydimethylsiloxane (PDMS) dense layer composite membrane, and a non-porous PDMS membrane. The best-performing membrane with respect to its CO_2 separation efficiency and acceptable water transfer rate was selected for further analysis. Building on the insights from Chapter 4 (124) and published studies (40, 145), four amino acids with the highest cyclic capacities (glycine, sarcosine, proline, and taurine) were selected to evaluate CO_2 desorption performance using the chosen membrane module in MVR rig. Furthermore, the effect of process conditions (e.g., regeneration temperature) was studied. For C-MVR, a comprehensive set of trials of commercial acidic cation resins with different concentrations (3wt% and 6wt%) for various solvents were conducted. To gain a better understanding of the catalyst performance under different conditions, the effects of regeneration temperature, solvent concentration, and additives were investigated. The findings of this study provide a strong foundation for applying a green, energy-efficient integrated system of catalytic solvent regeneration and MVR in sustainable DAC processes.

5.2 Results and Discussion

5.2.1 Membrane Module Performance

Initially three different HFMCs, each with distinct characteristics, membrane resistance, and CO_2 transfer mechanism, were considered and evaluated (**Table 3.2** and **Figure A.8**). These tests were conducted using 3M GlyK at 90 °C. In selecting a suitable membrane module for liquid-based DAC operations, CO_2 flux plays a critical role, while the water transfer rate through the fibers is also an important consideration. The latter significantly impacts the size and energy requirements for the condenser and vacuum pump, as well as the ease of MVR

operation on a large scale. As illustrated in **Figure 5.1a-c**, $HFMC_3$ exhibited the highest CO_2 flux and the lowest water to CO_2 flux ratio in the MVR DAC. This is primarily related to the coated ultra-thin PDMS layer (a rate-determining layer for CO_2 permeance), which minimizes membrane resistance and accelerates CO_2 transfer. Furthermore, due to the pervaporation mechanism governing the transfer process, CO_2 selectivity was enhanced (95, 146). Interestingly, despite having a porous structure and the lowest membrane resistance, $HFMC_1$ showed lower CO_2 flux as compared to $HFMC_3$. A primary cause for this behavior is pore wetting, a common issue in porous membrane modules that leads to reduced CO_2 removal efficiency. This issue can be minimized by adjusting the membrane pore size and hydrophobicity (material selection) (147). The significant water flux, due to water convective flow through the larger pores, and consequently high ratio of water to CO_2 flux indicates the occurrence of this issue in $HFMC_1$. Among the HFMCs, $HFMC_2$ demonstrated both the lowest CO_2 and water flux. This is mainly related to the existence of a thick hydrophobic dense PDMS layer (55μm), which considerably increases membrane resistance and lowers both CO_2 and water flux. Despite having the lowest water flux, the CO_2 flux for $HFMC_2$ is 58.3% lower than $HFMC_3$, highlighting the rate-determining effect of the PDMS layer thickness. Hence, $HFMC_3$ (the ultra-thin dense membrane layer) was selected as the suitable membrane for further MVR DAC analysis. Top-view and cross-sectional SEM images, along with EDX elemental analysis of the $HFMC_3$ fibers, are provided in **Figure A.10**. To measure the accuracy and repeatability of the rig and the experiments, two more trials were conducted at 90 °C with $HFMC_3$ using 3M GlyK. The results are shown in **Figure A.11**, highlighting compelling accuracy and repeatability of the MVR apparatus.

5.2.2 Amino Acid Performance

Figure 5.1d, e illustrate the performance of four amino acid salts, including TauK, GlyK, SarK, and ProK with a concentration of 3M in the MVR DAC system. Due to the thermal stability of

$HFMC_3$, 100 °C was selected as the operating temperature. **Figure 5.1d** shows the CO_2 flux profiles of the amino acid salts along with their temperature profiles over time. As the solvent temperature increased and approached 90-100 °C, the CO_2 analyzer and flow meter started detecting high purity CO_2 at the vacuum pump outlet. The observed delay between the temperature profile and CO_2 detection is due to the low amount of desorbed CO_2 (because of the low surface area of $HFMC_3$) and the volume of the system before the CO_2 analyzer. As the operation continued at the stabilized temperature, the CO_2 flux increased and achieved the stabilized conditions, which was considered the final CO_2 flux for the trial. Comparing the stabilized flux reported in **Figure 5.1e**, TauK demonstrated the highest CO_2 transfer rate, being 59.4% greater than GlyK. This can primarily be attributed to the sulfonic acid group ($SO_3^-H^+$), which gives taurine acidic properties, making it easier to deprotonate during regeneration and release protons. This facilitates the breakdown of carbamate, liberating greater amounts of CO_2 from the solution which is consistent with our observation in recent study (145). For the other solvents, GlyK, SarK, and ProK were in descending order of the CO_2 flux, respectively. These results are well aligned with our previous study on the DAC cyclic capacity of various solvents in the temperature range of 25-98 °C (40). For determining the water transfer rate for different solvents in $HFMC_3$, the amount of water collected in each trial was accurately measured. **Figure 5.1e** shows that GlyK exhibited the highest water flux, followed by TauK and SarK in second and third place, respectively, while ProK recorded the lowest. The order and behavior can be likely attributed to the hydrophobicity and hydrophilicity degree of the amino acid salts. It is notable that the high CO_2 flux for TauK resulted in the lowest water to CO_2 ratio flux among the examined solvents. This, combined with the remarkable thermal stability of TauK,(145) makes it a suitable choice for MVR DAC.

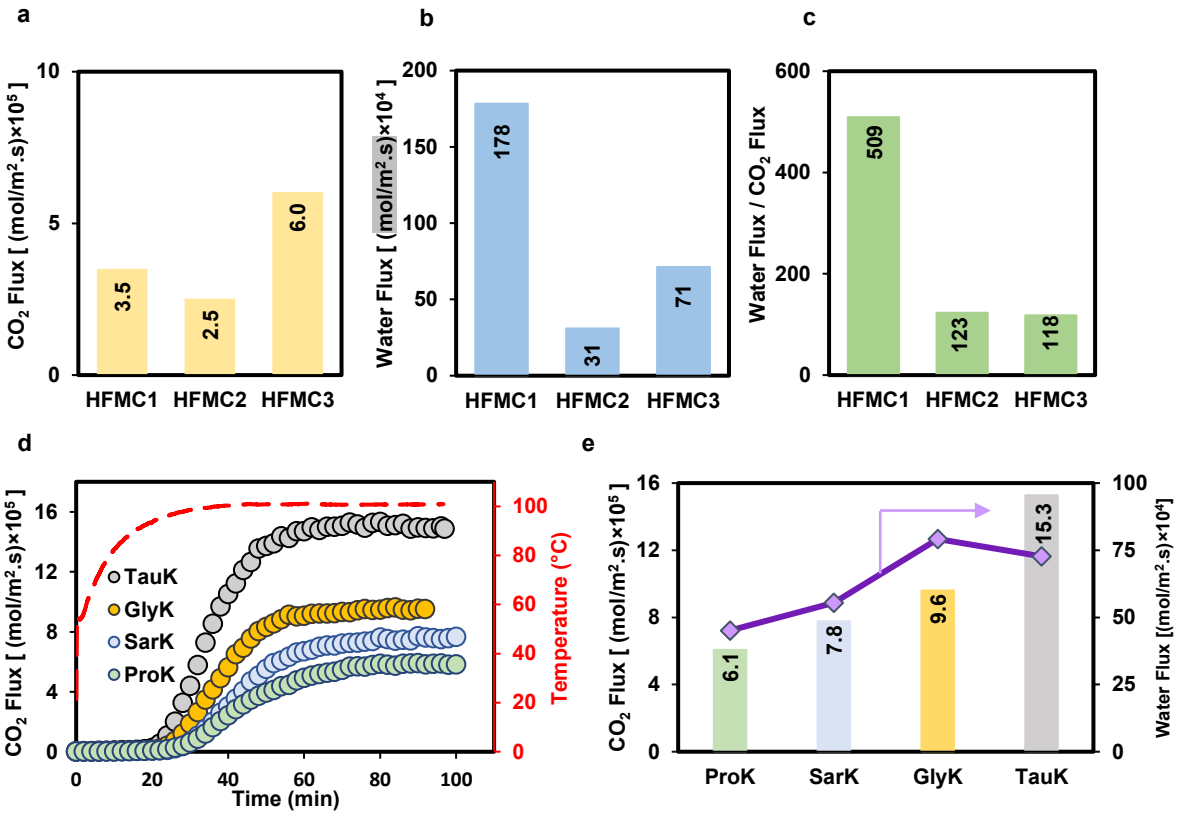

Figure 5.1. a) CO_2 flux, b) water flux, and c) ratio of water to CO_2 flux for three used HFMCs at 90 °C. d) CO_2 desorption profiles over time, and e) water flux and CO_2 flux of various 3M amino acids at 100 °C. All trials were accomplished at 2-4 kPa(a), 0.25 L/min.

5.2.3 Solvent Temperature and Flow Rate

To gain a better understanding of the MVR DAC process, the role of crucial parameters such as regeneration temperature and solvent flow rate were assessed on the CO_2 flux. Two amino acid salts, 3 M TauK and 3 M GlyK (**Figure 5.2a**), having the highest CO_2 desorption kinetics among the studied solvent were selected to screen their performance in temperature ranges of 80-100 °C. **Figure 5.2b** depicts the various temperature profiles and corresponding CO_2 desorption curves for 3 M TauK over time. As illustrated, an increase in temperature leads to an increase in CO_2 desorption kinetics, driven by a higher CO_2 equilibrium partial pressure, and reaction rate across the membrane. Notably, the trials using lower temperatures were longer due to the reduced number of desorbed CO_2 moles and, consequently, more time was needed to achieve a stabilized condition. **Figure 5.2c** shows the stabilized CO_2 flux values for 3 M

TauK and 3 M GlyK, where in all temperature ranges, TauK outperforms GlyK. Additionally, TauK significantly enhanced its CO_2 desorption performance (over ~180%, from 5.4×10^{-5} to 15.3×10^{-5} mol/m^2.s) by increasing the temperature from 80 to 100 °C, while GlyK showed ~120% improvement (4.3×10^{-5} to 9.6×10^{-5} mol/m^2.s). This is mainly attributed to the different molecular structures of the two amino acids and the presence of a sulfonic acid group in TauK, which is more effective for proton exchange (TauK deprotonation) at high temperatures (40, 43). Hence, to maximize the CO_2 desorption efficiency of the MVR in DAC, 100 °C was chosen as a suitable regeneration temperature.

The hydrodynamics of the MVR system are another key feature that was evaluated. **Figure 5.2d** highlights the effect of solvent flow rate on CO_2 desorption performance for 3 M GlyK at 100 °C. As shown, a minor change was observed as the flow rate decreased from 0.25 to 0.05 L/min. The Reynolds number (Re) (**Figure 5.2d**) in these flow ranges suggested that the solvent flow stayed in the laminar regime. This can explain the non-effectiveness of the solvent flow rate on the stripping performance. Thus, more experiments can be accomplished in the future in a wider range of solvent flow rates and Re values to analyze the hydrodynamic effects on the performance of the system in DAC. Additionally, it would be advantageous for MVR to operate at a lower solvent flow rate with a specific and constant efficiency, as this would require less thermal energy for continuous solvent heating.

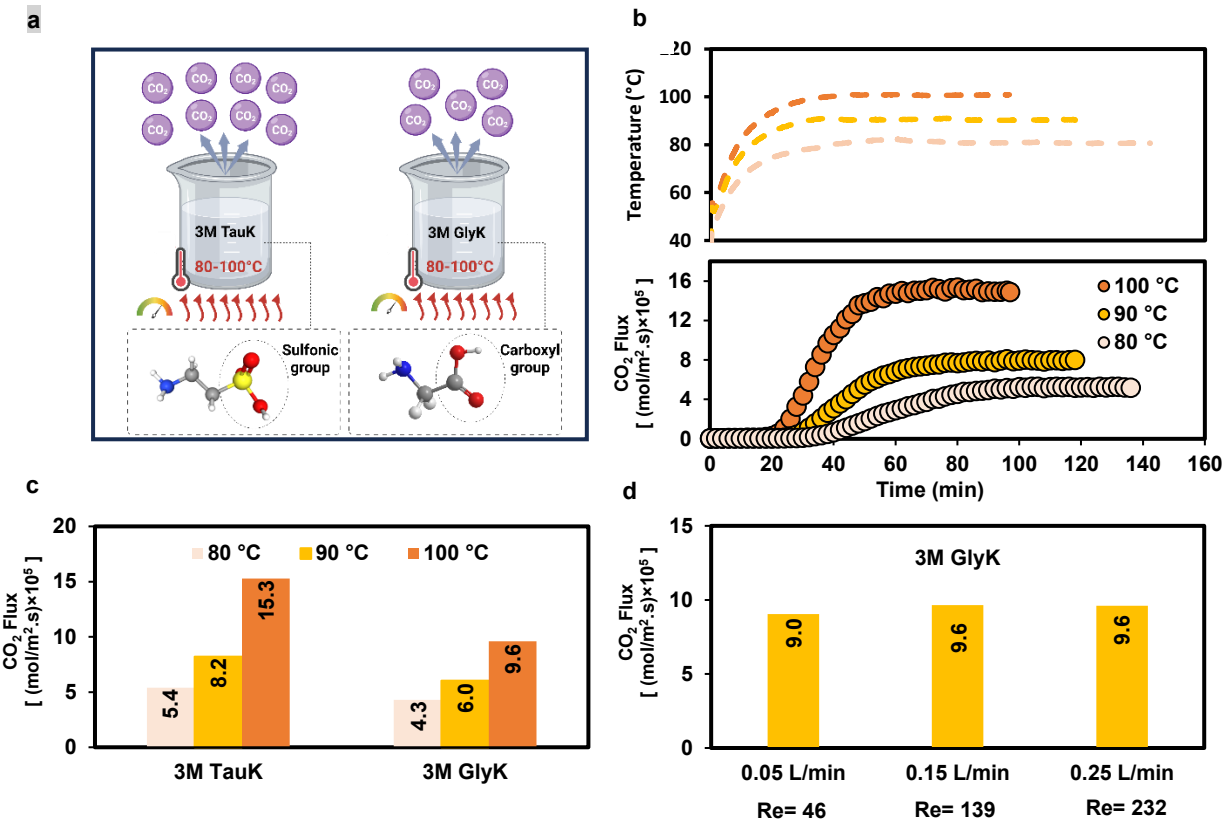

Figure 5.2. a) A schematic illustrating the superior performance of TauK over GlyK across the entire regeneration temperature range of 80-100 °C. b) 3 M TauK CO_2 desorption profiles over time at various temperatures. c) 3 M TauK and GlyK CO_2 flux at various temperatures. d) 3 M GlyK CO_2 flux at 100 °C under different solvent flow rates. All trials were accomplished at 2-4 kPa(a). Solvent flow rates set to 0.25 L/min for (b, c).

5.2.4 Catalytic Membrane Vacuum Regeneration (C-MVR)

For C-MVR DAC trials, a catalyst fixed bed filled with strong, acidic resin beads functionalized with $SO_3^-H^+$ (schematically shown in **Figure 5.3a**) was added to the solvent circulation loop to analyze its effect on CO_2 desorption kinetics. Two types of ion exchange resins were employed with distinct physicochemical properties, crosslinking, and acidic strength.

To start the C-MVR DAC trials, a concentration of 3wt% was selected for both types of catalysts (Resin A and B) to analyze their impact on enhancing CO_2 desorption kinetics. Based on our previous study,(40) since GlyK showed considerable desorption improvement with acidic catalysts, the first catalytic trials assessed 3 M GlyK being regenerated at 100 °C. Interestingly, Resin B, resulted in negligible improvement in the CO_2 desorptive flux.

However, Resin A exhibited an enhancement in CO_2 flux by 21.2%. Based on the SEM and TEM results (**Figure 5.3a, Figure A.12, and Figure A.13**), both catalysts showed the same morphology, porous amorphous structure, and bead size distributions. TEM-EDX mapping on crushed catalysts further confirmed the integrated distribution of carbon, sulfur, and oxygen (**Figure 5.3a**, and **Figure A.12e**). However, XPS results highlighted that Resin A had 3-fold more sulfur content (14.8 at.%) compared to Resin B (4.8%), a strong indicator of an increased amount of Brønsted acid sites (**Figure 5.3b**). Brønsted acid sites play a crucial role in enhancing catalyst performance by effectively acting as proton donors. This functionality facilitates key reactions such as deprotonation and carbamate breakdown, thereby improving CO_2 desorption rates (34). Several studies in the literature have discussed possible catalytic mechanisms, most of which focus on 5M monoethanolamine (MEA) solvent under flue gas conditions (33). A few works have investigated amino acid solvents (103, 115), particularly in the context of DAC (40). Nevertheless, nearly all studies follow a similar mechanistic pathway involving three main steps: (1) chemisorption and proton transfer, (2) structural rearrangement (isomerization), and (3) dissociation.

To further investigate the properties of the resins, **Figure 5.3c, d** depict the XPS analysis for S2p spectrum of the two catalysts, Resin A and B, respectively. The binding energies at 168.5 (i.e., S 2p3/2) and 169.7 eV (i.e., S2p1/2), related to SOH and SO, confirm the presence of $-SO_3^-H^+$ groups (103, 148). Comparing the intensity peaks in the XPS spectra of **Figure 5.3c, d**, Resin A intensity peaks are considerably higher than Resin B, highlighting stronger acidity. Further analysis by XPS characterization was performed for O1s, and C1s of Resin A (**Figure A.14a,b**) to also show carbon, O-H and O-S binding energies. Additionally, characterization using FTIR (**Figure A.15**) confirmed the XPS results (**Figure 5.3b-d**). To accurately measure the elemental content of the catalysts, CHNS analysis was conducted and reported in **Table A.1**. Based on the reported values, the normalized sulfur to carbon ratio (S/C) for Resin A is

four times higher than for Resin B, which confirms a stronger acidity. Therefore, for the rest of the C-MVR experiments, Resin A was utilized.

Figure 5.3e shows the CO_2 desorption performance of 3 M TauK with (3wt% and 6wt%) and without catalyst (blank). Comparing the curves with the blank, it is compelling to see that the CO_2 flux ramp starts at lower temperature ranges when the catalyst is present. This highlights the impact of the resin beads on the MVR process, which can facilitate and increase the quantity of CO_2 liberated by exchanging protons in lower temperature ranges in a certain timeframe. This results in an increase in the CO_2 partial pressure on the liquid side of the membrane module, ultimately leading to a higher CO_2 flux. Continuing the operation at a constant regeneration temperature, the CO_2 flux curves stabilized at 15.3×10^{-5}, 17.9×10^{-5}, and 20.5×10^{-5} mol/m^2.s for the blank, 3wt%, and 6wt% catalyst, respectively, equivalent to a 17.0% and 34.5% enhancement (**Figure 5.3f, g**). The result shows that by doubling the catalyst concentration for TauK, the enhancement is also doubled. In addition, it demonstrates the effectiveness and applicability of acidic cation resins in a fixed bed in the MVR process using an ultra-thin dense layer membrane.

To evaluate the catalyst impact on different amino acid salts with different molecular structures and CO_2-containig species, the same trials were conducted for 3 M GlyK and SarK. According to **Figure 5.3f, g**, in the presence of 3wt% and 6wt% resin beads, the GlyK CO_2 desorption performance was promoted by 21.2% and 64.4%, respectively, with the latter being the highest observed catalyst improvement. Interestingly, for SarK, which has the highest DAC-loaded saturation point (420 ppm CO_2 and 25 °C) compared to TauK and GlyK (**Figure A.9**) demonstrated the poorest catalytic effect, only 22.9% in the presence of a 6wt% catalyst. As reported in our previous study on catalytic solvent regeneration in the DAC process,(40) the acidic catalyst had the highest impact on CO_2 desorption with GlyK and the least impact with SarK among the short-chain amino acids. Several factors may contribute to this behavior,

including the nature of CO_2-containing species, the strength of acidity and basicity (pKa values), molecular weight, and water solubility (103). To gain a better understanding of how these parameters influence catalytic performance, a comprehensive study involving various amino acids with different physicochemical properties should be conducted in future work. In the case of TauK, despite its large cyclic CO_2 capacity,(145) it exhibited a lower catalytic effect compared to GlyK. One possible reason is the presence of a sulfonic acid group in the taurine structure, which facilitates the deprotonation of protonated taurine and increases the availability of free protons. This could reduce the relative impact of the catalyst when compared to GlyK.

Figure 5.3h shows the relative heat duty using a 6wt% catalyst for different solvents. Considering the catalyst performance, GlyK and TauK exhibited a 39.1%, and 25.2% reduction in thermal energy input, respectively. Nonetheless, among all the conducted C-MVR trials, the highest recorded CO_2 flux was for TauK (20.5×10^{-5} mol/m^2.s) which was 29.7% more than GlyK (15.8×10^{-5} mol/m^2.s) (**Figure 5.3f**). CO_2 flux is a critical parameter in the MVR process, as it influences overall efficiency, solvent cyclic capacity, system size, and both capital and operating costs. To further investigate, the CO_2 transfer rates for the 6wt% catalyst were used to estimate the thermal energy consumption in the C-MVR system using Equation 3.8. The results showed thermal energy consumption of 8.6 GJ/tCO_2 for TauK and 11.2 GJ/tCO_2 for GlyK. Despite TauK's lower catalyst enhancement and higher relative heat duty, its higher CO_2 flux led to a 23.2% reduction in final energy consumption compared to GlyK.

To compare the regeneration energy of the current system with other DAC technologies, the total thermal energy consumption was estimated by adding the enthalpy of desorption for 3 M TauK (2.04 GJ/tCO_2)(149) to the calculated energy input (8.6 GJ/tCO_2), resulting in a total of 10.6 GJ/tCO_2. **Table 5.1** summarizes the reported thermal energy requirements of several well-established DAC technologies.

Table 5.1. Thermal energy consumption for well-established DAC technologies

Technology	System type	Thermal energy needs	Thermal energy consumption (GJ/tCO_2)	Thermal energy source	Reference
Carbon Engineering	Liquid solvent	900 °C	5.3-8.81	Natural gas with CCS	(54, 150)
Climeworks	Solid sorbent	80-120 °C	5.8-14.5	Non-fossil energy resources (geothermal,	(7, 137, 151)
Global Thermostat Company	Solid sorbent	105-120 °C	4.4	Energy resource agnostic	(150, 151)

Due to various reported energy consumption for number of technologies in **Table 5.1**, a range of values is provided. While Carbon Engineering's liquid-based DAC process demonstrates relatively lower energy consumption, it operates at extremely high temperatures (around 900 °C), which require heat from fossil fuel combustion. Compared to other DAC systems in **Table 5.1**, a particularly promising and green sustainable approach is the temperature-vacuum swing adsorption (TVSA) process, which employs amine-functionalized, biodegradable cellulose sorbents. This system captures CO_2 and regenerates it under vacuum at temperatures between 80-120 °C (137). Notably, TVSA is also the core technology used by Climeworks. Comparing the energy consumption of the TVSA process with the C-MVR system developed in this work, the values fall well within the same range. This highlights the potential of the C-MVR system as sustainable and scalable liquid-based DAC technology.

Notably, using a larger ultra-thin dense membrane module with greater surface area than $HFMC_3$ could enhance the total number of CO_2 desorption and further reduce energy consumption which is a part of future work of this study.

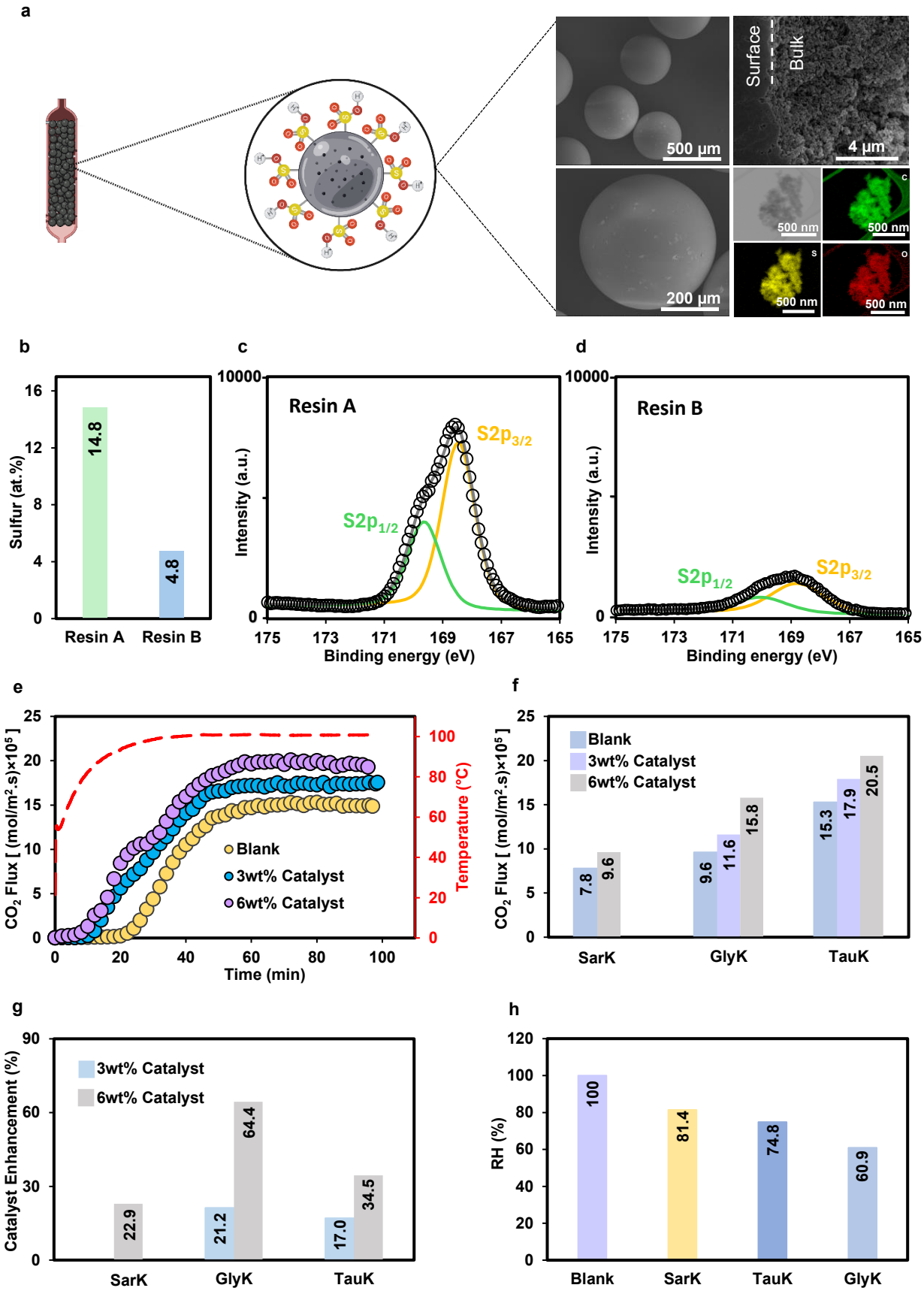

Figure 5.3. a) Schematic diagram of acidic cation resins, SEM images and TEM-EDX mapping of Resin A. b) Sulfur content analyzed by XPS for two cation resins. c) High-resolution XPS spectra of Resin A, and d) Resin B. e) 3 M TauK CO_2 desorption profiles over

time, and f) CO_2 flux values for various 3 M amino acids without/with catalyst for different concentrations. g) Catalyst enhancement values for different concentrations and various 3 M amino acids. h) Relative heat duty using 6wt% catalyst for 3 M amino acids. All trials were accomplished at 100 °C, 2-4 $kPa_{(a)}$, 0.25 L/min, using Resin A. No catalyst was used for blank solvent.

5.2.5 Catalyst Impact by Solvent Condition

To further examine crucial variables in the C-MVR process, the catalyst effectiveness was investigated at lower temperature ranges (90 °C) for TauK and GlyK with the highest observed catalytic effect on CO_2 desorption performance. All trials were accomplished with a fixed catalyst concentration of 6wt%. The CO_2 desorption curves at 90 °C are depicted in **Figure 5.4a, b**, and the corresponding final stabilized CO_2 flux and catalyst improvements are shown in **Figure 5f**. Comparing the results with 100 °C (**Figure 5.3f, g**), it can be seen that by decreasing the regeneration temperature, the ultimate CO_2 flux and the catalytic impact both decrease. In fact, a 10 °C decrease in regeneration temperature reduced the catalyst performance from 64.4% to 48.9% for 3 M GlyK and from 34.5% to 20.7% for 3 M TauK. Notably, the CO_2 flux for TauK was halved. Hence, increasing the temperature enhanced catalyst activation in the process (40).

One of the limitations of applying green amino acids on a large scale is the potential formation of solids in the solution in lower absorption temperature ranges, and at high CO_2 loadings or high solvent concentrations (76). This can cause operational problems and reduce the CO_2 uptake rate (152). It is notable that during CO_2 absorption in the TauK (near its saturation point) and after C-MVR trials, the formation of solids was noticed in the solution. Therefore, considering the ultra-low partial pressure of CO_2 in air, which contributes to lower saturation points in DAC processes, the CO_2 desorption performance was assessed at two additional TauK concentrations (2 M and 2.5 M). The evaluations were conducted both with and without catalysts to assess system efficiency and monitor any potential precipitation. The results revealed that lowering the solvent concentration significantly minimized precipitation (**Figure**

A.16). However, as expected, **Figure 5.4c, d**, **f** show that reducing the TauK concentration from 3 M to 2.5 M and 2 M led to a decline in both CO_2 flux and catalyst effectiveness. In fact, in the presence of 6wt% catalyst, comparing the CO_2 transfer rate of 3 M to 2 M TauK at 100 °C, a 28.8% loss (20.5×10^{-5} to 14.6×10^{-5} mol/m^2.s) was observed. The reduction can be ascribed to a decrease in the number of solvent molecules in the solution, causing a decrease in the number of carbamate molecules. This can negatively affect the proton exchange mechanism of catalysts and subsequent CO_2 flux across the membrane. Therefore, to keep the CO_2 flux and efficiency of the C-MVR as high as possible without any potential precipitation in the process, potassium carbonate (K_2CO_3) was used as an additive to 3 M TauK solution and tested in the C-MVR rig at 100 °C. K_2CO_3 is widely recognized as a suitable solvent for CO_2 removal in a range of industries due to its stability, environmental friendliness, and cost-effectiveness (153). However, its slow reaction rate with CO_2 poses significant challenges for its widespread application (154, 155). In this study, K_2CO_3 was selected as a 0.5 M additive to the 3 M TauK solution due to its buffering effect, which helps control pH and minimize precipitation (156-158). **Figure 5.4e, f** shows the resulting CO_2 desorption performance curves, CO_2 fluxes, and catalyst enhancement for the 3 M TauK+0.5 M K_2CO_3 solution. Compared to the results of 3 M TauK, the formation of precipitation in the solvent used was significantly reduced (**Figure A.16**). The CO_2 transfer rate and catalyst effect showed only a minimal reduction, from 34.5% (**Figure 5.3f, g**) to 32.5% (**Figure 5.4e, f**), despite the basic behavior of the added K_2CO_3, which could adversely affect the regeneration process. Considering these observations, optimizing the concentrations of TauK and K_2CO_3 would be beneficial to further adjust the CO_2 transfer rate, minimize any potential precipitation, and operational issues.

5.2.6 Catalyst Stability

The stability of ion exchange resins was investigated in the four consecutives C-MVR trials at 100 °C for 3 M TauK. As shown in **Figure 5.4g**, the catalyst performance dropped by 4.9% for the first cycle followed by 1.5% reduction for the second and third. The latter reduction highlighted the successful and continuous proton exchange mechanism in the catalytic solvent regeneration process for resin beads which can recover the lost protons. Furthermore, XPS analysis confirmed the stability in intensity of SOH and SO groups and content of sulfur and O-H bonds in different cycles of the catalyst (**Figure 5.4h** and **Figure A.14c**). Also, it is notable that for full recovery of acidic cation resins after long-term operation, it can easily be regenerated by strong acids such as sulfuric acid (H_2SO_4) or hydrochloric acid (HCl).

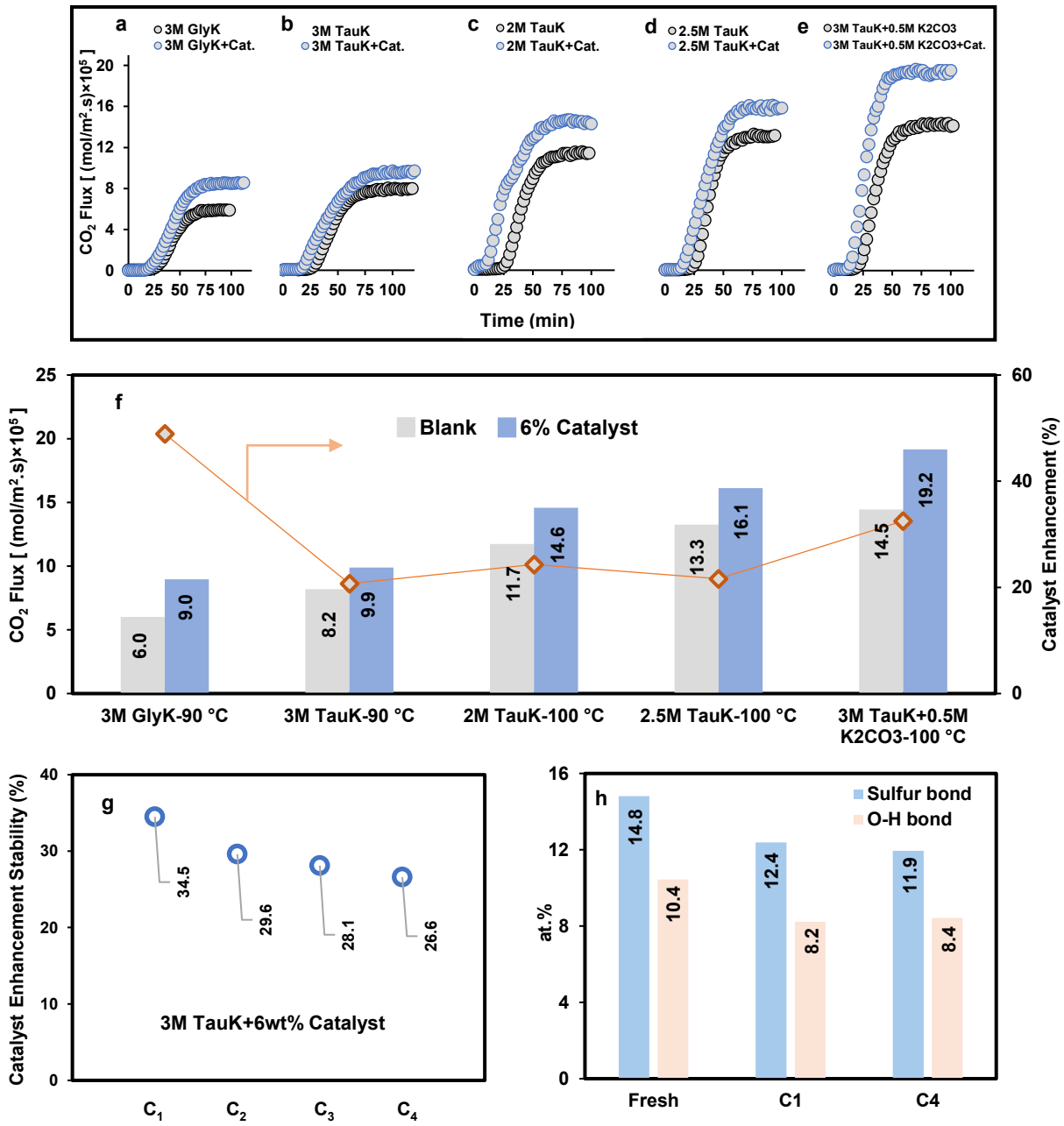

Figure 5.4. a) CO_2 desorption profiles for GlyK, and b) TauK with/without catalyst at 90 °C. c) CO_2 desorption profiles for 2 M TauK, d) 2.5 M TauK, and e) 3 M TauK+0.5 M K_2CO_3 with/without catalyst at 100 °C. f) CO_2 flux and catalyst enhancement values for (a-e). g) Catalyst stability in four cycles. h) Sulfur and O-H bond content for fresh, first and forth cycles. All trials were accomplished at 2-4 kPa(a), 0.25 L/min, using Resin A (6wt% concentration).

5.3 Conclusion

In this study, a sustainable integrated system of solid acid catalysts (ion exchange resins) and low-temperature membrane vacuum regeneration (MVR) using green amino acid salts was developed and analyzed for use in DAC systems. For non-catalytic trials, various commercial membrane modules with distinct features and transfer mechanisms (membrane distillation and

pervaporation) were assessed. Ultra-thin dense PDMS composite membrane was selected as a suitable contactor for MVR in DAC. Among the four screened green amino acid salts, TauK exhibited the highest CO_2 separation performance (59.4% higher compared to GlyK). Further parametric analysis was performed at different regeneration temperatures (80-100 °C) and solvent flow rates (0.05-0.25 L/min). From 80 to 100 °C, a major improvement (over ~180%) in CO_2 desorption performance was measured for TauK and no considerable effect was observed by a change in solvent flow. For catalytic experiments (C-MVR), the performance of 3wt% and 6wt% of commercial acidic cation resins with various green amino acid salts was assessed. The results showed that doubling the catalyst concentration doubles or triples the catalyst effectiveness, depending on the solvent type. Among the amino acid salts, the maximum catalyst enhancement (using 6wt% concentration) was observed on GlyK with a value of 64.4%, followed by 34.5% for TauK. The catalyst enhancement resulted in up to a 39.1% reduction in thermal energy input. Despite the lower catalytic impact on TauK, the highest CO_2 flux and lowest thermal energy consumption values were recorded for TauK. Furthermore, a 10 °C decrease in regeneration temperature resulted in a ~14-15% reduction in the catalyst enhancement parameter (CE%). To minimize any potential solid formation in TauK, C-MVR trials at lower concentrations and in the presence of K_2CO_3 as an additive were conducted. Lower solvent concentrations resulted in lower CO_2 desorption rates and catalyst effects. Additionally, adding K_2CO_3 minimized solid formation and had a minimal effect on the CO_2 desorption performance and catalyst effect. The results of this study clearly illustrate the suitability of integrating catalyst solvent regeneration with MVR for a sustainable and energy-efficient liquid-based DAC.

This chapter presented the integration of MVR units with catalytic solvent regeneration as a step toward a more energy-efficient and sustainable DAC process. Several commercial membrane modules with different specifications and mass transfer mechanisms were evaluated, and a thin PDMS composite membrane was identified as the most suitable contactor. Among the amino acid salts studied, TauK consistently demonstrated superior CO_2 separation performance at different conditions. The integration of the MVR unit with acidic ion-exchange catalysts significantly enhanced solvent regeneration efficiency, resulting in a notable reduction in thermal energy demand of up to 40%. These findings confirm the potential of combining catalytic solvent regeneration with MVR as a promising approach for advancing efficient and sustainable DAC technologies. Building on the insights gained in this chapter and the successful evaluation of advanced energy-efficient technologies, the next chapter further develops the system by coupling the MVR unit and catalytic regeneration with a hybrid solvent system. TauK is selected as the primary component in the hybrid blend due to its superior performance demonstrated in this chapter. Notably, composite metal oxide catalysts were synthesized and evaluated for MVR operation due to excellent observed performance in previous studies.

CHAPTER 6

Catalytic Hybrid Solvent Regeneration in Membrane Vacuum Processes for Direct Air Capture

.

The chapter has resulted in the following publication under review:

Momeni A, Anisi H, McQuillan RV, Alivand MS, Zavabeti A, Askari S, Zhang R, Stevens GW, Mumford KA. Catalytic Hybrid Solvent Regeneration in Membrane Vacuum Processes for Direct Air Capture. ***Under Review***.

6.1 Introduction

Direct air capture (DAC) has emerged as a key technology in addressing climate change, offering the capability to remove CO_2 directly from the atmosphere and contributing to achieving net-zero emissions targets (57). Despite its potential, DAC is an energy-intensive process, with significant technical and economic challenges (6). Solvent-based technology, a viable and mature approach for CO_2 capture (including in DAC), uses liquid as a sorbent to capture CO_2. However, it requires substantial thermal energy and a high operating temperature (typically 120-140 °C) to regenerate the solvent by breaking the bonds of CO_2-bound species (14, 159).

Given these challenges, various strategies have been explored to reduce energy consumption, including phase-change solvents (30), crystallization-based regeneration (11), hybrid solvents (32), and catalytic solvent regeneration (33). In the context of DAC, improving energy efficiency is even more critical due to the ultra-low CO_2 concentration (~0.04%) and partial pressure in ambient air, which results in significantly lower equilibrium loadings compared to flue gas systems (29). Therefore, selecting an appropriate solvent and combining multiple energy-efficient regeneration techniques would be a promising approach to reduce energy input while enhancing the durability, reliability and sustainability of liquid-based DAC systems, ultimately paving the way for the large-scale deployment.

Hybrid solvents (mixtures of two or more CO_2-capturing absorbents) have emerged as a viable strategy for carbon capture, particularly in reducing the energy required for solvent regeneration (50). By mixing various solvents with distinct properties, the blends can outperform single-solvent systems, enhancing CO_2 absorption efficiency while lowering regeneration energy demands (52). While extensive research has been conducted on amine-based solvent blends for point-source CO_2 capture, their application in DAC remains largely

unexplored. This gap is especially notable for amino acid salt solutions, which are suitable for capturing CO_2 from ambient air due to their unique properties of low volatility, oxidation resistance, and environmental compatibility (160, 161). In this regard, investigating the performance of suitable amino acid solvent blends could offer a practical and energy-efficient pathway for advancing solvent-based DAC.

In addition to hybrid solvents, catalytic solvent regeneration has emerged as another promising approach to reducing the energy penalty in liquid-based CO_2 capture technologies (43). By incorporating solid acid catalysts during low-temperature regeneration (typically 80-100 °C), CO_2 desorption can be significantly enhanced, lowering the thermal energy required for solvent regeneration (34). A wide range of solid acid catalysts including zeolites (35), metal oxides (36), mesoporous silica (37), and carbon-based materials (38) have been introduced and fabricated for this purpose, each offering distinct physicochemical properties and have been tested with different solvent classes, including conventional amines, solvent blends, and amino acid-based solutions (39) with few under DAC conditions (40). Among these catalysts, sulfated zirconia (SZ) has received considerable attention due to its strong acidity, environmentally benign nature, ease of synthesis and remarkable enhancement when supported on a mesoporous structure (e.g., SiO_2, Al_2O_3, MCM-41), benefiting from a high density of Lewis and Brønsted acid sites, as well as large accessible area of the superacid sites (41, 42). The catalytic activity of SZ can be further enhanced by metal doping, which introduces basic sites and strengthens both Brønsted and Lewis acid sites (43). Among various metals, Fe-modified catalysts have demonstrated considerable catalytic effectiveness, attributed to iron's ability to enhance both acidic and basic sites (44, 45). Therefore, the fabrication of Fe-modified sulfated zirconia (Fe-SZ) on mesoporous SiO_2 or Al_2O_3 supports is considered in this work to evaluate its performance in a membrane vacuum regeneration (MVR) system.

Hence, assessing catalytic enhancement with hybrid solvents within a MVR unit, which is a practical, low-temperature, and sustainable process, can provide highly impactful and valuable insights into the energy efficiency of scalable DAC systems which has not been investigated yet. In this study, a series of Fe-promoted SZ (Fe-SZ) catalysts supported by mesoporous silica and alumina (Fe-SZ/SiO_2 and Fe-SZ/Al_2O_3) were synthesized and integrated into a fixed-bed system coupled with a low-temperature MVR DAC unit. Based on the insights from Chapters 4 (124) and 5 (128) and previous studies (40, 145), GlyK, SarK, and TauK demonstrated high CO_2 desorption performance and suitable thermal stability, with taurine showing particularly strong stability. These solvents were selected as single amino acid candidates, while a hybrid blend of TauK (as the primary component with the best cyclic capacity) and SarK (with the highest basicity) was chosen to evaluate performance in the designed rig. The influence of the fabricated catalysts on CO_2 desorption performance and energy reduction was further assessed at 90 °C.

To start experiments, the CO_2 and water separation performance of three hollow fiber membrane contactors (HFMCs) were assessed. Catalytic MVR trials were conducted using Fe-SZ/Al_2O_3 and Fe-SZ/SiO_2 with varying SZ/SiO_2 mass ratios (1/1, 1/2, and 2/1), followed by an evaluation of the impact of varying catalyst concentrations. Next, the solvent regeneration performance of various single and hybrid amino acid solvents was investigated, leading to the selection of the most effective blend, giving the highest CO_2 flux and lowest energy consumption. In the final stage, to further enhance the energy efficiency of the MVR unit, catalytic trials were conducted using both single solvents and the selected optimal blend. The findings of this study provide valuable insights into energy efficiency, feasibility, and benefits of integrating multiple energy-efficient technologies, including low-temperature MVR, hybrid solvents, and catalytic solvent regeneration, into DAC processes.

6.2 Results and Discussion

6.2.1 Membrane Module Performance

To evaluate the CO_2 stripping and water flux performance of various HFMCs, 3M GlyK was used as the benchmark solvent (124, 128, 133). The CO_2 desorption flux profiles for each HFMC are shown in **Figure A.17**. **Figure 6.1b-d** summarizes the maximum CO_2 flux achieved during the operation, along with the corresponding water flux and the water to CO_2 flux ratio. As shown, $HFMC_1$, with reported specification in **Table 3.3**, exhibited the highest CO_2 flux (19.7×10^{-5} mol/m^2.s) as well as the highest water flux (93×10^{-4} mol/m^2.s). In contrast, $HFMC_2$, which had a similar pore size to $HFMC_1$ but included an additional thin dense coating (3-5 μm), demonstrated a comparable CO_2 flux while significantly reduced water flux (from 93×10^{-4} to 74×10^{-4} mol/m^2.s). This behavior is attributed to the pervaporation mechanism in $HFMC_2$, facilitated by a thin non-porous PDMS layer. This coating acts as a barrier against pore wetting and convective water transport, while still permitting selective CO_2 diffusion via the solution-diffusion mechanism (91).

Alternatively, in membranes without a coating layer, pore wetting can be mitigated by narrowing the pore size distribution. This increases the breakthrough pressure, reducing the possibility of liquid breakthrough into the gas-filled pores (162). In this regard, the performance of $HFMC_3$, which featured narrower pores size distribution, was examined. As shown in **Figure 6.1b, c,** this led to a considerable reduction in water flux, achieving equal performance to $HFMC_2$. However, the smaller pore size also introduced additional mass transfer resistance, resulting in a lower CO_2 flux compared to both $HFMC_1$ and $HFMC_2$ (~16% reduction). This highlights the crucial importance of optimizing membrane pore structure in membrane distillation systems to achieve an effective balance between CO_2 and water transport (21, 86). To compare overall performance, the water to CO_2 flux ratio was reported for all modules (**Figure 6.1d**). $HFMC_2$ demonstrated the most favorable ratio of 38, confirming the effective

role of the thin PDMS layer and pervaporation mechanism in enhancing CO_2 selectivity in MVR system in liquid-based DAC applications. Therefore, $HFMC_2$ was selected as a suitable module for conducting the remainder of the experiments. To assess the repeatability and accuracy of the experimental setup, desorption tests with 3M GlyK and $HFMC_2$ were repeated three times. **Figure A.18** presents the results, showing minimal variation and confirming the high consistency of the data.

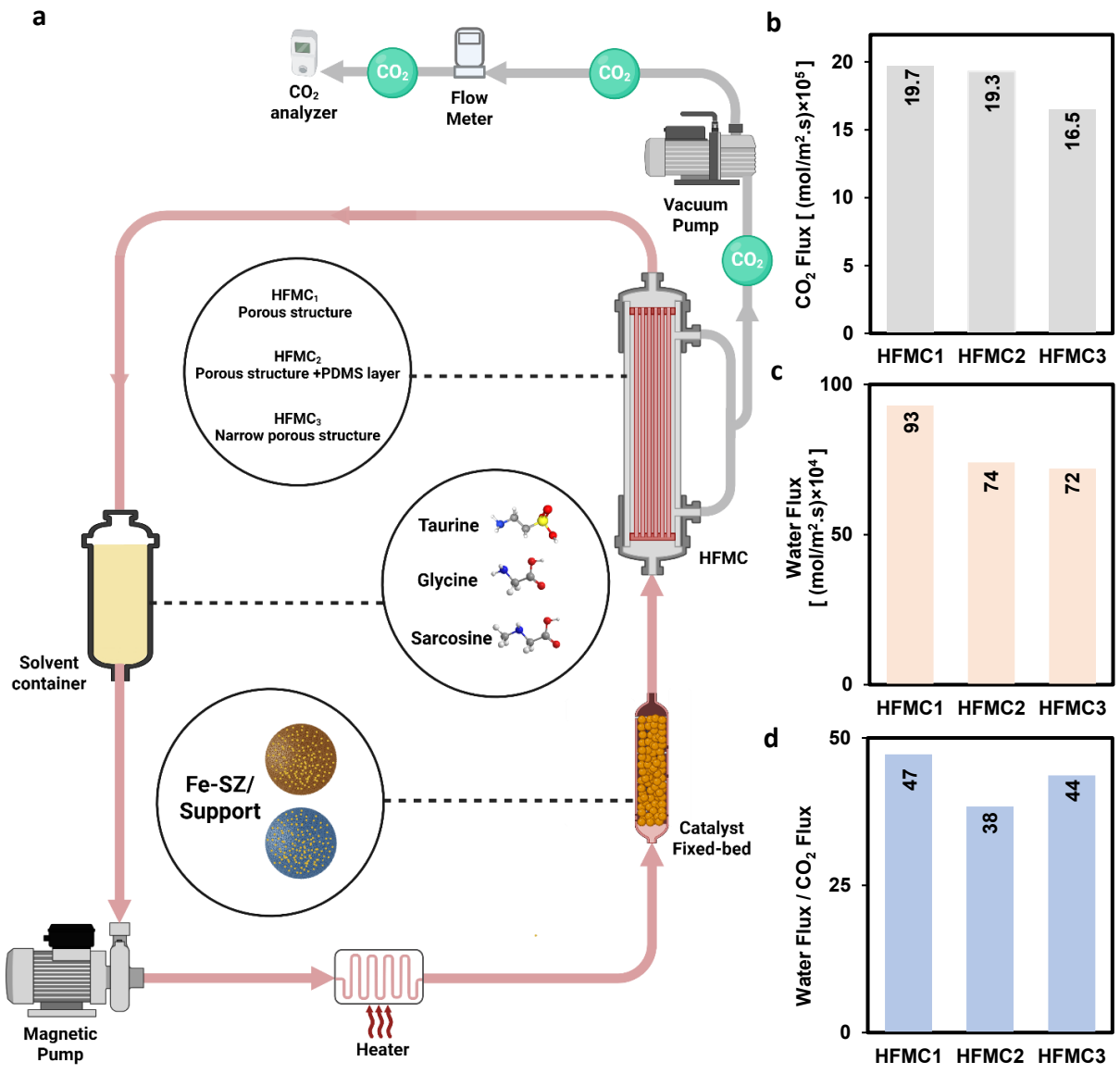

Figure 6.1. a) Schematic flow diagram of MVR unit with fixed bed catalyst. HFMCs performance detailing b) maximum CO_2 flux, c) Water flux, and d) Water flux to CO_2 flux ratio.

6.2.2 Composite Solid Acid Catalyst

6.2.2.1 Catalytic Support (SiO_2 vs. Al_2O_3)

Catalysts were synthesized by impregnating two distinct catalytic supports, SiO_2 and Al_2O_3, following the procedure described and schematically illustrated in **Figure 6.2a**. The resulting catalysts, Fe(10%)-SZ/SiO_2(1/1) and Fe(10%)-SZ/Al_2O_3(1/1), were placed in a fixed-bed chamber and loaded to 6wt% concentration to evaluate their effectiveness. MVR trials were conducted using 3M GlyK at 90 °C.

Under the mentioned conditions, the two catalysts exhibited notably different performance. The Al_2O_3-supported catalyst showed only a minimal improvement in CO_2 desorption flux, with enhancement below 2%. In contrast, the SiO_2-supported catalyst demonstrated an enhancement of 25.6%. Such superior performance of SiO_2 over Al_2O_3 in catalytic regeneration has been observed in previous studies, both as a standalone catalyst and as a catalytic support (41, 42, 163). Although the performance difference in supported catalyst configurations was relatively moderate, SiO_2-supported catalysts generally outperform their Al_2O_3-based counterparts due to enhancements in Brønsted acidity and textural properties (41, 43). Furthermore, in this study, the SiO_2 support exhibited a larger average pore size (~50 nm) compared to Al_2O_3 (~30 nm), which can facilitate a more stable integration of Fe-SZ into its mesoporous structure and improve accessibility of active sites during regeneration.

Figure 6.2b shows the morphological and compositional characterizations of the impregnated SiO_2 support using SEM, and TEM-EDX analyses. SEM images display that the catalyst support exhibited a relatively smooth surface morphology, suggesting uniform surface coverage and interaction between the support and loaded Fe-SZ species. At higher magnifications, the SEM images also highlighted the preserved porous network of the support, which is essential for maintaining accessibility to active sites. Furthermore, TEM-EDX

confirmed the uniform dispersion of zirconium, sulfur, and iron across the support matrix, indicating successful anchoring of the Fe-SZ component into the porous framework. High resolution TEM images of the Fe-SZ/SiO_2(1/1) sample provide close-up views in different magnification revealing the nanostructured morphology of the synthesized catalyst along with the amorphous structure of SiO_2 (**Figure A.19**).

Following the morphological and elemental analysis of Fe-SZ/SiO_2(1/1), XPS was used to examine the surface chemical states and bonding environment of the synthesized catalyst (**Figure 6.2c-e**). According to **Figure 6.2c**, the S 2p spectrum exhibited a characteristic doublet at approximately 169–170.5 eV, corresponding to the S 2p3/2, and S 2p1/2 binding energies of sulfate species (SO_4^{2-}) (164), which play an important role in catalytic activity through their high electron negativity and generation of Brønsted acid sites (165, 166). The Zr 3d spectrum showed two main peaks at around 183.5.eV (Zr 3d5/2) and 185.9 eV (Zr 3d3/2), which are attributed to Zr (IV), likely ones coordinated within the sulfated framework due to higher bonding energies compared to ZrO_2 (166, 167). The Fe 2p spectrum displayed a prominent peak near 711 eV (Fe 2p3/2), and 724 (Fe 2p1/2) accompanied by a distinct satellite feature, which is characteristic of Fe^{3+} species (168). This confirms that iron is predominantly present in a trivalent state, mainly as Fe_2O_3-like species (45, 169). Additionally, the O 1s spectrum (**Figure A.20**) was deconvoluted into two components: a peak near 529.8 eV, attributed to metal-oxygen bonds (Zr-O, Fe-O), and a main one near 532.4 eV, related to the surface sulfate groups and hydroxyl groups (-OH) and Si-O-Si (167, 170). These results collectively indicate the successful loading of SO_4^{2-}, Zr^{4+}, and Fe^{3+} species into the porous SiO_2 matrix, supporting the formation of a well-dispersed, catalytically active Fe-SZ structure.

The CO_2 desorption profiles of 3M GlyK regenerated at 90 °C, with and without the Fe-SZ/SiO_2(1/1) catalyst, are shown in **Figure 6.2f**. As illustrated, upon heating the solvent, the CO_2 desorption flux initially increased due to the high CO_2 loading and the accelerated

breakdown of less stable CO_2-containing species in GlyK (115). As the solvent temperature approached the setpoint and stabilized, the CO_2 flux reached a peak followed by a decline. This behavior, observed in previous studies, is attributed to the regeneration of more stable CO_2 species and the progressive depletion of CO_2 from the solvent (115). The latter leads to a reduction in CO_2 partial pressure on the solvent side of the membrane, thereby decreasing the driving force for mass transfer and resulting in a drop in CO_2 flux. Compared to the blank trial, the presence of the SiO_2 promoted with Fe-SZ catalyst led to an earlier onset of CO_2 desorption and a higher peak flux (19.3×10^{-5} to 21.0×10^{-5} mol/m^2.s). This enhancement is indicative of accelerated CO_2 desorption kinetics, enabled by the acidic and basic active sites of the catalyst that facilitate the breakdown of carbamate and bicarbonate species through proton transfer mechanisms (34, 43). This can lead to a higher partial pressure of CO_2 on the solvent side and increase flux. Moreover, the gradual CO_2 flux reduction once the temperature stabilized implies continued catalytic activity on breakdown CO_2-containg species under reduced solvent CO_2 loading conditions, which contributes to overall higher CO_2 moles desorption and efficient regeneration.

The overall catalytic effect was quantified using Equations 3.11 and 3.13, as shown in **Figure 6.2g**. The SiO_2 supported catalyst enabled a 25.6% increase in CO_2 desorption over 30 minutes of operation, raising the total amount of desorbed CO_2 from 244 to 307 mmol for 3M GlyK. These results highlight the potential of Fe-SZ/SiO_2 as an effective and suitable catalytic material for energy- efficient solvent regeneration in MVR processes.

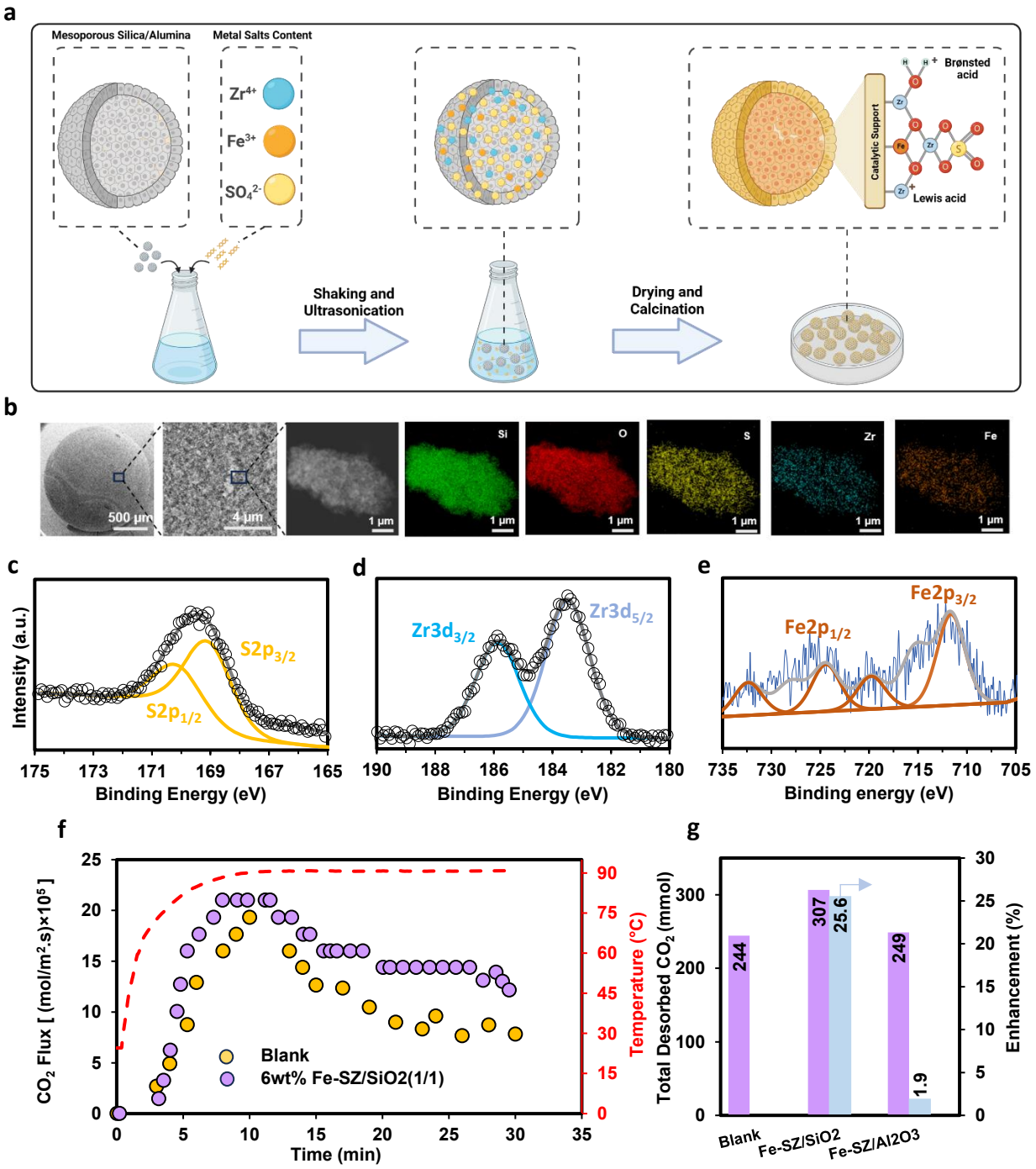

Figure 6.2. a) Schematic synthesis procedure (impregnation method) for two mesoporous substrate silica and alumina. b) SEM images and TEM-EDX mapping of Fe-SZ/SiO_2(1/1). High-resolution XPS spectra of the Fe-SZ/SiO_2(1/1) catalyst showing core-level signals of c) S 2p, d) Zr 3d, and e) Fe 2p. f) CO_2 flux profiles with and without Fe-SZ/SiO_2(1/1). g) Total desorbed CO_2 and catalyst enhancement of Fe-SZ/SiO_2(1/1) and Fe-SZ/Al_2O_3(1/1). All MVR trials were accomplished using 3M GlyK at 90 °C. No catalyst is used for blank solvent. All catalysts were doped with 10% Fe.

6.2.2.2 SZ to SiO_2 ratio

To evaluate the effect of different mass ratios of SZ on the SiO_2 support, catalysts were synthesized at 1/2 and 2/1 ratios and their catalytic effectiveness were measured and compared with the baseline 1/1. **Figure 6.3a**, and **Figure A.21a** present the CO_2 desorption profiles of using 6wt% concentration of 1/2 and 2/1 ratios, respectively in 3M GlyK. As shown in **Figure 6.3a**, the Fe-SZ/SiO_2 (1/2) exhibited a noticeable increase in CO_2 desorption during the initial heating stage. The earlier onset of desorption compared to the blank solvent suggests that the catalyst promotes CO_2 desorption during the heating ramp. Furthermore, the CO_2 flux remained consistently higher throughout the stabilized temperature zone, indicating the catalyst activity in that region. According to **Figure 6.3a**, the Fe-SZ/SiO_2 (1/2) increased the total CO_2 desorption amount from 244 to 278 mmol, corresponding to a 13.7% improvement. Notably, this value is approximately 46% lower than the one achieved with the 1/1 ratio of SZ to SiO_2. Increasing the Zr and S loading on SiO_2, Fe-SZ/SiO_2(2/1), not only failed to further improve performance but also resulted in a decline relative to both the 1/1 and 1/2 ratios, achieving only a ~4.0% enhancement (**Figure A.21a**). This decline is attributed to oversulfation of the catalytic support, resulting from the doubled sulfur content in Fe-SZ/SiO_2(2/1). Such excessive SZ loading on the support can lead to non-uniform dispersion on the surface of support and block mesopores (171, 172), as clearly observed on the catalyst surface through SEM and SEM/EDX analyses (**Figure A.21b**). This condition can hinder the accessibility to acidic active sites of ZrO_2 and Fe_2O_3, which are major contributors for creating Brønsted and Lewis acid sites for catalytic performance (166, 173).

To further investigate the acid site distribution within the SiO_2-supported catalysts, NH_3-TPD analysis was conducted on all synthesized samples. The desorption profiles are presented in **Figure 6.3b**, and the corresponding quantified acidity values are listed in **Table A.2**. In this technique, low-temperature desorption peaks (~100-200 °C) are typically attributed to weak

acid sites, whilst peaks in the 200-400 °C range correspond to moderate acid sites, and high-temperature peaks above 400 °C indicate strong acid sites (33). According to the results, all Fe-SZ/SiO_2 catalysts demonstrated a pronounced total acidity, predominantly in the strong acid region (>400 °C), with negligible desorption in the weak to moderate regions. Additionally, the featureless profile of pristine SiO_2 confirms its lack of acidic functionality, emphasizing the critical role of Fe-SZ in introducing and enhancing catalyst acidity. This observed increase in acidity can be further quantified by examining the total acid sites (TAS). The trend in TAS across the catalysts followed the order of 2/1 > 1/1 > 1/2 > SiO_2 (**Table A.2**). The high TAS, combined with the mesoporous structure of the support which improves accessibility to carbamate species, is a key factor contributing to the enhanced catalytic performance (174). As previously discussed, despite 2/1 sample having the highest acidity and acid strength, its relatively poor performance is attributed to excessive sulfate deposition and pore blockage. Comparing the 1/1 and 1/2 ratios, the 1/1 catalyst exhibited higher TAS than the 1/2 sample, along with a distinct high-temperature desorption peak at 678 °C, indicating the presence of stronger acid sites. This may reflect a more favorable ratio of Zr sites coordinated to sulfate groups and Zr–OH groups interacting with SO_4^{2-}, both of which are known to contribute to strong acidity in sulfated zirconia catalysts (172, 175). Therefore, the superior catalytic performance of the 1/1 sample can be attributed to its combination of stronger acidity and greater TAS density compared to 1/2, as well as more accessible and uniformly dispersed acid sites compared to the oversulfated 2/1 sample.

To further evaluate the role of basic sites in catalyst effectiveness, CO_2-TPD analysis was conducted on all synthesized samples. The corresponding data are presented in **Figure 6.3d** and **Table A.2**. Results confirmed that the 1/1 sample possessed higher basic sites density compared to 1/2 and strongest basic sites (desorption peak at 681 °C) among all, which play a critical role in the deprotonation of protonated amino acid species (44, 45).

6.2.2.3 Catalyst Concentration and Stability

To investigate the effect of catalyst loading on system performance, energy reduction, and to determine its optimal value, the catalyst concentration was increased from 6 wt% to 9 wt% and 12 wt%. **Figure 6.3c** displays the CO_2 desorption profiles for 3M GlyK with 9 wt% catalyst in MVR unit. As shown, the presence of increasing amount of catalyst had a remarkable impact on CO_2 desorption rates, evident in the regions where the solvent temperature rises, at the peak flux, and in the stabilized temperature zone; **Figure 6.3e**, **f** highlight this impact. Upon increasing the catalyst concentration to 9 wt%, the maximum CO_2 flux improved from 19.3×10^{-5} to 28.2×10^{-5} mol/m^2.s, and the total desorbed CO_2 increased from 244 to 377 mmol, corresponding to a 54.3% catalytic enhancement. This improvement is more than two-fold compared to that observed with 6 wt% catalyst. This enhancement results mainly from the greater number of accessible acidic and basic sites that facilitate the deprotonation of H^+GlyK and the breakdown of carbamate and bicarbonate species. These effects promote greater CO_2 release in the solvent, raise the partial pressure on the solvent side of the membrane, and ultimately contribute to the observed increase in flux (128, 129). To determine if this positive trend would continue with the same intensity, a 12wt% fixed bed catalyst trial was conducted (**Figure A.22a**). The outcome showed a clear improvement, with the peak CO_2 flux reaching 30.2×10^{-5} mol/m^2.s, and the enhancement rising to 67.5%, as shown in **Figure 6.3e**, **f**. Notably, the magnitude of improvement from 6 wt% to 9 wt% (112%) was greater than that from 9 wt% to 12 wt% (24.3%), suggesting a reduced catalytic effect beyond a certain concentration, indicating a presence of an optimum. This can be primarily due to the solvent approaching its CO_2 equilibrium as the catalyst amount increases in the system, considering the presence of catalyst does not alter the thermodynamic equilibrium (41, 176). Under these conditions, the system shifts from kinetically limited to one constrained by thermodynamics (116). Hence, to identify the optimum catalyst concentration, the enhancement factor was calculated using

Equation 3.14, and the corresponding values are reported in **Figure 6.3f**. As shown, the use of 9 wt% catalyst resulted in the highest enhancement factor of 6.0 and was therefore selected as the optimal concentration for further evaluations.

For relative heat duty and thermal energy consumption, both parameters were calculated using Equations 3.15 and 3.16 and are reported in **Figure 6.3g**. Accordingly, at 9 wt% and 12 wt%, the heat duty decreased by 35.2% and 40.3% as compared to the blank, respectively, reducing the thermal energy requirement from 7.8 to 5.1 and 4.7 GJ/tCO_2. These reductions clearly demonstrate the importance of catalyst presence in the MVR system and its significant role in reducing energy demand under DAC conditions.

Since the 9 wt% Fe-SZ/SiO_2 (1/1) was identified as the optimal catalyst concentration and support ratio (SZ/SiO_2), its stability was evaluated over four regeneration cycles using 3 M GlyK at 90 °C (**Figure A.22b**). As shown, the RH% increased from 64.8% in cycle 1 to 68.8% in cycle 2, representing an increase of approximately 6.2%. From cycle 2 to cycle 4, RH% rose more gradually from 68.8% to 71.4%, a change of about 3.8% over two cycles. This trend suggests that the catalyst experiences a decline in effectiveness after the first cycle, likely due to surface chemical changes, but begins to stabilize in subsequent cycles. The results highlight the catalyst recyclability and its ability to retain performance across repeated regeneration cycles.

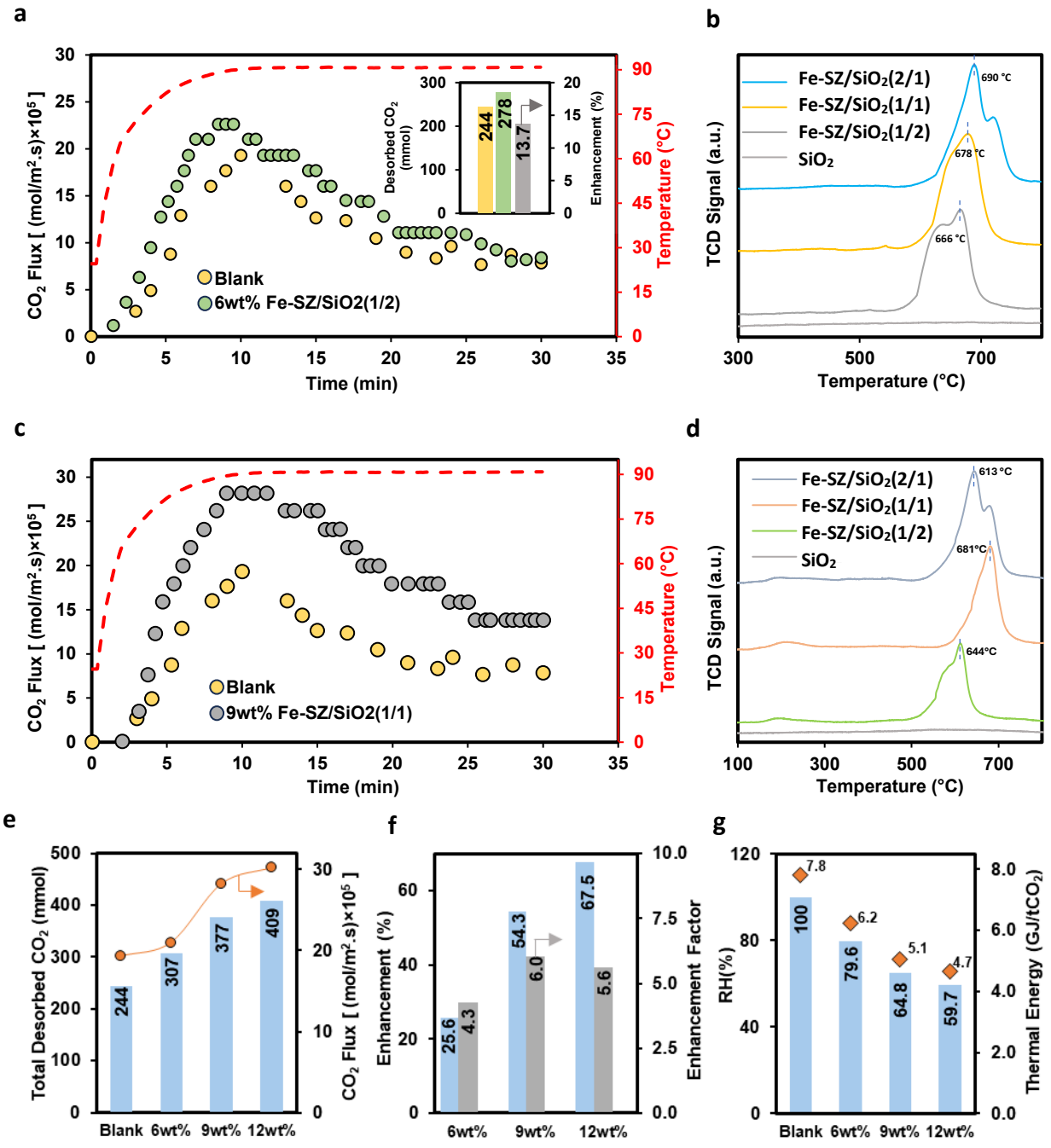

Figure 6.3. a) CO_2 flux curves and total desorbed CO_2 with and without 6wt% Fe-SZ/SiO_2(1/2), and catalyst enhancement. b) NH_3-TPD spectra of catalysts. c) CO_2 flux curves with and without 9wt% Fe-SZ/SiO_2(1/1). d) CO_2-TPD spectra of catalysts. e) Total desorption CO_2 amount, maximum CO_2 flux, f) catalyst enhancements, enhancement factor, g) relative heat duty, and thermal energy consumption of Fe-SZ/SiO_2(1/1) with 10% Fe doped at different catalyst concentrations. All MVR trials were accomplished using 3M GlyK at 90 °C. No catalyst is used for blank solvent.

6.2.3 Hybrid Amino Acid Solvents

By evaluating the performance of 3M GlyK in previous sections, the regeneration performance of two additional single amino acid solvents, 3M SarK and 3M TauK, were also examined. To analyze and optimize any possible improvements using hybrid solvents in MVR, a series of mixtures were prepared using 3M TauK as the main solvent, combined with varying concentrations of SarK (0.5M to 1.5M). **Figure 6.4a** presents the CO_2 DAC absorption equilibrium points for both the single solvents, previously reported in our study (40, 128), and the hybrid solvents, measured at 25°C. According to **Figure 6.4a**, increasing the SarK concentration in the 3M TauK solution up to 1.5M resulted in an increase in DAC equilibrium CO_2 uptake from 0.29 to 0.37 mol/mol. This improvement is primarily attributed to the higher CO_2 uptake capacity of SarK compared to TauK, which shifts the equilibrium upward upon its addition.

Figure 6.4b shows the CO_2 desorption profiles of the prepared solvents over a 30-minute run, while **Figure 6.4c, d** display the maximum achieved CO_2 flux and total desorbed CO_2, respectively. As shown, SarK exhibited the poorest regeneration performance among the tested solvents, consistent with previous observations (128, 145), achieving a maximum CO_2 flux of 19.2 $\times 10^{-5}$ mol/m^2.s and a total desorbed CO_2 amount of 224 mmol. This can be attributed to the stronger basic nature of SarK (higher pKa value) compared to the other evaluated solvents, despite its superior CO_2 absorption capacity (145, 177). In contrast, 3M TauK demonstrated considerably better desorption performance than both GlyK and SarK. It achieved a maximum CO_2 flux of 32.5 $\times 10^{-5}$ mol/m^2.s and a total desorbed amount of 348 mmol of CO_2, 55.3% higher than SarK. This superior performance is linked to the unique chemical structure of taurine, specifically the presence of the sulfonic acid group with high electronegativity (178). This group induces a strong inductive effect that lowers the pKa (179) compared to GlyK and

SarK, facilitating the deprotonation of protonated taurine (H^+TauK) and accelerating CO_2 desorption rates.

For the hybrid solvents, blending 3M TauK with 0.5M to 1.5M SarK significantly enhanced CO_2 desorption performance in all cases (**Figure 6.4b-d**). With the addition of only 0.5M SarK, the maximum CO_2 flux reached 44.3×10^{-5} mol/m^2.s with 526 mmol total desorbed CO_2, whilst the addition of 1M SarK further improved this to 53.9×10^{-5} mol/m^2.s and 589 mmol, corresponding to 51.1% and 69.2% improvements over 3M TauK alone, respectively. One of the main reasons for this observed behavior is the higher total molarity of the hybrid solvent which can lead to increased CO_2 absorption capacity (**Figure 6.4a**), resulting in the formation of a greater total number of CO_2-containg species. Breaking down a larger quantity of CO_2-containing compounds during regeneration allows for enhanced CO_2 liberation and improved performance (110, 124). This was confirmed by ^{13}C-NMR analysis of CO_2 loaded 3M TauK, and hybrid solvents with varying SarK concentrations (**Figure 8.23**), used to evaluate the quantity of CO_2-containing species present. Based on the spectral results and the intensity of the peak and area around 164.2 ppm, the quantity of carbamate species increased steadily (up to 30%) with the addition of 1.5M SarK. Considering the 3M TauK as major content in the hybrid solution, it seems that the coupling of H^+TauK deprotonation (a better proton provider than H^+SarK) with the increased carbamate species is the reason for the considerable CO_2 desorption enhancement observed. However, with continued the MVR trials, an interesting trend emerged when the SarK concentration increased beyond 1M. The CO_2 desorption performance declined, having a lower total desorbed CO_2 amount compared to the 3M TauK+0.5M SarK (506 mmol versus 526 mmol). This can be attributed to both the physical and chemical properties of the solvent. Increasing the SarK content raises the overall molarity, which in turn increases the viscosity of the solution and can reduce regeneration efficiency (180). On the chemical side, the strongly basic nature of SarK (due to its high pKa) can also

begin to negatively affect regeneration beyond a certain concentration. In other words, the amount of SarK added to TauK introduces a trade-off between beneficial and adverse effects. Based on this balance, 3M TauK+1M SarK was identified as the optimum hybrid solvent formulation.

The water transfer rate in membrane module for all prepared solutions was also evaluated. As shown in **Figure 6.4c**, among the single solvents, SarK exhibited the lowest water flux, followed by TauK and GlyK. This trend was consistent with previous findings and can be attributed to differences in molecular weight, viscosity and degree of hydrophilicity properties of the amino acids (128). For the hybrid solvents, increasing the total molarity further reduces water transfer, due to the higher molecular weight, viscosity, and greater amino acid concentration in the solution, highlighting their suitability for use in MVR systems.

Finally, **Figure 6.4d** presents the thermal energy consumption required for regeneration of all single and hybrid solvents. As shown, adding 1M SarK to 3M TauK reduced the regeneration energy from 5.5 GJ/tCO_2 to a minimum energy value of 3.2 GJ/tCO_2, demonstrating the effectiveness of hybrid solvent application on improving energy efficiency in DAC processes.

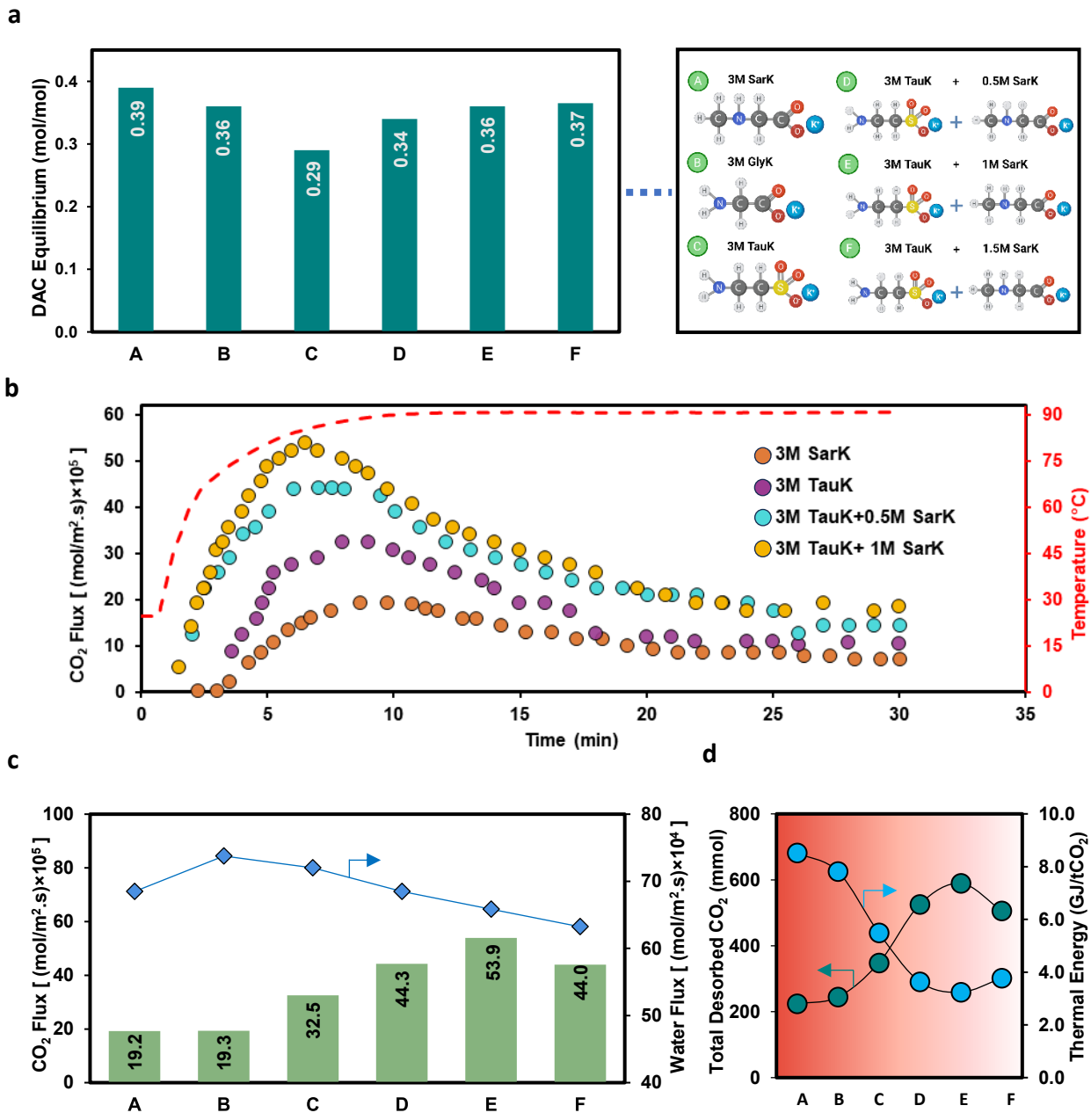

Figure 6.4. a) Measured CO_2 DAC equilibrium points for hybrid amino acid solvents alongside obtained values for single solvents in our previous studies (124, 128) (**A**-3M SarK, **B**-3M GlyK, **C**-3M TauK, **D**-3M TauK+0.5M SarK, **E**-3M TauK+1M SarK, **F**-3M TauK+1.5M SarK). b) CO_2 desorption flux profiles, c) maximum CO_2 flux, water flux, d) total desorbed CO_2, and thermal energy consumption for single and hybrid amino acid solvents. All MVR trials were conducted at 90 °C.

6.2.4 Catalytic Hybrid Amino Acid Solvents in MVR

To further evaluate the performance of a system combining hybrid solvents with catalytic solvent regeneration, a series of catalytic trials were conducted on SarK, TauK, and the selected hybrid solvent, 3M TauK+1M SarK. **Figure 6.5a-c** presents the catalytic CO_2 desorption

profiles of mentioned solvents compared to their blank performance. As shown in the profiles, all solvents exhibited an improvement in cumulative CO_2 desorption by using 9 wt% Fe-SZ/SiO_2(1/1) catalyst. The quantified values for these performances are presented in **Figure 6.5d, e,** highlighting the catalytic enhancements achieved up to 54.3%. As discussed earlier in this work and observed in previous studies (40, 128), among the evaluated short-chain single amino acids, 3M GlyK exhibited the highest catalytic effectiveness. For 3M SarK, due to its much higher pKa relative to GlyK and TauK, the addition of 9 wt% catalyst resulted in a relatively minor improvement, increasing the total desorbed CO_2 from 224 mmol to 271 mmol, corresponding to a 21.0% enhancement. This limited effect is consistent with the earlier discussed negative impact of SarK's strong basic nature on efficient regeneration when used at high concentrations; Similar catalytic behavior for SarK has been observed under DAC conditions with various catalysts (40, 128). For TauK, a 25.9% improvement was recorded, which is lower than that observed with GlyK. This behavior is mainly due to the sulfonic acid groups in TauK, which provide readily available protons by H^+TauK, thereby reducing its catalytic effect (128).

For a mixture of TauK and SarK solution, catalytic regeneration resulted in a 24.8% improvement, promoting cumulative CO_2 desorption from 589 mmol to 735 mmol. The latter is the highest recorded cumulative CO_2 desorption value in this study. It is noteworthy that, although the relative catalytic enhancements for TauK and TauK+SarK are quite similar, the absolute enhancement (the difference in total desorbed CO_2 between the catalytic trial and the blank trial) achieved by the hybrid solution was the highest among all the solvents. As shown in **Figure 6.5e**, catalytic regeneration of the TauK+SarK mixture increased the total desorbed CO_2 by 146 mmol compared to the other solvents, demonstrating a greater net improvement in regeneration performance. The main factor contributing to this improvement is the higher overall molarity and the greater availability of the carbamate species in the solution. However,

the higher proportion of TauK in the hybrid solvent, which provides available protons, along with the presence of more stable carbamate species formed from strongly basic SarK, may partially limit further catalytic enhancement.

To better illustrate the impact of hybrid solvent integration with catalytic solvent regeneration on system energy efficiency, the relative heat duty using different solutions with and without 9 wt% Fe-SZ/SiO_2(1/1) is shown in **Figure 6.5f**. Considering GlyK as a benchmark, the catalyst reduced the RH of GlyK, SarK, and TauK to 64.8%, 90.1%, and 55.8%, respectively. Notably, the combination of hybrid solvent with the catalyst further reduced the RH to 33.2%, corresponding to a 66.8% reduction in energy consumption. According to **Figure 6.5g**, which presents catalytic energy consumption for different solutions, the minimum recorded energy consumption belongs to the catalyst-hybrid solvent combination, reaching 2.6 GJ/tCO_2. This result, along with the observed improved performance, highlights the importance of integrating energy-efficient technologies and demonstrates the significant potential of this approach for developing a sustainable and energy-efficient DAC process.

It is noted that the reported energy values here represent only the sensible heat component, calculated using Equation 3.15. To estimate the total thermal energy consumption, additional factors such as the heat of reaction and heat loss associated with water transfer through fibers should also be considered. Due to the lack of available data for the used hybrid solvent, the heat of reaction was assumed to be equivalent to that of 3M TauK (2.0 GJ/tCO_2) (149). The heat loss through water vapor transfer for 3M TauK+1M SarK was estimated to be 1.9 GJ/tCO_2, assuming 90% heat recovery efficiency via a heat pump. When comsbined with the calculated sensible heat of 2.6 GJ/tCO_2, the total energy consumption is estimated to be 6.5 GJ/tCO_2, which is comparable to that of well-established DAC technologies (Table 5.1) (128).

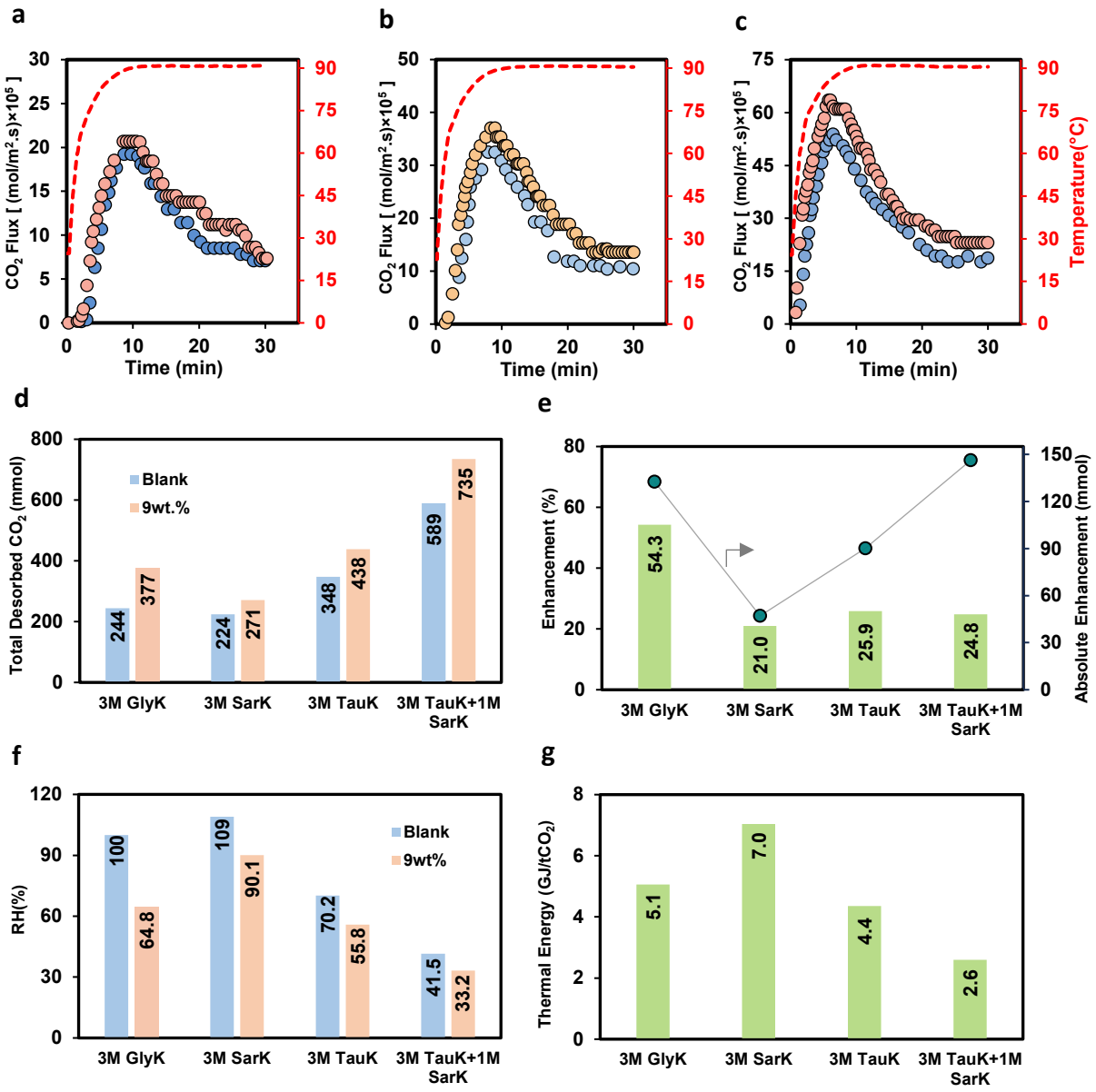

Figure 6.5. CO_2 flux profiles for a) 3M SarK, b) 3M TauK, and c) 3M TauK+1M SarK with and without catalyst. d) Total desorption CO_2 amount for single and hybrid solvent with and without catalyst, and e) corresponding relative and absolute enhancement of catalyst. f) Relative heat duties in comparison with 3M GlyK performance. g) Thermal energy consumption of catalytic single and hybrid solvents. All MVR trials were accomplished at 90 °C. Fe-SZ/SiO_2(1/1) with 10% Fe doped used as catalyst and the concentration was kept at 9wt% in all experiments. No catalyst is used for blank solvent.

6.3 Conclusion

In this study, a systematic analysis was conducted to investigate the integration effects of MVR, hybrid solvents, and catalysts on the energy efficiency of the regeneration section under DAC conditions. In the first stage, three HFMCs with various structural configurations were tested

in the MVR rig and the one with thin coated PDMS layer exhibited the most favorable results. In the next stage, Fe-SZ catalysts supported on alumina and silica were synthesized using the impregnation method. It was demonstrated that silica-based catalysts outperformed their alumina counterparts. Furthermore, a series of MVR analyses were conducted with different synthesized ratios of SZ to SiO_2, and the 1/1 ratio showed the best performance. The effect of catalyst amount in system was also evaluated, and 9 wt% fixed bed catalyst was identified as the optimal concentration, achieving a 35.2% reduction in the system's energy input. Following this, the impact of hybrid solvents based on TauK and SarK with varying SarK concentrations was examined. Among all formulations, 3M TauK+1M SarK showed the highest CO_2 desorption rate, resulting in a 69.2% improvement in cumulative CO_2 desorption compared to 3M TauK alone. After selecting the optimal hybrid formulation, the final stage involved integrating the hybrid solvent with the catalytic solvent regeneration in MVR unit, leading to a significant reduction in the relative heat duty to 33.2% compared to GlyK as a benchmark solvent and achieving a thermal energy consumption as low as 2.6 GJ/tCO_2. This study highlights the importance of integrating energy-efficient technologies to develop a practical and sustainable DAC process.

CHAPTER 7

Conclusion and outlooks

7.1 Thesis Summary

DAC is increasingly recognized as a critical technology for addressing climate crisis, offering the ability to remove CO_2 from the atmosphere and support progress toward net-zero emission targets. Despite progress, current DAC systems continue to face high energy consumption and considerable technical and economic barriers. One of the most established methods for DAC is the liquid-based approach, which uses solvents to capture CO_2 from ambient air. Yet, regenerating the CO_2-loaded solvents typically requires high operating temperatures and significant thermal energy to release the absorbed CO_2, making the process energy intensive and costly, while also accelerating solvent degradation. To address these limitations, it is essential to select suitable contactors capable of operating efficiently at low temperatures, along with solvents that are chemically and thermally suited to the specific conditions of DAC systems. In addition, integrating low-temperature, energy-efficient regeneration methods such as MVR, catalytic solvent regeneration, and hybrid solvent systems can further reduce the overall energy demand. Hence, this thesis investigates the CO_2 separation performance of HFMCs under DAC condition using green amino acid-based solvents for both absorption and desorption stages, with a particular focus on the desorption step, which is the energy demanding section. Furthermore, the potential energy savings from integrating multiple energy-efficient technologies to lower the overall energy demand of liquid-based DAC systems are evaluated.

In Chapter 4, two liquid-based DAC unit absorption, desorption using HFMCs were designed and developed. Trials under various operating conditions, utilizing non-porous HFMCs and different types of green amino acid salt aqueous solutions for absorption and vacuum low-temperature desorption were conducted. Regarding absorption, parametric analyses were carried out to optimize CO_2 separation efficiency by varying solvent temperature and concentration. Five amino acid salts were screened in long-term operation at 20 °C. Stable CO_2

absorption performance over a major part of the operation highlighted the potential of using amino acid solutions. GlyK was selected as the most suitable solvent for DAC among those evaluated in this chapter. For the MVR process, a systematic analysis of key variables was also carried out. The results showed that operating at higher temperatures (70-90 °C) and under vacuum pressures (21-81 $kPa_{(a)}$) considerably enhanced the CO_2 removal flux. Moreover, operating the vacuum system without any sweep gas was found to be more favorable, as it avoided excessive water loss. To investigate the impact of membrane module characteristics on CO_2 separation efficiency, a validated model was employed to analyze the effect of membrane dense layer thickness on DAC absorption and desorption performance. The simulation results demonstrated a substantial improvement in CO_2 separation, over 100%, as the dense layer thickness was reduced from 55 µm to 1 µm. This chapter provided a comprehensive understanding of the performance of various green amino acid solvents in HFMC-based absorption and low-temperature MVR, while also emphasizing the critical role of membrane characteristics in enhancing CO_2 separation efficiency.

Building on the knowledge gained in Chapter 4, Chapter 5 focuses on the further development of the MVR unit, which was integrated with catalytic solvent regeneration to enhance the sustainability and energy-efficiency of the DAC system. In the non-catalytic experiments, various commercial membrane modules with distinct properties were evaluated. An ultra-thin dense PDMS composite membrane was identified as a suitable contactor for MVR in DAC applications. Among the four green amino acid salts tested, TauK demonstrated the highest CO_2 separation performance, achieving a 59.4% improvement compared to GlyK. Additional parametric studies were conducted at varying regeneration temperatures (80–100 °C) and solvent flow rates. In the catalytic experiments (C-MVR), the performance of 3 wt% and 6 wt% commercial acidic cation resins was evaluated with different amino acid salts. Among the tested solvents, GlyK exhibited the highest catalytic enhancement at 64.4% with 6 wt%

catalyst, followed by TauK at 34.5%. This catalytic effect contributed to a reduction in thermal energy input of up to 39.1%. Despite a lower catalytic response, TauK delivered the highest CO_2 flux and the lowest thermal energy consumption (10.6 GJ/tCO_2), comparable to established DAC technologies. To prevent any precipitation in TauK, K_2CO_3 was added to the 3M TauK solution, which had minimal impact on desorption kinetics and catalytic performance. Overall, the results confirm the potential of integrating catalytic solvent regeneration with MVR as a promising pathway toward more energy-efficient and sustainable liquid-based DAC systems.

In Chapter 6, further enhancements were made to the MVR unit to improve its performance and lower energy demand. The unit was integrated with both hybrid solvents and a composite metal oxide catalyst. For employing new HFMCs with different characteristics, the MVR system was also scaled up. In the first phase, three HFMCs with different structural configurations were tested. The module with a thin coated PDMS layer delivered the most favorable results, outperforming all previously evaluated HFMCs in previous chapters. In the next phase, Fe-SZ catalysts supported on silica and alumina were synthesized using the impregnation method. Silica-supported catalysts demonstrated superior performance, and among various formulations, Fe-SZ/SiO_2 (1/1) at 9 wt% was identified as optimal, achieving a 35.2% reduction in thermal energy input. Subsequently, the performance of hybrid solvents based on TauK and SarK, with varying SarK concentrations, was evaluated. The formulation of 3 M TauK + 1 M SarK exhibited the highest CO_2 desorption rate, resulting in a 69.2% increase in cumulative CO_2 desorption compared to 3 M TauK alone. After identifying the optimal hybrid formulation, it was integrated with catalytic solvent regeneration in the MVR unit. This final configuration led to a substantial reduction in relative heat duty to 33.2% compared to GlyK, with a total thermal energy consumption of 6.5 GJ/tCO_2.

Overall, this thesis provided a detailed review of liquid-based DAC of CO_2 systems, with a focus on enhancing energy-efficiency and sustainability of the process. The findings clearly demonstrate that the selection of suitable contactors and solvents, together with the integration of multiple advanced, energy-efficient technologies, plays a critical role in reducing the overall energy demand. Three energy-efficient technologies were examined and their impacts on CO_2 separation and energy consumption were demonstrated: low-temperature membrane vacuum regeneration, catalytic solvent regeneration, and hybrid solvent regeneration. The results highlight that DAC systems operating at low temperatures, when combined with these technologies, can significantly minimize energy input, paving the way for sustainable and energy-efficient DAC processes suitable for large-scale deployment.

7.2 Recommendations for Future Work

This thesis has explored the CO_2 separation efficiency of liquid-based DAC systems using green amino acid salts and HFMCs, with particular emphasis on the integration of low-temperature, energy-efficient technologies to minimize thermal energy requirements for solvent regeneration. The following outlines recommend future work in this field:

- In Chapter 4, a membrane module was used as a contactor in the absorption process to evaluate the kinetic and thermodynamic behavior of various amino acid solutions under DAC conditions. Another suitable contactor for DAC absorption process are cooling towers, particularly for large-scale applications, due to the ability to operate at high air-to-solvent ratios while maintaining a low pressure drop. Therefore, designing and developing a bench-scale cooling tower to study the kinetics of CO_2 capture and the associated operating conditions using green amino acid salt solutions would be a valuable step toward understanding the performance and potential deployment of such contactors in liquid-based DAC systems.

- Another important step in designing and developing a DAC system is conducting a techno-economic analysis (TEA) to understand how various parameters affect the overall process cost in the system configuration proposed in this thesis. TEA is especially crucial for DAC systems, as high costs remain a major limitation to their large-scale deployment. For a comprehensive and accurate TEA of a DAC CO_2 capture unit, it is essential to evaluate both capital costs and operating costs for the absorption and desorption sections, considering key factors like equipment sizing, energy consumption, and solvent use. This analysis helps identify cost drivers and areas where improvements can be made to enhance the economic viability of liquid-based DAC technology.
- Another important parameter is the geometry and size of the catalyst used. In this thesis, a foundation was established by integrating a fixed bed of spherical solid acid catalyst with the MVR unit to enhance CO_2 desorption performance under DAC conditions. In this context, investigating catalysts with different geometries that can impose lower pressure drop, provide higher surface area, and serve as support for the deposition of diverse range of functional groups or nanoscale catalysts would be a valuable direction for future research. This would enable a more detailed and comprehensive evaluation of various catalysts in this application.
- Studying heat integration and recovery in liquid-based DAC systems is essential for improving overall energy efficiency. This can be achieved through two practical approaches, passive heat recovery using heat exchangers, and active heat recovery using heat pumps. Both methods offer effective strategies to capture and reuse thermal energy that would otherwise be lost at various points in the process. A detailed investigation combining simulation and experimental work can provide deeper insights

into the feasibility, efficiency, and optimal integration of these techniques within liquid-based DAC systems.

- To further evaluate, understand, and optimize the performance of the proposed system across a broader range of operating conditions, machine learning (ML) can serve as a powerful tool for data-driven analysis and process optimization. By utilizing the experimental data already collected in this study using various HFMCs, solvents, and catalysts (with different properties) under diverse process conditions, along with other available datasets, ML techniques can be applied to identify hidden patterns, quantify the impact of key parameters, and predict system behavior under wider spectrum of operational scenarios.

Appendix

A.1. Supplementary Information of Chapter 4

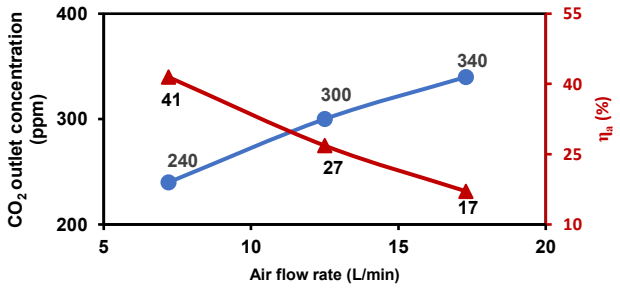

Figure A.1. Effect of air flow rate on CO_2 absorption efficiency (η_a) for 1 M GlyK at 20°C, solvent flow rate=0.25 L/min

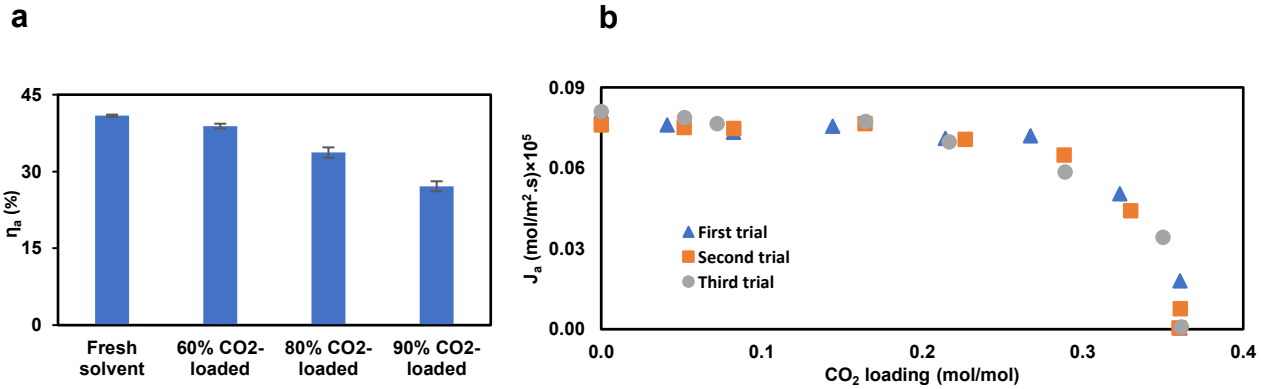

Figure A.2. Accuracy and repeatability of DAC-absorption unit over three long-term trials for 1 M GlyK **a)** Absorption efficiency (η_a) versus solvent loaded percentage. **b)** Absorption flux (J_a) versus solvent loadings. All the trials were completed at 20 °C, air flow rate = 7.2 L/min, and solvent flow rate = 0.25 L/min.

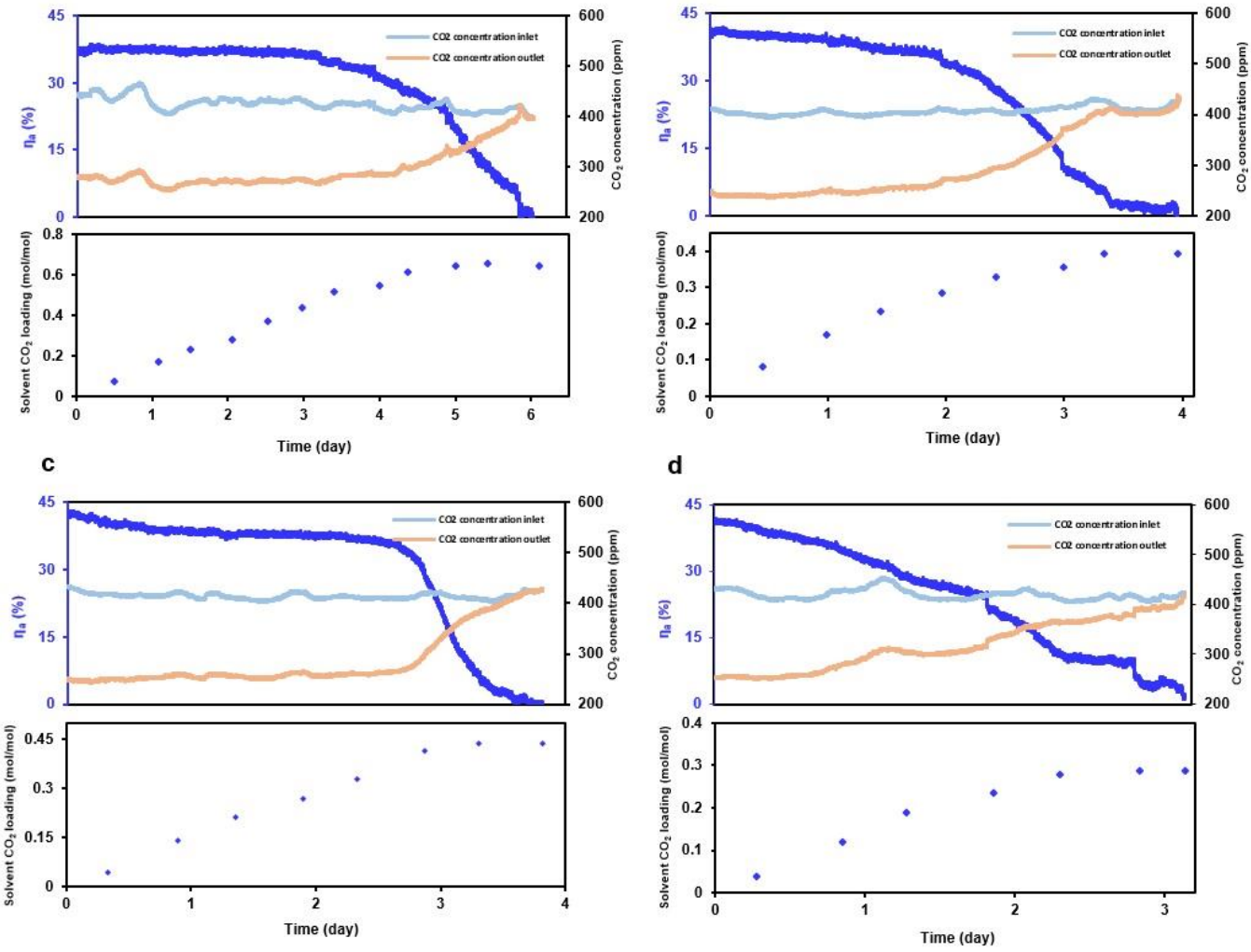

Figure A.3. Amino acid absorption efficiency (η_a) in long-term operation at different solvent loadings for 1 M **a)** LysK. **b)** SarK. **c)** ProK. **d)** HisK. All the trials were completed at 20 °C, air flow rate = 7.2 L/min, and solvent flow rate = 0.25 L/min.

Figure A.4. Insolubility of 3 M LysK in water for aqueous solution preparation

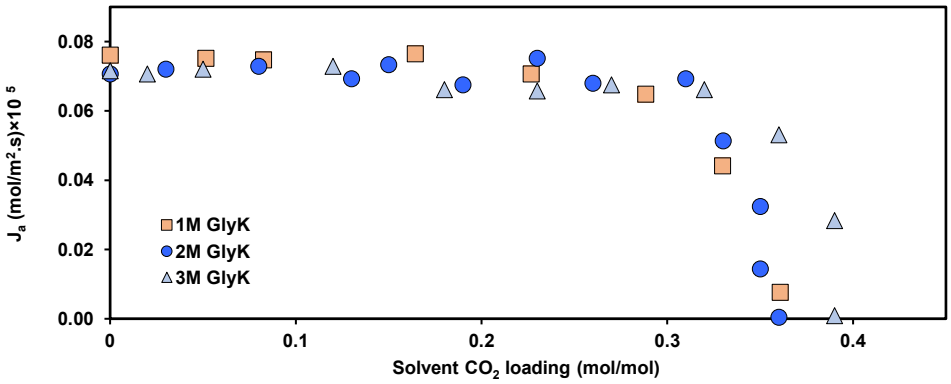

Figure A.5. The kinetic performance (absorption flux, J_a) of GlyK at different concentrations in various solvent loading conditions. All data were obtained at 20 °C, air flow rate = 7.2 L/min, and solvent flow rate = 0.25 L/min.

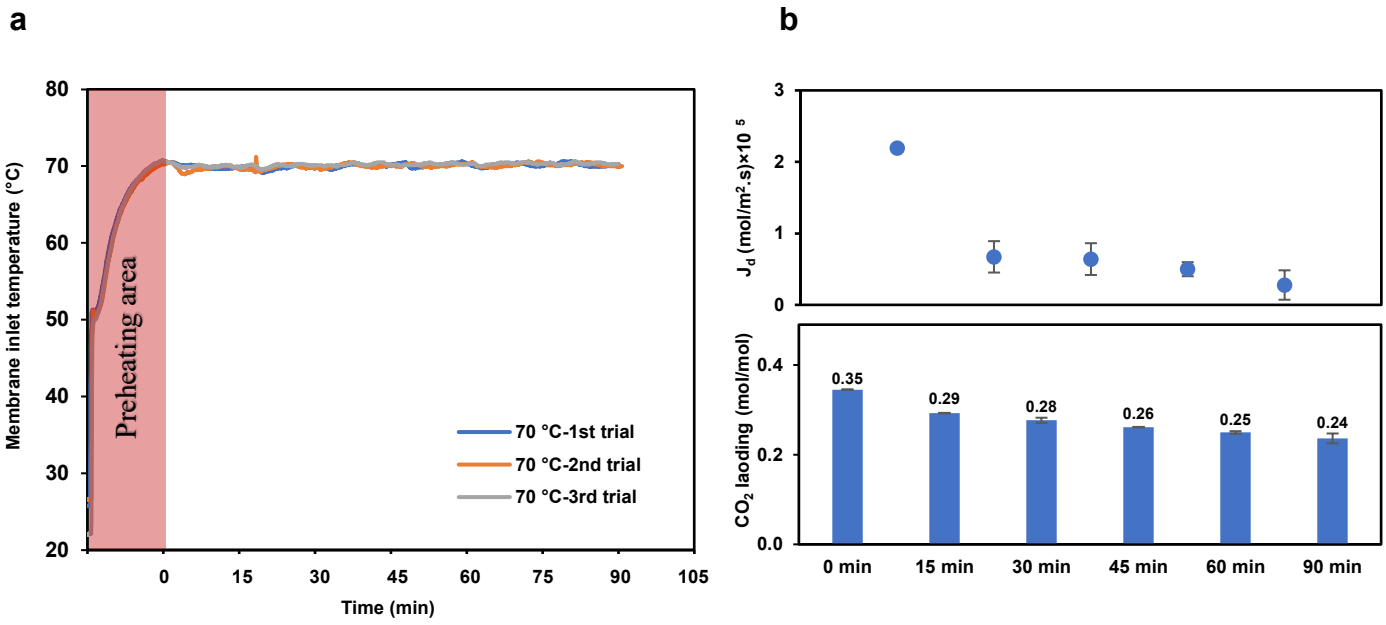

Figure A.6. Accuracy and repeatability of vacuum low-temperature DAC-desorption unit over three trials for 1 M GlyK. **a)** Temperature profile. **b)** CO_2 desorption flux (J_d) within the range of different solvent loadings. The data were obtained at 70°C, 21 $kPa_{(a)}$ and solvent flow rate = 0.25 L/min.

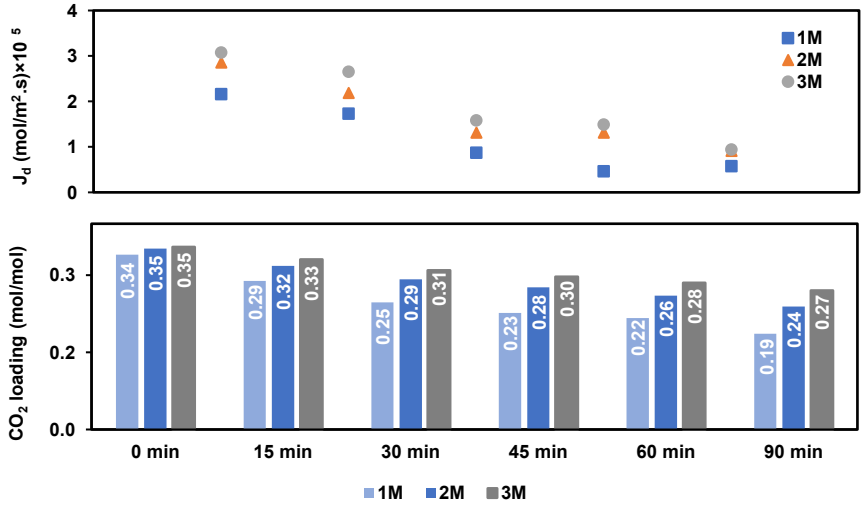

Figure A.7. GlyK DAC-desorption flux (Jd) at different solvent concentration and solvent CO_2 loading ranges. All data were obtained at 80°C, 21 kPa(a) and solvent flow rate = 0.25 L/min

A.2. Supplementary Information of Chapter 5

Figure A.8. Three evaluated commercial HFMCs

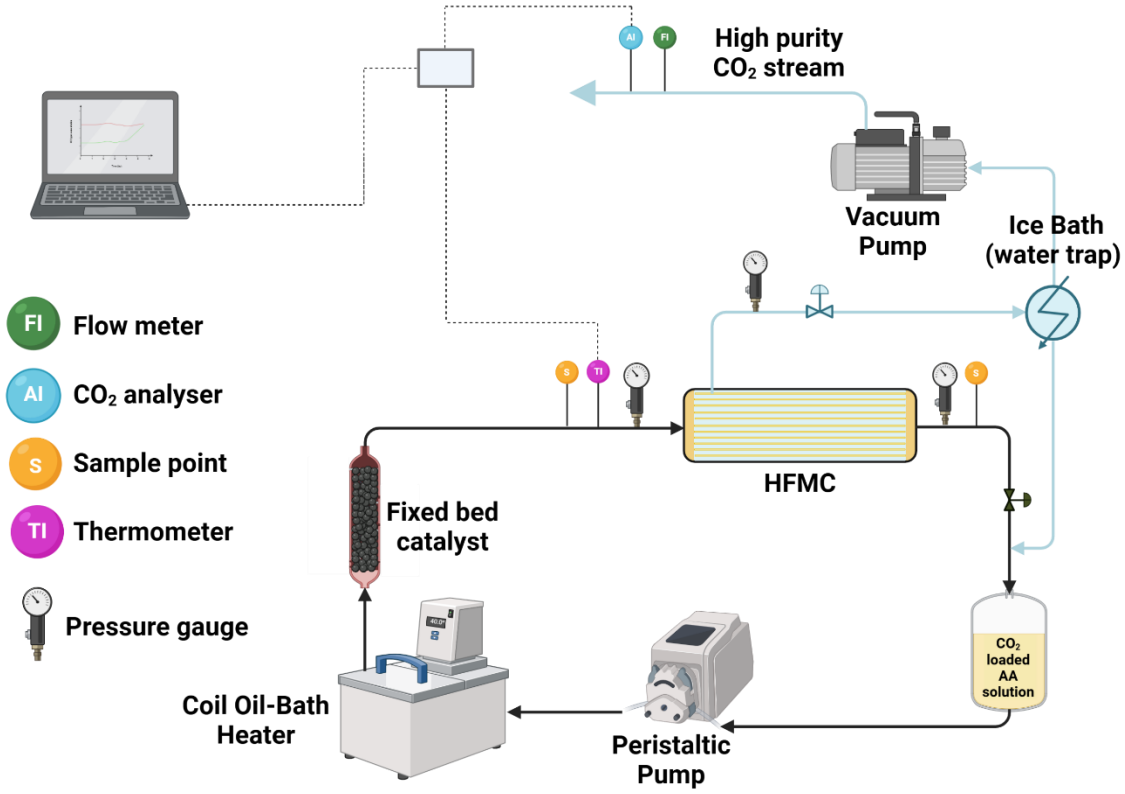

Scheme A.1. Detailed schematic diagram of C-MVR unit

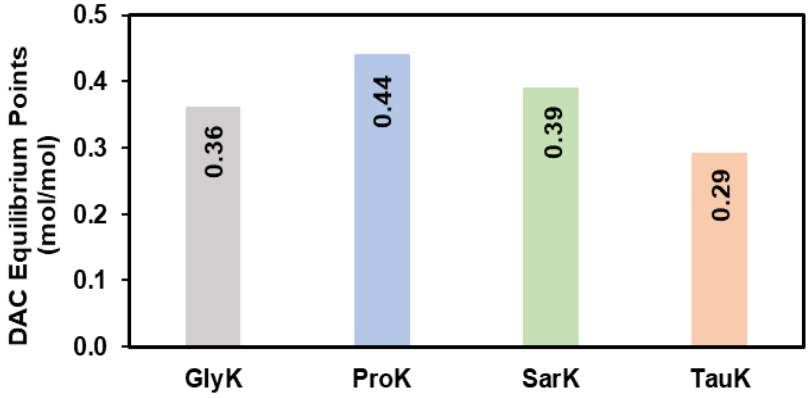

Figure A.9. DAC equilibrium points for various used amino acid salts solutions

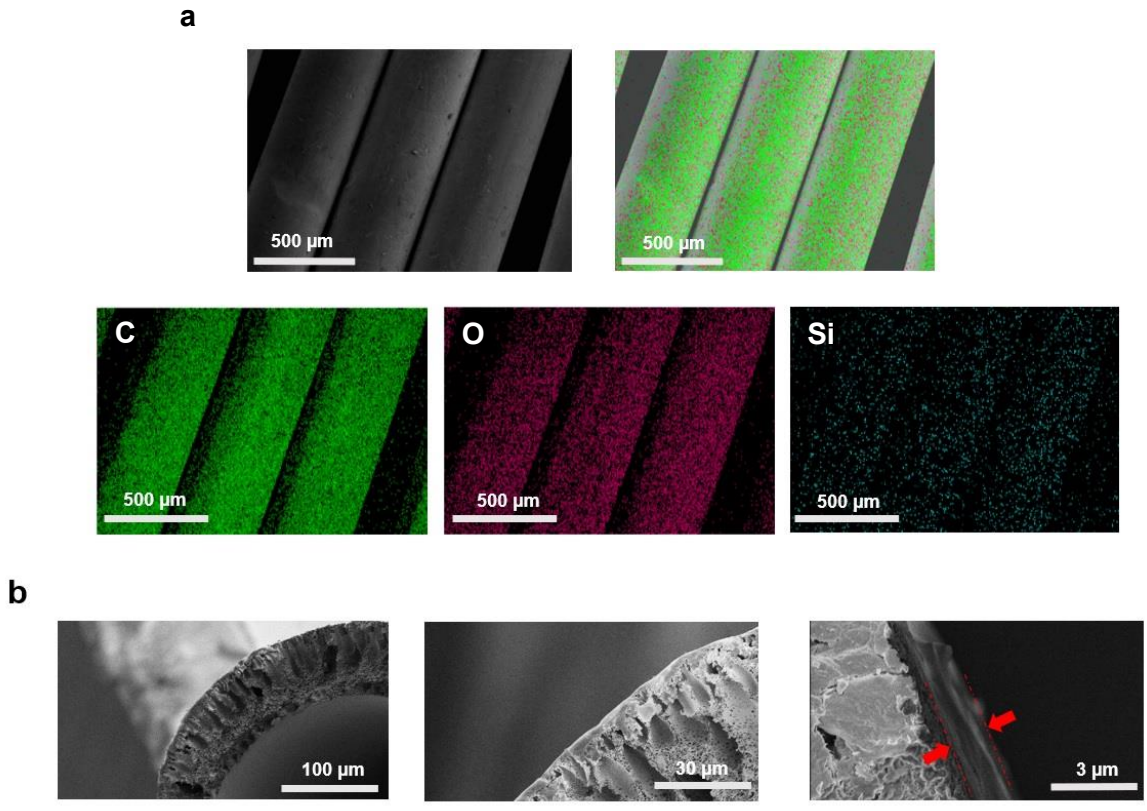

Figure A.10. a) Top-view SEM and EDX elemental analysis of multiple fibers, highlighting the PDMS coating layer elemental distribution. b) Cross-sectional SEM images at different scales (100 µm to 3 µm), illustrating the thickness and uniformity of the PDMS coating layer.

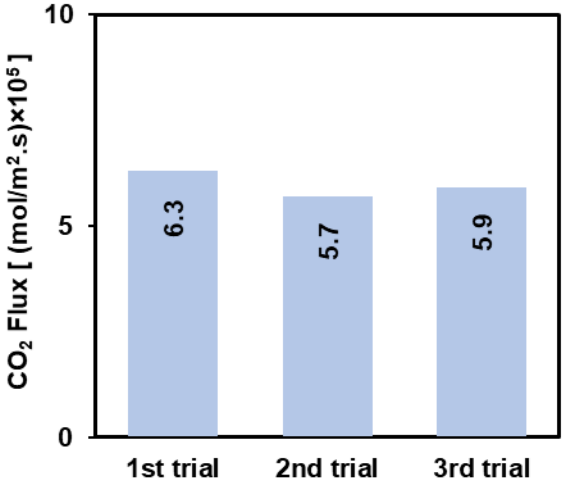

Figure A.11. Repeatability and accuracy of MVR rig in three consecutive trials. All trials were conducted for 3M GlyK, at 90 °C, 2-4 $kPa_{(a)}$, 0.25 L/min.

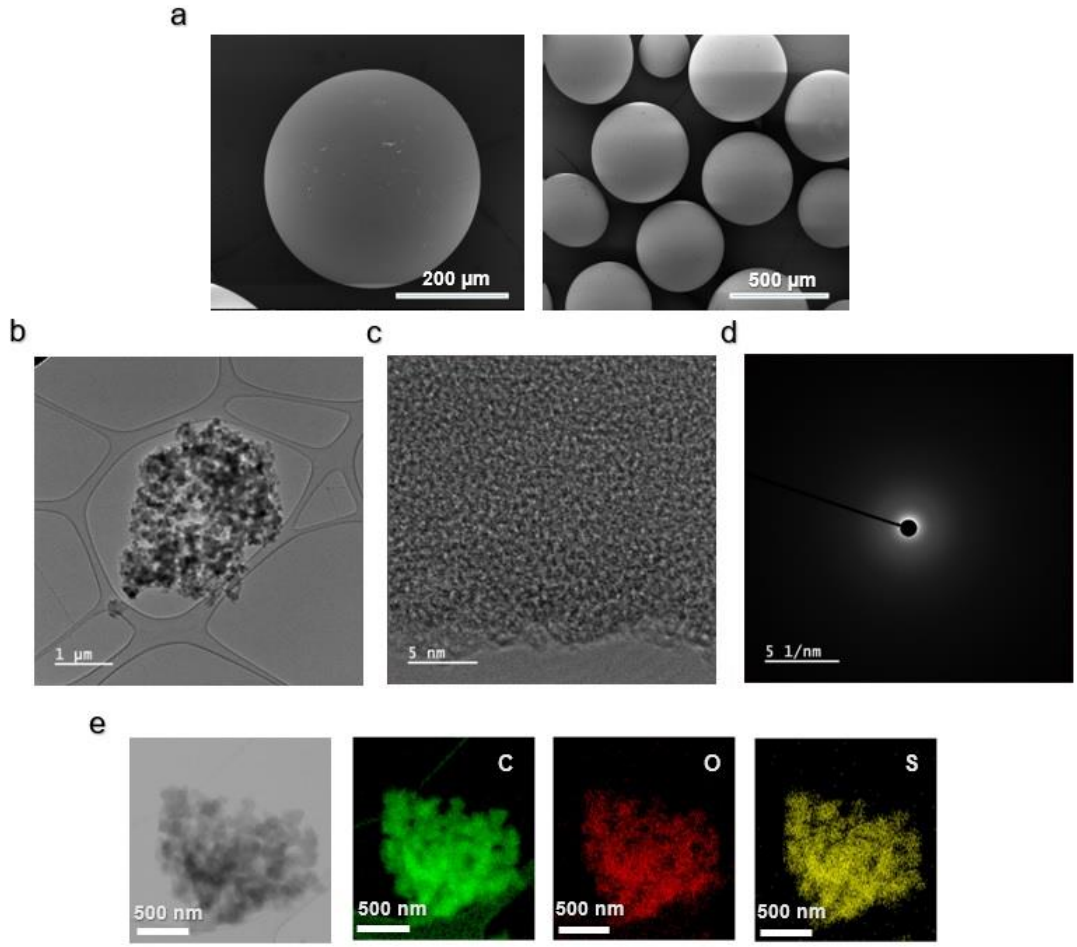

Figure A.12. a) SEM images, b) TEM low-magnification, c) high resolution, d) SAED images, and e) TEM-EDX mapping for Resin B. The high resolution and SAED images show amorphous nature of catalyst.

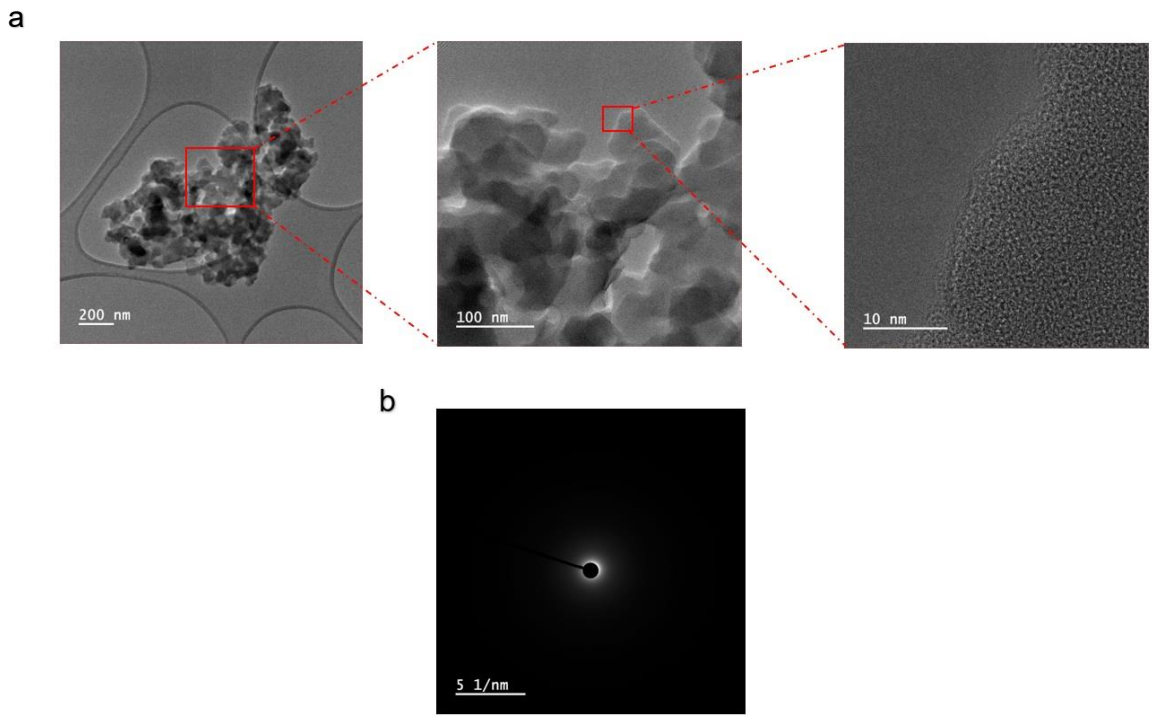

Figure A.13. a) Low magnification, high-resolution TEM, and b) SAED images of Resin A showing amorphous catalyst materials.

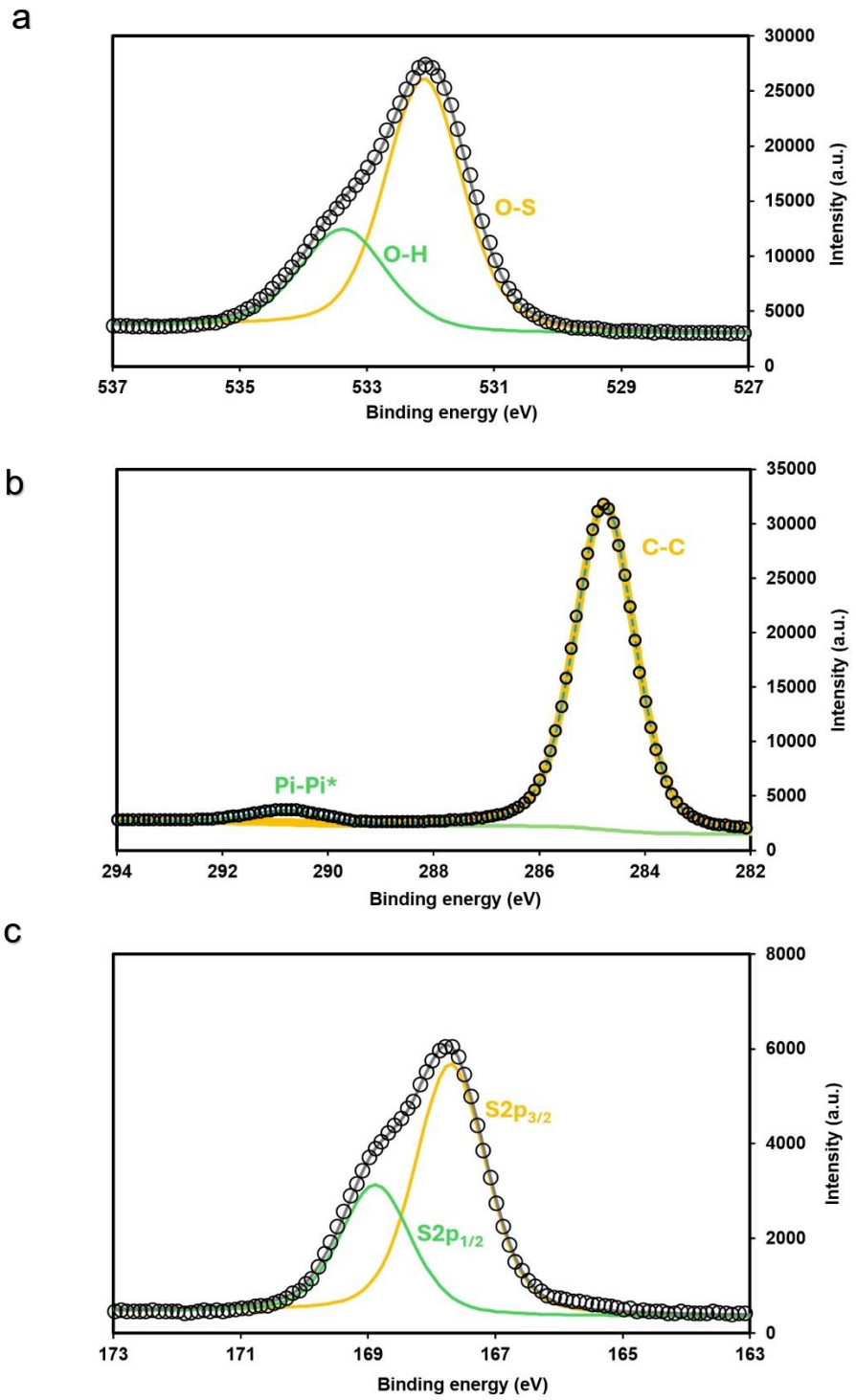

Figure A.14. Resin A XPS spectrum for a) O-S and O-H scan,(181-183) b) carbon scan (184-186) of fresh catalyst, and c) sulfonate functional group for used catalyst (one cycle)(103, 148).

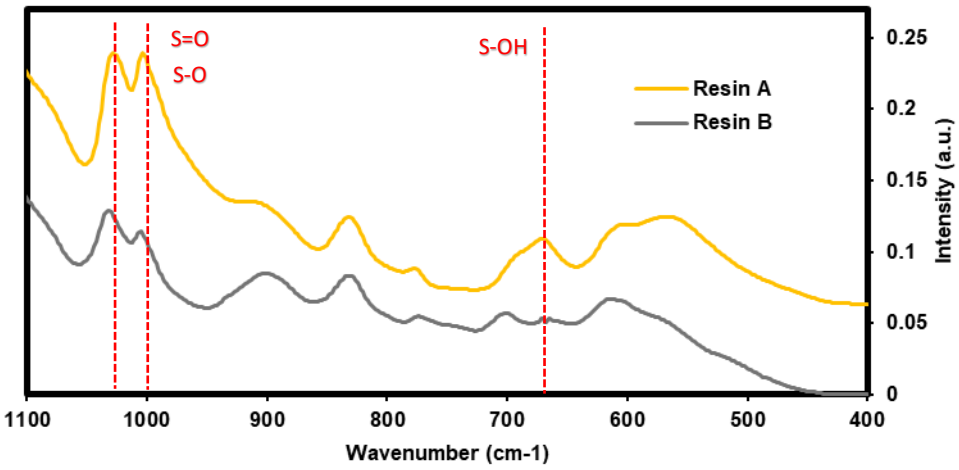

Figure A.15. FTIR spectra for catalysts Resin A and B (187, 188).

Table A.1. Weight percentage elements analysis of catalysts using CHNS method

Elements (wt.%)	C	H	N	S
Resin A	19.9	7.0	-	9.5
Resin B	63.6	10.7	-	7.5

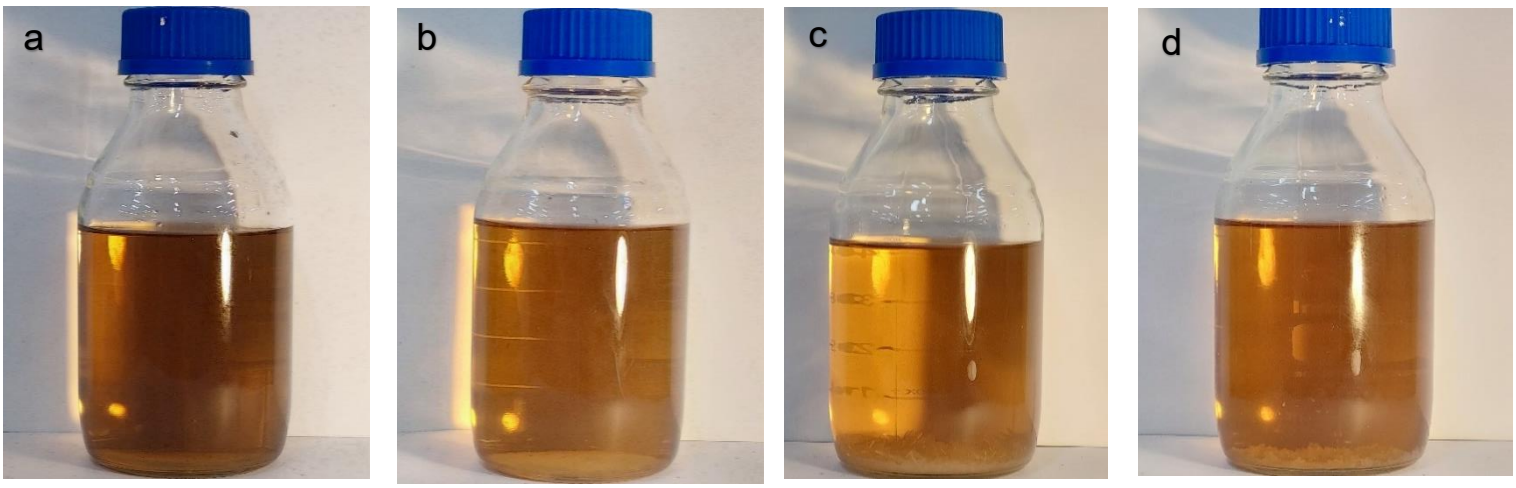

Figure A.16. Observed precipitations for a) 2M TauK, b) 2.5M TauK, c) 3M TauK, and d) 3M TauK+0.5M K_2CO_3.

A.3. Supplementary Information of Chapter 6

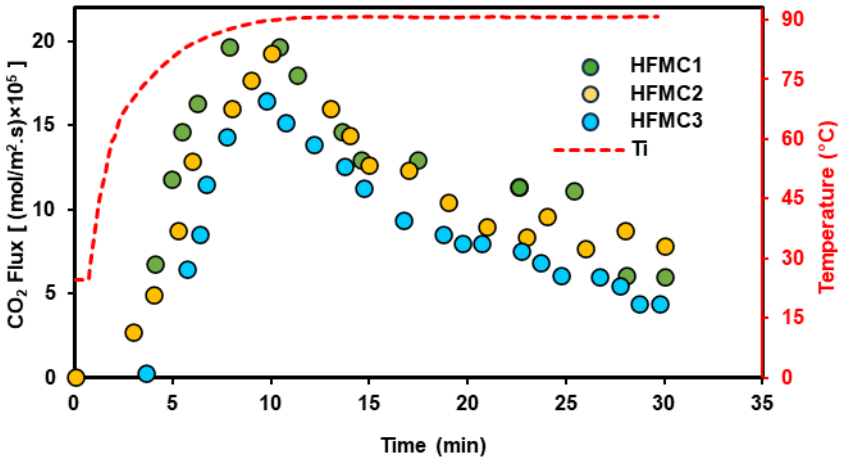

Figure A.17. CO_2 desorption flux profiles of three used HFMC

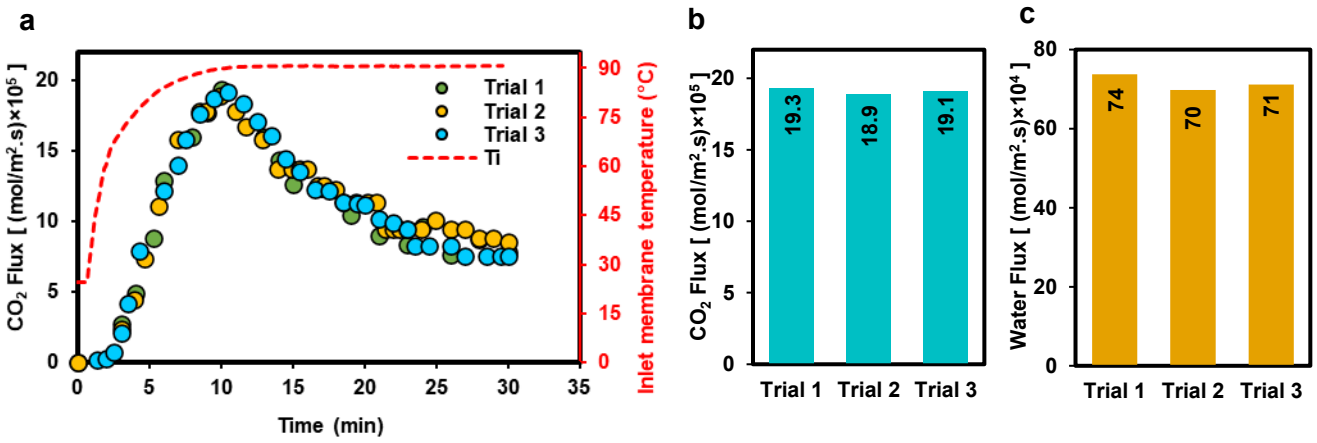

Figure A.18. a) CO_2 desorption flux profiles, b) max. CO_2 flux, and c) water flux of three trials of 3M GlyK at 90 °C.

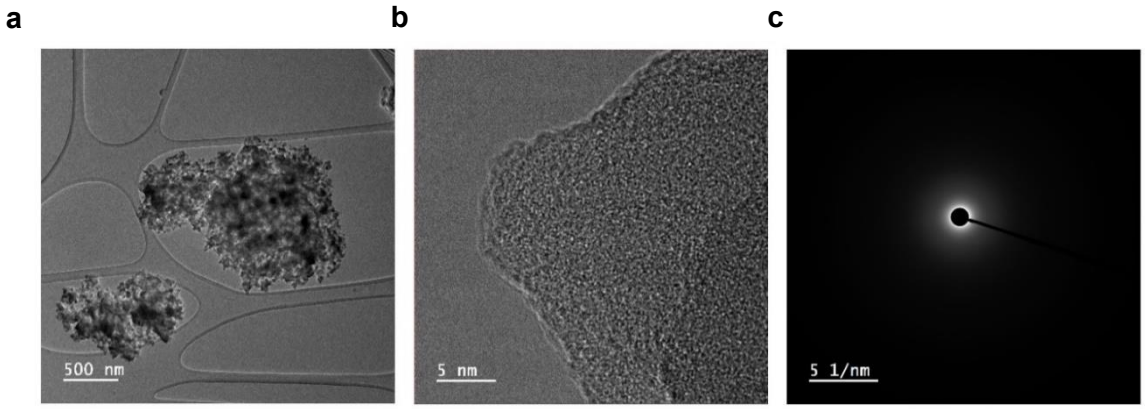

Figure A.19. a) TEM low-magnification, b) high resolution, and C) SAED image of Fe-SZ/SiO_2(1/1).

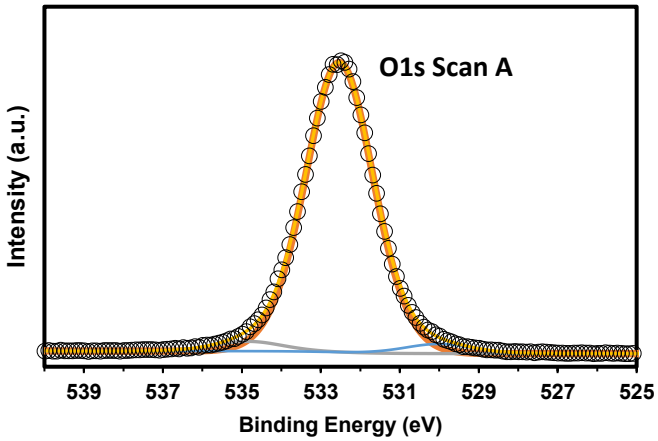

Figure A.20. The deconvoluted O 1s spectra of XPS for Fe-SZ/SiO_2(1/1) catalyst

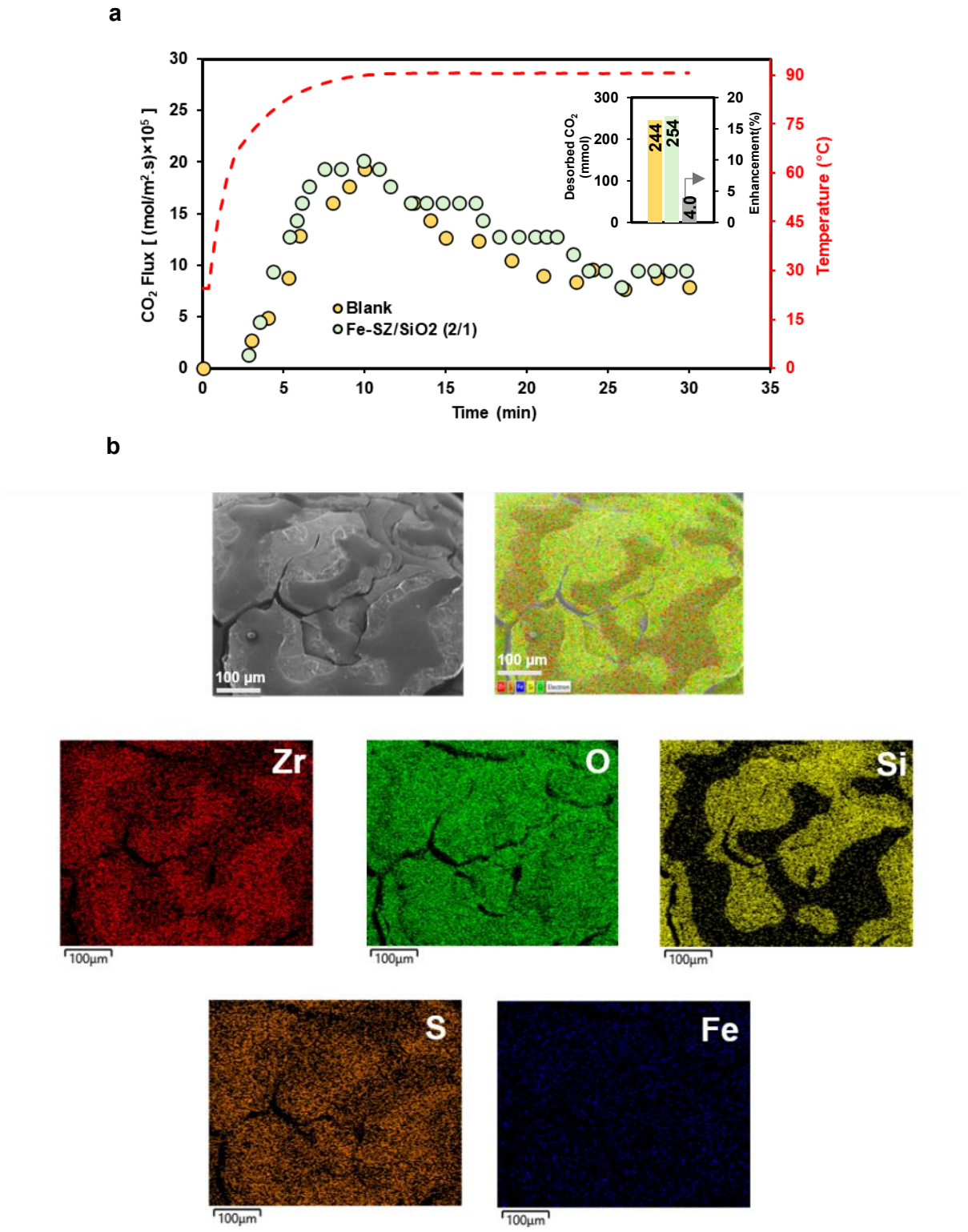

Figure A.21. a) CO_2 flux curves and total desorbed CO_2 with and without 6wt% Fe-SZ/SiO_2(2/1), and catalyst enhancement. b) SEM-EDX images of Fe-SZ/SiO_2(2/1) highlight non-uniform dispersion of SZ on the SiO_2 support.

Table A.2. Total acidity and basicity strengths of various synthesized samples, measured by NH_3-TPD and CO_2-TPD analyses.

Samples	Total Acidity Strength (mmol/g)	Total Basicity Strength (mmol/g)
Fe-SZ/SiO_2(1/2)	2.01	1.11
Fe-SZ/SiO_2(1/1)	2.09	1.24
Fe-SZ/SiO_2(2/1)	2.15	1.86

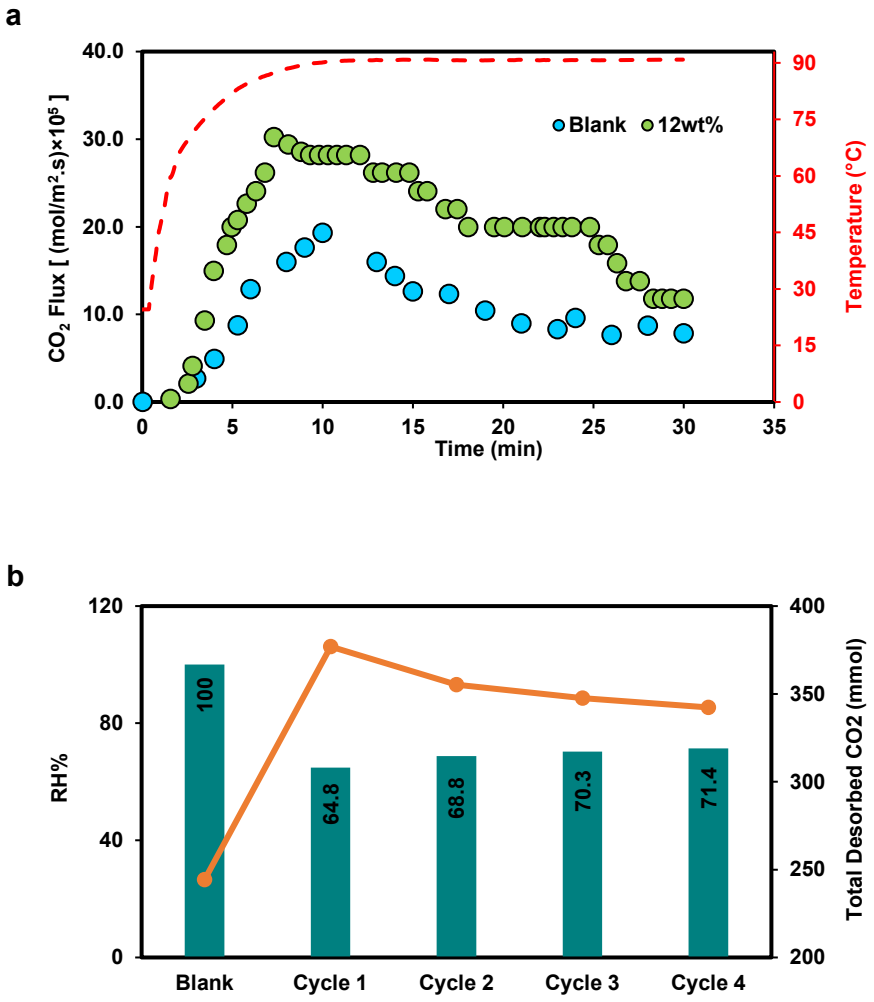

Figure A.22. a) CO_2 flux profile with and without 12wt% Fe-SZ/SiO_2(1/1). b) Catalyst stability in four cycles for 9wt% Fe-SZ/SiO_2(1/1). All MVR trials accomplished at 90°C using 3M GlyK. No catalyst is used for the blank trial.

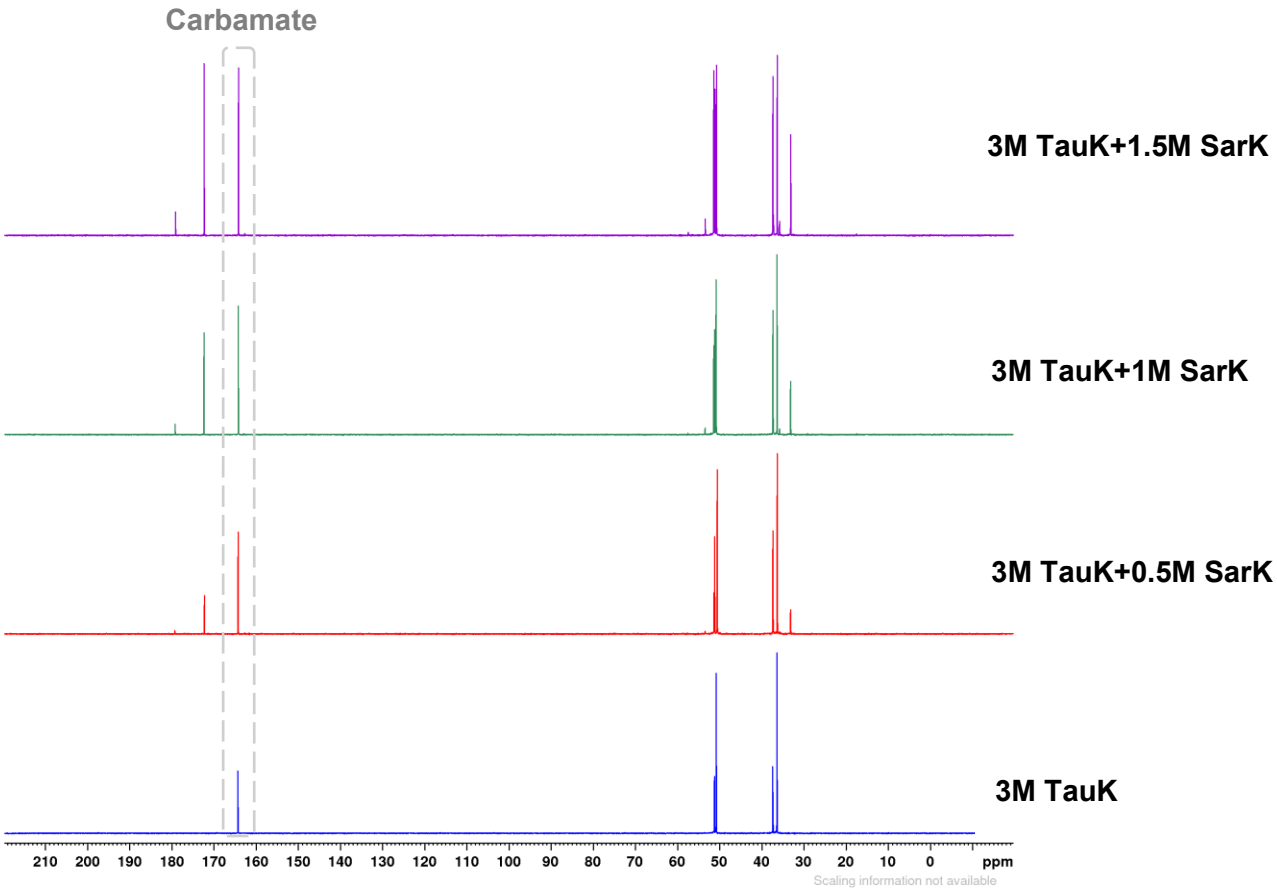

Figure A.23. ^{13}C NMR spectra for CO_2 loaded single and hybrid solvents.

References

1. Cox PM, Betts RA, Jones CD, Spall SA, Totterdell IJ. Acceleration of global warming due to carbon-cycle feedbacks in a coupled climate model. Nature. 2000;408(6809):184-7.

2. EcoWatch. Atmospheric CO_2 Passes 420 ppm for First Time Ever 2021.

3. IPCC, Global Warming of 1.5◦C 2018.

4. Kriegler E, Bauer N, Popp A, Humpenöder F, Leimbach M, Strefler J, et al. Fossil-fueled development (SSP5): An energy and resource intensive scenario for the 21st century. Global Environmental Change. 2017;42:297-315.

5. Lackner KZ, Hans-Joachim; Grimes, Patrick. Carbon Dioxide Extraction from Air: Is It An Option?, 1999.

6. Sabatino F, Grimm A, Gallucci F, van Sint Annaland M, Kramer GJ, Gazzani M. A comparative energy and costs assessment and optimization for direct air capture technologies. Joule. 2021;5(8):2047-76.

7. McQueen N, Gomes KV, McCormick C, Blumanthal K, Pisciotta M, Wilcox J. A review of direct air capture (DAC): scaling up commercial technologies and innovating for the future. Progress in Energy. 2021;3(3):032001.

8. Zhu X, Xie W, Wu J, Miao Y, Xiang C, Chen C, et al. Recent advances in direct air capture by adsorption. Chemical Society Reviews. 2022;51(15):6574-651.

9. Dutcher B, Fan M, Russell AG. Amine-Based CO_2 Capture Technology Development from the Beginning of 2013-A Review. ACS Applied Materials & Interfaces. 2015;7(4):2137-48.

10. Kim S, Shi H, Lee JY. CO_2 absorption mechanism in amine solvents and enhancement of CO_2 capture capability in blended amine solvent. International Journal of Greenhouse Gas Control. 2016;45:181-8.

11. Brethomé FM, Williams NJ, Seipp CA, Kidder MK, Custelcean R. Direct air capture of CO_2 via aqueous-phase absorption and crystalline-phase release using concentrated solar power. Nature Energy. 2018;3(7):553-9.

12. Custelcean R, Williams NJ, Garrabrant KA, Agullo P, Brethomé FM, Martin HJ, Kidder MK. Direct Air Capture of CO_2 with Aqueous Amino Acids and Solid Bis-iminoguanidines (BIGs). Industrial & Engineering Chemistry Research. 2019;58(51):23338-46.

13. Kiani A, Jiang K, Feron P. Techno-Economic Assessment for CO_2 Capture From Air Using a Conventional Liquid-Based Absorption Process. Frontiers in Energy Research. 2020;8.

14. Balraj A, Kumar MS, Ramamoorthy SV, Sukumar S. A Critical Review on CO_2 Stripping/Carbon-Rich Solvent Regeneration: Process Intensification by Combined Sonication and Nanoparticles. Industrial & Engineering Chemistry Research. 2025;64(8):4554-67.

15. Budzianowski WM. Explorative analysis of advanced solvent processes for energy efficient carbon dioxide capture by gas–liquid absorption. International Journal of Greenhouse Gas Control. 2016;49:108-20.

16. Laribi S, Dubois L, De Weireld G, Thomas D. Study of the post-combustion CO_2 capture process by absorption-regeneration using amine solvents applied to cement plant flue gases with high CO_2 contents. International Journal of Greenhouse Gas Control. 2019;90:102799.

17. Lee S, Kim J, Lee E, Hong S. Improving the performance of membrane contactors for carbon dioxide stripping from water: Experimental and theoretical analysis. Journal of Membrane Science. 2022;654:120552.

18. Rivero J, Lieber A, Snodgrass C, Neal Z, Hildebrandt M, Gamble W, Hornbostel K. Demonstration of direct ocean carbon capture using hollow fiber membrane contactors. Chemical Engineering Journal. 2023;470:143868.

19. Sun J, Xu P, Gong D, Kong X, Fu K, Chen X, et al. Study on robust absorption performance of hydrophilic membrane contactor for direct air capture. Separation and Purification Technology. 2023;309:122978.

20. Castro-Muñoz R, Zamidi Ahmad M, Malankowska M, Coronas J. A new relevant membrane application: CO_2 direct air capture (DAC). Chemical Engineering Journal. 2022;446:137047.

21. Kim S, Scholes CA, Heath DE, Kentish SE. Gas-liquid membrane contactors for carbon dioxide separation: A review. Chemical Engineering Journal. 2021;411:128468.

22. Vadillo JM, Gómez-Coma L, Garea A, Irabien A. Hollow Fiber Membrane Contactors in CO_2 Desorption: A Review. Energy & Fuels. 2021;35(1):111-36.

23. Simons TJ, Hield P, Pas SJ. A novel experimental apparatus for the study of low temperature regeneration CO_2 capture solvents using hollow fibre membrane contactors. International Journal of Greenhouse Gas Control. 2018;78:228-35.

24. Alivand MS, Stevens GW, Mumford KA. Reply to: The impact of thermodynamics when using a catalyst for conventional carbon capture solvent regeneration. Nature Communications. 2023;14(1):4137.

25. Ibrahim MH, El-Naas MH, Zhang Z, Van der Bruggen B. CO_2 Capture Using Hollow Fiber Membranes: A Review of Membrane Wetting. Energy & Fuels. 2018;32(2):963-78.

26. Xue K, Fu H, Chen H, Zhang H, Gao D. Investigation of membrane wetting for CO_2 capture by gas–liquid contactor based on ceramic membrane. Separation and Purification Technology. 2023;304:122309.

27. Scholes CA, Kentish SE, Stevens GW, Jin J, deMontigny D. Thin-film composite membrane contactors for desorption of CO_2 from Monoethanolamine at elevated temperatures. Separation and Purification Technology. 2015;156:841-7.

28. Dai Z, Ansaloni L, Deng L. Precombustion CO_2 Capture in Polymeric Hollow Fiber Membrane Contactors Using Ionic Liquids: Porous Membrane versus Nonporous Composite Membrane. Industrial & Engineering Chemistry Research. 2016;55(20):5983-92.

29. Breyer C, Fasihi M, Bajamundi C, Creutzig F. Direct Air Capture of CO_2: A Key Technology for Ambitious Climate Change Mitigation. Joule. 2019;3(9):2053-7.

30. Alivand MS, Mazaheri O, Wu Y, Stevens GW, Scholes CA, Mumford KA. Development of aqueous-based phase change amino acid solvents for energy-efficient CO_2 capture: The role of antisolvent. Applied Energy. 2019;256:113911.

31. Li X, Liu J, Jiang W, Gao G, Wu F, Luo C, Zhang L. Low energy-consuming CO_2 capture by phase change absorbents of amine/alcohol/H_2O. Separation and Purification Technology. 2021;275:119181.

32. Aghel B, Janati S, Wongwises S, Shadloo MS. Review on CO_2 capture by blended amine solutions. International Journal of Greenhouse Gas Control. 2022;119:103715.

33. Li T, Yu Q, Barzagli F, Li Ce, Che M, Zhang Z, Zhang R. Energy efficient catalytic CO_2 desorption: mechanism, technological progress and perspective. Carbon Capture Science & Technology. 2023;6:100099.

34. Alivand MS, Mazaheri O, Wu Y, Zavabeti A, Christofferson AJ, Meftahi N, et al. Engineered assembly of water-dispersible nanocatalysts enables low-cost and green CO_2 capture. Nature Communications. 2022;13(1):1249.

35. Bhatti UH, Shah AK, Hussain A, Khan HA, Park CY, Nam SC, Baek IH. Catalytic activity of facilely synthesized mesoporous HZSM-5 catalysts for optimizing the CO_2 desorption rate from CO_2-rich amine solutions. Chemical Engineering Journal. 2020;389:123439.

36. Chen Z, Xing L, Zhan G, Huang Z, Bai X, Wang R, et al. Integration of strong oxide-support interaction and mesoporous confinement to engineer efficient and durable Zr/Al_2O_3 for

catalytic solvent regeneration in CO_2 capture. Applied Catalysis B: Environment and Energy. 2024;351:124000.

37. Yao Y, Xing B, Chen J, Ren Y, Ma Y, Zhang Y, Zhang L. Enhanced catalytic regeneration of amine solutions using novel Cu/HZSM-5/MCM-41 catalysts. Journal of Environmental Chemical Engineering. 2025;13(2):116104.

38. Bairq ZAS, Gao H, Murshed FAM, Tontiwachwuthikul P, Liang Z. Modified Heterogeneous Catalyst-Aided Regeneration of CO_2 Capture Amines: A Promising Perspective for a Drastic Reduction in Energy Consumption. ACS Sustainable Chemistry & Engineering. 2020;8(25):9526-36.

39. Zhang X, Huang Y, Gao H, Luo X, Liang Z, Tontiwachwuthikul P. Zeolite catalyst-aided tri-solvent blend amine regeneration: An alternative pathway to reduce the energy consumption in amine-based CO_2 capture process. Applied Energy. 2019;240:827-41.

40. Alivand MS, McQuillan RV, Momeni A, Zavabeti A, Stevens GW, Mumford KA. Facile Fabrication of Monodispersed Carbon Sphere: A Pathway Toward Energy-Efficient Direct Air Capture (DAC) Using Amino Acids. Small. 2023;19(30):2300150.

41. Zhang X, Hong J, Liu H, Luo X, Olson W, Tontiwachwuthikul P, Liang Z. SO_4^{2-}/ZrO_2 supported on γ-Al_2O_3 as a catalyst for CO_2 desorption from CO_2-loaded monoethanolamine solutions. AIChE Journal. 2018;64(11):3988-4001.

42. Ali Saleh Bairq Z, Gao H, Huang Y, Zhang H, Liang Z. Enhancing CO_2 desorption performance in rich MEA solution by addition of $SO_4^{2-}/ZrO_2/SiO_2$ bifunctional catalyst. Applied Energy. 2019;252:113440.

43. Alivand MS, Mazaheri O, Wu Y, Stevens GW, Scholes CA, Mumford KA. Catalytic Solvent Regeneration for Energy-Efficient CO_2 Capture. ACS Sustainable Chemistry & Engineering. 2020;8(51):18755-88.

44. Zhang X, Huang Y, Yang J, Gao H, Huang Y, Luo X, et al. Amine-based CO_2 capture aided by acid-basic bifunctional catalyst: Advancement of amine regeneration using metal modified MCM-41. Chemical Engineering Journal. 2020;383:123077.

45. Zhang X, Zhu Z, Sun X, Yang J, Gao H, Huang Y, et al. Reducing Energy Penalty of CO_2 Capture Using Fe Promoted SO_4^{2-}/ZrO_2/MCM-41 Catalyst. Environmental Science & Technology. 2019;53(10):6094-102.

46. Hegarty J, Shindel B, Sukhareva D, Barsoum ML, Farha OK, Dravid V. Expanding the Library of Ions for Moisture-Swing Carbon Capture. Environmental Science & Technology. 2023;57(50):21080-91.

47. El-Mehalmey WA, Ibrahim AH, Youssef AFA, Abuzalat O, Mousa MS, Mayhoub AS, Alkordi MH. Anion-Exchange Electrospun Mixed-Matrix Polymer Fibers of Colesevelam for Water Treatment. ACS Applied Materials & Interfaces. 2023.

48. Thuy Vu TT, Liu S, Jonušis M, Jonušienė S, Choi J, Kawano R, et al. Sustainable One-Pot Synthesis of 5-(Hydroxymethyl)furfural from C6-Sugars by Enhanced H^+ Exchange Heterogeneous Catalysis. ACS Sustainable Chemistry & Engineering. 2023;11(48):17130-41.

49. Shu Q, Haug M, Tedesco M, Kuntke P, Hamelers HVM. Direct Air Capture Using Electrochemically Regenerated Anion Exchange Resins. Environmental Science & Technology. 2022;56(16):11559-66.

50. Hossain MS, Kumar D, Azad MAS, Azam SMS, Amin MSA, Mozumder MSI. A Comparative Study on CO_2 Capture Efficiency Using Single and Blended Solvent. Process Integration and Optimization for Sustainability. 2024;8(2):565-76.

51. Liu J, Li X, Zhang Z, Li L, Bi Y, Zhang L. Promotion of CO_2 capture performance using piperazine (PZ) and diethylenetriamine (DETA) bi-solvent blends. Greenhouse Gases: Science and Technology. 2019;9(2):349-59.

52. Knuutila HK, Rennemo R, Ciftja AF. New solvent blends for post-combustion CO_2 capture. Green Energy & Environment. 2019;4(4):439-52.

53. Fuss S, Lamb WF, Callaghan MW, Hilaire J, Creutzig F, Amann T, et al. Negative emissions—Part 2: Costs, potentials and side effects. Environmental Research Letters. 2018;13(6):063002.

54. Keith DW, Holmes G, St. Angelo D, Heidel K. A Process for Capturing CO_2 from the Atmosphere. Joule. 2018;2(8):1573-94.

55. Lackner K, Ziock H-J, Grimes P. Carbon Dioxide Extraction from Air: Is It An Option?

56. Beuttler C, Charles L, Wurzbacher J. The Role of Direct Air Capture in Mitigation of Anthropogenic Greenhouse Gas Emissions. Frontiers in Climate. 2019;1.

57. Sodiq A, Abdullatif Y, Aissa B, Ostovar A, Nassar N, El-Naas M, Amhamed A. A review on progress made in direct air capture of CO_2. Environmental Technology & Innovation. 2023;29:102991.

58. Xu H, Yu L, Chong C, Wang F. A comprehensive review on direct air carbon capture (DAC) technology by adsorption: From fundamentals to applications. Energy Conversion and Management. 2024;322:119119.

59. An K, Li K, Yang C-M, Brechtl J, Nawaz K. A comprehensive review on regeneration strategies for direct air capture. Journal of CO_2 Utilization. 2023;76:102587.

60. Holmes G, Keith DW. An air liquid contactor for large-scale capture of CO_2 from air. Philosophical Transactions of the Royal Society A: Mathematical, Physical and Engineering Sciences. 2012;370(1974):4380-403.

61. Astarita G. Absorption of Carbon Dioxide into Alkaline Solutions in Packed Towers. Industrial & Engineering Chemistry Fundamentals. 1963;2(4):294-7.

62. Mahmoudkhani M, Heidel KR, Ferreira JC, Keith DW, Cherry RS. Low energy packed tower and caustic recovery for direct capture of CO_2 from air. Energy Procedia. 2009;1(1):1535-42.

63. Zeman FS, Lackner KS. Capturing carbon dioxide directly from the atmosphere. World Resource Review. 2004;16(2):157-72.

64. Svendsen HF, Hessen ET, Mejdell T. Carbon dioxide capture by absorption, challenges and possibilities. Chemical Engineering Journal. 2011;171(3):718-24.

65. Pinto DDD, Zaidy SAH, Hartono A, Svendsen HF. Evaluation of a phase change solvent for CO_2 capture: Absorption and desorption tests. International Journal of Greenhouse Gas Control. 2014;28:318-27.

66. Idem R, Wilson M, Tontiwachwuthikul P, Chakma A, Veawab A, Aroonwilas A, Gelowitz D. Pilot Plant Studies of the CO_2 Capture Performance of Aqueous MEA and Mixed MEA/MDEA Solvents at the University of Regina CO_2 Capture Technology Development Plant and the Boundary Dam CO_2 Capture Demonstration Plant. Industrial & Engineering Chemistry Research. 2006;45(8):2414-20.

67. Salmon S, House A. Chapter 2 - Enzyme-catalyzed Solvents for CO_2 Separation. In: Shi F, Morreale B, editors. Novel Materials for Carbon Dioxide Mitigation Technology. Amsterdam: Elsevier; 2015. p. 23-86.

68. Mumford KA, Wu Y, Smith KH, Stevens GW. Review of solvent based carbon-dioxide capture technologies. Frontiers of Chemical Science and Engineering. 2015;9(2):125-41.

69. Barzagli F, Giorgi C, Mani F, Peruzzini M. Screening Study of Different Amine-Based Solutions as Sorbents for Direct CO_2 Capture from Air. ACS Sustainable Chemistry & Engineering. 2020;8(37):14013-21.

70. Soo XYD, Lee JJC, Wu W-Y, Tao L, Wang C, Zhu Q, Bu J. Advancements in CO_2 capture by absorption and adsorption: A comprehensive review. Journal of CO_2 Utilization. 2024;81:102727.

71. Buvik V, Høisæter KK, Vevelstad SJ, Knuutila HK. A review of degradation and emissions in post-combustion CO_2 capture pilot plants. International Journal of Greenhouse Gas Control. 2021;106:103246.

72. Goff GS, Rochelle GT. Monoethanolamine Degradation: O_2 Mass Transfer Effects under CO_2 Capture Conditions. Industrial & Engineering Chemistry Research. 2004;43(20):6400-8.

73. Kiani A, Conway W, Abdellah MH, Puxty G, Minor A-J, Kluivers G, et al. A study on degradation and CO_2 capture performance of aqueous amino acid salts for direct air capture applications. Greenhouse Gases: Science and Technology. 2024;14(5):859-70.

74. Abdellah MH, Kiani A, Conway W, Puxty G, Feron P. The effects of counter ion on CO_2 capture performance of amino acid salt solutions for direct air capture applications. Separation and Purification Technology. 2025;358:130390.

75. Zhang Z, Li Y, Zhang W, Wang J, Soltanian MR, Olabi AG. Effectiveness of amino acid salt solutions in capturing CO_2: A review. Renewable and Sustainable Energy Reviews. 2018;98:179-88.

76. Ramezani R, Mazinani S, Di Felice R. State-of-the-art of CO_2 capture with amino acid salt solutions. 2022;38(3):273-99.

77. Custelcean R. Direct Air Capture of CO_2 Using Solvents. Annual Review of Chemical and Biomolecular Engineering. 2022;13(Volume 13, 2022):217-34.

78. Abdellah MH, Kiani A, Conway W, Puxty G, Feron P. A mass transfer study of CO_2 absorption in aqueous solutions of isomeric forms of sodium alaninate for direct air capture application. Chemical Engineering Journal. 2024;481:148765.

79. He X, He H, Barzagli F, Amer MW, Li Ce, Zhang R. Analysis of the energy consumption in solvent regeneration processes using binary amine blends for CO_2 capture. Energy. 2023;270:126903.

80. Vaidya PD, Kenig EY. CO_2-Alkanolamine Reaction Kinetics: A Review of Recent Studies. Chemical Engineering & Technology. 2007;30(11):1467-74.

81. Hu X, Huang J, He X, Luo Q, Li Ce, Zhou C, Zhang R. Analyzing the potential benefits of trio-amine systems for enhancing the CO_2 desorption processes. Fuel. 2022;316:123216.

82. Waseem M, Al-Marzouqi M, Ghasem N. A review of catalytically enhanced CO_2-rich amine solutions regeneration. Journal of Environmental Chemical Engineering. 2023;11(4):110188.

83. Babin A, Bougie F, Rodrigue D, Iliuta MC. A closer look on the development and commercialization of membrane contactors for mass transfer and separation processes. Separation and Purification Technology. 2019;227:115679.

84. Scholes CA, Kentish SE, Qader A. Membrane gas-solvent contactor pilot plant trials for post-combustion CO_2 capture. Separation and Purification Technology. 2020;237:116470.

85. Scholes CA, Qader A, Stevens GW, Kentish SE. Membrane Gas-Solvent Contactor Pilot Plant Trials of CO_2 Absorption from Flue Gas. Separation Science and Technology. 2014;49(16):2449-58.

86. Khaisri S, deMontigny D, Tontiwachwuthikul P, Jiraratananon R. CO_2 stripping from monoethanolamine using a membrane contactor. Journal of Membrane Science. 2011;376(1):110-8.

87. Nieminen H, Järvinen L, Ruuskanen V, Laari A, Koiranen T, Ahola J. Insights into a membrane contactor based demonstration unit for CO_2 capture. Separation and Purification Technology. 2020;231:115951.

88. Wang Z, Fang M, Pan Y, Yan S, Luo Z. Amine-based absorbents selection for CO_2 membrane vacuum regeneration technology by combined absorption–desorption analysis. Chemical Engineering Science. 2013;93:238-49.

89. Fang M, Wang Z, Yan S, Cen Q, Luo Z. CO_2 desorption from rich alkanolamine solution by using membrane vacuum regeneration technology. International Journal of Greenhouse Gas Control. 2012;9:507-21.

90. Low BT, Zhao L, Merkel TC, Weber M, Stolten D. A parametric study of the impact of membrane materials and process operating conditions on carbon capture from humidified flue gas. Journal of Membrane Science. 2013;431:139-55.

91. Scholes CA, Kentish SE, Stevens GW, deMontigny D. Comparison of thin film composite and microporous membrane contactors for CO_2 absorption into monoethanolamine. International Journal of Greenhouse Gas Control. 2015;42:66-74.

92. Franco JA, Kentish SE, Perera JM, Stevens GW. Poly(tetrafluoroethylene) Sputtered Polypropylene Membranes for Carbon Dioxide Separation in Membrane Gas Absorption. Industrial & Engineering Chemistry Research. 2011;50(7):4011-20.

93. Scholes CA, Jin J, Stevens GW, Kentish SE. Competitive permeation of gas and water vapour in high free volume polymeric membranes. Journal of Polymer Science Part B: Polymer Physics. 2015;53(10):719-28.

94. Kim S, Heath DE, Kentish SE. Improved carbon dioxide stripping by membrane contactors using hydrophobic electrospun poly(vinylidene fluoride-co-hexafluoro propylene) (PVDF-HFP) membranes. Chemical Engineering Journal. 2022;428:131247.

95. Ahn H, Kim J, Kim J-H. Low-temperature vacuum stripping of CO_2 from aqueous amine solutions using thin-film silicalite-filled PDMS composite membranes. International Journal of Greenhouse Gas Control. 2013;18:165-72.

96. Kosaraju P, Kovvali AS, Korikov A, Sirkar KK. Hollow Fiber Membrane Contactor Based CO_2 Absorption−Stripping Using Novel Solvents and Membranes. Industrial & Engineering Chemistry Research. 2005;44(5):1250-8.

97. Han H, Scofield JMP, Gurr PA, Webley PA, Qiao GG. Ultrathin membrane with robust and superior CO_2 permeance by precision control of multilayer structures. Chemical Engineering Journal. 2023;462:142087.

98. Lin Y-J, Rochelle GT. Approaching a reversible stripping process for CO_2 capture. Chemical Engineering Journal. 2016;283:1033-43.

99. Liu F, Fang M, Dong W, Wang T, Xia Z, Wang Q, Luo Z. Carbon dioxide absorption in aqueous alkanolamine blends for biphasic solvents screening and evaluation. Applied Energy. 2019;233-234:468-77.

100. Huang Q, Jing G, Zhou X, Lv B, Zhou Z. A novel biphasic solvent of amino-functionalized ionic liquid for CO_2 capture: High efficiency and regenerability. Journal of CO_2 Utilization. 2018;25:22-30.

101. Mohsin HM, Johari K, Shariff AM. Virgin coconut oil (VCO) and potassium glycinate (PG) mixture as absorbent for carbon dioxide capture. Fuel. 2018;232:454-62.

102. Idem R, Shi H, Gelowitz D, Tontiwachwuthikul P. Catalytic method and apparatus for separating a gaseous component from an incoming gas stream. Google Patents; 2011.

103. Alivand MS, Mazaheri O, Wu Y, Zavabeti A, Stevens GW, Scholes CA, Mumford KA. Water-Dispersible Nanocatalysts with Engineered Structures: The New Generation of Nanomaterials for Energy-Efficient CO_2 Capture. ACS Applied Materials & Interfaces. 2021;13(48):57294-305.

104. Caplow M. Kinetics of carbamate formation and breakdown. Journal of the American Chemical Society. 1968;90(24):6795-803.

105. Danckwerts PV. The reaction of CO_2 with ethanolamines. Chemical Engineering Science. 1979;34(4):443-6.

106. Zhang X, Zhang R, Liu H, Gao H, Liang Z. Evaluating CO_2 desorption performance in CO_2-loaded aqueous tri-solvent blend amines with and without solid acid catalysts. Applied Energy. 2018;218:417-29.

107. Lv B, Guo B, Zhou Z, Jing G. Mechanisms of CO_2 Capture into Monoethanolamine Solution with Different CO_2 Loading during the Absorption/Desorption Processes. Environmental Science & Technology. 2015;49(17):10728-35.

108. Shi H, Zheng L, Huang M, Zuo Y, Kang S, Huang Y, et al. Catalytic-CO2-Desorption Studies of DEA and DEA–MEA Blended Solutions with the Aid of Lewis and Brønsted Acids. Industrial & Engineering Chemistry Research. 2018;57(34):11505-16.

109. Natewong P, Prasongthum N, Reubroycharoen P, Idem R. Evaluating the CO_2 Capture Performance Using a BEA-AMP Biblend Amine Solvent with Novel High-Performing Absorber and Desorber Catalysts in a Bench-Scale CO_2 Capture Pilot Plant. Energy & Fuels. 2019;33(4):3390-402.

110. Liu H, Zhang X, Gao H, Liang Z, Idem R, Tontiwachwuthikul P. Investigation of CO_2 Regeneration in Single and Blended Amine Solvents with and without Catalyst. Industrial & Engineering Chemistry Research. 2017;56(27):7656-64.

111. Srisang W, Pouryousefi F, Osei PA, Decardi-Nelson B, Akachuku A, Tontiwachwuthikul P, Idem R. CO_2 capture efficiency and heat duty of solid acid catalyst-aided CO_2 desorption using blends of primary-tertiary amines. International Journal of Greenhouse Gas Control. 2018;69:52-9.

112. Bhatti UH, Shah AK, Kim JN, You JK, Choi SH, Lim DH, et al. Effects of Transition Metal Oxide Catalysts on MEA Solvent Regeneration for the Post-Combustion Carbon Capture Process. ACS Sustainable Chemistry & Engineering. 2017;5(7):5862-8.

113. Sinfelt JH. Chemistry of catalytic processes, by Bruce C. Gates, James R. Katzer, and G. C. A. Schuit. Mcgraw-Hill, 1979, 464 pp. $28.50. AIChE Journal. 1979;25(4):734-.

114. Zhang X, Liu H, Liang Z, Idem R, Tontiwachwuthikul P, Jaber Al-Marri M, Benamor A. Reducing energy consumption of CO_2 desorption in CO_2-loaded aqueous amine solution using Al_2O_3/HZSM-5 bifunctional catalysts. Applied Energy. 2018;229:562-76.

115. Deka DJ, Jang GG, Kasturi A, Stamberga D, Keum JK, Custelcean R, Tsouris C. Pronounced reduction in the regeneration energy of potassium sarcosinate CO_2 capture solvent using TiO_2. Separation and Purification Technology. 2025;354:128850.

116. Zhang X, Zhang X, Liu H, Li W, Xiao M, Gao H, Liang Z. Reduction of energy requirement of CO_2 desorption from a rich CO_2-loaded MEA solution by using solid acid catalysts. Applied Energy. 2017;202:673-84.

117. Prasongthum N, Natewong P, Reubroycharoen P, Idem R. Solvent Regeneration of a CO_2-Loaded BEA–AMP Bi-Blend Amine Solvent with the Aid of a Solid Brønsted $Ce(SO_4)_2/ZrO_2$ Superacid Catalyst. Energy & Fuels. 2019;33(2):1334-43.

118. Xu Y, Jin B, Jiang H, Li L, Wei J. Investigation of the regeneration of a CO_2-loaded ammonia solution with solid acid catalysts: A promising alternative for reducing regeneration energy. Fuel Processing Technology. 2020;205:106452.

119. Ko YG, Shin SS, Choi US. Primary, secondary, and tertiary amines for CO_2 capture: Designing for mesoporous CO_2 adsorbents. Journal of Colloid and Interface Science. 2011;361(2):594-602.

120. Alivand MS, Mazaheri O, Wu Y, Stevens GW, Scholes CA, Mumford KA. Preparation of Nanoporous Carbonaceous Promoters for Enhanced CO_2 Absorption in Tertiary Amines. Engineering. 2020;6(12):1381-94.

121. Bhatti UH, Nam S, Park S, Baek IH. Performance and Mechanism of Metal Oxide Catalyst-Aided Amine Solvent Regeneration. ACS Sustainable Chemistry & Engineering. 2018;6(9):12079-87.

122. Shi H, Naami A, Idem R, Tontiwachwuthikul P. Catalytic and non catalytic solvent regeneration during absorption-based CO_2 capture with single and blended reactive amine solvents. International Journal of Greenhouse Gas Control. 2014;26:39-50.

123. Hu X, Yu Q, Cui Y, Huang J, Shiko E, Zhou Y, et al. Toward Solvent Development for Industrial CO_2 Capture by Optimizing the Catalyst–Amine Formulation for Lower Energy Consumption in the Solvent Regeneration Process. Energy & Fuels. 2019;33(11):11507-15.

124. Momeni A, McQuillan RV, Alivand MS, Zavabeti A, Stevens GW, Mumford KA. Direct air capture of CO_2 using green amino acid salts. Chemical Engineering Journal. 2024;480:147934.

125. Soumbati Y, Bouatou I, Abushaban A, Belmabkhout Y, Necibi MC. Review of membrane distillation for desalination applications: Advanced modeling, specific energy consumption, and water production cost. Journal of Water Process Engineering. 2025;71:107296.

126. Najib A, Orfi J, Alansary H, Ali E, Abdulwahed Z, Alzahrani S, Chafidz A. An experimental investigation of a solar-driven desalination system based on multi-effect membrane distillation. Desalination and Water Treatment. 2020;198:1-18.

127. Farquet P. Efficiency redefined: The role of heat pumps and MVR in sustainable distillation. White Paperby (Sulzer). November 2024.

128. Momeni A, McQuillan RV, Anisi H, Alivand MS, Zavabeti A, Stevens GW, et al. Catalytic Membrane Vacuum Regeneration: Enhancing Energy Efficiency and Renewable Compatibility in Direct Air Capture. Small.21(25):2503023.

129. Guo Y, Zhang H, Fu K, Chen X, Qiu M, Fan Y. Integration of solid acid catalyst and ceramic membrane to boost amine-based CO_2 desorption. Energy. 2023;274:127329.

130. Wang Z, Fang M, Ma Q, Zhao Z, Wang T, Luo Z. Membrane Stripping Technology for CO_2 Desorption from CO_2-rich Absorbents with Low Energy Consumption. Energy Procedia. 2014;63:765-72.

131. Qi D, Zhang K, Tian G, Jiang B, Huang Y. Stretchable Electronics Based on PDMS Substrates. Advanced Materials. 2021;33(6):2003155.

132. Ansaloni L, Hartono A, Awais M, Knuutila HK, Deng L. CO_2 capture using highly viscous amine blends in non-porous membrane contactors. Chemical Engineering Journal. 2019;359:1581-91.

133. McQuillan RV, Momeni A, Alivand MS, Stevens GW, Mumford KA. Evaluation of potassium glycinate as a green solvent for direct air capture and modelling its performance in hollow fiber membrane contactors. Chemical Engineering Journal. 2024;481:148764.

134. Kasturi A, Gug Jang G, Dona-Tella Akin A, Jackson A, Jun J, Stamberga D, et al. An effective air–liquid contactor for CO_2 direct air capture using aqueous solvents. Separation and Purification Technology. 2023;324:124398.

135. Ozkan M, Nayak SP, Ruiz AD, Jiang W. Current status and pillars of direct air capture technologies. iScience. 2022;25(4):103990.

136. Seipp CA, Williams NJ, Kidder MK, Custelcean R. CO(2) Capture from Ambient Air by Crystallization with a Guanidine Sorbent. Angew Chem Int Ed Engl. 2017;56(4):1042-5.

137. Akaya H, Lamnini S, Sehaqui H, Jacquemin J. Amine-Functionalized Cellulose as Promising Materials for Direct CO_2 Capture: A Review. ACS Applied Materials & Interfaces. 2025;17(11):16380-95.

138. Wang S, Shang C, Deng Y, Baeyens J, Plisko TV, Bildyukevich AV, et al. CO_2 capture from flue gas using EAE-1DMA2P solvent in a packed column. Chemical Engineering Journal. 2024;480:147918.

139. Li G, Shen X, Jiao X, Xie F, Hua J, Lin H, et al. Novel tri-solvent amines absorption for flue gas CO_2 capture: Efficient absorption and regeneration with low energy consumption. Chemical Engineering Journal. 2024;493:152699.

140. Supap T, Chintana S, Raphael I, and Tontiwachwuthikul PPT. Part 2: Solvent management: solvent stability and amine degradation in CO_2 capture processes. Carbon Management. 2011;2(5):551-66.

141. An K, Li K, Yang C-M, Brechtl J, Stamberga D, Zhang M, Nawaz K. Direct air capture with amino acid solvent: Operational optimization using a crossflow air-liquid contactor. AIChE Journal.n/a(n/a):e18429.

142. Vadillo JM, Díaz-Sainz G, Gómez-Coma L, Garea A, Irabien A. Chemical and Physical Ionic Liquids in CO_2 Capture System Using Membrane Vacuum Regeneration. Membranes. 2022;12(8):785.

143. Scholes CA. Membrane gas-solvent contactor process for efficient carbon capture from multiple emission sources within an industrial complex. Chemical Engineering Science. 2023;278:118915.

144. Wang X, Song C. Carbon Capture From Flue Gas and the Atmosphere: A Perspective. Frontiers in Energy Research. 2020;8.

145. Anisi H, McQuillan RV, Alivand MS, Stevens GW, Momeni A, Mazaheri O, Mumford KA. Synergistic Effect of Amino Acid Salt Hybrid Systems for DAC of CO_2. ACS Sustainable Chemistry & Engineering. 2025;13(12):4691-702.

146. Liu G, Jin W. Pervaporation membrane materials: Recent trends and perspectives. Journal of Membrane Science. 2021;636:119557.

147. Chamani H, Woloszyn J, Matsuura T, Rana D, Lan CQ. Pore wetting in membrane distillation: A comprehensive review. Progress in Materials Science. 2021;122:100843.

148. Zotti G, Zecchin S, Schiavon G, Louwet F, Groenendaal L, Crispin X, et al. Electrochemical and XPS Studies toward the Role of Monomeric and Polymeric Sulfonate Counterions in the Synthesis, Composition, and Properties of Poly(3,4-ethylenedioxythiophene). Macromolecules. 2003;36(9):3337-44.

149. Hartono A, Kim I, Knuutila HK, van der Ham LV, Goetheer E. Calorimetric Studies of Precipitating Solvent System. Energy Procedia. 2017;114:744-55.

150. Katie Lebling, Haley Leslie-Bole, Zach Byrum, Bridgwater L. 6 Things to Know About Direct Air Capture. [Available from: https://www.wri.org/insights/direct-air-capture-resource-considerations-and-costs-carbon-removal.

151. David Sandalow JF, Colin McCormick. Direct Air Capture of Carbon Dioxide. ICEF Roadmap2018.

152. Kumar PS, Hogendoorn JA, Feron PHM, Versteeg GF. Equilibrium Solubility of CO_2 in Aqueous Potassium Taurate Solutions: Part 1. Crystallization in Carbon Dioxide Loaded Aqueous Salt Solutions of Amino Acids. Industrial & Engineering Chemistry Research. 2003;42(12):2832-40.

153. Isa F, Zabiri H, Ng NKS, Shariff AM. CO_2 removal via promoted potassium carbonate: A review on modeling and simulation techniques. International Journal of Greenhouse Gas Control. 2018;76:236-65.

154. Thee H. Reactive absorption of carbon dioxide into promoted potassium carbonate solvents: University of Melbourne, Department of Chemical and Biomolecular Engineering; 2013.

155. Thee H, Smith KH, da Silva G, Kentish SE, Stevens GW. Carbon dioxide absorption into unpromoted and borate-catalyzed potassium carbonate solutions. Chemical Engineering Journal. 2012;181-182:694-701.

156. de Oliveira AF. BUFFERING FUNCTION: A GENERAL APPROACH FOR BUFFER BEHAVIOR. The Journal of Engineering and Exact Sciences. 2020;6(3):0387-96.

157. Cullinane JT, Rochelle GT. Thermodynamics of aqueous potassium carbonate, piperazine, and carbon dioxide. Fluid Phase Equilibria. 2005;227(2):197-213.

158. Tseng H-C, Lee C-Y, Weng W-L, Shiah IM. Solubilities of amino acids in water at various pH values under 298.15K. Fluid Phase Equilibria. 2009;285(1):90-5.

159. Sanz-Pérez ES, Murdock CR, Didas SA, Jones CW. Direct Capture of CO_2 from Ambient Air. Chemical Reviews. 2016;116(19):11840-76.

160. An K, Li K, Yang C-M, Brechtl J, Stamberga D, Zhang M, Nawaz K. Direct air capture with amino acid solvent: Operational optimization using a crossflow air-liquid contactor. AIChE Journal. 2024;70(9):e18429.

161. Stamberga D, Thiele NA, Custelcean R. Synergistic direct air capture of CO_2 with aqueous guanidine/amino acid solvents. MRS Advances. 2022;7(19):399-403.

162. Lu J-G, Zheng Y-F, Cheng M-D. Wetting mechanism in mass transfer process of hydrophobic membrane gas absorption. Journal of Membrane Science. 2008;308(1):180-90.

163. Wang T, Yu W, Liu F, Fang M, Farooq M, Luo Z. Enhanced CO_2 Absorption and Desorption by Monoethanolamine (MEA)-Based Nanoparticle Suspensions. Industrial & Engineering Chemistry Research. 2016;55(28):7830-8.

164. Geng Z, Yang Y, Wang Y, Zhu T, Xu W. Catalytic regeneration of amine-based absorbents for CO_2 capture: The effect of acidic sites and accessibility. Separation and Purification Technology. 2023;327:124889.

165. Kim G, Tran AV, Keum Y, Kim TY, Song CK, Lee HJ, et al. Water-induced regeneration of active acid sites in Al-MCM-41-SO_4 during continuous fructose dehydration. Chemical Engineering Journal. 2025;507:160472.

166. Li M, Askari S, Niu Y, Li T, Zavabeti A, Alivand MS, et al. One-step synthesis of SO_4^{2-}/ZrO_2-SEP solid-acid catalyst for energy-efficient CO_2 capture. Separation and Purification Technology. 2025;359:130577.

167. McQuillan RV, Niu Y, Momeni A, Zavabeti A, Jafari M, Alivand MS, et al. Employing SO_4^{2-}/ZrO_2 Super-Acid catalysts for Energy-Efficient direct air capture of CO_2. Separation and Purification Technology. 2025;376:133895.

168. Cong Y, Chen M, Xu T, Zhang Y, Wang Q. Tantalum and aluminum co-doped iron oxide as a robust photocatalyst for water oxidation. Applied Catalysis B: Environmental. 2014;147:733-40.

169. Liu W-J, Zeng F-X, Jiang H, Zhang X-S, Li W-W. Composite Fe_2O_3 and ZrO_2/Al_2O_3 photocatalyst: Preparation, characterization, and studies on the photocatalytic activity and chemical stability. Chemical Engineering Journal. 2012;180:9-18.

170. Choi Y, Kim T, Lee H, Park J, Park J, Ryu D, Jeon W. Bottom-up plasma-enhanced atomic layer deposition of SiO_2 by utilizing growth inhibition using NH_3 plasma pre-treatment for seamless gap-fill process. Scientific Reports. 2022;12(1):15756.

171. Al-Hazmi MH, Apblett AW. Benzylation of benzene over sulfated zirconia supported in MCM-41 using a single source precursor. Catalysis Science & Technology. 2011;1(4):621-30.

172. Fraenkel D. Structure of Sulfated Metal Oxides and Its Correlation with Catalytic Activity. Industrial & Engineering Chemistry Research. 1997;36(1):52-9.

173. Sekewael SJ, Pratika RA, Hauli L, Amin AK, Utami M, Wijaya K. Recent Progress on Sulfated Nanozirconia as a Solid Acid Catalyst in the Hydrocracking Reaction. Catalysts. 2022;12(2):191.

174. Zhang R, Zhou L, Li T, Niu Y, Liu H, Xiao R, et al. A green approach to CO_2 capture using fly ash-based catalysts: Performance and mechanistic insights. Fuel. 2025;394:135098.

175. Hino M, Kurashige M, Matsuhashi H, Arata K. The surface structure of sulfated zirconia: Studies of XPS and thermal analysis. Thermochimica Acta. 2006;441(1):35-41.

176. Yang C, Li T, Sema T, Tantikhajorngosol P, Jiang J, Bai X, et al. Heat and mass transfer of a novel CO_2 desorption process integrated with highly turbulent catalytic heat exchanger. Fuel. 2024;359:130028.

177. Ciftja AF, Hartono A, Svendsen HF. Selection of Amine Amino Acids Salt Systems for CO_2 Capture. Energy Procedia. 2013;37:1597-604.

178. Yildiz EA, Pepe Y, Erdener D, Karatay A, Boyacioglu B, Ünver H, et al. Effect of group electronegativity on spectroscopic, biological, chromogenic sensing and optical properties of 2-formyl-benzene sulfonic acid sodium salt-based Schiff bases. Journal of Molecular Structure. 2023;1286:135611.

179. Lara-Popoca J, Thoke HS, Stock RP, Rudino-Pinera E, Bagatolli LA. Inductive effects in amino acids and peptides: Ionization constants and tryptophan fluorescence. Biochemistry and Biophysics Reports. 2020;24:100802.

180. Vadillo JM, Gómez-Coma L, Garea A, Irabien A. CO_2 Desorption Performance from Imidazolium Ionic Liquids by Membrane Vacuum Regeneration Technology. Membranes, 2020; 10(9).

181. Lemoine A, Invernizzi R, Salvato Vallverdu G, Olchowka J, Guerlou-Demourgues L, Baraille I, Flahaut D. Relating the Electrochemical Behavior of Birnessite to the Morphology

and Specific Surface: Interest of Studying the Surface Reactivity. ACS Applied Energy Materials. 2022;5(10):12359-72.

182. Nguyen HTT, Jung D, Park C-Y, Kang DJ. Synthesis of single-crystalline sodium vanadate nanowires based on chemical solution deposition method. Materials Chemistry and Physics. 2015;165:19-24.

183. Burke PJ, Bayindir Z, Kipouros GJ. X-ray photoelectron spectroscopy (XPS) investigation of the surface film on magnesium powders. Appl Spectrosc. 2012;66(5):510-8.

184. Andreia M, João Paulo CA, Francisco Anderson SL, Monica L-C, Ana Flavia N. Enhanced photovoltaic performance of inverted hybrid bulk-heterojunction solar cells using TiO_2/reduced graphene oxide films as electron transport layers. Journal of Photonics for Energy. 2015;5(1):057408.

185. Smith M, Scudiero L, Espinal J, McEwen J-S, Garcia-Perez M. Improving the deconvolution and interpretation of XPS spectra from chars by ab initio calculations. Carbon. 2016;110:155-71.

186. Wang H, Linford M. X-ray Photoelectron Spectroscopy and Auger Electron Spectroscopy: Comparison and Basic Principles. Vacuum Technology and Coating. 2015.

187. Lazar L, Bandrabur B, Tataru-Fărmuş RE, Drobotă M, Bulgariu L, Gutt G. FTIR analysis of ion exchange resins with application in permanent hard water softening. Environmental Engineering and Management Journal. 2014;13(9):2145-52.

188. Kausar A. Fabrication and Characteristics of Poly(benzimidazole/fluoro/ether/siloxane/amide)/Sulfonated Polystyrene/Silica Nanoparticle-Based Proton Exchange Membranes Doped With Phosphoric Acid. International Journal of Polymeric Materials and Polymeric Biomaterials. 2015;64(4):184-91.